2013

DEVELOPMENT OF A CONSTITUTIVE MODEL OF COMPACTED SHALES AND DETERMINATION OF THE EFFECT OF WEATHERING ON ITS PARAMETERS

Isabel Cristina Gomez-Gutierrez
University of Kentucky, isabel.gutierrez@uky.edu

STUDENT AGREEMENT:

I represent that my thesis or dissertation and abstract are my original work. Proper attribution has been given to all outside sources. I understand that I am solely responsible for obtaining any needed copyright permissions. I have obtained and attached hereto needed written permission statements(s) from the owner(s) of each third-party copyrighted matter to be included in my work, allowing electronic distribution (if such use is not permitted by the fair use doctrine).

I hereby grant to The University of Kentucky and its agents the non-exclusive license to archive and make accessible my work in whole or in part in all forms of media, now or hereafter known. I agree that the document mentioned above may be made available immediately for worldwide access unless a preapproved embargo applies.

I retain all other ownership rights to the copyright of my work. I also retain the right to use in future works (such as articles or books) all or part of my work. I understand that I am free to register the copyright to my work.

REVIEW, APPROVAL AND ACCEPTANCE

The document mentioned above has been reviewed and accepted by the student's advisor, on behalf of the advisory committee, and by the Director of Graduate Studies (DGS), on behalf of the program; we verify that this is the final, approved version of the student's dissertation including all changes required by the advisory committee. The undersigned agree to abide by the statements above.

Isabel Cristina Gomez-Gutierrez, Student

Dr. L. Sebastian Bryson, Major Professor

Dr. Yi-Tin Wang, Director of Graduate Studies

DEVELOPMENT OF A CONSTITUTIVE MODEL OF COMPACTED SHALES AND DETERMINATION OF THE EFFECT OF WEATHERING ON ITS PARAMETERS

DISSERTATION

A dissertation submitted in partial fulfillment of the
requirements for the degree of Doctor of Philosophy in the
College of Engineering at the
University of Kentucky

By
Isabel Cristina Gomez-Gutierrez
Lexington, Kentucky
Director: Dr. L. Sebastian Bryson, Ph.D., P.E., Associate Professor of Civil Engineering
Lexington, Kentucky
2013

ABSTRACT OF DISSERTATION

DEVELOPMENT OF A CONSTITUTIVE MODEL OF COMPACTED SHALES AND DETERMINATION OF THE EFFECT OF WEATHERING ON ITS PARAMETERS

Compacted shales cause problems because they tend to degrade with time due to weathering. Degradation results in the shale deteriorating from a hard rock-like material to a soft fine-grained soil mass with lower shear strength and high deformability. Consequently, common problems that occur in embankments constructed with compacted shales include settlement and instabilities. Therefore, accelerating weathering prior to compaction by wetting and breaking down the shales before placement can reduce the deterioration during the service life of the construction. Extensive laboratory testing was performed in order to characterize the mechanical behavior of compacted shales.

Critical State theory is a clever framework that describes the mechanical behavior of soils with a simple system of equations that explains all the aspects of compression and shear of soils. NorSand is a model constructed in the framework of the Critical State theory that decouples the yield loci from the normally consolidated line. This characteristic made this model suitable for compacted shales. Also, empirical evidence showed that the plastic behavior of compacted shales is controlled by a Nova type flow rule that is a function of the mineralogical characteristics of the shales. This finding has implications in the shape of the yield loci and the hardening rule.

KEYWORDS: compacted shales, clay minerals, durability, weathering, flow rule.

Isabel Cristina Gomez Gutierrez

Student's Signature

12/18/2013

Date

DEVELOPMENT OF A CONSTITUTIVE MODEL OF COMPACTED SHALES AND DETERMINATION OF THE EFFECT OF WEATHERING ON ITS PARAMETERS

By

Isabel Cristina Gomez-Gutierrez

L. Sebastian Bryson
Director of Dissertation

Yi. Tin Wang
Director of Graduate Studies

12/18/2013

To my Family and Friends

ACKNOWLEDGEMENTS

I would like to thank Dr. Bryson, my professors, my friends, my family, and all the wonderful people that made my life in US better.

TABLE OF CONTENT

LIST OF TABLES

LIST OF FIGURES

CHAPTER 1

1. Introduction

1.1. Synopsis of the problem

In many regions of the United States and around the world, shales are widely used as a construction material for highway embankments due to the lack of other more appropriate materials. The embankments constructed with compacted shale are often associated with high repair and maintenance cost, and frequently require major remedial work. These materials cause problems because they tend to degrade with time due to weathering. Degradation results in the shale deteriorating from a hard rock-like material with high frictional resistance to a soft fine-grained soil mass with lower shear strength and high deformability. There are diverse type of shales that display different behaviors during excavation, compaction, and service life. Soft, non-durable shales are easily crushed and weathered in a short time span, and therefore can behave as soil fills. Hard, durable shales are difficult to crush, take more time to weather, and behave as rock fills. Also, there are hard, non-durable shales that are a frequent source of problems because for a short time they behave as rock fills, but a high susceptibility of weathering makes them behave as soil over long period of time.

Therefore, common problems that occur in embankments constructed with compacted shales include excessive settlement, and local and global instabilities. The more serious problems typically occur in wet areas where the compacted shale is subjected to repeated seasonal cycles of wetting and drying (Strohm et al., 1978).

Researchers such as Abeyesekera et al. (1979); Witsman and Lovell (1979), Lovel and Johnson (1981), Oakland and Lovell (1984), Surenda (1980), Halle et al. (1981), Liang and Lovell (1983), Hopkins (1988), Caswell and Trak (1985), Nwabuokei and Lovell (1986), Manasseh and Olufemi (2008) Yoshida and Hosokawa (2004), Aziz et al. (2010), Kalinski (2010), and Nahazanan et al. (2013) have performed studies regarding the effect of durability, mineralogy, water content, dry unit weight, grain size distribution, and

energy of compaction in the mechanical behavior of compacted shales. All these studies came to the same conclusion that small grain size, previous soaking (i.e. weathering), high water content, and high dry unit weight (i.e. high energy of compaction) improve the behavior of compacted shales. The aim is to accelerate the weathering so that it occurs before the compaction and reduces the permeability in order to decrease the effect of seasonal cycles of wetting and drying.

1.2. Conceptual basis

There are different methodologies used to improve the mechanical behavior of compacted shales. These methodologies are based on the idea of accelerating weathering prior to compaction by breaking down the shales before placement and reducing deterioration caused by slaking during the service life. In order to reach this goal, some methodologies recommend the use of chemical additives (Surenda, 1980; Reeves et al., 2006). Other methodologies recommend accelerating weathering by mechanically crushing the rocks to small grain size and soaking the material with water before compaction (Bishop et al., 1986; Hopkins, 1988; Machan et al., 1989; Hopkins and Beckham, 1998; Oregon Department of Transportation, 1998; Hopkins, 2004; Indiana Department of Transportation, 2011). Both methodologies are based on the theory that the mechanical behavior of a material is directly related to its mineralogical composition, crushing methodology and energy, grain size distribution, water content, density, and energy of compaction (Pye and Miller, 1990; Noble, 1977; Reeves et al., 2006).

However, the effect of the time of soaking to accelerate the weathering in the mechanical behavior of compacted shales has been poorly studied.

The majority of the simplest elastic plastic constitutive models, such as Druker-Prager or Mohr-Coulomb, neglect the effect of the void ratio in the behavior of soils such that they treat each sand density as a different material with properties to be estimated by experiments. The most complex constitutive models, such as Hypoplastic or Plastic Hardening, are mathematically complex and require many parameters and a great deal of time to apply.

Critical state theory is a clever framework that couples the yield locus size to void ratio in

a way that explains how and why the behavior changes with density (Jefferies, 1993). The theory describes the mechanical behavior of soils with a simple system of equations that explains all the aspects of compression and shear within a well-defined group of parameters (Schofield and Wroth, 1968; Roscoe and Burland, et al., 1968; Jefferies and Been, 2006). The application of this theory to compacted shales has not been attempted.

This research seeks to investigate in detail which mechanical parameters improve or degrade with the soaking before compaction and shear and the description of this phenomenon in the framework of critical state theory.

1.3. Objective of research

1.3.1. General objective

To characterize under the critical state theory the mechanical behavior of compacted Paleozoic shales of Kentucky subject to accelerated weathering.

1.3.2. Specific objectives

- Perform index, mineralogical, and mechanical testing of crushed and compacted shales from Kentucky.
- Describe the mineralogical, index, durability, and mechanical behavioral characteristics of crushed and compacted shales, and find the relationship among them.
- Model mathematically the mechanical behavior of improved compacted shales in the framework of Critical State theory.

1.4. Relevance of the research

Shales are close to 80 percent of the rocks that outcrop on the earth's surface. Therefore, shales are commonly used in the construction of embankments and backfills because these materials are in close proximity of the construction activities. This research will present a better understanding of the behavior of compacted shales, and a better understanding of the variation of the parameters in order to formulate better predictions.

This attempt is a step toward future implementation of these results in more advanced numerical methods.

1.5. Content of the thesis – Outline of the dissertation:

- Chapter 2 presents the theoretical background of the research. The first part of the chapter presents the shale definition, typical composition, and their influence on weathering characteristics. The second part of the chapter presents the general behavior of compacted shales, and the third part shows the theoretical bases of the mechanical behavior of soils.
- Chapter 3 presents the sample characterization through mineralogical composition. The first part of the chapter presents where the shale samples were collected and a description of the geological formations, to which the samples belong. The second part presents the mineralogical tests that were performed. The third part presents results and a discussion of the mineralogical tests.
- Chapter 4 presents the sample preparation and characterization by index properties and durability. The first part shows the methodology that was used to prepare the samples, the second and third parts show the index and durability properties, and the fourth part presents the results and conclusions through a discussion of the characteristics of the grain size distribution of the sample, the relation to index properties and durability, and the effect of the mineralogical content on the index properties and durability.
- Chapter 5 presents the sample characterization through the consolidated isotropically undrained triaxial tests. The chapter presents the procedure and the description of the triaxial testing. Also it presents the results and discussion of the influence of index properties, durability, and mineralogical characteristics on the mechanical parameters of compacted shales. This chapter also presents the effect of soaking on the behavior of compacted shales.
- Chapter 6 presents a discussion of the behavior of compacted shales in the critical state and in the peak state. This chapter also presents the influence of mineralogical composition, index properties, and durability on the critical state parameters.
- Chapter 7 presents the performance of the critical state models on the compacted

shales of this study.

- Chapter 8 presents a modification of the NorSand Critical State model, taking into account the observed behavior of compacted shales.
- Chapter 9 presents the conclusions and recommendations

.

CHAPTER 2

2. Background of research

Below is presented the theoretical background of the investigation. This chapter is divided in two parts: The first part presents the characteristics of the most common minerals in shales and explains the soil water interaction that produces weathering. The second part presents the recommendations to build compacted shale embankments and the constitutive model that will be used to describe the mechanical behavior of such embankments.

2.1. Shale composition

To understand the mechanical behavior of compacted shales it is important to delineate the definition of shale for this study. Mud is a mix of unknown proportions of silt and clay size particles in unconsolidated sediments. Mudrocks are any sediment made up of silt and/or clay that has suffered diagenesis. If most of the particles are clay size, the rock is called claystone and if most of the particles are silt size it is siltstone. Mixtures of both components are named mudstone. Shale is a term originally applied to mudrocks by logger engineers, and usually shales are referred to mudstones that present fissility (Nichols, 2009). For this study, shale is a mudstone that is a fine-grained detrital sedimentary rock composed of clays, quartz, and other minerals such as carbonates, feldspars, pyrite, or iron oxides, and organic matter (Boggs, 2009).

The color of the shales is related to their composition and therefore their mechanical behavior. Dark-colored shales contain organic matter and pyrite. These kinds of shales were deposited in an anoxic environment of deep marine waters or shallow waters with a rich source of organic matter. Brownish-red-colored shales contain iron oxides, and were deposited in oxygen-rich shallow waters (Nichols, 2009).

Mudrocks or shales can be considered consolidated silt and clays deposits that have undergone diagenesis, which converts soil into indurated rock. Diagenesis is the physical and chemical changes that transform unconsolidated sediments such as sand, mud,

carbonate, and organic matter into indurate rock of sandstone, shale, limestone, and coal, respectively, as they are buried (Nichols, 2009; Walther, 2009). Diagenesis occurs due to the accumulation of sediments that increase overburden pressure; then, cementation and compaction increase the unit weight, decrease the void ratio, expel the pore water, and break down the organic matter. The little water that remains is almost all in the interlayers of clays and adsorbed by clay surfaces. (Nichols, 2009; Walteher, 2009). Diagenesis occurs at low temperature and pressure, below 250 °C and up to 5km.

Gibbsite, kaolinite, or smectite form at shallow depths and low temperatures as a result of weathering due to meteoric water flow (Bjolykke, 1998). In general, the reaction is rock (feldspar, mica) + water = (gibbsite, kaolinite, or smectite) + cations (K^+).

These clay minerals become unstable with increase in burial, temperature, and/or time (Bjolykke, 1998). The reversed weathering is characterized by the reaction (kaolinite, smectite) + cations (K^+) = aluminosilicate (illite) + quartz + water.

2.1.1. Mineralogical composition

Shales are composed of clay minerals, quartz, and other minerals.

2.1.1.1. Clay Minerals

Clay minerals are silicates that belongs to the group of phyllosilicates. They are composed of Si^{4+} tetrahedral sheets, and Al^{3+} and Mg^{2+} octahedral sheets. When the tetrahedral and octahedral sheets are joined in a layer, the resulting structure can be either electrically neutral, or negatively or positively charged due to isomorphic substitutions of Si^{4+}, Al^{3+}, Mg^{2+}, and Fe^{3+} and Fe^{2+}. However, all the minerals must be electrically neutral. Therefore, the electrical neutrality is reached by the occupancy of the faces, edges and interlayer spaces by exchangeable ions (Brigatti et al, 2006). The large high specific area (surface area per weight) due to the crystal structure and imbalances in the charges make the clay minerals highly reactive. The principal clay minerals in shales are kaolinite, smectite, illite, and chlorite.

Kaolinite is a 1:1 clay mineral composed of one tetrahedral sheet attached to one Al octahedral sheet. It has a rigid structure without isomorphic substitutions that cannot

expand. The specific area and the CEC are low. Kaolinite is stable under a high range of pressure and temperature. Kaolinite is found in silt and coarse clay sizes (Murray, 2006). The formation of kaolinite requires the dissolution of feldspars, mica, or other clays through the flow of meteoric water that removes cations such as Na^+ and K^+ (Bjolykke, 1998). This means that kaolinite is common in wet environments. Also, it is possible that kaolinite will transform into dickite during diagenesis at high burial depth and temperature.

Smectite is a group of clay minerals common in soils in dry environments. Smectite slowly converts to illite during diagenesis. Smectite group are 2:1 clay minerals composed of one Al octahedral sheet between two tetrahedral sheets joined by OH bonds. There is an isomorphic substitution of one Si^{4+} by one Al^{3+} in the tetrahedral sheet, which produces charge imbalances that are solved by ions of Ca^{2+} and H_30^+ in the interlayers. Therefore, smectites have an extremely high reactivity, specific area, and CEC (Murray, 2006).

The conversion of smectite into illite is named the I/S transformation. The I/S transformation occurs because there is an exchange of Ca^{2+} for K^+ in the interlayers. This transformation produces mixed layers of illite-smectite that change proportion as the diagenesis progresses. During this transformation, a low-temperature quartz forms and K-feldspar dissolves because it is the source of K^+. The I/S transformation starts at 70 °C (around 2 – 3 km) and finishes at 200 °C (about 6.5-8 km), with no smectite remaining (Bjolykke, 1998; Walther, 2009). At temperatures higher than 300 °C (around 10-12 km) metamorphism starts and illite recrystallizes to sericite and muscovite (Reeves et al., 2006; Walther, 2009). Also, kaolinite and K-feldspar react to form illite at temperatures between 130 °C and 140 °C (around 4 km) (Bjolykke, 1998).

Due to the exchange of Ca^{2+} for K^+ and, unlike smectites, illite has a firm structure that does not present high expansion. Therefore, the specific area and CEC are low. Illite can be found in coarse clay, silt and fine sand fraction (Murray, 2006).

Another common clay mineral in shales is chlorite. Chlorite is a 2:1:1 clay mineral composed of one Mg octahedral sheet in the middle of two 2:1 sheets. Chlorite has a rigid structure that does not expand. It has a low specific area and low CEC. It can be found in

silt and coarse clay fraction (Murray, 2006). Chlorite has two geneses. It is a byproduct of the I/S transformation, forming mixed layers chlorite-illite, and is also the result of the reaction of kaolinite with quartz. Both genesis are possible only if there is a source of Mg and Fe. Chlorite starts to form at approximately 80 °C and around 2.5 km (Bjolykke, 1998; Walther, 2009).

2.1.1.2. Quartz

Quartz is a tectosilicate composed of a dense structure of SiO_4^{-4} tetrahedral wherein each oxygen is shared by the other two tetrahedrals to give a SiO_2. Quartz has a low specific area. Quartz can be found in fine sand, silt, and clay sizes.

2.1.1.3. Other minerals in shales

Other minerals commonly present in shales are feldspar, carbonates, pyrite, or iron oxides (Boggs, 2009; Walther, 2009).

Feldspars are also tectosilicates with a dense crystalline structure. They have the general composition of $(AlSi_3O_8)^-$ and can attach with K^+, Ca^{+2} or Na^+. In shales it is deposited along with clays and quartz. It is dissolved during the I/S transformation.

Carbonates are a group of minerals that are the combination of a carbonate anion $(CO_3)^{-2}$ with cations such as Ca^{+2}, Mg^{+2} and Fe^{+2} that form calcite, $CaCO_3$, dolomite $CaMg(CO_3)_2$, and siderate $Fe(CO3)_2$. In shales, carbonates are formed as a cement in the deposits of mud during sedimentation and diagenesis of the shales. However, shales also have Calcite that are deposited along with clays and quartz. Carbonates dissolve in acid environments, producing CO_2 and H_2O.

Pyrite is an iron sulfide FeS_2 that in shales occurs by the reaction during the diagenesis of H_2S with Fe^{2+} in anoxic environments rich in organic matter. Pyrite oxidizes in the presence of water and oxygen producing iron oxides, usually limonite and sulfuric acid. This acid can dissolve the carbonates and chlorite.

In brownish-red-colored shales there are iron oxides such a Limonite ($FeO(OH)\cdot nH_2O$) and Hematite (Fe_2O_3). They are indicative of an environment rich in oxygen.

Some shales can contain gypsum. Gypsum is a hydrated calcium sulfite ($CaSO_4\cdot H_2O$)

that is the product of the oxidation of pyrite and the dissolution of calcite together. Gypsum indicates that the shale starts the process of weathering.

2.1.2. Weathering and soil/rock-water interaction

Weathering is the breakdown of rocks into smaller rock particles (i.e. sediments). Weathering can be mechanical or chemical. Mechanical weathering is the physical disintegration of rock into small fragments, each with the same or with just slightly altered properties as the original material. This type of weathering can result from temperature changes (freezing and thawing), moisture changes (cycles of wetting and drying), exposure to air, unloading of rock masses (sheet joints), and biogenic processes (plants, animals, etc.). Chemical weathering is a process that occurs due to the change of the environmental conditions of the rock that made some of the minerals unstable under the new environmental conditions that produce matter transferred from unstable minerals to more stable mineral or soluble species. Chemical weathering is dependent on the presence of atmospheric reactants (i.e. oxygen, carbon dioxide), temperature, and presence of chemically active fluids (i.e. water). Chemical weathering can also be increased by pollutants such as acid rain, smoke emissions, nitrogen oxides, etc. (Morgenstern and Eigenbrod, 1974; Essington, 2004). Chemical weathering is accelerated by mechanical weathering.

The weathering of compacted shales is directly related to the weathering of the individual particles of shales that compose the compacted material. But in turn, the process of crushing the shales to a given size is per se a mechanical weathering. The construction of compacted shales implies that the particles of shales will wet to a given water content under atmospheric conditions.

During the wetting, soil/rock-water interaction occurs. Figure 2.1 shows a sketch that explains the processes that take place when a piece of shale is placed in water. When pieces of shale samples are initially submerged in pure water, an ion exchange process starts between the attached cations in the surface of the mineral, especially clay minerals and the hydronium ion (H_3O^+). The H_3O^+ attaches to the face of the clay particles, and the cations go into solution. The ion exchange causes an increase in pH due to the

remaining hydroxyl ion (OH^-) after the ion exchange. This process is time-dependent and will occur until all the cations on the clay face are exchange by H_3O^+ or when the aqueous solution becomes saturated with the cations and cannot hold more cations. The basal surface of clay minerals are negatively charged due to the isomorphic substitutions while the charge in the edge's site dependents on the pH. Therefore, with the increase of the pH the edges of the clay minerals become negatively charged with the subsequent repulsion between particles that cause dispersion (Wallace, 1998). Also, there are dispersion when carbonates dilsolved due to the increase of pH.

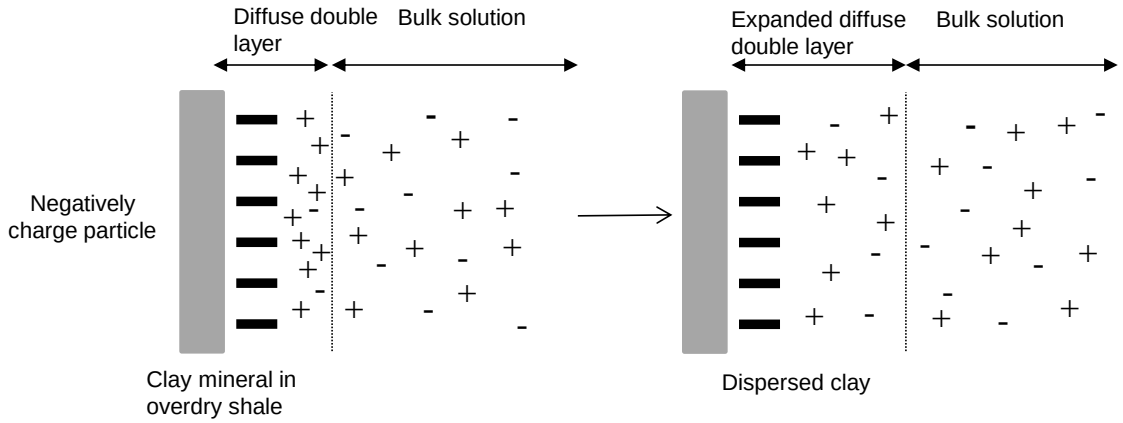

Figure 2.1 Mechanism of dispersion when a piece of shale is submerged in water (modify Reeves et al., 2006).

The dispersion of the clay minerals in shales is the cause of slaking. Slaking results in the formation of fractures and the flaking of shales. The measurement of this slaking is done by the slake durability tests. The two most commonly used slaking tests are the jar-slake test (Wood and Deo, 1975; Shamburger et al., 1975), and the slake durability test (Franklin and Chandra, 1972).

The jar-slake test requires samples to be immersed in water for a specified amount of time, with periodic observations of the characteristics of the samples with time. This test is qualitative. The slake durability test (ASTM D4644) also requires samples to be immersed in water while being tumbled in a wire mesh drum over 10 minutes for two cycles of wetting and drying. The relation between the initial weight and the final weight is the slake durability index, $Id_{(2)}$. Bryson et al. (2012) proposed the loss slake test that

follows the same procedure as the slake durability test with the difference that in this test only one cycle of wetting and drying is necessary, and the procedure is done for 10, 25, 60, and 120 minutes. The result of this test is the lost slake index, LSI, which represents the logarithmic decay of durability with the time of cycling. Finally, Kinkerdon and Bryson (2013) proposed the electrical jar test that is similar to the jar test, but EC and pH measurements are performed during different periods of time to evaluate changes of these parameters in the water where the particles of shales are submerged. A parameter S_{jar} is evaluated as the slope of change of EC with time in a semilog space.

Finally, Noble (1977) and Pye and Miller (1990) concluded that before one constructs a compacted shale ebankment, the following mineralogical characteristics have to be considered:

a. Occurrence of pyrite and calcite, as gypsum can form with weathering in their presence, and therefore swelling will occur.
b. Occurrence of carbonates and illite in a potentially acidic environment, because illite can weather to one of the clays of the smectite group, and swelling will occur.
c. Occurrence of pyrite and chlorite in a potentially acidic environment, because chlorite can weather to one of the clays of the vermiculite, and swelling will occur.
d. In extremely acidic environments the dissolution of kaolinite forms gibbsite, allophane, and amorphous gel.

Some of these reactions occur quickly. Therefore, if the shale is left soaking for some time before compaction, this reaction can be completed before the construction of the embankment and the swelling can be controlled.

2.2. Mechanical Behavior of compacted shales

The behavior of compacted shale is strongly influenced by the composition of the shale particles, the grain size distribution of the broken shale, and the compaction energy used. The compaction process employed for embankment construction consists on breaking up and crushing shale mass into small pieces. Then, the shale is compacted to an optimum water content, ω_{opt} and dry unit weight, γ_d, commonly given by compaction tests results. Usually, these compaction tests are performed for shale samples that are wetted with only

the water necessary to reach the optimum water content, and after a short time the test is performed. The results of these tests are mechanical parameters that describe the compacted shale behavior in the short term, and do not describe how the material properties are affected by wetting over long periods of time.

In the 1970s' it was observed that most highway embankments and earth dams that were constructed with compacted shales presented problems of high settlements, high susceptibility to swell, and slope instability. For these reasons, the U.S. Department of Transportation conducted the research "Design and Construction of Shale Embankments" to evaluate the main problems, causes, and solutions for shale embankments failure around the United States (Strohm, 1980). They found three main causes for shale embankment failure. The first cause was the infiltration of surface water or subsurface seepage water that wet the embankment due to a lack of adequate benching and drainage of underlying slopes. The second was the construction of rock fills with hard nondurable shales, which when wet slake or soften into small fragments. The third cause was the uncontrolled mixing of soil, shale, and hard rocks (i.e. sandstone and limestone) for rock fills that prevent adequate compaction. When embankments are wet or inundated, these three concerns cause the particles of shale to slake or soften, resulting in the creation of cavities that result in large settlements (Strohm, 1980). For Strohm (1980), the main problem was to determine which shales were durable enough to be used for rock fills in thick lifts and which must be broken down and compacted as soil in thin lifts.

As a result of the U.S. Department of Transportation research, it was recommended that the slake durability test (Franklin and Chandra, 1980) and the jar slaking test (Wood and Deo, 1975; Shamburger et al., 1975) be used to get criteria for the classification of shales as soil-like shale or rock-like shale. It is also recommended to excavate and separately compact shale, limestone, and sandstone within the embankment. Compacted shales are treated as a soil and is located in the central portion of the embankment. Sandstone and limestone is treated as rock fills and is located in the shells with steep slopes. Hard nondurable shale requires extra crushing (blasting or impaction) to break down large pieces for proper compaction in thin lifts. Finally, any rock filter can be constructed with crushed shales (Strohm, 1980).

This section shows the studies that have been performed to understand the mechanical behavior of compacted shales and the recommendations to improve the material properties by accelerating the weathering through mechanically crushing and soaking before compaction.

2.2.1. General behavior of compacted shale

Abeyesekera et al. (1979), Witsman and Lovell (1979), Johnson and Lovell (1979), Oakland and Lovell (1984), Halle and Lovell (1981), Halle (1981), Nwabuokei and Lovell (1986), Surendra (1980), and Liang and Lovell (1982) between others studied compaction methods, degradation due to compaction, laboratory testing to evaluate slaking potential, and additives to control the slaking of shales. Similar research was performed for shales that are used in Kentucky to construct compacted shale embankments (Hopkins and Deen, 1984; Bishop et al., 1986; Hopkins, 1988; Hopkins, 2007). Several studies have also been completed that investigated the mechanical behavior of dry, wet, and short- and long-term saturated compacted shales (Wu et al., 1993; Yoshida et al., 2004; Aziz et al., 2010; Nahazanan et al., 20013). Other studies have evaluated the wetting-induced compression (Lawton et al., 1992; Lim and Miller, 2004). There are also studies about the big settlement problems of coal mine landfills, which are often constructed with uncontrolled mixes of sandstones, limestones, and shales (Kalinski, 2010).

In particular, Abeyesekera et al. (1979), Witsman and Lovell (1979), and Hopkins (1988) performed consolidated undrained triaxial tests in unweathered and weathered samples of compacted shales. The specimens were compacted with crushed or weathered samples that were previously wetted in order to reach optimum water content. The grain size distribution of the crushed shale, the water content, the dry unit weight, and the compaction energy were controlled. The researchers found that the compaction process imparted an as-compacted prestress pressure to the shale. When the consolidation pressure was small compared to the prestress pressure, the compacted shale behaved as a highly OC clay. When these pressures were equal or near equal to the consolidation pressure, the behavior was similar to that of normally consolidated, NC clay. The significance of this finding is that NC soils typically experience more deformation and

exhibit lower shear strength than OC soils. This suggests that shear behavior of compacted shale is heavily dependent upon the compaction energy used to compact the specimens.

Liang and Lovell (1983) studied the behavior of samples taken from shale embankments and the relationship among shear behavior, water content, dry unit weight, roller type, and number of roller passes. They found that the water content had a major influence on the shear behavior. Specifically, samples with low water content tend to be stiffer and have a tendency to dilate at small strains.

2.2.2. Improvement of compacted shales

All of the studies cited in the previous section have found that compression, shear behavior, and shear strength are influenced by the degree of compaction. Immersion causes important increments in volumetric compression during consolidation, reduction in mobilized shear stress, change in dilatant nature during shear and enormous volumetric compression during consolidation and drastic loss of strength parameters. These problems can be controlled depending on the type of shales. In general, all shales, and in particular non-durable shales, should be crushed to small grain sizes, and soaked in water over some time such that the material slakes or softens before compaction. This material should be compacted in thin layers with high water content, and high dry unit weight. In this way, permeability will be low, which will prevent the effects of cycles of seasoned wetting and drying.

2.3. Critical State Constitutive Models

This section also presents the mathematical framework that will be used to describe the mechanical behavior of compacted shales.

Constitutive models are a group of mathematical relationships between stresses and strains that describe the behavior of a single element of soil in a continuum used for solving geotechnical problems under general stress conditions with finite element, finite difference, and other numerical techniques (Lade, 2006). For this dissertation, the Critical State framework was selected to describe the behavior of compacted shales because it is

relatively simple in its mathematical expressions and its parameters are well-known parameters of the classical soil mechanics that can be calculated with simple tests such as consolidation and triaxial tests. The first Critical State models – the Cam Clay model (CC) by Roscoe and Schofield (1963) and Schofield and Wroth (1968), and the Modified Cam Clay (MCC) by Roscoe and Burland (1968) - were formulated to describe the behavior of remolded clays. In the 90s and 2000s Jefferies and coworkers modified the CC model for application to sands and created the NorSand model (Jefferies, 1993 and Jefferies and Been, 2006). NorSand is an extension of the CC model to simulate static liquefaction, liquefaction triggered by cyclic loads and dilative failure of sands. The main assumptions of these models are that the soil is isotropic and homogeneous, a single yield locus exists at any instant, there is no intrinsic cohesion between soil particles, stress is coaxial with strain increment, and strain increment is normal to the yield locus.

All the mathematical expressions are presented in terms of octahedral stresses in axisymmetric condition:

$$p' = \frac{\sigma'_a + 2\sigma'_r}{3} = p - u \qquad [2.1a]$$

$$q = \sigma_a - \sigma_r \qquad [2.1b]$$

$$\dot{\varepsilon}_p = \dot{\varepsilon}_a + 2\dot{\varepsilon}_r \qquad [2.2a]$$

$$\dot{\varepsilon}_q = \frac{2\left(\dot{\varepsilon}_a - \dot{\varepsilon}_r\right)}{3} \qquad [2.2b]$$

Where σ_a' and σ_r' are the effective axial and radial normal stresses, $\dot{\varepsilon}_a$ and $\dot{\varepsilon}_r$ are the increment in the axial and radial strain, *p*' is the effective mean stress, *q* is the deviatoric or shear stress, and $\dot{\varepsilon}_p$ and $\dot{\varepsilon}_q$ are the increment of total volumetric and shear strains. Compressive stresses and strains are considered positive. The total strains are the summation of the elastic and plastic strains:

$$\dot{\varepsilon}_p = \dot{\varepsilon}_p^e + \dot{\varepsilon}_p^p \qquad [2.3a]$$

$$\dot{\varepsilon}_q = \dot{\varepsilon}_q^e + \dot{\varepsilon}_q^p \qquad [2.3b]$$

2.3.1. General definitions

2.3.1.1. Formulation for remolded clay

Figure 2.2 shows the compression and critical state curves of a remolded clay. The isotropic normally consolidated line *iso-ncl*, of a remolded clay is unique and is given by:

$$e = e_{\lambda} - \lambda_{ncl} \ln(p') \qquad [2.4]$$

Where e is the void ratio, λ_{ncl} is the slope in the e - $ln(p')$ space and e_{λ} is a reference value of the void ratio when p'=1kPa. Equation [2.4] represents the elastic-plastic change of void ratio during isotropic loading. The elastic unload reload line, *url*, has the form:

$$e = e_{k} - \kappa \ln(p') \qquad [2.5]$$

where κ is the slope and e_k is a reference value when p'=1kPa. The critical state line, *csl*, in e - $ln(p')$ space is:

$$e_c = \Gamma - \lambda_s \ln(p'_c) \qquad [2.6]$$

where e_c is the void ratio at CS, λ_s is the slope and Γ is a reference value when p'=1kPa, p'_c is the mean stress at the critical state. For remolded clays it can be assumed that the *iso-ncl* is parallel to *csl* (i.e. λ_s = λ_{ncl}). λ_s, κ, and Γ are assumed to be unique material properties of the soil.

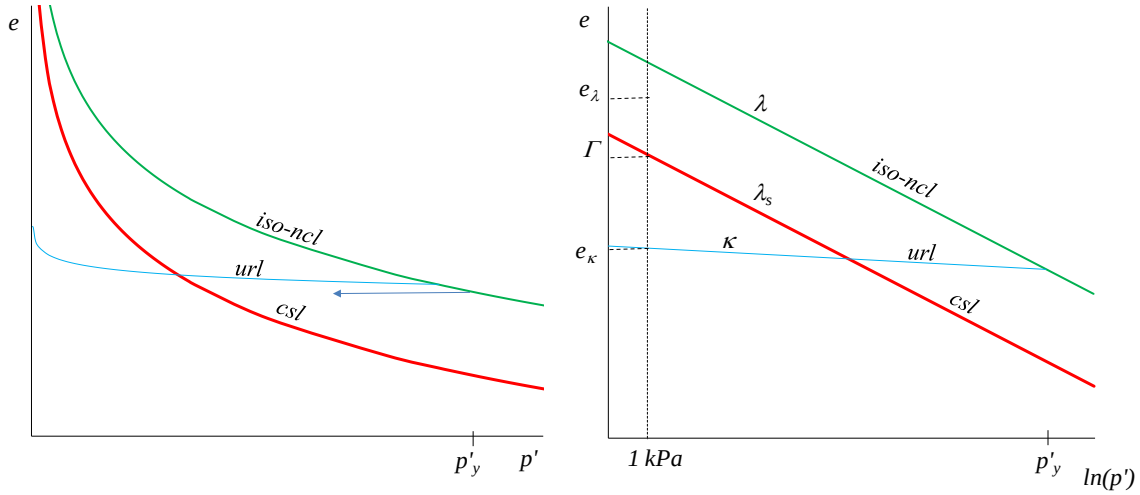

Figure 2.2. Compression curve (after Wood, 1991).

2.3.1.2. Formulation for sands

Real soils exist in a spectrum of states that made the soil exist in a given stress condition at different void ratios (Jefferies and Been, 2006). Therefore, there is an infinite number of normally consolidated lines, not parallel to *csl*, which depend on the initial void ratio at deposition time or at soil compaction process. This is especially true in the case of sands. In order to characterize the state of the soil the following two parameters are required: the state parameter, ψ, and the overconsolidation ratio, R. The state parameter links void ratio and stress levels and R represents the proximity of a state point to its yield locus (Jefferies and Been, 2006). They are given by:

$$\psi = e - e_c \qquad [2.7]$$

$$R = \frac{p'_y}{p'} \qquad [2.8]$$

where e_c is the value of e at the *csl* in a hypothetical constant mean stress triaxial test, p'_y is the yielding pressure. This yielding pressure is a preconsolidation pressure or is the projection of the yield locus p'_y that has not been experienced by the soil (Jefferies and Been, 2006). Figure 2.3 shows the characteristics of the compression curves for sands.

The infinite number of *ncl* lines perfectly explain why dense sands consolidated at high stress conditions compress and loose sands dilate at low stress conditions during shear. When the state of the sample is above the *csl* the sample compresses. If the state is below the *csl* the sample dilates.

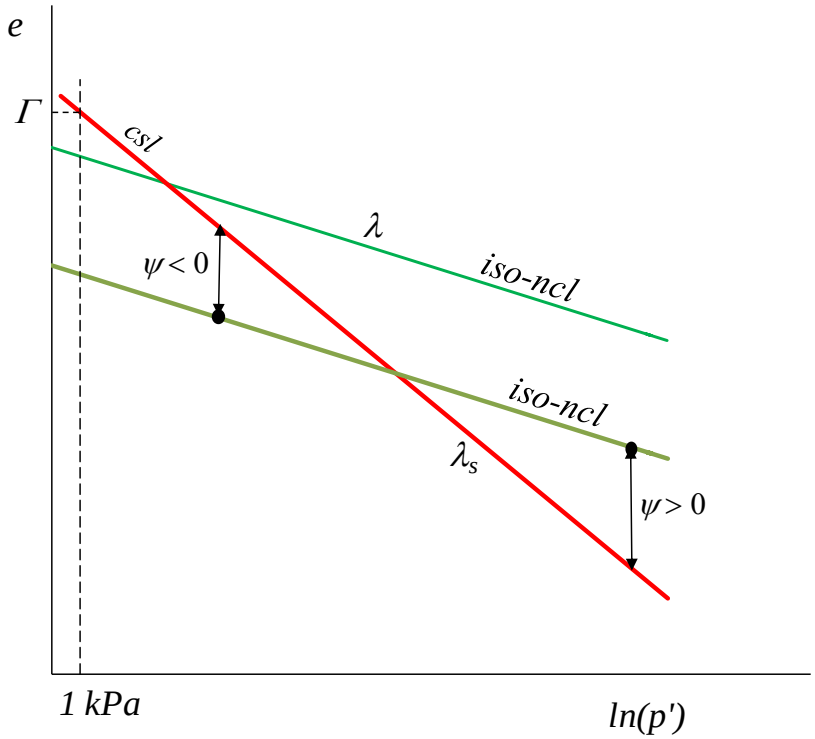

Figure 2.3. Infinite number of *iso-ncl* lines (modify from Jefferies and Shuttle, 2006).

2.3.2. Critical state

The critical state (CS) is a condition of perfect plasticity that follows the axioms below:

Axiom 1: A unique critical state locus exist:

$$\exists C(e,q,p')|_{\dot{p}'=0} \ \ni \ \dot{\varepsilon}_p^p \equiv 0 \text{ and } \ddot{\varepsilon}_p^p \equiv 0 \ \ \forall \varepsilon_q \qquad [2.9a]$$

This axiom can be written in terms of dilatancy as:

$$\exists C(e,q,p')|_{\dot{p}'=0} \ \ni \ \mathrm{D}^p \equiv 0 \text{ and } \dot{D}^p \equiv 0 \ \ \forall \varepsilon_q \qquad [2.9b]$$

where the dilatancy, D^p is the ratio between the volumetric and shear strains:

$$D^p = \frac{\dot{\varepsilon}_p^p}{\dot{\varepsilon}_q^p} \qquad [2.10]$$

Axiom 2: The soil state moves to the critical state with increasing shear strain:

$$\psi \to 0 \ as \ \varepsilon_q \to \infty \qquad [2.11]$$

Axiom 1 implies that at CS

$$q - Mp' = 0 \qquad [2.12]$$

Axiom 2 states that a soil reaches the CS only when both the dilatancy and rate of dilatancy are zero. The locus of the CS in the $e - q - p'$ space is given by:

$$e_c = \Gamma - \lambda_s \ln(p'_c) \qquad [2.13a]$$

$$q_c = M_{tc} p'_c \qquad [2.13b]$$

where the subscript c refers to the CS locus; $M_{tc} = \frac{q_c}{p'_c}$ is the stress ratio at the CS and a function of the critical state friction angle, ϕ'_{cs} and the Lode angle, θ. Lode angle is the angular coordinate of a cylindrical coordinate system {z, r, θ} for which the z-axis point along the hydrostatic path and {r, θ} are polar coordinates on any constant pressure at current stress state. z and r are functions of the first and second invariants of the deviatoric stress tensor, respectively; therefore, they represent the hydrostatic and the deviatoric components of the stress tensor. The angular component θ indicates the magnitude of the intermediate principal stress, σ'_2 in relation to the major principal stress, σ'_1, and the minor principal stress, σ'_3, and is a function of the second and third invariants of the deviatoric stress tensor (Wolf, 2008). In the case of a Compression Triaxial test:

$$M_{tc} = \frac{6\sin\phi'_{cs}}{3 - \sin\phi'_{cs}} \qquad [2.14]$$

The CS of saturated cohesive soil reached an undrained condition (i.e. load at constant volume or monotonic load) that can be described by the Tresca failure criterion, which establishes that failure occurs when the stresses reach a point of one half of the maximum stress difference:

$$S_u = \frac{(\sigma'_1 - \sigma'_3)_{\max}}{2} \qquad [2.15]$$

where S_u is the undrained shear strength. Su is related to the CS parameters by

$$S_u = \frac{M}{2}\exp\left(\frac{\Gamma - e_0}{\lambda}\right) \quad [2.16]$$

S_u is proportional to the mean pressure, and for NC cohesive soils this is a stress-state dependent property. For OC soils, S_u is proportional to the mean pressure and the overconsolidation ratio (Skempton, 1957; Ladd and Foott, 1974; Jamiolkowski et al., 1985; Mesri, 1988; Ladd, 1991). Inside the CS framework of this study the normalized undrained shear strength is:

$$\left(\frac{Su}{p'_o}\right) = \frac{q_{cs}}{2p'_o} \quad [2.17]$$

When the soil is not cohesive the Tresca failure criterion is not suitable. When a clean sand with a state of $\psi_o < 0$ is sheared under undrained conditions they reach a stress state such that:

$$\dot{p} > 0 \text{ and } \ddot{p} \equiv 0 \forall \varepsilon_q \quad [2.18]$$

This condition was named by Li (1997) as the Undrained Shear Dilative Failure. However, this condition cannot be permanent because the moment will arrive when the mean stress will stop changing; otherwise, the sample would explode (Li, 1997). When a clean sand with state $\psi_o > 0$ is sheared an under undrained condition, it hardens until it reaches a maximum stress difference, and finally soften until reach the CS.

2.3.3. Elastic Behavior - Hooke's Law

The increments of elastic volumetric and elastic shear strains are related to the mean and shear stresses by:

$$\dot{\varepsilon}_p^e = \frac{1}{K'}\dot{p}' = \frac{\kappa}{1+e}\frac{\dot{p}'}{p'} \quad [2.19a]$$

$$\dot{\varepsilon}_q^e = \frac{1}{3G'}\dot{q}' \quad [2.19b]$$

$$K' = \frac{E}{3(1-2\nu)} = \frac{1+e}{\kappa}p' \quad [2.20a]$$

$$G = \frac{E}{2(1+\nu)} = \frac{3(1-2\nu)}{2(1+\nu)} K' \qquad [2.20b]$$

where *K'* is the Bulk Modulus, *G* is the Shear Modulus, *E* is the Young's Modulus, and ν is the Poisson's ratio. Equation [2.19a] shows that the elastic change in the volumetric strain is a function of the current mean stresses.

The isotropic elastic κ-model shown in Equation [2.20b] neglects elastic shear by making *G* depend on the void ratio and mean stress and not on the soil fabric. For sands, bender elements should be used to measure G_{max} of the specimen before the shear (Jefferies and Been, 2006). Rewriting equations [2.19a] and [2.20b] to get the shear rigidity, I_r:

$$I_r = \frac{G}{p'} \qquad [2.21]$$

Before the Critical State theories were developed, undrained soil behavior was modeled through a total stress approach. The total stress approach addressed the undrained conditions by making $\nu \rightarrow 0.5$ to impose constant volume. However, undrained loading is a boundary condition, not a fundamental aspect of soil behavior (Jefferies and Been, 2006). Therefore, a material property such as ν cannot change. The basic condition for undrained loading, neglecting the elastic compressibility of soil particles and pore water, is:

$$\dot{\varepsilon}_p = 0 \Leftrightarrow \dot{\varepsilon}_p^p = -\dot{\varepsilon}_p^e \qquad [2.22]$$

This means that zero volumetric strain rate overall does not mean zero volumetric plastic strain and zero elastic strain (Jefferies and Been, 2006). The undrained condition also implies that Equation [2.3a] can be written as:

$$\dot{\varepsilon}_q = \dot{\varepsilon}_a \qquad [2.23]$$

2.3.4. Plastic behavior

2.3.4.1. Plastic potential

The plastic potential is a function that controls the mechanism of plastic deformation by:

$$\dot{\varepsilon}_p^p = \Lambda \frac{\partial g}{\partial p'} \quad [2.24a]$$

$$\dot{\varepsilon}_q^p = \Lambda \frac{\partial g}{\partial q} \quad [2.24b]$$

where $\dot{\varepsilon}_p^p$ and $\dot{\varepsilon}_q^p$ are the plastic components of the volumetric and shear strains, *g* is the plastic potential and Λ is a non-negative scalar number. The plastic potential has the form:

$$g(p', q, p'_y) = 0 \quad [2.25a]$$

$$p'_y = p'_y(\varepsilon_p^p, \varepsilon_q^p) \quad [2.25b]$$

where p'_y controls the size of any particular member of a plastic potential function.

2.3.4.2. Yield criterion:

The yield criterion is a locus that determines when the stress conditions are such that the plastic deformations start to occur:

$$f(p', q, p'_y) = 0 \quad [2.26]$$

p'_y also controls the size of the yield loci. When $f < 0$, plastic deformation does not occur, when $f = 0$ the plastic deformations start to occur, and when $f > 0$ admissible stress conditions do not exist.

2.3.4.3. Flow Rule

By work-energy equilibrium (Rowe, 1962; Roscoe and Schofield, 1963), the flow rule or stress–dilatancy relationship is:

$$D^p = M - \eta \quad [2.27]$$

where

$$\eta = \frac{q}{p'} \quad [2.28]$$

is the stress ratio that represents the mobilized friction and *M* represents the dissipation of the plastic work during the shear. Flow rule is a relationship that relatea the change of the increment of plastic strains (i.e. dilatancy) with the change of stresses (i.e. stress ratio) as shear occurs. This relation applies to all stress histories (Jefferies and Been, 2006). However, for the CC model, *M* is perceived to be a "true" fundamental value where $M = M_{tc}$:

$$D^p = M_{tc} - \eta \qquad [2.29]$$

The postulate of normality assumes that the plastic strain increment vector is normal to the yield locus and in the outer direction (Wood, 1990):

$$D^p = -\frac{\dot{q}}{\dot{p}} \qquad [2.30]$$

This means that the material follows an associated flow rule and $f = g$. It has been found that metals follow associated flow rules while frictional blocks do not. In analysis of the Tatsuoka and Ishihara (1974) and Barden and Khayatt (1966) experiments in sands, Jefferies (1993) observed that normality was fulfilled. It is assumed an associated flow rule because otherwise the model will be complex and will have a lot of parameters that make the model difficult to apply (Wood, 1990).

Assuming that the soil obeys the postulate of normality from equations [2.29] and [2.30], the equation that controls the plastic behavior of CC model is:

$$\frac{q}{p'} - \frac{\dot{q}}{\dot{p}'} = M_{tc} \qquad [2.31]$$

Solving this equation with the border condition $p' = p'_y$ when $\eta = 0$, the plastic potential-yield locus is:

$$g = f = \eta - M_{tc} \ln\left(\frac{p'_y}{p'}\right) = 0 \qquad [2.32]$$

When a soil follows an isotropic consolidation stress path, D^p is indeterminate; however, according to Equation [2.27], $D^p = M_{tc}$, which is incorrect. This can be observed in Figure 2.4a. Therefore, Roscoe and Burland (1968) reinterpreted the work-

energy equilibrium to have a flow rule that described isotropic consolidation stress paths without going against the principle of the conservation of energy. They arrived at the MCC flow rule:

$$D^p = \frac{M_{tc}{}^2 - \eta^2}{2\eta} \qquad [2.33]$$

Figure 2.4 shows this flow rue. Appling the normality assumption of Equation [2.28] the equation that controls plastic behavior of MCC model is:

$$\left(\frac{q}{p'}\right)^2 + 2\left(\frac{q}{p'}\right)\frac{\dot{q}}{\dot{p}'} = M_{tc}{}^2 \qquad [2.34]$$

Under the border condition $p' = p'_y$ when $\eta = 0$, the plastic potential-yield locus is:

$$g = f = \eta^2 - M_c{}^2\left(\frac{p'_y}{p'} - 1\right) = 0 \qquad [2.35]$$

Figure 2.4a shows the yield loci of CC and MCC. Figure 2.4b shows this yield loci in space $q - p'$ normalized to p'_y. The figure shows that the area under the MCC yield locus is greater than the CC yield locus. This mean that MCC can hold more elastic deformation than CC does.

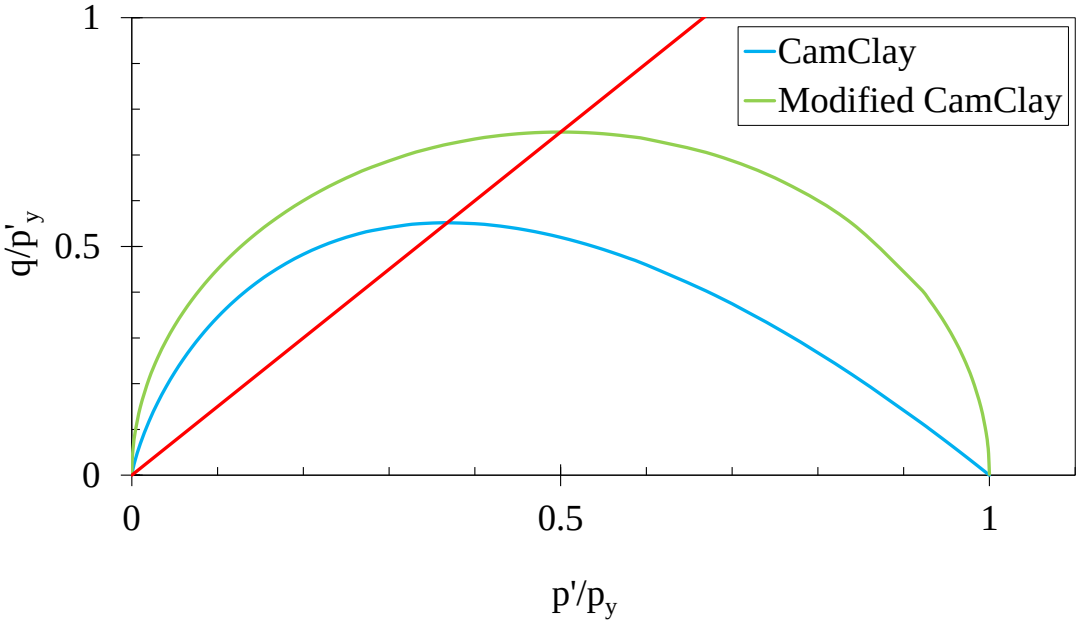

Figure 2.4. CC and MCC yield loci in $q - p'$ space.

Nova and Wood (1979) and Nova (1982), after analyzing results of triaxial tests on sands, proposed the following flow rule:

$$D^p = \frac{M_{tc} - \eta}{\mu} \qquad [2.36]$$

This flow rule implies that the work – energy equilibrium is (Jefferies, 1997):

$$q\dot{\varepsilon}_q^p + p'\dot{\varepsilon}_p^p = M_{tc} \mid \dot{\varepsilon}_q^p \mid + Np'\dot{\varepsilon}_p^p \qquad [2.37]$$

where $\mu = 1 - N$. The left part of equation represents only the plastic work because the elastic work is recoverable. The right part of the equation represents the energy dissipation throgh friction ($M_{tc} \mid \dot{\varepsilon}_q^p \mid$) and a store plastic work ($Np'\dot{\varepsilon}_p^p$). Even though this concept is difficult to receive, $Np'\dot{\varepsilon}_p^p$ represents the portion of work that is stored when the grains are forced apart and the fall back toward their previous position when the stress is released (Jefferies, 1997; Collins, 2005).

The flow rules of CC and MCC, and Nova (1979) work only if there is only one *ncl*, or to a given initial void ratio because all the yield loci are coupled to the *ncl* in the space *e* – *p*'. However, in the case of real soils and specifically of sands there are infinite *ncl*.

The NorSand model solves this problem by proposing a new flow rule that meets the following these conditions (Jefferies, 1993):

- The yield locus has to intercept the *p*'-axis at zero because of the assumption of no cohesion.
- The existence of *ncl* requires that the yield locus intercept the *p*'-axis at non zero value.
- The assumption of a single yield locus requires that these two points be connected by a single convex curve.

In order to meet these conditions, NorSand assumes there exists a family of yield loci with a condition of $\dot{\varepsilon}_p = 0$ with $\ddot{\varepsilon}_p \neq 0$ that evolves with shear toward the CS until reaching the yield locus in the CS where $\dot{\varepsilon}_p = 0$ and $\ddot{\varepsilon}_p \equiv 0$. These yield loci can be

regarded as an image of the CS due to meeting one condition of the CS: $\dot{\varepsilon}_p^p = 0$. The point where $\dot{\varepsilon}_p^p = 0$ and $\ddot{\varepsilon}_p \neq 0$ is named the image condition, IC and occurs at the mean stress p'_i. This condition is observed in some overconsolidated clays and dense sands due to the change from negative to positive of the pore water pressure, which produces the mean stress change from compression to extension.

This state was named by Ishihara (1975) the "phase transformation," by Li (1997) the "pseudo steady state," by Nova and Wood (1979) the "transition state," and by Jefferies (1993) the "image condition." However, for Jefferies and Been (2006) the IC is not a phase change, steady state, or pseudo condition.

In this way, the flow rule or stress-dilatancy relationship of NorSand is given by:

$$D^p = M_i - \eta \qquad [2.38]$$

where M_i is the stress ratio at IC. Appling the postulate of normality, the equation that controls de plastic behavior of NorSand is:

$$\frac{q}{p'} - \frac{\dot{q}}{\dot{p}'} = M_i \qquad [2.39]$$

and solving with the border condition $p' = p'_i$ when $\eta = M_i$, the plastic potential - yield loci is:

$$g = f = \eta - M_i\left(1 - \ln\left(\frac{p'}{p'_i}\right)\right) = 0 \qquad [2.40]$$

Figure 2.4 shows the shape of this yield loci. The figure shows that NorSand converges to CC in the CS.

2.3.4.4. Minimum dilatancy - maximum stress ratio: Peak state

Figure 2.5 shows experimental data for consolidated triaxial tests by Jefferies and Been (2006). The graph shows that for triaxial compression the relation between minimum dilatancy $D^p_{\min}$ and the stress ratio at Peak State $\eta_{\max}$ is:

$$D^{p}{}_{\min} = \frac{M_{tc} - \eta_{\max}}{(1-N)} \qquad [2.41]$$

where N is the volumetric coupling coefficient and is a positive constant. This relationship has the same form as the Nova Flow Rule (i.e. stress-dilatancy relationship) at the peak state, PS (Nova and Wood, 1979 and Nova, 1982). Figure 2.5 shows that the relation between $D^{p}_{\min}$ and $\eta_{\max}$ is not only characteristic for each soil but also depends on the θ.

When $N = 0$, Equation [2.41] converges to CC flow rule at PS.

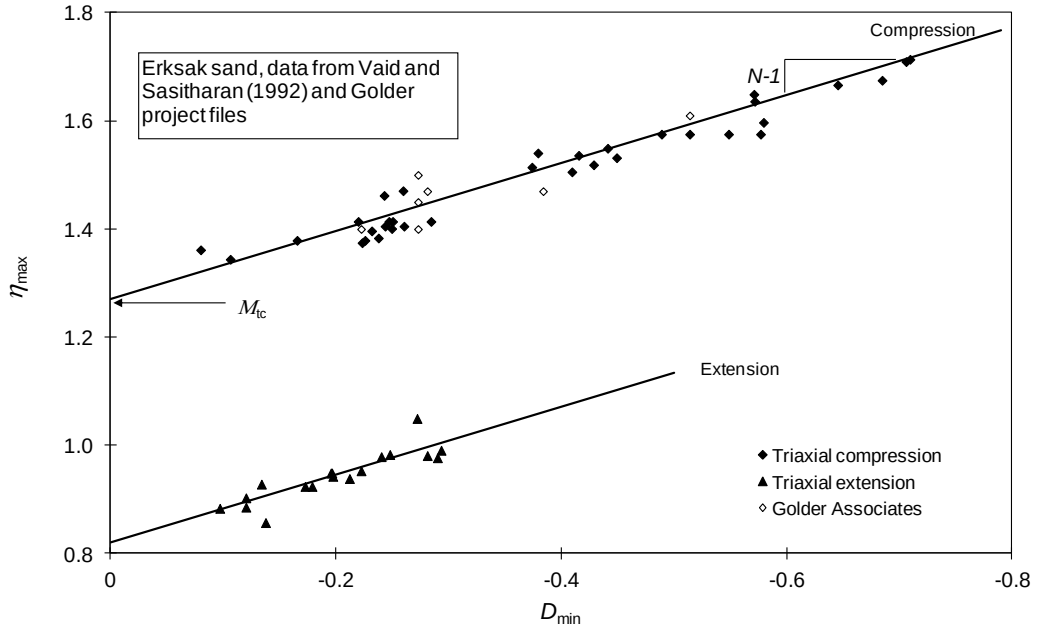

Figure 2.5. Relation between minimum dilatancy and maximum stress ratio (Jefferies and Been, 2006).

Figure 2.6 shows the variation of $D^{p}_{\min}$ with ψ_i of drained and undrained triaxial tests of sands to sandy silts. The figure shows a strong relationship between these two variables with the form:

$$D^{p}{}_{\min} = \chi_{tc}\psi_i \qquad [2.42]$$

where χ_{tc} is the dilatancy constant.

Because NorSand has an associated flow rule, it is necessary to limit the minimum dilatancy. This limit corresponds with the maximum value that the mean stress can take

at the current minimum allowable $D_{\min}^{p}$ value. The maximum size of the yield locus is:

$$\left(\frac{p_i}{p}\right)_{\max} = \exp\left(\frac{-\chi_{tc}\psi_i}{M_i}\right) \qquad [2.43]$$

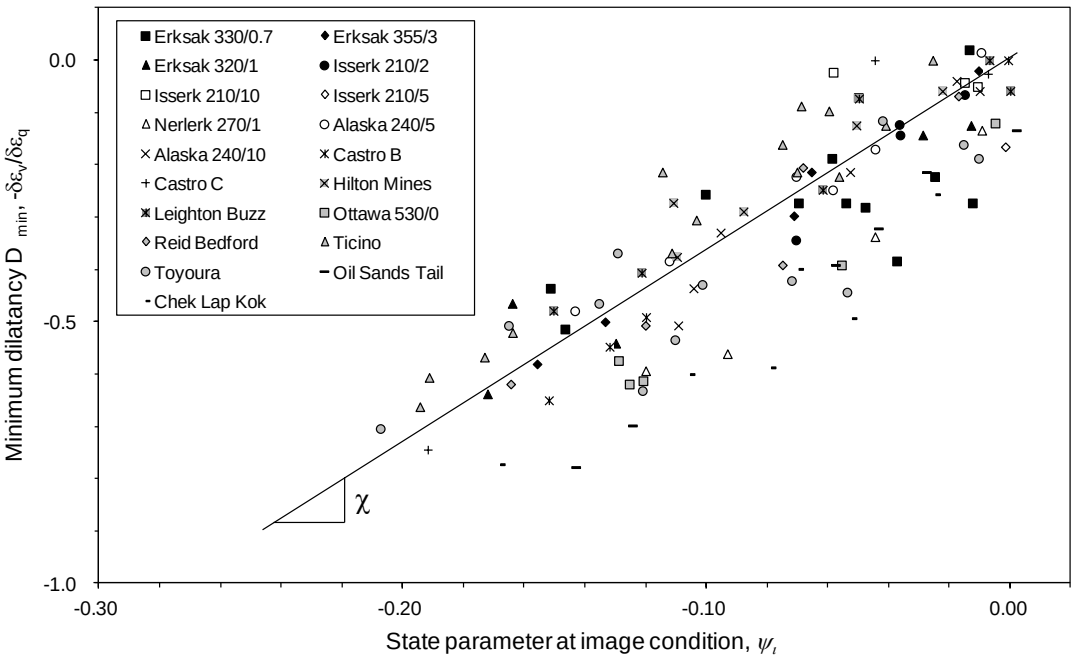

Figure 2.6. Variation of $D_{\min}$ with state parameter at the IC (Jefferies and Been, 2006).

Combining [2.41] with [2.42], M_i is:

$$M_i = M_{tc} - N\chi_{tc}\,|\psi_i| \qquad [2.44]$$

Figure 2.7 shows all the characteristics of the NorSand model. Figure 2.7a shows the yield locus contracting toward the CS. Because the yield locus is contracting, the vector of dilatancy is always positive until reach $D^p = 0$ in the CS. Figure 2.7b shows the yield locus expanding toward the CS. Because the yield locus is expanding, the vector of dilatancy is always negative until reach $D^p = 0$ in the CS.

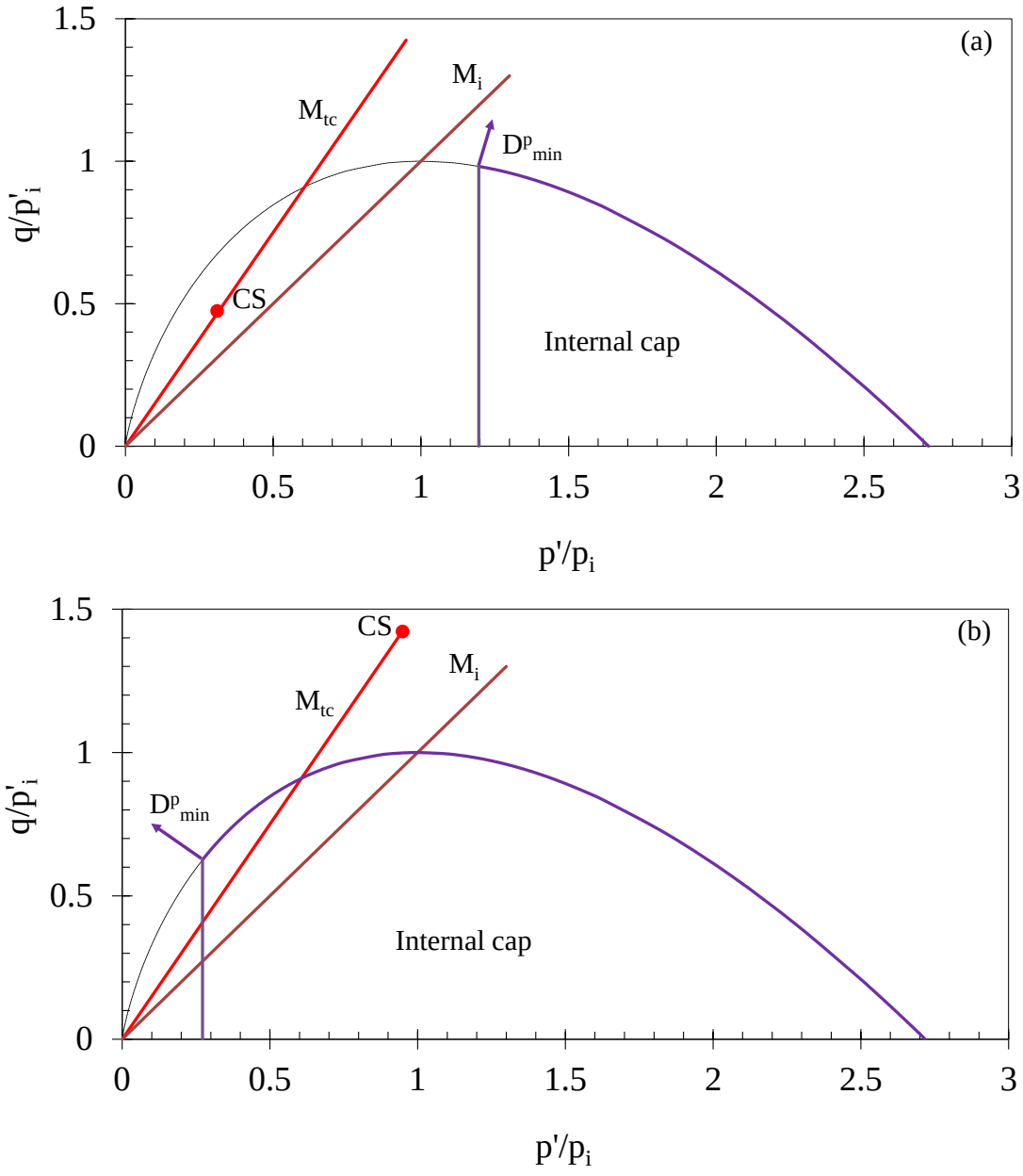

Figure 2.7. NorSand model (a) yield locus contracting to CS, (b) yield locus expanding to CS (after Jefferies and Been, 2006).

2.3.4.5. Hardening rule:

The hardening rule describes the magnitude of the plastic deformation increments and how yield loci expand by fully fitting the second axiom. CC and MCC can harden only by the changes of volumetric strain because there is only one *ncl*. Then, the hardening rule is:

$$\frac{\dot{p}'_y}{p'_y} = \frac{(1+e)}{(\lambda-\kappa)}\dot{\varepsilon}_p^p \qquad [2.45]$$

However, NorSand cannot harden by change in volumetric strain because of the existence of infinite *ncl* that decouple the yield loci from the *ncl* (Jefferies and Been, 2006); therefore, NorSand hardens through control of the change of p'_i and its relation with $\dot{\varepsilon}_p^q$. Empirically, Jefferies and Been (2006) found that hardening is also a function of the shear stress level. In this way the hardening rule is:

$$\frac{\dot{p}'_i}{p'_i} = H\left(\frac{p'}{p'_i}\right)^2\left(\left(\frac{p'_i}{p'}\right)_{\max} - \frac{p'_i}{p'}\right)\dot{\varepsilon}_q^p \qquad [2.46]$$

where *H* is a hardening modulus, which Jefferies and Been (2006) found to be a function of soil fabric and ψ. *H* is calculated by trial and error.

NorSand has two softening rules. One is due to rotation of the principal stresses because of dynamic loads. The other is a softening inside the yield locus; that is, a static softening observed after the CS is reached that causes the internal cap to contract. This softening has the form:

$$\frac{\dot{p}'_i}{p'} = \frac{H}{2}\left|\dot{\varepsilon}_q^p\right| \qquad [2.47]$$

Table 2.1 shows the principal components of the CC, MCC, and NorSand models. Table 2.2 shows the parameters necessary to perform simulations using Critical State models. The consolidation and *csl* parameters can be calculated through CIU or CID triaxial tests. The hardening parameter *H* is estimated by trial and error.

Table 2.1. Principal component summaries of the Critical State models CC, MCC, and NorSand.

	Cam Clay	**Modify Cam Clay**	**NorSand**
Elasticity behavior – Hoek's Law	$\dot{\varepsilon}_p^e = \frac{1}{K'}\dot{p}' = \frac{\kappa}{1+e}\frac{\dot{p}'}{p'}$ $\dot{\varepsilon}_q^e = \frac{1}{3G'}\dot{q}'$		
	$K' = \frac{E}{3(1-2\nu)} = \frac{1+e}{\kappa}p'$ $G = \frac{E}{2(1+\nu)'} = \frac{3(1-2\nu)}{2(1+\nu)'}K'$		$I_r = \frac{G_{\max}}{p'}$ $I_k = \frac{K'_{\max}}{p'} = \frac{1+e}{\kappa} = I_r\frac{2(1+\nu)}{3(1-2\nu)}$
Flow Rule or Stress-dilatancy relationship	$D^p = M_{tc} - \eta$	$D^p = \frac{M_{tc}{}^2 - \eta^2}{2\eta}$	$D^p = M_i - \eta$
Plastic potential = Yield locus	$g = f = \eta - M_c \ln\left(\frac{p'_y}{p'}\right) = 0$	$g = f = \eta^2 - M_c{}^2\left(\frac{p'_y}{p'} - 1\right) = 0$	$g = f = \eta - M_i\left(1 - \ln\left(\frac{p'}{p'_i}\right)\right) = 0$
Hardening Rule	$\frac{\dot{p}'_y}{p'_y} = \frac{(1+e)}{(\lambda-\kappa)}\dot{\varepsilon}_p^p$		$\frac{\dot{p}'_i}{p'_i} = H\frac{M_i}{M_{i,tc}}\left(\frac{p'}{p'_i}\right)^2\left(\left(\frac{p'_i}{p'}\right)_{\max} - \frac{p'_i}{p'}\right)\dot{\varepsilon}_q^p$
Internal cap Softening Rule	There is not softening		$\frac{\dot{p}'_i}{p'} = \frac{H}{2}\frac{M_i}{M_{i,tc}}\lvert\dot{\varepsilon}_q^p\rvert$

Table 2.2. Soil parameters of CC, MCC, and NorSand.

Parameter		Type	Method of determination	Model
λ_{ncl}	Compression index	Material property	Isotropic consolidation	CC MCC
κ	Swelling index	Material property	Isotropic consolidation	CC MCC
G_{max}	Shear modulus	Function of E, ν, κ, e, p', and fabric	Equation [2.20d] or Bender elements	NorSand
ν	Poisson's ratio	Material property	Assumed	CC MCC NorSand
ϕ'_c	Critical state friction angle	Material property	One CIU or CID triaxial test	CC MCC NorSand
Γ	Reference value *csl* in e - p' space	Material property	At least three CIU or CID triaxial tests	NorSand
λ_s	Slope *csl* in e - p' space	Material property	At least three CIU or CID triaxial tests	NorSand
χ	Dilatancy constant	Model parameter, function of fabric	At least three CIU or CID triaxial tests	NorSand
N	Volumetric coupling coefficient	Model parameter	At least three CIU or CID triaxial tests	NorSand
H	Hardening index	Function of fabric and ψ	Trial and error	NorSand

CHAPTER 3

3. Sample characterization: Mineralogy composition

This chapter describes the geological formation to which the shale samples belong and shows where the location where the samples were collected. This chapter also describes mineralogical testing procedures performed to characterize the shale samples and the geological classification of the shales.

3.1. Study Shales

The shales were sampled by Kirkendoll (2012) in the course of this study. The goal was to obtain several shale samples of diverse durability, geological age and formations. Kirkendoll (2012) collected the samples from new excavations located on a variety of construction projects; one of the samples was obtained via surplus core taken from a proposed mining location.

Table 3.1 shows the geologic names of each shale formation, the geologic period and the physical description of each sample. The specimens were assumed to be representative of hard and soft shales with high, medium, and low durability.

All the shales of this study were dark colored, which indicate they contain organic matter and pyrite. They indicate an anoxic environment of sedimentation in deep marine water or shallow water with a rich source of organic matter. Shales with brownish red color indicate they deposited in oxygen rich water of shallow water (Nichols, 2009).

Table 3.1. Location and geological name of the shales of this study (Kirkendoll, 2012).

Geologic name	Geologic period	Location	Environment of deposition
Grundy	Pennsylvanian	Clay County, Ky	Near-shore to swampy
Carbondale	Pennsylvanian	Webster County, Ky	Near-shore to swampy
Fort Payne	Mississippian	Taylor County, Ky	Marine basin
Tradewater	Pennsylvanian	Philpot, Ky	Near-shore to swampy
Bull Fork	Ordovician	Boone County, Ky	Shallow marine water

The following section presents, in order of older to younger, the geological description of each shale according to the geologic map of Kentucky and texts edited by McDowell (1986) in USGS (http://pubs.usgs.gov/prof/p1151h/contents.html). Figure 3.1 shows the approximate locations from which the samples were taken on a geologic map of Kentucky. Samples were taken from the Ordovician, Mississippian and Pennsylvanian periods.

The Bull Fork Formation is an upper Ordovician formation that outcrops in central and north-central Kentucky. It was deposited in shallow marine water in tropical latitudes, and is composed of fossiliferous limestone interbedded with shale in about equal amounts. Most of this limestone is nearly free of quartz silt and clay. The Bull Fork shale is highly calcareous, silty, and fissile, and ranges from very sparsely fossiliferous to very fossiliferous. It is greenish gray or olive gray in color when fresh and yellowish gray when weathered.

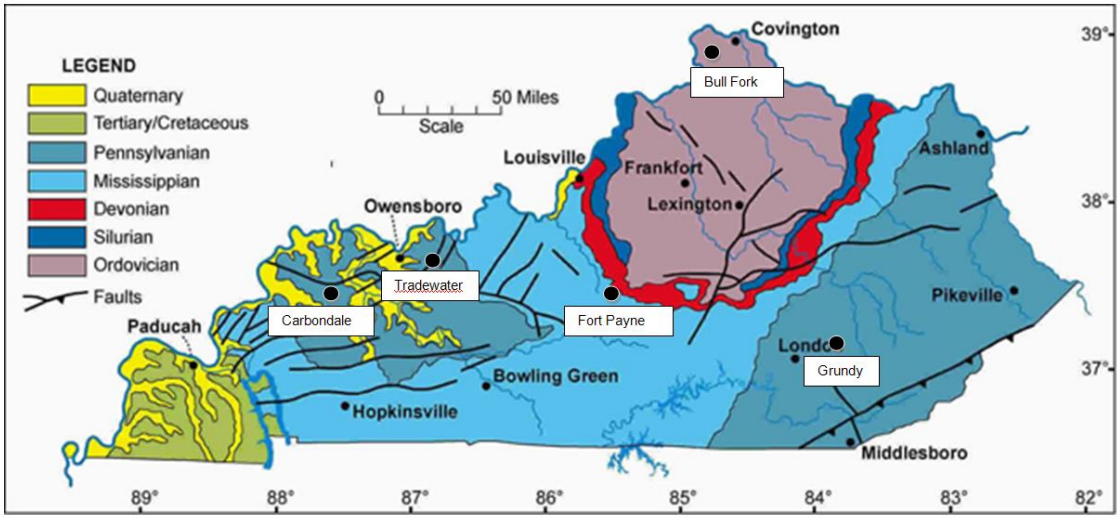

Figure 3.1. Geologic map of Kentucky (Kentucky Geological Survey, 2009).

The Fort Payne Formation is a Mississippian formation that outcrops over much of south-central Kentucky. It was deposited as marine basin fill adjacent to the southeast of the Borden deltaic sediments. It consists of gray to black dolomitic siltstone and cherty, dolomitic limestone. This formation thins northward in central Kentucky, where it is more silty, shaly, and dolomitic, and less siliceous (McDowell, 1986).

The Grundy, Carbondale, and Tradewater formations are Pennsylvanian. In Kentucky,

the Pennsylvanian formations outcrop in two areas of Kentucky: the Appalachian basin and the Eastern Interior. The most common rocks are sandstone, siltstone, and shale (McDowell, 1986). These formations were deposited in nearshore to swampy environments.

The Grundy Formation (Breathitt Group) outcrops in the Appalachian basin. It consists of sequences of gray siltstone and shale, subgraywacke, and minor amounts of limestone. The formation, which underlies all of eastern Kentucky, contains most of the economic deposits of coal in eastern Kentucky (McDowell, 1986).

The Tradewater Formation outcrops in the Eastern Interior. This formation is composed of about equal amounts of sandstone, siltstone, and shale, and contains several beds of limestone as well as several economic coal beds (McDowell, 1986).

Finally, the Carbondale formation outcrops in the Eastern Interior. It consists of siltstone, shale, and some locally prominent sandstone units. The formation contains many thin but extensive argillaceous limestone beds as well as many of the thicker and more economic coal beds of the western Kentucky coal field (McDowell, 1986).

3.2. Mineralogy tests

For this portion of the research, powder X-ray diffraction (XRD), thermogravimetric analysis, and cation exchange capacity (CEC) tests were performed on the shale samples in order to determinate their mineralogical content.

3.2.1. Powder X-Ray diffraction

The XRD tests were performed with a Siemens D500 powder diffractometer with Ni-filtered Cu sources and graphite diffracted beam monochrometers shown in Figure 3.2. The continuous change of an incident angle of an X-ray beam of 1.541838Å wavelength in a powder sample results in a spectrum of diffraction intensity versus two times the incident angle, θ. The shape of the spectrum is unique for each mineral, so it is possible to determine mineralogical content with this experiment.

This experiment was performed on two types of samples, the first group of samples were fine-size samples passed through a No. 200 sieve, and the second group were clay-size

samples. The procedures of these experiments are presented in subsequent sections.

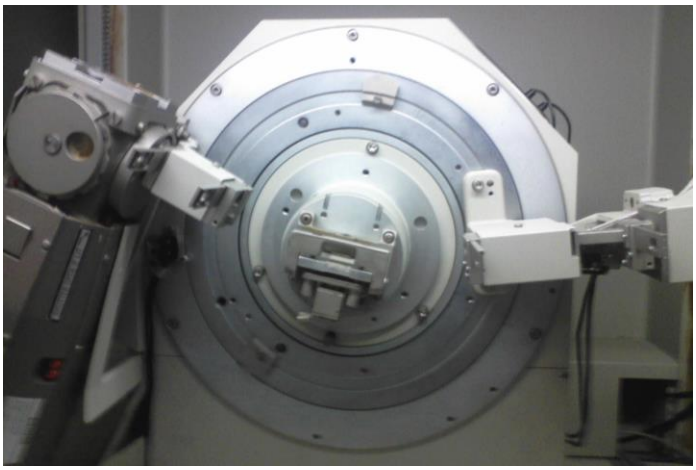

Figure 3.2. Siemens D500 powder diffractometer.

3.2.1.1. XRD test on fine fraction samples without pretreatment

Fine-size crushed samples (i.e. passed through a No. 200 sieve) were used to perform the XRD tests. As shown in Figure 3.3, the samples were placed in a container and then put inside the X-ray diffractometer in order to run the test. The scan range was 2° to 60° at 1°/minute and a step size of 0.1°.

The resulting spectrum was analyzed using the *Traces* program, version 6.4.0 (Diffraction Technology, Pty, Ltd). The interpretation of the spectrum was performed looking for the minerals that produce the d-spacing patterns observed in the spectrum. Table 3.2 shows the first 3 d-spacing peaks (i.e. 001, 002, and 003 crystal planes) for the typical minerals in shales.

3.2.1.2. XRD test on clay fraction samples with pretreatment

Carbonates, pyrite, iron oxides, and organic matter cement and aggregate clay minerals and prevent their dispersion. Therefore, they should be removed in order to facilitate fractionation. Air-dried crushed samples passed through a No. 200 (fine-size) were used to do the pretreatment. The pretreatment was performed following the procedures given by Jackson (1969) and Kunze and Dixon (1985). A summarize of these procedures are shown in Appendix A.

Table 3.2. d-spacing in (Å) of the first three peaks for the typical non-clay minerals of shales. http://webmineral.com.

Mineral	001	002	003
Quartz	4.257	3.342	1.8179
K-Feldspar	4.02	3.80	3.18
Calcite	3.035	2.285	2.095
Dolomite	2.883	2.191	1.785
Siderite	3.59	2.79	1.734
Pyrite	2.71	2.43	1.63
Gypsum	7.63	4.28	3.07
Hematite	2.69	2.51	1.69
Gohetite	4.18	2.69	2.45

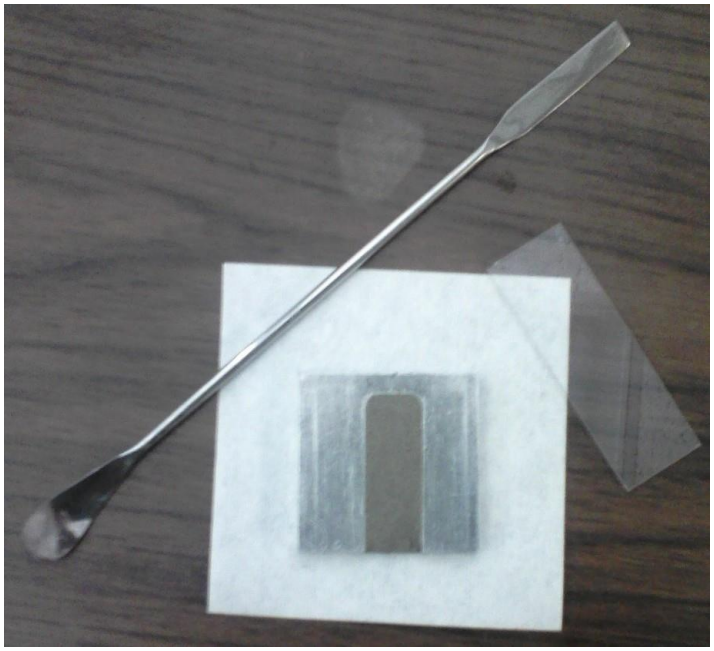

Figure 3.3. Fine-size sample used for the powder XRD test.

Air-dried crushed samples passed through a No. 200 (fine-size) were used to do the pretreatement. After the pretreatment and fractionation, the slides for the XRD test were done. The procedure by Jackson (1969), Drever (1973), and Karathanasis and Hajek (1981) was followed to do the slides (see Appendix A). One Mg-saturated, one Mg-Glycerol-saturated and one K-saturated slides were done. Figure 3.4 shows the appearance of one of the slides. The slides were put inside the X-ray diffractometer in order to run the test. The scan range was also 2° to 60° at 1°/minute and a step size of 0.1°.

The resulting spectra were analyzed using *Traces* program, version 6.4.0 (Diffraction Technology, Pty, Ltd) looking for the d-spacing peaks for each clay mineral shown in Table 3.3. The first column shows the d-spacing of the three first peaks for each clay (i.e. 001, 002, and 003 crystal planes). The other columns show the d-spacing of the first peak.

Figure 3.4. Slide with sample after pretreatment used to run the XRD test.

Table 3.3. d-spacing in Å of the 3 first peaks in Mg and first peak in the others slides. (Karathanasis, 2010).

Mineral	Mg	Mg-glycol	K room	K100	K300	K550
Smectite	001: 14-15 002: 7.3 003: 4.8	17-18	12.4-12.8		9.8-10.1	9.8-1.01
Chlorite	001: 14-15 002: 7.3 003: 4.8	14-15	14-15	14-15	14-15	14-15. Increase in intensity
Illite	001: 10 002: 5 003: 3.3	10	10	10	10	10
Kaolinite	001: 7, 002: 3.5 003: 2.3	7	7	7	7	Dehydroxylation at 400-500C

3.2.1.3. Quantification

The quantification was performed following Karathanasis (1981) procedure. This method assumes that the area of the spectrum under the first peak of the mineral is proportional to

the quantity of that mineral in the sample. The areas were calculated using the software Traces Program Version 6.4.0 (Diffraction Technology, Pty, Ltd). The background was erased and the base line was calculated. Figure 3.5 shows the area under the spectrum of the first peak of illite in a Mg saturated sample. The percentage of a mineral in a sample is given by

$$\%Mineral = \frac{Area\ under\ \ peak_i}{\sum_i Area\ under\ all\ \ peaks} \qquad [3.1]$$

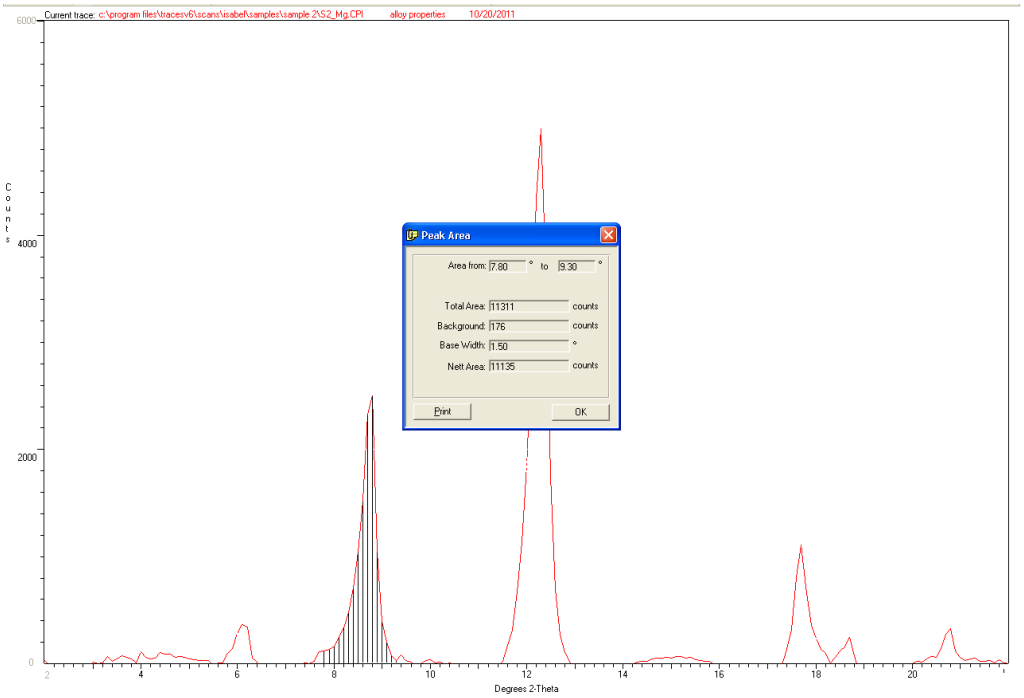

Figure 3.5. Area under the first peak of illite in the spectrum of Mg saturated.

3.2.2. Thermal analysis

In order to have an estimate of the carbonate content in the shale samples, thermogravimetric (TG) and derivative thermogravimetric (DTG) tests (TG-DTG) were run simultaneously on crushed samples passed through a No. 200 sieve. The thermogravimetric analysis is based on the weight loss of the samples due to the destruction of the crystalline structure of the minerals when they are heated at different temperatures. The principal reactions are dehydration and evaporation that occur at a lower temperature between 20°C - 300°C, dehydroxylation of the clay minerals ($(OH)^-$

$\rightarrow H_2O$), and decarbonation of carbonates ($(CO_3)^{2+} \rightarrow CO_2$) at temperatures higher than 250°C (Karathanasis, 2008).

Even though the temperatures of decarbonation for siderite, dolomite, and calcite are well-defined, factors such as particle size, heating rate, crystallinity, impurities and mixtures of several carbonates change the temperature regions (Karathanasis, 2008). Also, there is overlapping of temperature when there are kaolinite and carbonates in the sample. Table 3.4 shows the temperature regions for the carbonates minerals.

Table 3.4. Temperature regions to identify carbonates when the crystals are not pure (from Karatanasis, 2008).

Mineral	Temperature region
Siderite	500 – 600°C
Magnesite	600 – 700°C
$MgCO_3$ phase of dolomite	700 – 800°C
$CaCO_3$ phase of dolomite and calcite	>900

The quantification of carbonates was performed following the procedure by Karathanasis (2008). The percentage of carbonates in the samples was calculated by

$$\%C = \frac{\Delta W}{W_l} 100 \qquad [3.2]$$

where percent C is the content of the mineral, ΔW is the percentage of the measured weight loss during heating inside the range temperature, and W_l is the weight loss, for Calcite is 440 g/ka, Dolomite is 47.6 g/ka, Magnesite is 52.4 g/ka, and Siderite 37.9 g/ka (Karathanasis, 2008).

3.2.3. Cation exchange capacity

The CEC was measured following the instructions by Sposito (1989). This method is based on displace native cations by an index cation. The index cation is displaced by another cation. Then, the moles of the displaced index cation represents the moles of exchangeable surface charge per unit mass of sample (Jackson, 1956). Appendix A describes the followed procedure.

3.3. Results and discussion of Mineralogy testing

This section shows the results of the XRD, TGA, and CEC tests performed in crushed shale samples. It also shows the relation between the mineralogical content with index properties and durability.

3.3.1. Clay minerals

Figures 3.6a and 3.6b show the XRD patterns of the clay minerals of the Carbondale and Bull Fork samples. The first peak of each mineral is shown in the figures. Appendix B shows the patters of all the shale samples. All the samples contain in different proportions chlorite (Ch), illite (I), kaolinite (K), and clay-sized quartz (Qz).

The small peak between chlorite and illite can be mixed-layers of illite-smectite (I-S) residue of the I/S transformation, or they can be mixed-layers of illite-chlorite due to the formation of chlorite as a by-product of I/S transformation (Bjorlykke, 1998; Lindgreen et al., 2002).

All the shales presented a very clear 001 chlorite peak. The 002 chlorite peak can overlap the 001 kaolinite peak. The occurrence of kaolinite was confirmed because this peak was not present in the pattern K550. Also, the TGA patterns showed a peak between 550°C and 600 °C (Figure 3.8) that correspond to kaolinite. The quantification was done using the XRD patterns; therefore, the quantification is approximated due to the overlapping of 002 chlorite and 001 kaolinite peaks. However, taking into account that chlorite is less than 12 percent of the content of all the shales, the quantification presented here is good enough.

Figures 3.6a and 3.6b show that the crystallinity of the minerals is high because the XRD patterns are clear with low "noise".

Table 3.5 shows the proportions of clay minerals of these samples. Most of the minerals were illite and kaolinite, while chlorite and clay-sized Qz content were low. Similarly with A_c and durability, Fort Payne was different from the other shales because it had the highest content of clay-sized Qz with 13 percent, while the other shales had between 3 and 4 percent. Fort Payne also had the lowest content of Kaolinite. Bull Fork had the highest content of chlorite with 12 percent, while the other shales had less than 8 percent.

I-S was less than or equal to 1 percent for all shales, while Bull Fork did not present these minerals. It is possible that the low content of I-S is due to these shales date from the Paleozoic era.

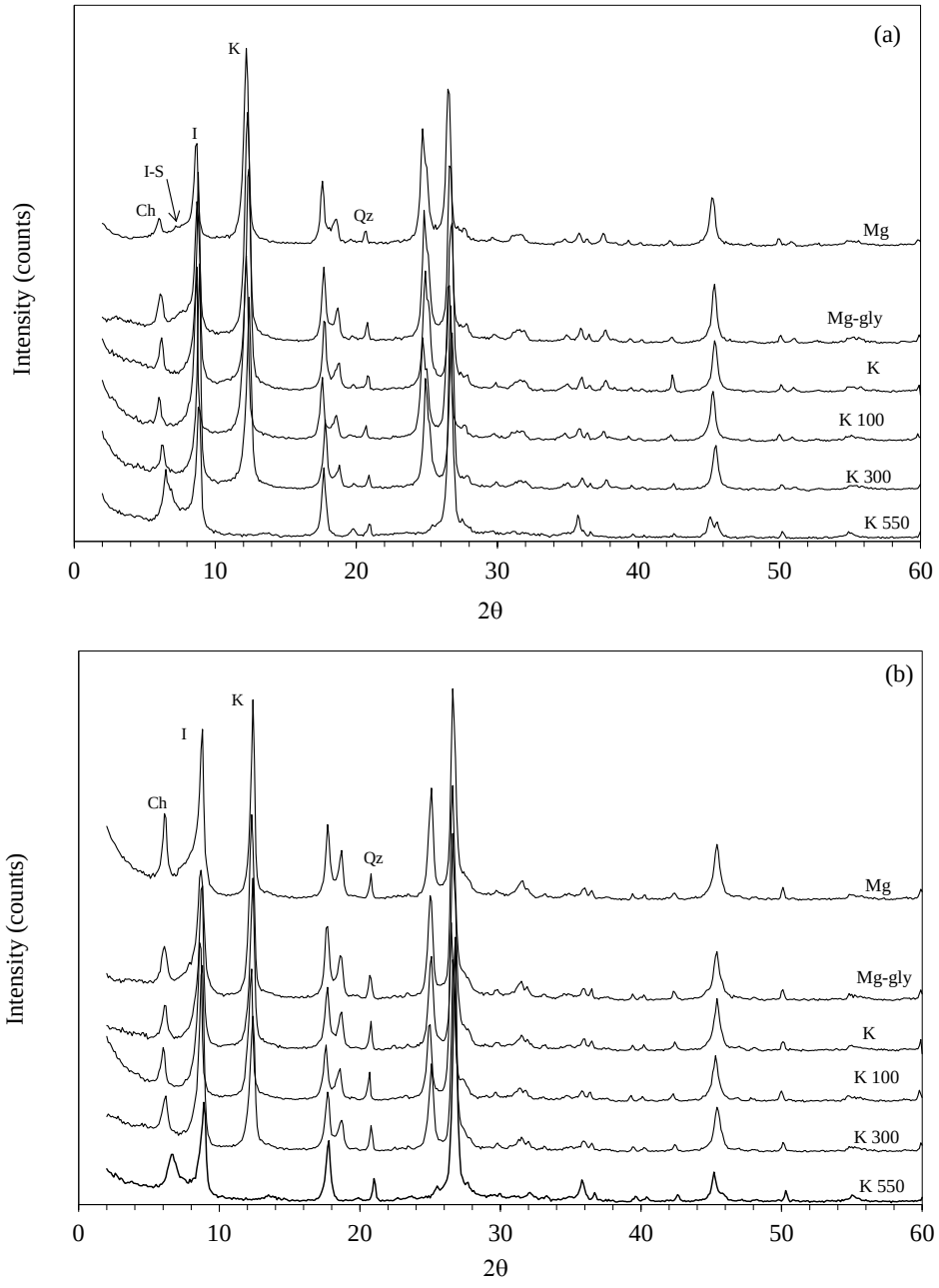

Figure 3.6. XRD patterns of the clay mineral of (a) Carbondale and (b) Bulk Fork shales (Ch=chlorite, I-S=mixed layer illite-smectite, I=illite, K= kaolinite, Qz=quartz). Appendix B shows the XRD patterns for the five shales.

Table 3.5. XRD quantification of clay minerals.

Shale	Ch (%)	I-S (%)	I (%)	K (%)	Qz (%)	(Ch+I)/K
Grundy	8	< 1	40	47	4	1.03
Carbondale	3	< 1	28	65	3	0.48
Fort Payne	7	1	50	30	13	1.88
Tradewater	4	< 1	31	62	3	0.55
Bull Fork	12	0	42	43	4	1.27

Ch=chlorite, I-S=mixed layer Illite-smectite, I=Illite, K=kaolinite, Qz=quartz.

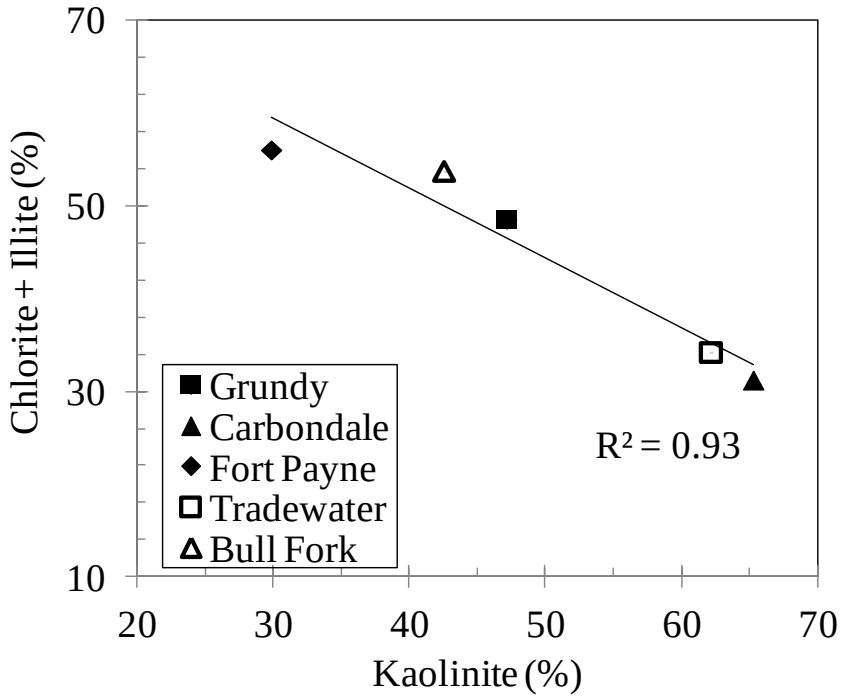

Figure 3.7. Relation between (a) chlorite plus illite with kaolinite.

Figure 3.7 shows that illite and chlorite increase as kaolinite decreases. This observation is related with the genesis of these clay minerals. Kaolinite is associated with wet environments with a high flow of meteoric water, while smectite occurs in dry environments. As was mentioned previously, Smectite converts into illite (i.e. I/S transformation). This transformation produces mixed layers of illite-smectite that change proportion as the diagenesis progresses. During this transformation, a low-temperature quartz forms and K-feldspar dissolves. The I/S transformation starts at 70 °C (around 2 – 3 km) and finishes at 200 °C (about 6.5-8 km), with no smectite remaining (Bjolykke,

1998; Walther, 2009). Chlorite has two geneses. It is a byproduct of the I/S transformation, forming mixed layers chlorite-illite, and is also the result of the reaction of kaolinite with quartz. This observation agrees with the strong increases in the amount of illite relative to kaolinite with depth observed by Bjolykke (1998) in the North sea.

The high R^2 of 0.93 shows that (Ch+I)/K is a ratio that can be used to characterize the shale samples. It was observed that Fort Payne and Bull Fork had (Ch+I)/K ratio higher than one. These two formations were formed in a marine environment. Carbondale and Tradewater had (Ch+I)/K ratio less than one. Finally, Grundy had a (Ch+I)/K ratio approximately at one. They were formed in a transitional environment.

3.3.2. Non-clay minerals

The evaluation of the complete mineralogical content of the shales was done with the interpretation of the characteristics of the reactions during the samples pretreatment, the XRD diffraction patterns in crushed samples passing through the No. 200 sieve, and TGA curves. Table 3.6 shows the characteristics of the reactions during the pretreatment.

Table 3.6. Characteristics of the chemical reactions during the pretreatment.

Shale	Carbonate removal	Iron removal	Organic matter
Grundy	Small reaction with clear supernatant	Strong reaction with red supernatant	No
Carbondale	No reaction with dark brown supernatant	Small reaction with dark brown supernatant	Yes
Fort Payne	Strong reaction with clear supernatant	Strong reaction with red supernatant	Yes
Tradewater	Small reaction with black supernatant	Small reaction with black supernatant	Yes
Bull Fork	Strong reaction with clear supernatant	Strong reaction with red supernatant	No

Fort Payne and Bull Fork had strong reactions during the carbonate removal, while the other shales had small reactions. This means that these two shales had a high content of carbonates. During the iron removal, Grundy, Fort Payne, and Bull Fork had strong

reactions, which indicates that there were iron minerals present, while Carbondale and Tradewater had very small reactions. During the pretreatment Carbondale and Tradewater had a black and dark brown supernatant; additionally, the supernatant of Carbondale, Tradewater, and Fort Payne formed black colored aggregates with a texture of plasticine that would not dissolve even with the pretreatment with H_2O_2. It is assumed that this material is kerogen typical in oil Shales (Chilingarian and Yen, 2011).

Figure 3.8a and 3.8b show the TGA patterns of the Carbondale and Bull Fork crushed shale samples passed through the No. 200 sieve. Appendix C shows the patterns and the calculation of carbonate content for all the shales.

All the patterns show kaolinite. Grundy and Carbondale had peaks between about 500 and 600°C that could be siderite. Grundy, Fort Payne, Tradewater, and Bulk Fork had a peak between about 600 and 750°C that could be dolomite (see Table 3.4). Table 3.7 shows the quantification of carbonates according to the TGA patterns.

Table 3.7. TGA quantification of carbonates from the crushed sample passed through the No. 200 sieve.

Shale	**Dolomite (%)**	**Siderite (%)**
Grundy	6	3
Carbondale	0	6
Fort Payne	19	0
Tradewater	5	0
Bull Fork	24	0

Figures 3.9a and 3.9b show the XRD patterns of the Carbondale and Bull Fork crushed samples. The first peak of each mineral is shown in the figures. The patterns of all five shales are presented in Appendix D. Table 3.8 shows the quantification and the CEC.

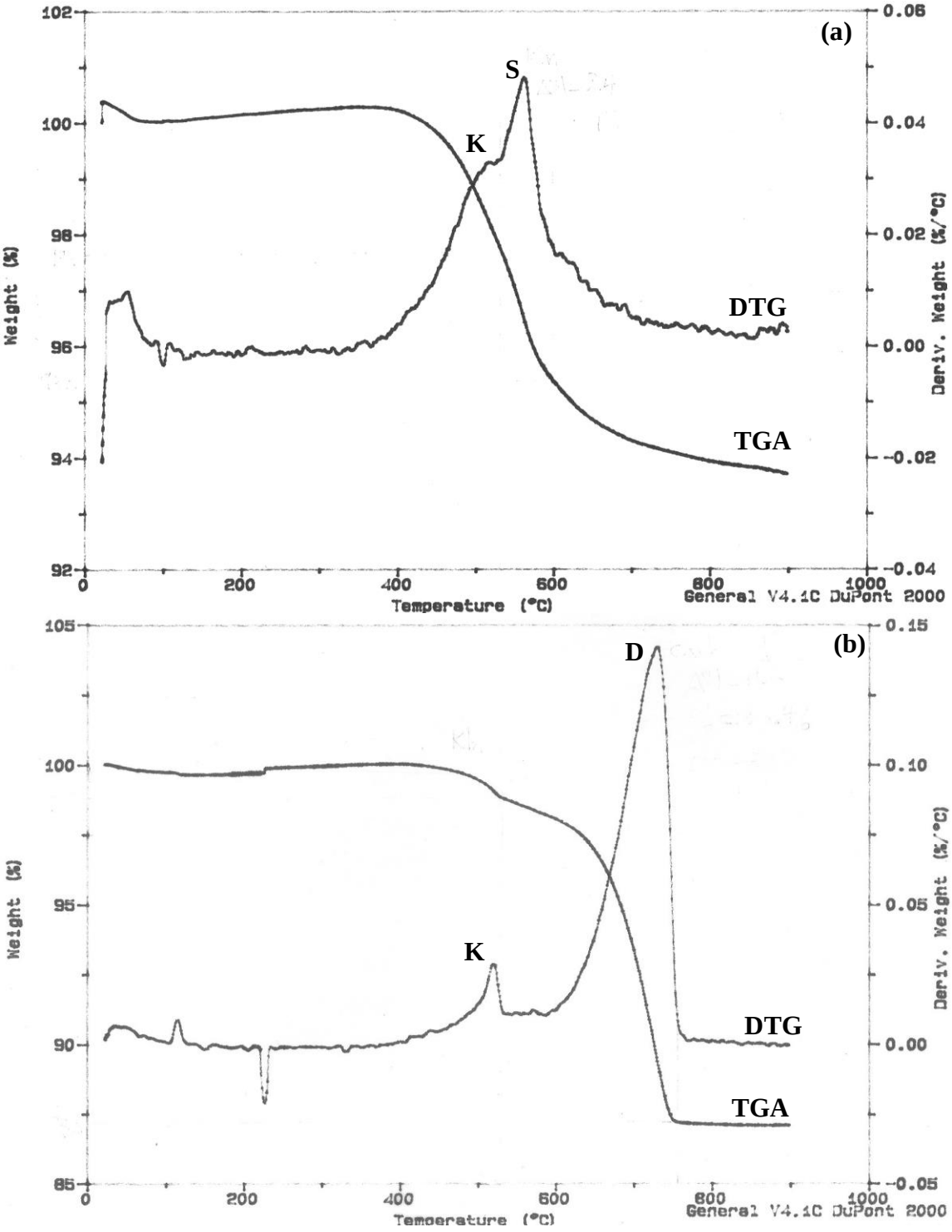

Figure 3.8. TGA and DTG patterns of (a) Carbondale and (b) Bull Fork shales (K=kaolinite, S=siderite, D= dolomite). Appendix C shows the TGA and DTG patterns for the five shales.

All the samples contain in different proportions clay minerals (i.e. chlorite, I-S, illite, and kaolinite), clay-sized and silt-sized quartz, feldspar, calcite, dolomite, siderite, and pyrite. Fort Payne also had Gypsum. This indicates that the Fort Payne sample was already suffering weathering. This shale is different than the other shales because in the clay minerals quantification had an especially high content of Qz and a low content of chlorite, illite, and kaolinite.

The XRD patterns of clay minerals (see Table 3.5) show that there is more kaolinite than illite, while the XRD patterns of fines (see Table 3.8) show the contrary. This contradiction could be due to the fact that clay minerals are aggregated by organic matter, carbonates, and iron minerals; therefore, the samples without pretreatment did not show the correct proportion of clay minerals.

Table 3.8. XRD quantification from crushed sample passed through the No. 200 sieve.

Shale	Chl (%)	I-S (%)	I (%)	K (%)	Qz (%)	F (%)	C (%)	D (%)	S (%)	P (%)	Gyp (%)	CEC cmol/kg
Grundy	7	< 1	35	22	16	3	4	5	6	0	0	84
Carbondale	8	< 1	37	23	19	5	7	0	0	<1	0	54
Fort Payne	2	< 1	9	3	29	4	3	43	0	2	4	88
Tradewater	4	< 1	30	22	24	1	4	0	12	3	0	88
Bull Fork	5	0	11	9	12	< 1	45	15	0	3	0	83

Ch=chlorite, I-S=mixed layer Illite-smectite, I=Illite, K=kaolinite, Qz=quartz, F=feldspar, C=calcite, D=dolomite, S=siderite, P=pyrite, Gyp= gypsum.

3.3.3. Geological classification of shale samples

Based on the results presented above, the shales were classified according to Figure 3.10 by Tucholke et al. (2004). This classification was chosen because it permits a comprehensive idea of the kind of material and it is simple enough based on the amount of available information.

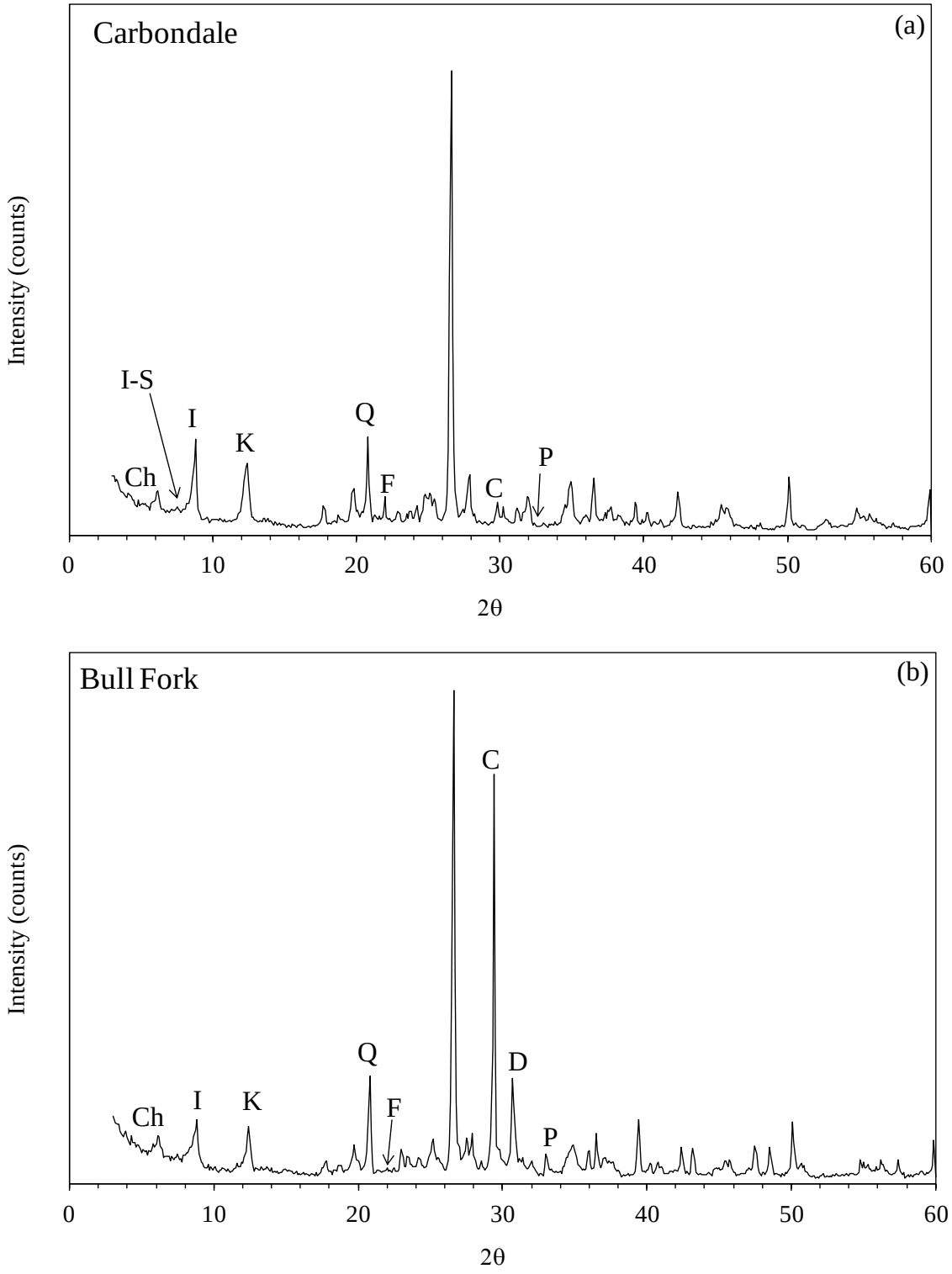

Figure 3.9. XRD patterns of crushed fines fraction of (a) Carbondale and (b) Bull Fork crushed shales (Ch=chlorite, I-S=mixed layer Illite-smectite, I=Illite, K=kaolinite, Qz=quartz, F=feldspar, C=calcite, D=dolomite, and P=pyrite).

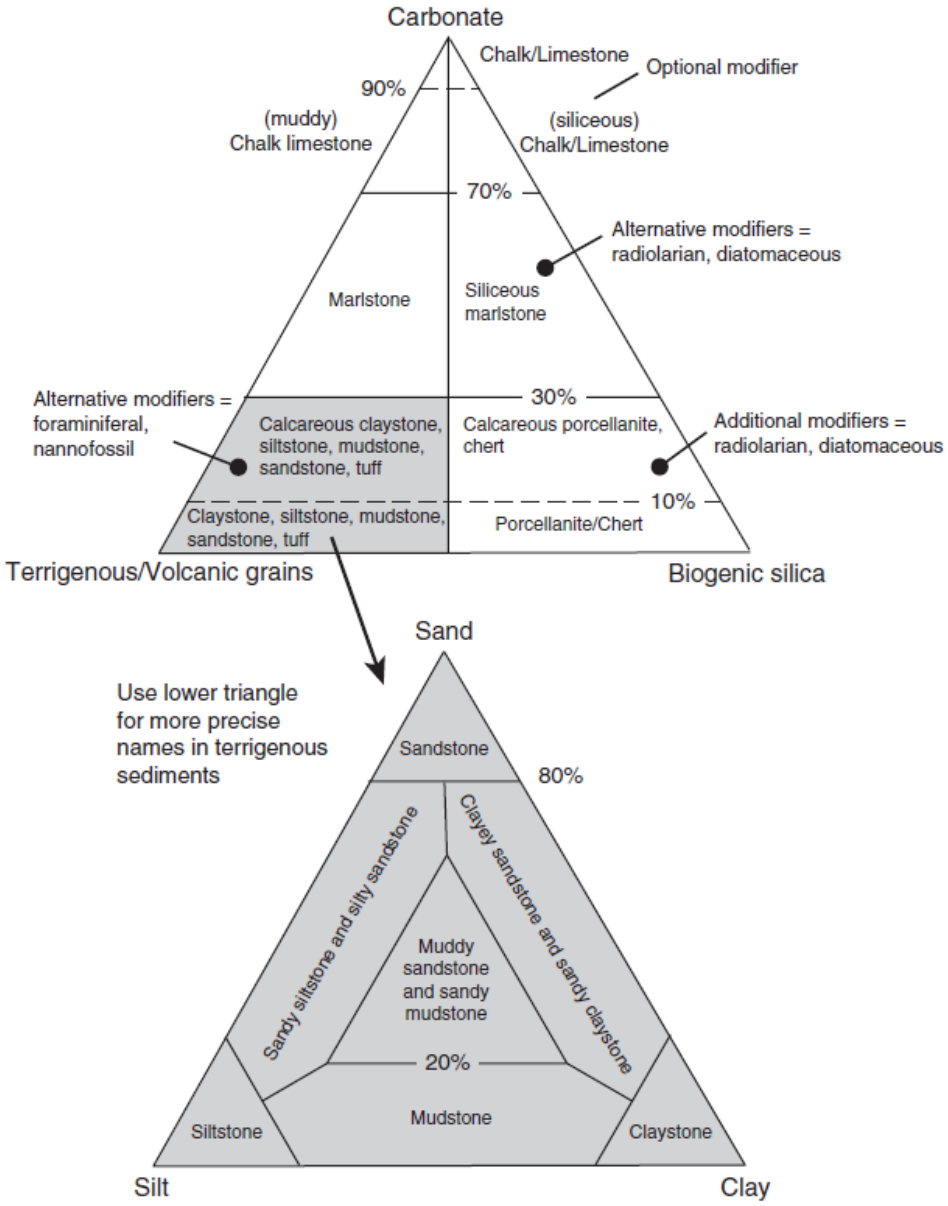

Figure 3.10. Sedimentary rock classification (Tucholke et al., 2004).

Grundy had around 64 percent of clay minerals, 16 percent of quartz, and less than 15 percent of carbonates (i.e. calcite, dolomite, and siderite). Grundy classified as a Calcareous Mudstone. Carbondale had around 68 percent clay minerals, 19 percent of quartz, and less than 7 percent of carbonates, and therefore classified as a Mudstone. Fort Payne had around 14 percent of clay minerals, 29 percent of quartz, and around 46 percent of carbonates, and therefore classified as a Marlstone. Fort Payne also had around 4 percent of Gypsum, which means the sample in the outcrop from which it was taken

had begun weathering. The other samples did not have gypsum. Tradewater had around 56 percent of clay minerals, 24 percent quartz, and 12 percent carbonates, and therefore classified as Calcareous Mudstone. Finally, Bull Fork had 25 percent of clays, 12 percent of quartz, and around 60 percent of calcite and dolomite, and therefore classified as a Marlstone. Table 3.9 shows the classification of the shales.

Table 3.9. Geological classification of the shales of this study.

Shale	**Geologic classification**
Grundy	Calcareous Mudstone
Carbondale	Mudstone
Fort Payne	Marlstone
Tradewater	Calcareous Mudstone
Bull Fork	Marlstone

It is important to note that when the samples were collected they were classified as shales by the construction engineers. However, geologic classification, taking into account the mineralogical content, results in the classification of Fort Payne and BullFork as a Marlstone. It should be taken into account that originally, the term shale was used by the petroleum engineers to classify hand samples of fissile mudstones.

CHAPTER 4

4. Sample characterization: Index Properties

After presenting the mineralogical characterization and geological classification of the shale samples; this chapter shows the index properties and the durability characteristics of crushed shales. This chapter is divided into four parts. The first part presents the sample preparation, the second and third parts present the index and durability testing, and the last part shows the results and discussion.

4.1. Sample preparation

After the shale samples were taken in the field, they were crushed by a jaw crusher to reduce the particle size (Kirkendoll, 2012). Figure 4.1 shows the jaw crusher. After initial crushing, 1000 g of pieces of crushed shale were passed through an 8 mm sieve and retained in No. 4 (4.76 mm) sieve shown in Figure 4.2a. The sieved sample was then further crushed in a proctor mold using a modified proctor hammer for 100 blows. Figure 4.2b shows the mold and the hammer. The energy used to crush the samples was:

$$E = \frac{N_{blows} \times W_{hammer} \times H_{drop}}{V_{mold}} = \frac{100 \times 4.54kgf \times 0.457m}{944cm^3} = 2{,}155kNm/m^3$$

where N_{blows} is the number of blows, W_{hammer} is the weight of the hammer, H_{drop} is the height of drop of hammer, and V_{mold} is the volume of the mold. The final crushed sample was used to perform index, mineralogical, and mechanical tests. Appendix E presents the detailed procedure followed to crush the samples.

After the sample was crushed, the grain size distribution (GSD) of the sample was calculated following the ASTM standard D422. Appendix F shows all the procedures and results of the GSD. The sieve analysis was performed using the No. 4, 10, 40, 200 and Pan sieve sizes as shown in Figure 4.2c. The hydrometer tests were performed with samples that passed through a No. 200 sieve size. The air-dried water content, the percentage of fines (percent passing No. 200 sieve size), the percentage of clay fraction,

CF (portion smaller than 0.002 mm in diameter), the percentage retained in the No. 4 sieve size, and the diameter in mm of the particles finer than 60 percent of the sample, D_{60}, finer than 30 percent of the sample, D_{30}, and finer than 10 percent, D_{10}, of the sample were determined. The uniformity coefficient, Cu, and the coefficient of curvature, Cc that were calculated as:

$$C_u = \frac{D_{60}}{D_{10}} \quad [3.1]$$

$$C_c = \frac{D_{30}^{\ 2}}{D_{60}D_{10}} \quad [3.2]$$

Figure 4.1. Jaw crusher used to reduce the sample size.

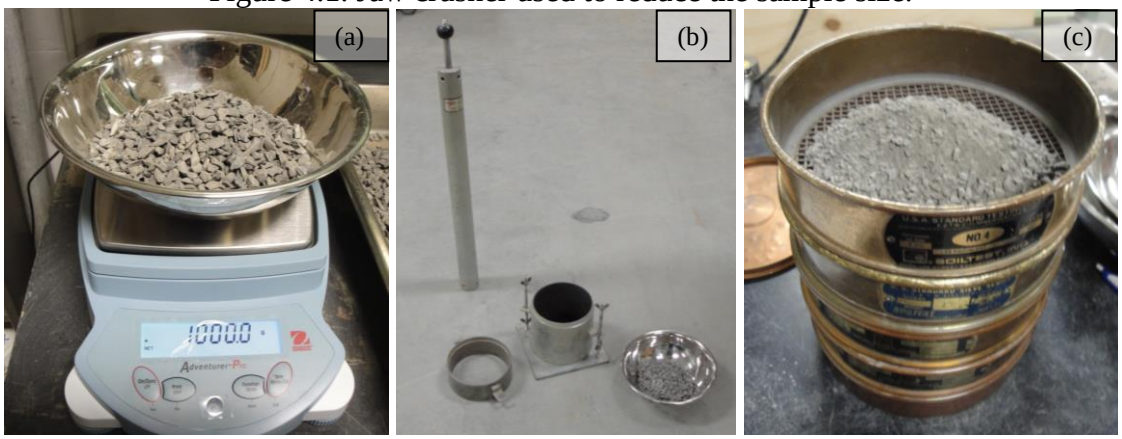

Figure 4.2. Preparation of the sample. (a) Sample passed through eight mm sieve and retained in No. 4 sieve. (b) Proctor mold and hammer used to crush the sample. (c) Sample after being crushed and ready to be sieved.

The main tests of this research were the CIU triaxial tests with a target specimen size of 70 mm in diameter by 150 mm in height. In order to follow the recommendation of ASTM D4767 that the ratio between the height of the triaxial specimen and the maximum grain size must be higher than 1/16, the maximum grain size used to do the triaxial specimens was 4.76 mm (i.e. passing No. 4 sieve size). Therefore, the gravel-sized samples were reduced to sand-sized samples with a new GSD that represented the GSD after the crushing process.

4.2. Index and durability tests

4.2.1. Index tests

The Atterberg Limits and specific gravity tests were performed by Kirkendoll (2012). The Atterberg Limits were conducted for crushed samples that passed through a No. 40 sieve size according to the ASTM D4318 procedure and the specific gravity, Gs according to the ASTM D854 procedure. Kirkendoll (2012) also performed natural water content tests on the samples. The natural water content in shales can change depending on a large number of variables such as the depth of the sample, the technique used to do the sampling, the regional and local water tables, etc. These variables were not controlled by Kirkendoll (2012). Therefore, the natural water content results for the crushed shales were not used in this research because of the heterogeneity of the procedures used to collect the samples.

4.2.2. Durability tests

Three durability indexes are analized in this research. The first test was the well-known Slake Durability of Shales and Similar Weak Rocks (ASTM D4644) test, in which the measurement of durability is given by the parameter slake durability index $Id_{(2)}$. The other test is the Lost Slake Test (Bryson et al., 2012), whose parameter is the lost slake index, LSI. These tests were performed by Kirkendoll (2012). Other durability test is the Electrical Jar tests, initialy presented by (Kirkendoll, 2012), whose parameter is the slope jar index, S_{jar}. The second and third tests are currently in the process of standardization.

This research uses the S_{jar} values obtained during this standardization.

4.3. Results and discussion

4.3.1. Grain size distribution of crushed shales

GSD characteristics are controlled by the intrinsic characteristics of the shales, the procedure of crushing, and the energy used to crush the sample. Therefore, it is hypothesized that if shales with different levels of durability are crushed using the same energy and procedure, the GSD parameters will be related to the characteristics of the shales.

Table 4.1 shows the GSD characteristics of the crushed shales in order of CF. The table shows the hygroscopic water content (i.e. air-dried water content), fines, CF, the percentage retained in the No. 4 sieve size, D_{60}, D_{30}, and D_{10}, and C_u and C_c. Finally, the table shows the Unified Soil Classification System (USCS) performed according to ASTM D2487. Figure 4.3 shows the GSD curves. Appendix F shows in detail the GSD for each crushed shale.

Table 4.1. Grain size distribution characteristics of the crushed sample.

Formation	Air-dried water content (%)	Fines (%)	CF (%)	Retained No. 4 (%)	D_{60}	D_{30}	D_{10}	C_u	C_c	Classification (USCS)
Grundy	0.6	4.3	0.97	47.9	5.4	2.8	0.6	9.7	2.7	SW
Carbondale	0.9	3.7	1.07	52.0	5.6	3.1	0.7	8.2	2.5	GW
Fort Payne	1.5	4.8	1.42	41.7	4.9	2.0	0.3	15.3	2.6	SW
Tradewater	1.3	4.2	1.52	45.0	5.2	2.3	0.4	12.7	2.4	SW
Bull Fork	1.1	5.8	2.09	40.7	4.8	1.7	0.2	21.8	2.7	SW

For Carbondale shale, 52 percent of the sample was retained in the No. 4 sieve size. For the other shales, between 40 percent and 48 percent of the sample was retained in the No. 4 sieve size. The fines were between 3.7 percent and 5.8 percent. The CF was between 0.95 percent and 2.10 percent. C_u was higher than 4 and C_c was between 1 and 3. Therefore, Carbondale classified as a well graded gravel (GW) and the other shales classified as well graded sands (SW).

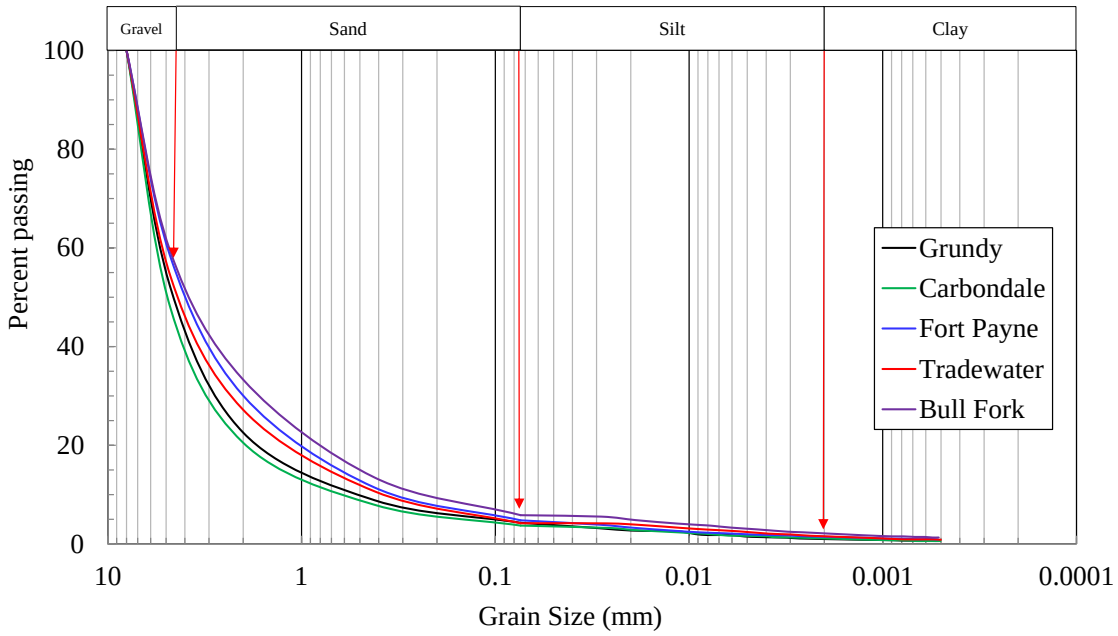

Figure 4.3. GSD of the crushed samples.

Because the samples were crushed using the same level of energy, it is expected that the characteristics of the GSD are consistent with the properties of the shales. Figure 4.4a shows the variation of C_u with CF. It can be observed that when CF increases, C_u increases; this means that when a type of crushed shale has a better gradation the sample has a higher CF. There is no clear relation between C_c and CF as shown in Figure 4.4b; this means that there is no relation between the shape of the GSD and the CF.

4.3.2. Atterberg limits

Table 4.2 shows the Atterberg limits: liquid limit, LL, plastic limit, PL, and plasticity index, PI, of the crushed shales. The table also shows the specific gravity, GS. Figure 4.5 shows the location of the samples in the plasticity chart. This chart will be used in the following section to do the classification of the crushed samples following the USCS.

Fort Payne is the only crushed shale under A-Line in the plasticity chart as shown in Figure 4.5. Fort Payne is different also because is the shale with the highest content of Quartz and the lowest content of clay minerals as shown in Table 3.8.

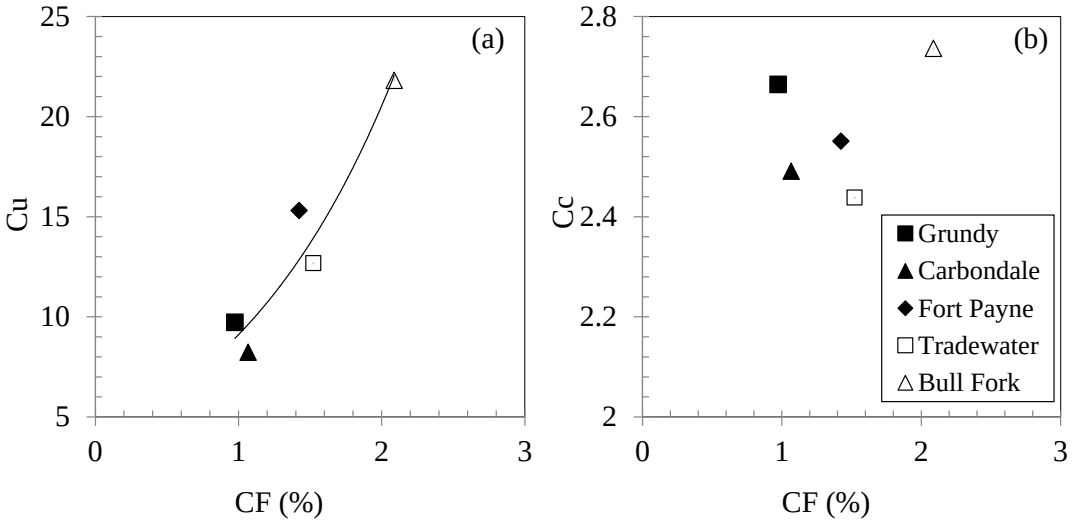

Figure 4.4. Grain size distribution curve characteristics of the crushed samples as a function of crushed clay fraction.

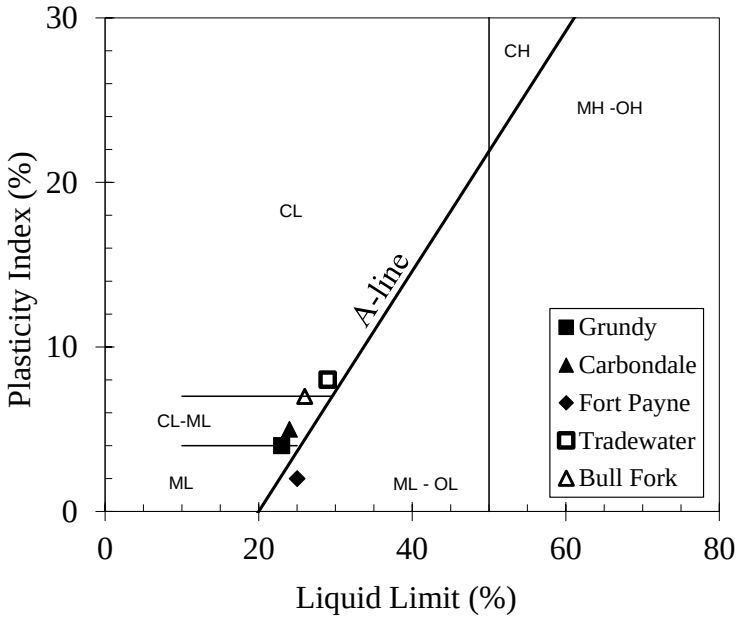

Figure 4.5. Plasticity chart.

Table 4.2. Atterberg limits and specific gravity.

Shale	LL	PI	Gs
Grundy	23	4	2.7
Carbondale	24	5	2.8
Fort Payne	25	2	2.6
Tradewater	29	8	2.7
Bull Fork	26	7	2.7

4.3.3. Grain size distribution of crushed shale for triaxial testing

Consolidated isotropically undrained (CIU) triaxial tests were performed in order to characterize the mechanical behavior of compacted shales. As will be shown in Chapter 5, the target specimen size of the triaxial specimens were 70 mm in diameter by 150 mm in height; therefore, the largest particle size has to be 4.76mm (sieve No. 4). Therefore, the crushed samples with the GSD shown in Figure 4.3 were reduced to samples with particles of a size less than 4.76mm. Appendix G shows in detail the GSD of each sample used to do the triaxial specimens.

Table 4.3 shows the GSD parameters of the crushed samples used to perform the CIU triaxial tests. These parameters are fines (silt plus clay), CF, C_u, and C_c, and activity, A_c. The table also shows the USCS classification. Figure 4.6 shows the variation of PI with CF, whose ratio is the A_c.

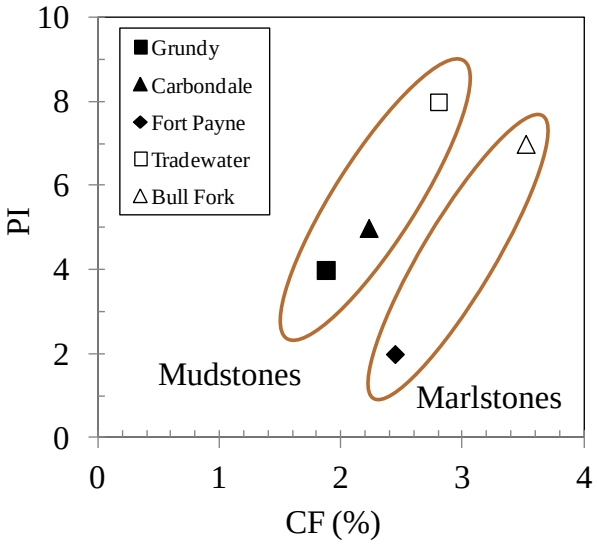

Figure 4.6. Variation of PI with CF.

Grundy, Carbondale, Tradewater, and Bull Fork had A_c higher than two and Fort Payne had an A_c of 0.8, as shown in Figure 4.6 and Table 4.3. Soils with A_c higher than 1.25 are considered active soils, between 1.25 and 0.75 normal soils, and lower than 0.75 inactive soils (Mitchell and Soga, 2005; Reeves et al., 2006). Therefore, crushed Grundy, Carbondale, Tradewater, and Bull Fork shales are active soils, while crushed Fort Payne shale is a normal soil.

Notice that the mudstones Grundy, Carbondale, a Tradewater follow a different trend than the marlstones Fort Payne and Bull Fork. Figure 4.7 shows the GSD curves of each crushed sample used to perform the CIU triaxial tests.

Table 4.3. Classification of the shales used to do the TXT tests.

Shale	Fines (%)	CF (%)	C_u	C_c	A_c	USCS Classification
Grundy	8.2	1.9	19.1	3.7	2.1	SW-SM
Carbondale	7.7	2.2	19.0	3.7	2.2	SW-SM-SC
Fort Payne	8.2	2.4	19.7	2.6	0.8	SW-SM
Tradewater	7.7	2.8	20.4	2.7	2.9	SW-SC
Bull Fork	9.8	3.5	27.9	2.9	2.0	SW-SC

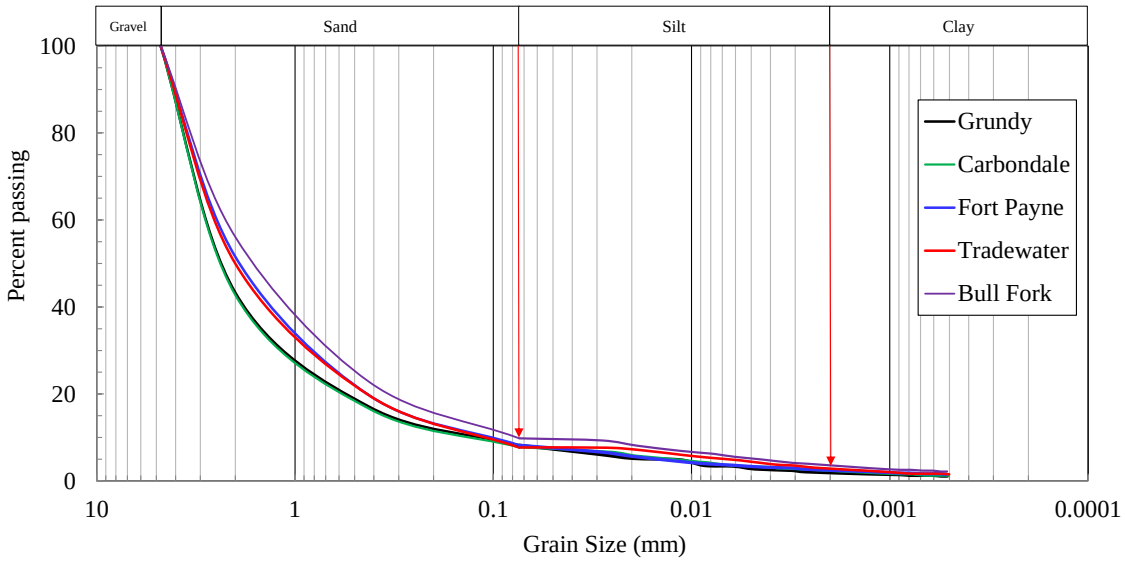

Figure 4.7. Grain size distribution of the tested samples.

All samples passed through the No. 4 sieve had less than 10 percent of fines, less than 3.5 percent of CF, C_u greater than 19, and C_c between 2.6 and 4. Grundy and Fort Payne had PI less than 4 percent, so they classified as SW-SM. Carbondale had PI of 5 percent, so it was classified as SW-SM-SC. Tradewater and Bull Fork had PI of 7 percent and 8 percent, respectively, so they were SW-SC. Notice that Tradewater and Bull Fork, which classified as SW-SC, had the highest CF (2.8 percent and 3.5 percent, respectively) and the highest C_u (20.4 and 20.4, respectively). Grundy, Carbondale and Fort Payne, which

classified as SW-SM, had the lowest CF, less than 2.4 percent. This dual classification means that even though the samples were sands, the content of clay and silt are enough to influence the behavior of the samples. The Gs ranged between 2.64 and 2.77.

4.3.4. Effect of mineralogical content in the index properties

Figures 4.8a to 4.8d show the variation of A_c with (CH+I)/K, fine size quartz, carbonates content, and total content of clay minerals. The Figures 4.8a and 4.8b show that A_c decreased with (CH+I)/K and increased with quartz content. The interpretation of this results is due to the CF, not the PI. Shales with high content of quartz and low proportion of chlorite and illite had lower CF; therefore, higher A_c. The graphs also show that Fort Payne had the highest (Ch+I)/K together with the highest quartz content; characteristic that was not observed in the other shales.

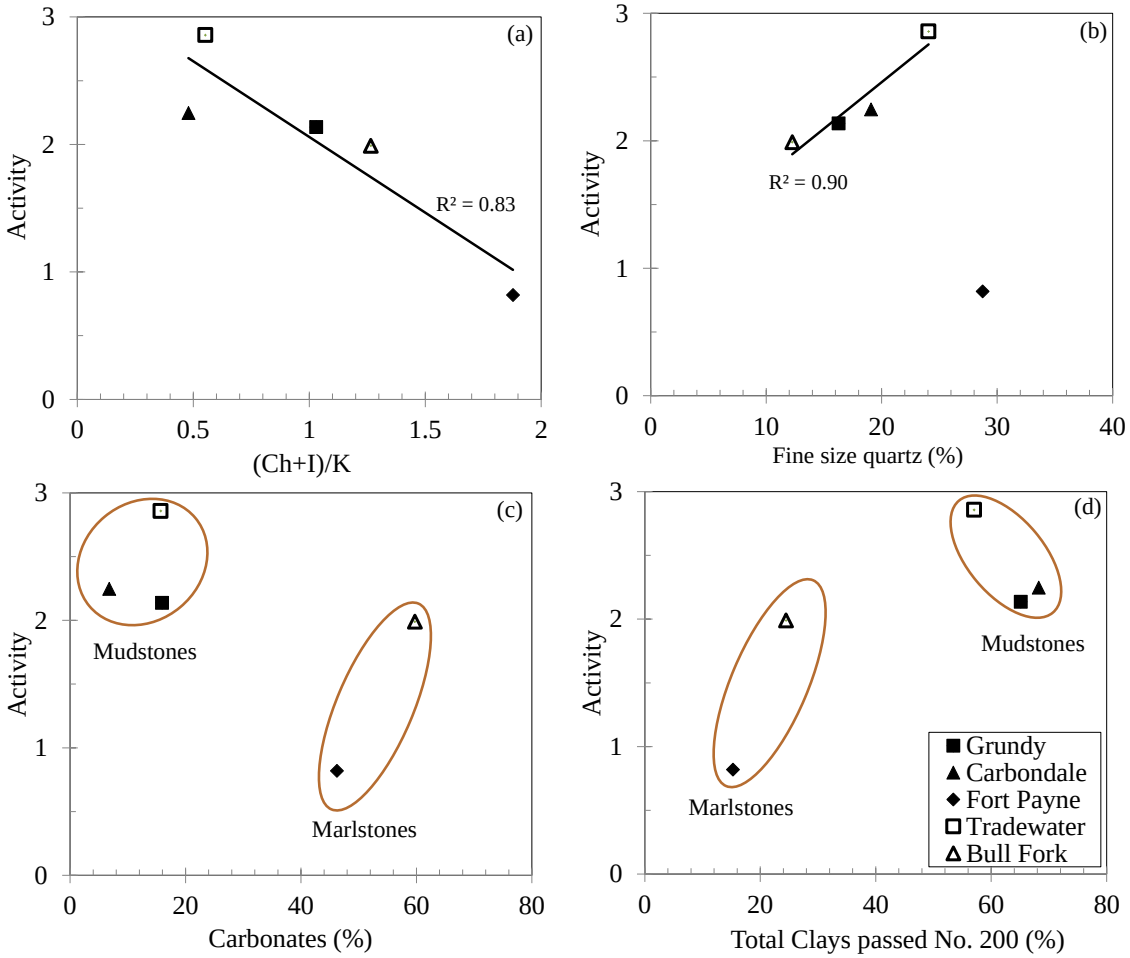

Figure 4.8. Variation of activity with (CH+I)/K ratio and fine size quartz.

The high R^2 (0.83 and 0.90) in Figures 4.8a and 4.8b demonstrates that the variability of A_c is explained by the type of clay minerals and the content of fine size quartz. Figures 4.8c and 4.8d show the variation of A_c with carbonates and the total content clay minerals. These graphs let to see the difference between mudstones and marlstones.

4.3.5. Relationship between index properties and durability

Table 4.4 shows the $Id_{(2)}$, LSI, and S_{jar} durability indexes of the shale samples of this study. According to $Id_{(2)}$ and LSI, Grundy, Carbondale, and Fort Payne are the hardest shales and Tradewater and Bull Fork the softest. However, Fort Payne and Bull Fork had contradictions between indexes. According to S_{jar}, Fort Payne is the less durable shale, but according to $Id_{(2)}$ and LSI is a durable shale. According to S_{jar}, Bull Fork is a durable shale, but $Id_{(2)}$ and LSI indicates that it is the less durable shale.

Table 4.4. Three different durability indexes.

Shale	**S_{jar}**	**LSI**	**$Id_{(2)}$ (%)**
Grundy	0.18	0.07	97
Carbondale	0.42	0.15	95
Fort Payne	0.61	0.07	93
Tradewater	0.54	0.50	81
Bull Fork	0.21	0.22	77

Figures 4.9a to 4.9c show the variation of the $Id_{(2)}$ with A_c, (Ch+I)/K, and fine quartz content. The graphs show that the three most durable shales (Grundy, Carbondale, and Fort Payne) and the softest shales (Tradewater and Bull Fork) clustered in two different groups. A clear trend with A_c, (Ch+I)/K, and fine quartz content was not observed.

Figures 4.10a to 4.10d show the variation of S_{jar} with $Id_{(2)}$, A_c, (Ch+I)/K, and fine quartz content. The Figure 4.10d shows that the quartz content controled the variability of S_{jar}, as well as Ac, with the exeption of Fort Payne. The S_{jar} was not related with the content of carbonates.

Figures 4.11a to 4.11d show the variation of LSI with $Id_{(2)}$, A_c, (Ch+I)/K, and fine quartz content. The figures show that there was not clear trend of LSI with the mineralogical

content and A_c. However, the graphs show that Grundy, Carbondale, and Fort Payne (mudstones) and Tradewater and Bull Fork (marlstones) clustered in two different groups.

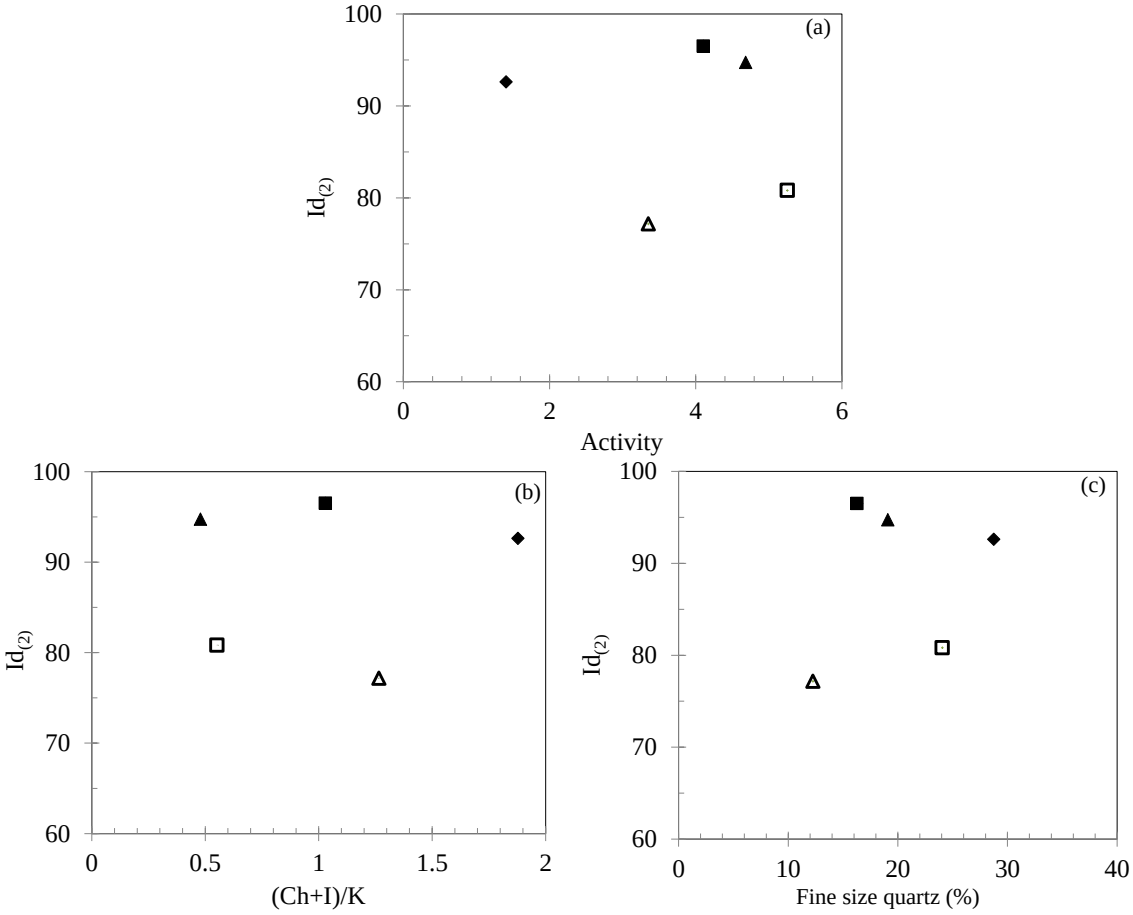

Figure 4.9. Variation of $Id_{(2)}$ with activity, (CH+I)/K, and fine size quartz.

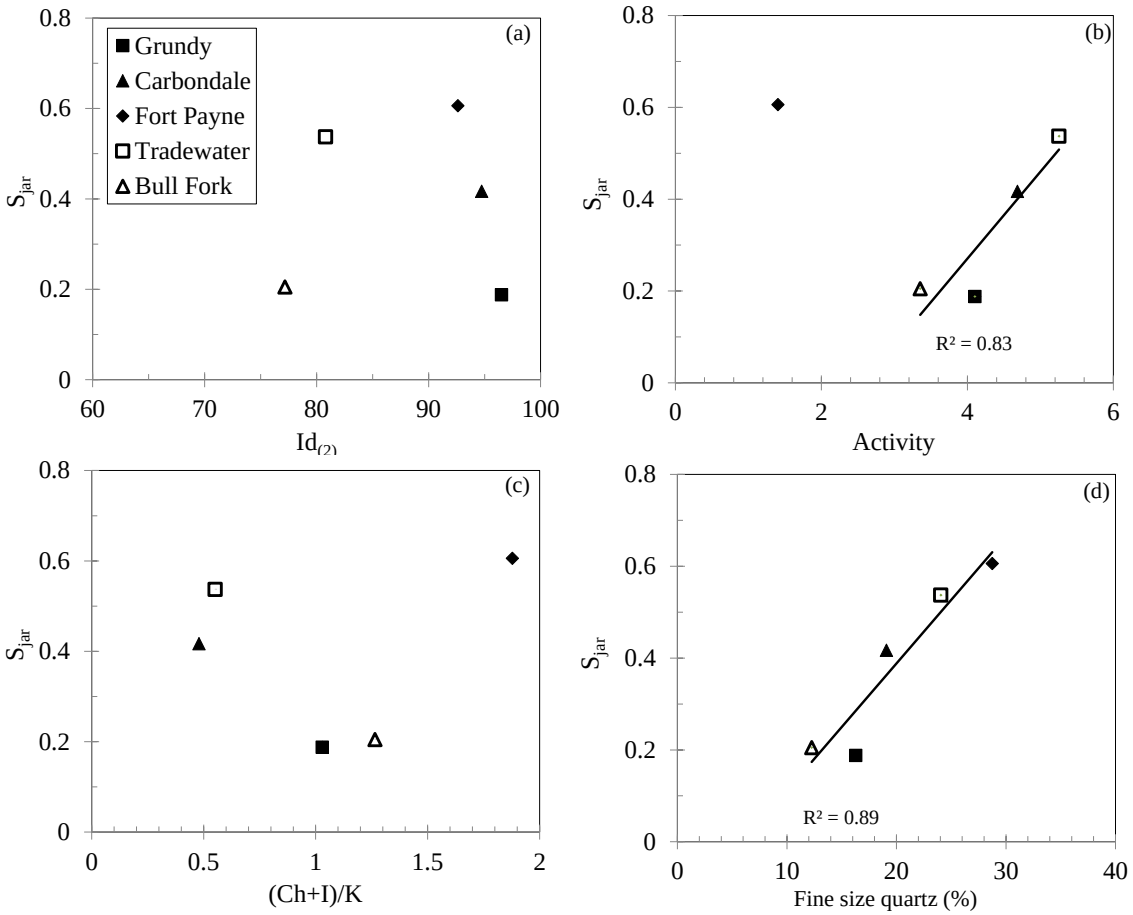

Figure 4.10. Variation of S_{jar} with $Id_{(2)}$, activity, (CH+I)/K, and fine size quartz.

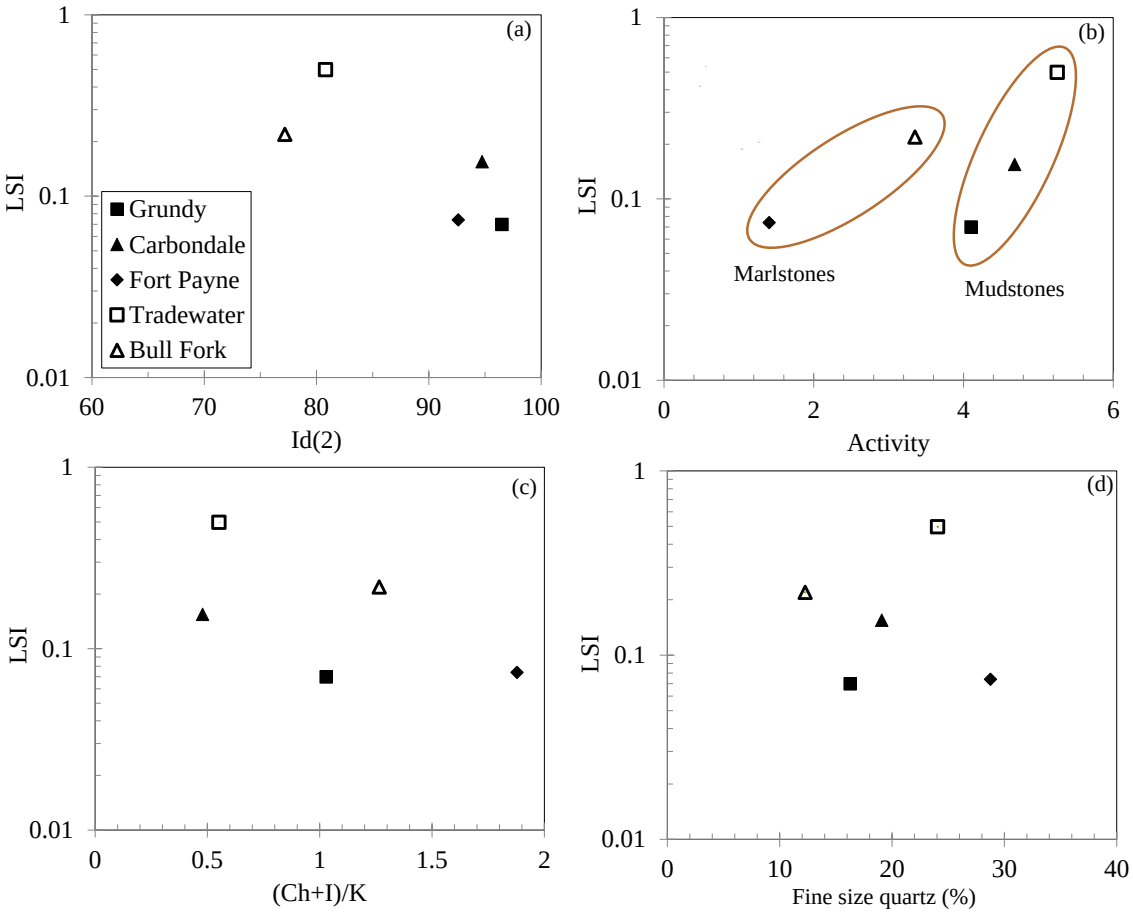

Figure 4.11. Variation of LSI with $Id_{(2)}$, activity, (CH+I)/K, and fine size quartz.

CHAPTER 5

5. Sample characterization: CIU triaxial tests

This chapter presents the laboratory testing performed to investigate the mechanical behavior of compacted shale to obtain input parameters for the NorSand model and to develop the framework for an improved model. This chapter is divided into two parts. The first part describes in detail the procedures followed to perform the experiments and the second presents the results and discussion.

5.1. Triaxial testing

In this research, Consolidated Isotropically Undrained Triaxial (CIU) tests were performed following ASTM D4767 with some modifications. Two set of experiments were performed. The first set of experiments was performed at high confining pressure, high density, and a positive state parameter. They were consolidated to such high pressure that R = 1.0. They were soaked during an extended period of time to study the influence of soaking time after consolidation on the mechanical behavior of compacted shales. Table 5.1 shows the list of tests that were performed to study the influence of soaking time in the behavior of the compacted shales. Grundy underwent one experiment, Fort Payne and Tradewater underwent two experiments, and Carbondale and Bull Fork underwent three experiments as shown Table 5.1. The other set of experiments were performed at low confining pressure, low density, and a negative state parameter. They were not left soaking and were consolidated to low stress levels. Together with the first set of experiments, they were carried out with the objective to study the effect of state parameter in the shear behavior. Table 5.2 shows the list of all the experiments used to study the effect of soaking time and additional tests in order to get information to construct the model. Appendix G shows in detail the characteristics of each sample used to do the triaxial specimens and Appendix H shows the complete procedure followed to construct the specimens of compacted shale, and how the CIU triaxial tests were performed. Each experiment was named as follows: Name of shale, year, month, day when the test was performed, and time in days that the sample was left soaking.

Table 5.1. Test performed to study the effect of soaking time.

Shale	Soaking time			
	0 days	6 days	12 days	20 days
Grundy	X			
Carbondale	X	X		X
Fort Payne	X	X		
Tradewater	X	X		
Bull Fork	X	X	X	

Table 5.2. Test performed for each compacted shale.

Shale	Complete Isotropic Consolidation	Undrained Shear
Grundy	2	3
Carbondale	3	4
Fort Payne	2	3
Tradewater	2	5
Bull Fork	3	3

5.1.1. Triaxial equipment

All triaxial tests were carried out using the Geocomp Triaxial testing machine Load Trac-II/Flow Trac-II system. This system fully automates the triaxial test of a soil specimen. The system consists of a LoadTrac-II load frame, two FlowTrac-II flow pumps for controlling volume and pressure for the cell and specimen, a computer with a network card for test control and data acquisition, and Microsoft Windows application software, called TRIAXIAL, for controlling a test and creating a report of the results. After a soil specimen is in place and the test conditions selected, the system runs the entire triaxial test automatically. The test data is stored in a file for reduction and analysis of the results. The system can perform isotropic and anisotropic consolidation tests as well as undrained and drained triaxial tests. The tests can be performed stress or strain controlled. Figure 5.1 shows the GeoComp Load Trac-II machine.

Figure 5.1. Picture of the Geocomp machine.

5.1.2. Test specimen preparation

The experiments were performed with air-dried samples. In order to get the GSDs shown in Figure 4.7, portions of crushed shale of Pan, retained No. 200 sieve size, retained No. 40 sieve size, retained No. 10 size – passed through a No. 4 sieve size were weighted and mixed. Figure 5.2a shows the appearance of the crushed Grundy shale for different sizes and Figure 5.2b the sample ready to be mixed.

Table 5.3 shows the target specimen dimensions. For each one of the shales, the target dry unit weight of the specimens was 1.7 g/cm^3.

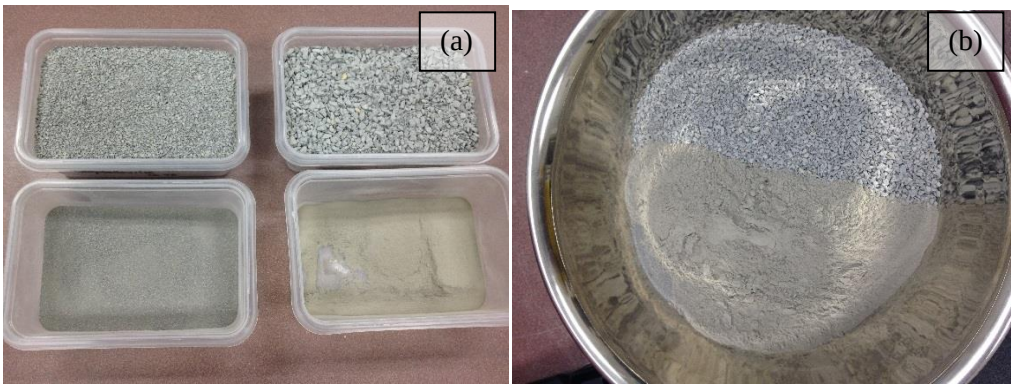

Figure 5.2. Crushed shale separated by grain size ready to be mixed.

Table 5.3. Target sample dimensions for the compacted shales of this study.

Diameter	D (cm)	7.1
Height	H_o (cm)	15.0
Area	A cm^2	39.6
Volume	V_o (cm^3)	593.9
Dry unit weight	γ_d (g/cm^3)	1.7
H/D	H/D	2.11
Largest particle size (LPZ)	LPZ (mm)	4.76
LPZ/D	< 1/6	0.067
Water content	Air-dried water content each sample	

To achieve a specimen with the target dimensions and unit weight, a triaxial cell with a pedestal of 71 mm bottom and top caps was used. A porous stone, filter paper and membrane was placed in the bottom cap of the pedestal as shown in Figures 5.3a and 5.3b.

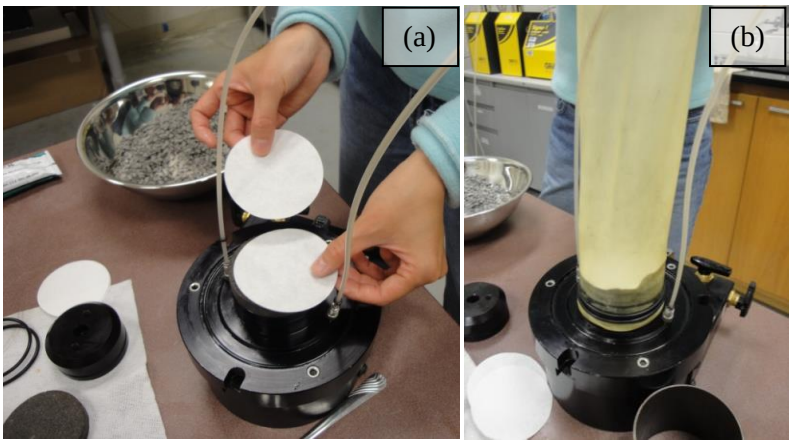

Figure 5.3. Pedestal of triaxial cell with a bottom and top cap of 71 mm. (a) Filter paper, and (b) membrane.

The membranes were 0.03048 mm thick. The size and shape of the specimen were controlled using a split mold. The crushed sample was mixed and placed inside the membrane and compacted using an 838 g hammer (Figures 5.4a and 5.4b).

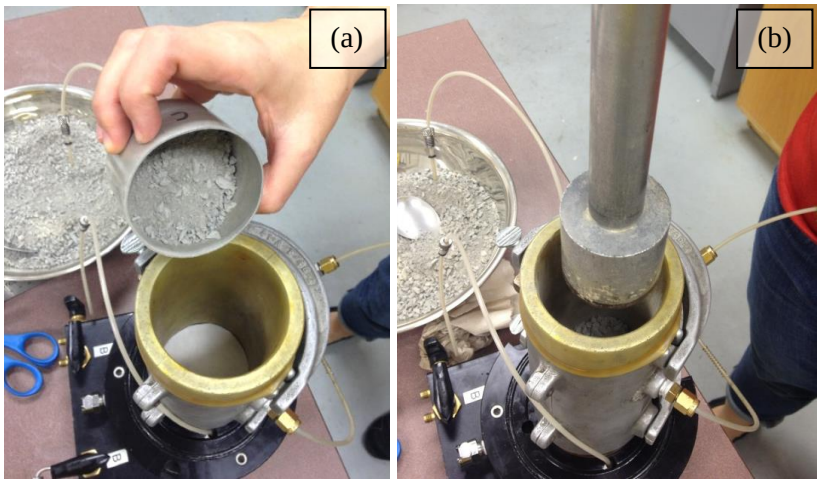

Figure 5.4. Preparation of the specimen. (a) Membrane stretched in the mold and sample ready to be put inside the mold. (b) Hammer used to compact the sample.

Vacuum was applied inside the specimen to remove the mold and keep the specimen shape. Figure 5.5 shows the appearance of the specimens.

Figure 5.5. Dry compacted shale specimen. This sample is under vacuum pressure. Notice the penetration of the membrane in the specimen.

5.1.3. Flooding and soaking

De-aired tap water was used to flooding and saturation. After the specimen was prepared, it was placed in the triaxial cell. The chamber was connected to a cell pressure pump applying a pressure of 20.68 kPa. The specimen was connected to a sample pressure pump in the bottom valve. The top specimen valve was opened in such a way that the specimen was at atmospheric pressure at the top. The software Triaxial.exe was started before the flooding with the objective of registering the change of height and volume of the sample during flooding. The bottom and top valves were opened as the software executed. Due to the difference in pressure between the bottom and top valves, the water flowed from the bottom to the top. Bubbles of air that were inside the specimen went through the top valve. Figure 5.6a shows the appearance of the sample during the flooding and Figure 5.6b shows the bubbles going of the sample. After pass three pump volumes of water through the sample, the top valve was closed and the specimen was left soaking during scheduled times. From this point the software took control of the test.

The specimens were soaked in the triaxial cell, and the samples were left to sit during different periods of time. These periods of time were one day, six days, 15 days, and 20 days. Figure 5.7 shows the appearance of the sample during soaking.

During soaking of all the specimens, the cell pressure, σ_{cell}, or total stress was 20.68 kPa, and the sample pressure, *u*, was 13.79 kPa. Therefore, the effective stress, σ', of the sample was 6.89 kPa.

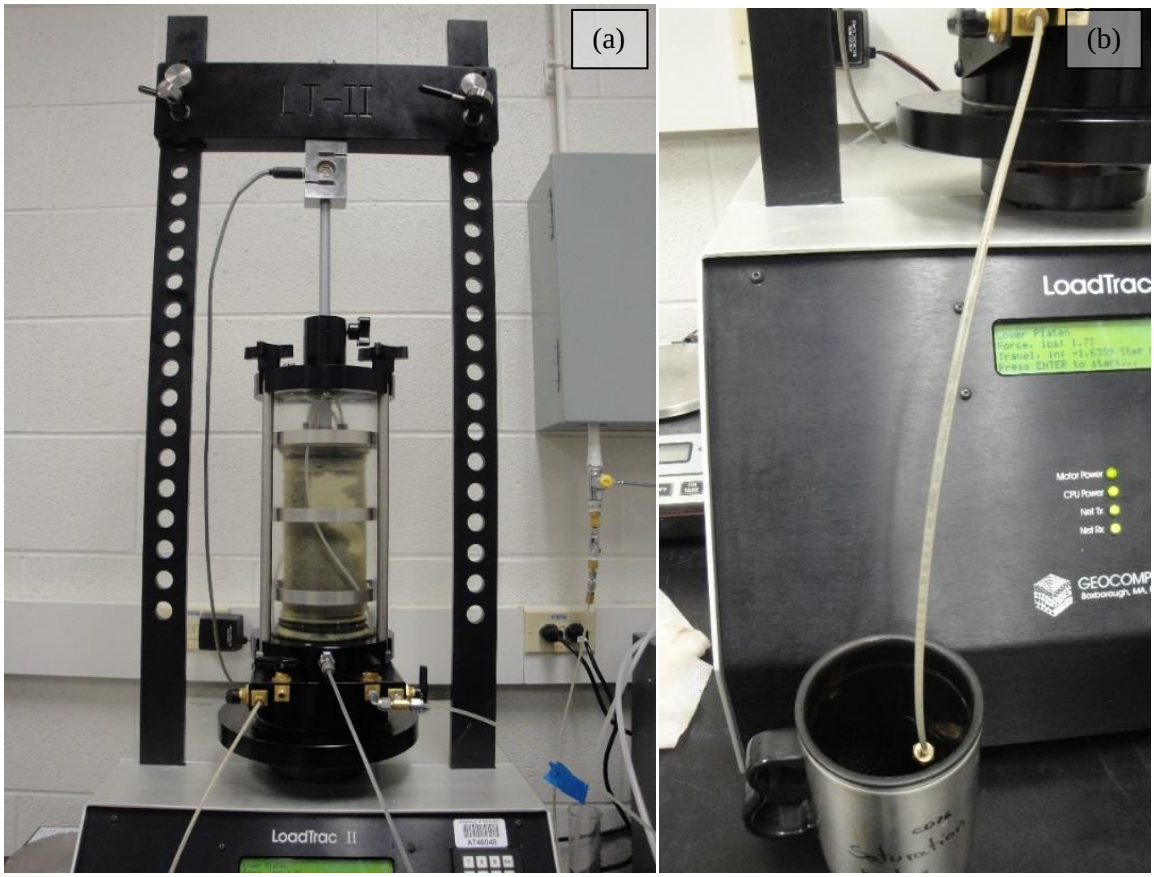

Figure 5.6. (a) Specimen during the flooding. (b) Bubbles going outside the sample through the top valve.


Figure 5.7. Specimen during the soaking.

Figures 5.8a and 5.8b show the change of height and volume of water that flowed through the specimen during flooding, soaking, and saturation for the specimen Carbondale120711_0. The specimen had a change in height of -0.37 mm during flooding and -0.25 mm during saturation for a total change in height of -0.62 mm. A negative sign means extension. This change in height was small enough to not be considered in the data reduction of every test. The area of the specimen was 39.03 cm^2; therefore, the change of volume was 2.46 cc. During the flooding, the volume of water that flowed into the specimen was 544.07 cc and the volume of water that flowed out of the specimen was 472 cc. Therefore, the water that stayed inside the specimen was 72.07 cc. During the saturation, 36.97 cc of water flowed inside the specimen. Therefore, the change of volume of voids during flooding and saturation was 115.6 cc. Taking into account that the initial total volume of the specimen was 577.60 cc and the initial volume of void was 224.64 cc, a change of 20 percent of volume occurred before the consolidation. Taking into account that the change of height was insignificant, it can be assumed that this change of voids only affected the fine of the sample, not the sand fraction. Therefore, this change of volume did not affect the structure of the sample. For this reason this change in volume was not considered in the data reduction of all the experiments.

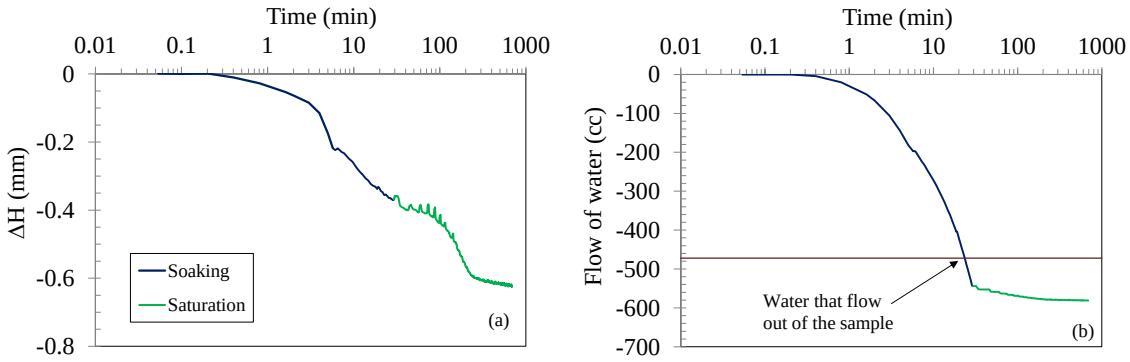

Figure 5.8. Change in height and volume during the soaking and saturation for a sample that was soaked over 0.2 days. Experiment Carbondale120711_0.

5.1.4. Saturation and isotropic consolidation

The saturation started after the soaking. The target B value was 0.95 and the target effective stress was 6.89 kPa. The maximum cell pressure was 380 kPa. Increments of 35 kPa with a rate of 68.95 kPa/min were applied to measure the B value.

When the saturation finished the isotropic consolidations started. The test consisted of three steps: an initial increment of cell pressure, σ_{cell} from 6.89 kPa to 344.73 kPa, unloaded to 68.95 kPa and reloaded again to 517.11 kPa. The reload went beyond the unload pressure in order to put the specimen in R=1.0. The isotropic consolidation was performed by controlling σ_{cell}. It was incremented continually at a low rate of 1.38 kPa/min. The increment in the pressure of the cell was small enough that the increment of the pore pressure had time to dissipate and the increment in the effective stress became the same as the increment in the total stress. Figure 5.9 shows the excess of pore pressure during the three steps of the isotropic consolidation of the test Tradewater20120924_6.

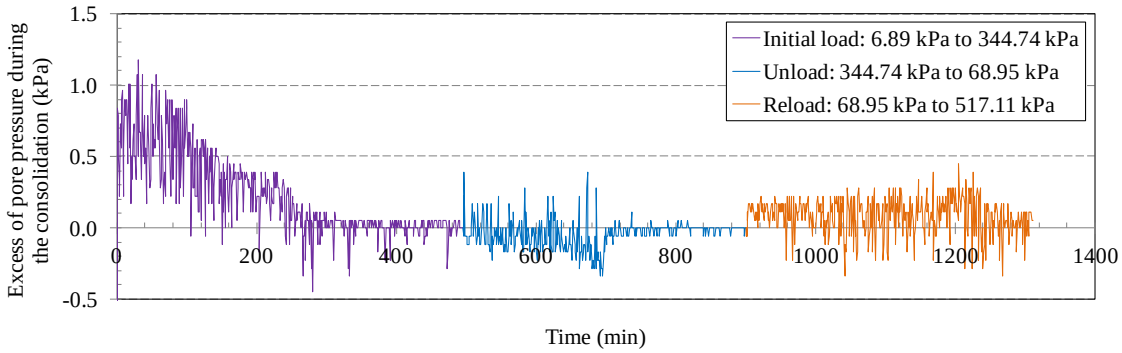

Figure 5.9. Excess of pore pressure during an Isotropic Consolidation test. Experiment: Tradewater120924_6.

The noise in the graph was due to the increment of σ_{cell} being applied at a constant rate. The excess of pore water pressure occurs due to increments in total stresses. Because the consolidation is a drain condition, the excess of pore pressure started to dissipate. However, additional increments in σ_{cell} produced additional excess of pore water pressure that was superimposed over the dissipation of the initial excess of pore water pressure. Therefore, the pattern shown in Figure 5.9 was formed. The rate of increment in σ_{cell} was so low that after 160 min the excess of pore water pressure was lower than 0.5 kPa. When the target pressure of the initial load was reached (300 min) all the excess of pore water pressure was dissipated. In the same way, when the unload started and the target pressure was reached (700 min), the excess of pore pressure dissipated. During

these two periods, the specimen underwent secondary consolidation or creep (i.e. excess of pore water pressure was completely dissipated).

Figure 5.10 shows the isotropic consolidation curve of this specimen. It can be observed that the methodology that was followed was good because there is a clean consolidation curve.

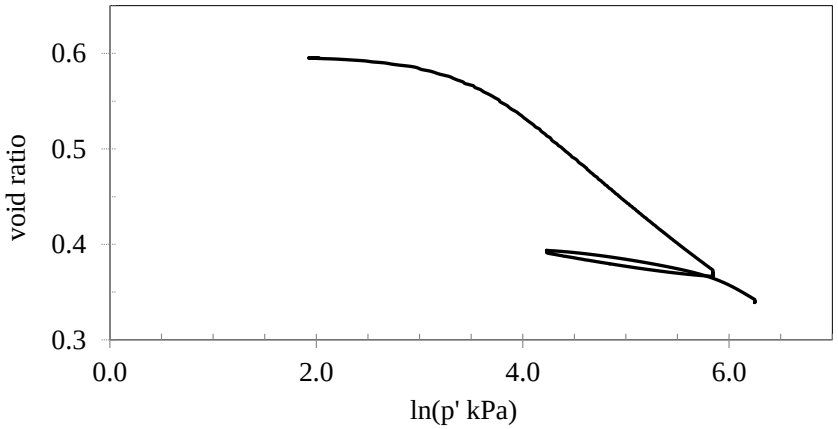

Figure 5.10. Isotropic Consolidation of de experiment Tradewater120924_6 shown in Figure 5.9.

Figures 5.5 and 5.11 show how the membrane penetrated the specimens. This phenomenon is common in gravels and sands. The membrane penetration affects mostly cyclic loading tests performed for determination of liquefaction potential (Lade and Hernandez, 1977). The factor of major influence is grain size. Confining pressure, rigidity and thickness of membrane have less influence (Baldi and Nova, 1984). Therefore, a correction for membrane penetration was not done. For this research all the tests were performed with similar GSD, same type of membrane, and same procedures.

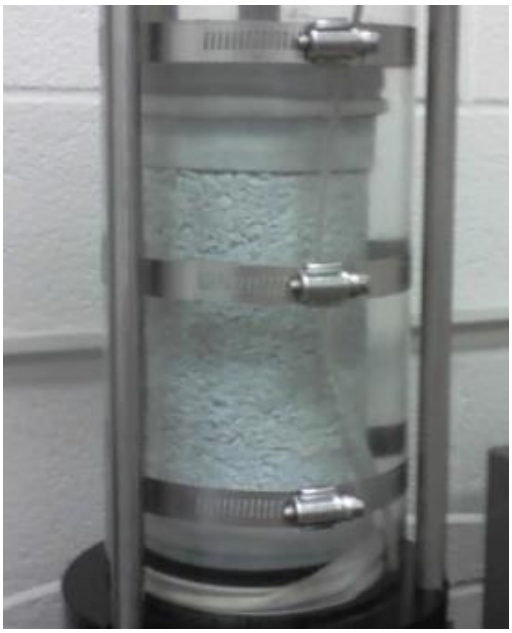

Figure 5.11. Appearance of the specimen after the Isotropic Consolidation.

5.1.5. Undrained shear procedure

When the isotropic consolidation finished, all the specimens were sheared under undrained conditions. The tests were strain controlled with an axial displacement at a rate of 0.2 percent/min until the sample reached an axial strain of 30 percent. Figure 5.12 shows the appearance of the sample after having been sheared.

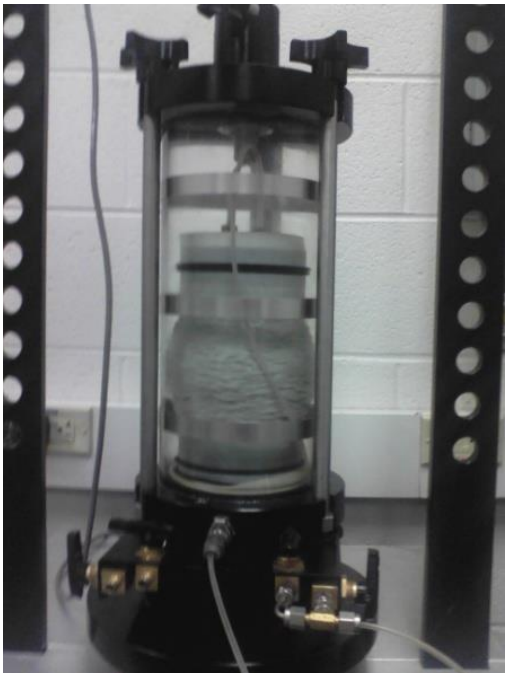

Figure 5.12. Sample after being shear.

5.1.6. Removing the specimen

The experiment finished when the shear was done. The sample was removed and the moisture content was measured. Figure 5.13 shows the appearance of the specimen when the test was finished and after the specimen was dried in the oven over 24 hours.

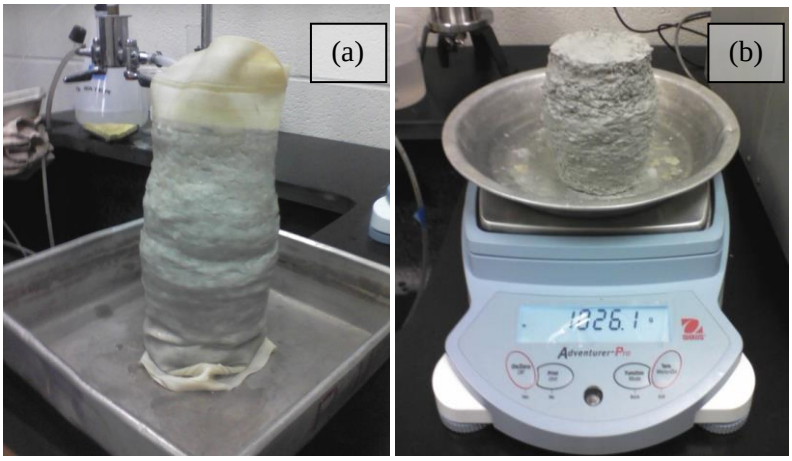

Figure 5.13. Appearance of the specimen after being tested, (a) after being removed from the cell and inside the membrane, and (b) after being dried in the oven over 24 hours.

5.2. CIU TXT results and discussion

There were two groups of compacted shales that demonstrated different behavior during the isotropic consolidation and undrained shear. The Carbondale, Grundy, and Fort Payne compacted shales are in the first group, which will be referred to as Type 1 compacted shales. The other group of compacted shales comprises Tradewater and Bull Fork, which will be referred to as Type 2 compacted shales.

5.2.1. Isotropic consolidation testing

5.2.1.1. Type 1 compacted shales

Figure 5.14 shows one example of an isotropic consolidation curve of the experiment Carbondale20120711_0. The curve has the following characteristics: an elastic region due to the initial load with a flat slope named here ι; a yielding point at a yielding pressure, p'_y, where the specimen went to the elastic-plastic region of the *iso-ncl* with slope λ_{ncl}; and an elastic region due to unload reload *url* with slope κ. Figure 5.14 also shows that the *url* had a greater curvature than the initial elastic load, and κ was higher

than ι.

ι was calculated as the slope of the initial part of the load; λ_{ncl} was calculated as the slope of the curve when the *iso-ncl* portion of the curve became linear and reached an ending point when the test was stopped; and κ was the slope between the beginning of the unload and the beginning of the reload. p'_y was calculated using a simplified method recommended by Budhu (2007) as the intersection of the initial elastic curve and the *iso-ncl*. Using the same methodology, the same parameters were calculated for Grundy and Fort Payne compacted shales.

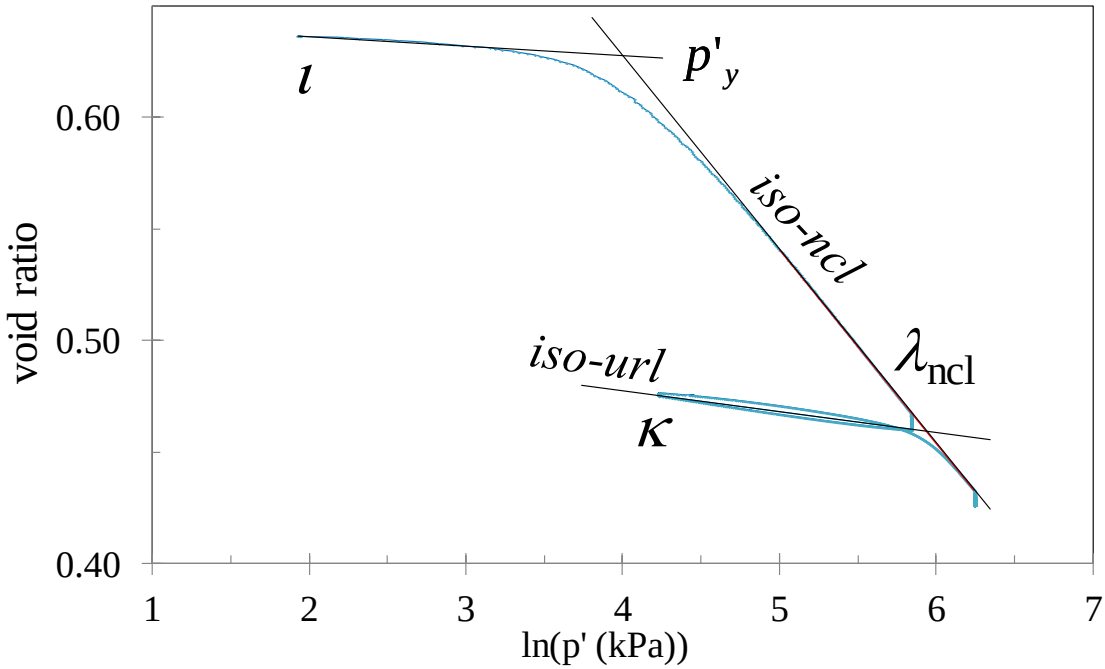

Figure 5.14. Parameters measured in the isotropic consolidation curve of the test Carbondale20120711_0.

Figures 5.15a, 5.15c, and 5.15e show the isotropic consolidation curves of Grundy, Carbondale, and Fort Payne compacted shales. Figures 5.15b, 5.15d, and 5.15f show the same consolidation curves, but instead of void ratio in the ordinate, they show the void ratio normalized to the initial void ratio. The Grundy compacted shale was weathered over 0 and 6 days; Carbondale was weathered over 0, 6, and 21 days; and Fort Payne was weathered over 0 and 6 days. Table 5.4 shows the results of the isotropic consolidation parameters of Carbondale, Grundy, and Fort Payne compacted shales as a function of

weathering time.

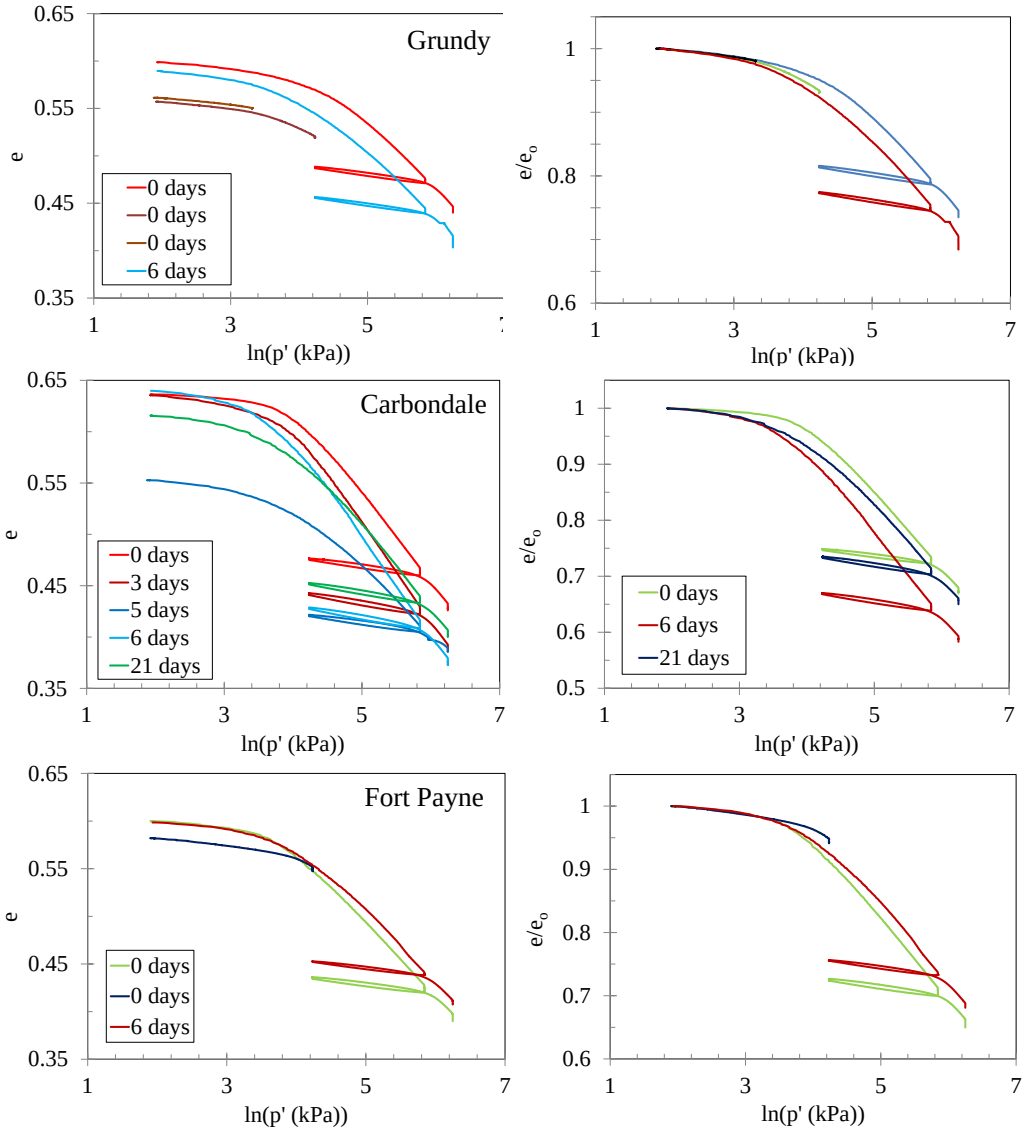

Figure 5.15. Isotropic consolidations of the Type 1 compacted shales.

Table 5.4. Results of isotropic consolidation of the Type 1 compacted shales.

Shale	Soaking time (days)	ι	κ	λ_{ncl}	p'_y (KPa)
Grundy	0	0.0068	0.0099	0.0717	77.8
	6	0.0090	0.0101	0.0726	61.1
Carbondale	0	0.0043	0.0094	0.0867	54.5
	6	0.0107	0.0117	0.0949	40.6
	21	0.0089	0.0113	0.0823	50.6
Fort Payne	0	0.0070	0.0091	0.0769	44.0
	6	0.0069	0.0083	0.0766	54.5

5.2.1.2. Type 2 compacted shales:

Figure 5.16 shows the isotropic consolidation curve of the BullFork20120713_ 0 sample and shows in detail how the isotropic consolidation parameters were measured. The curve exhibits the following characteristics: an elastic region due to the initial load, with a flat slope ι and a yielding point at p'_y, where the specimen went to an elastic-plastic region. The elastic-plastic region of these compacted shales was different than that of the Type 1 compacted shales. After the yielding point, the specimen followed a concave curve, suggesting the soil started to lose structure. After the curve became flatter, an unload-reload was applied and the specimen went to an elastic region, the *url* with slope κ. Figure 5.16 also shows that, in the same way as the Type 1 compacted shales, the *url* had more curvature than the initial load, and κ was higher than ι. The tests were reloaded in such a way that they passed the pressure where the sample was unloaded in order to go to the elastic-plastic region again. As shown in Figure 5.16, the characteristics of the reload were performed in order to achieve two objectives: to put the specimen in an NC or R=1.0 condition, and to arrive at a zone of complete destructuration. In this way the specimen arrived at a true *iso-ncl* with slope λ_{dstr}.

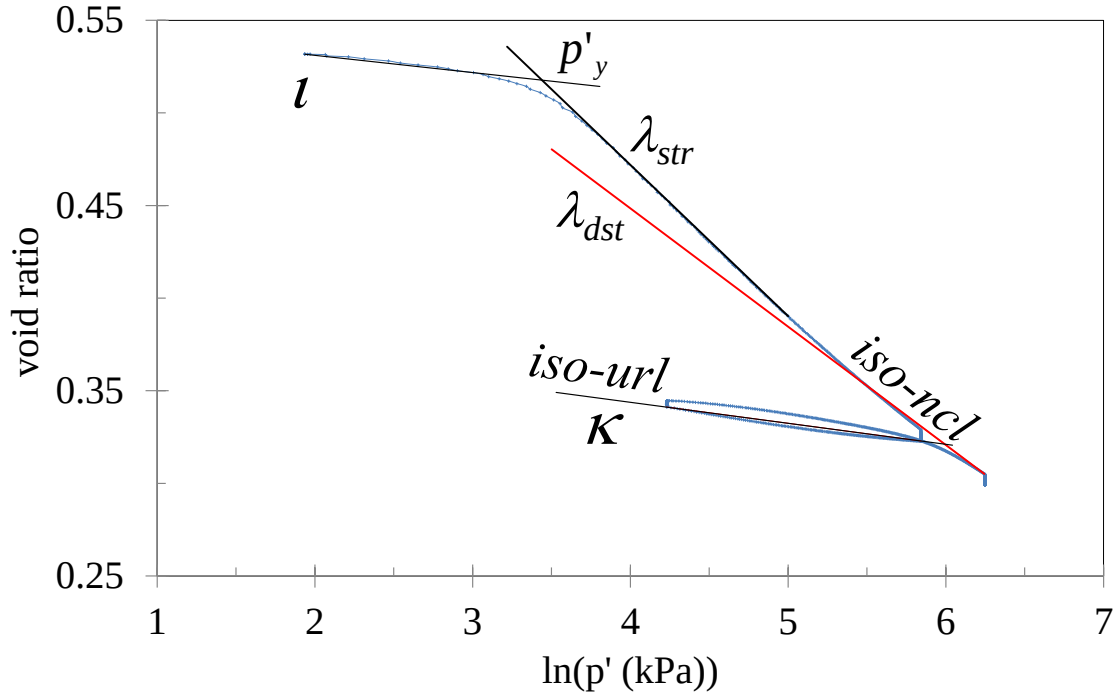

Figure 5.16. Parameters measured in the isotropic consolidation curve of the test BullFork20120713_ 0.

Figures 5.17a and 5.17c show the isotropic consolidation curves of Tradewater compacted shale weathered over 0 and 6 days and Bull Fork compacted shale weathered over 0, 6, and 14 days. Figures 5.17b and 5.17d show the same consolidation curves, but instead of void ratio in the ordinate, they show the void ratio normalized to the initial void ratio. Table 5.5 shows the parameters of the IC curves as a function of weathering time.

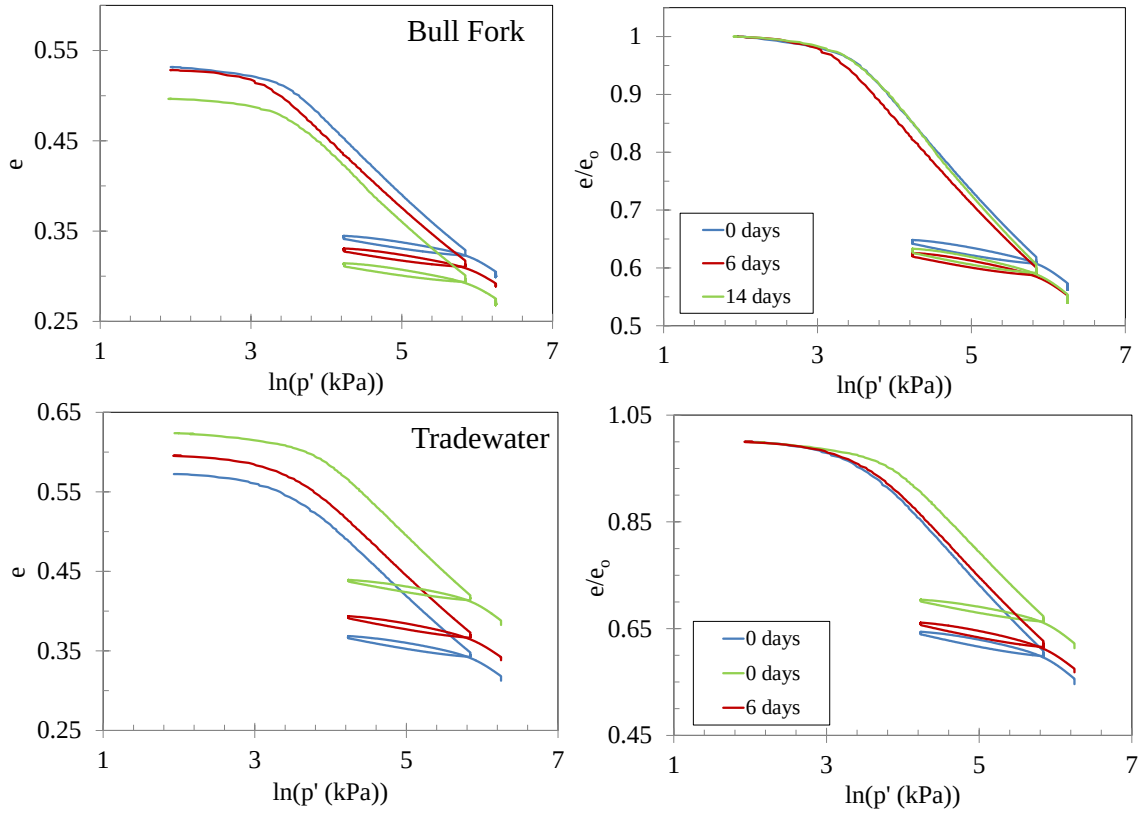

Figure 5.17. Isotropic consolidation of Type 2 compacted shales.

Table 5.5**.** Results of the isotropic consolidation for Type 2 compacted shales.

Shale	**Soaking time (days)**	**ι**	**κ**	**λ_{str}**	**λ_{dstr}**	**p'$_y$ (KPa)**
Tradewater	0	0.0115	0.0145	0.0895	0.0769	32.5
	6	0.0112	0.0153	0.0891	0.0787	33.3
Bull Fork	0	0.0093	0.0114	0.0816	0.0639	31.2
	6	0.0058	0.0108	0.0779	0.0641	22.9
	14	0.0083	0.0107	0.0805	0.0654	32.1

5.2.1.3. Analysis of the shape of isotropic consolidation curves

The typical isotropic consolidation curves of remolded clays arrive at a unique *iso-ncl* parallel to the *csl*, where λ_{ncl} is a well-distinguished properties of the material and e_λ is a function of θ (i.e. isotropic consolidation or anisotropic consolidation). Also, the elastic unload-reload is significant, which means that κ has a relatively high value. Otherwise, the typical isotropic consolidation curves of sands have an infinite number of *iso-ncl* that cross the *csl*. The slope of *iso-ncl* is λ_{ncl} and the slope of *csl* is λ_s. For sands e_λ is not unique and is a function of the initial void ratio. In sands the properties of the material are λ_s and Γ, and κ is virtually zero. The IC curves of clays and sands are also concave unless they have structure (i.e. sensitive or quick clays, cemented clays, and cemented sands). The destructuration of a soil occurs because the cement starts to break apart after the stresses pass p'_y (Liu and Carter, 2002).

Figures 5.15a to 5.15f show that the compression curves of Type 1 compacted shales did not go to a unique *iso-ncl*, and also p'_y did not change with the initial void ratio. This means that p'_y is not associated with the energy of compaction used to compact the triaxial specimens and should be associated to a loss of structure of the compacted material. Regarding Type 2 compacted shales, Figures 5.17a to 5.17d show that the compression curves were parallel and p'_y was also independent of the initial void ratio. These tests showed one important characteristic of sands: an infinite number of *iso-ncl* not parallel to *csl*.

Further evidence of dual behavior between clay and sand is shown in Figure 5.18a, 5.18b, and 5.18c. Before being tested the samples were well graded sands with less than 10 percent of fines, as shown in Figure 5.18a. When the test was finished, the specimen had two different appearances dependent on the durability of the sample and the consolidation pressure. Figures 5.18b and 5.18c show the specimen after the test finished. Figure 5.18b shows the specimen did not have cohesion when it was weathered over a short period of time or consolidated to low pressure. Figure 5.18c shows the specimen presented apparent cohesion when it was weathered over a prolonged period of time or consolidated to high pressure. Therefore, the samples began with the behavior of sands and finished with the behavior of clays. Another clay characteristic that the compacted shales

presented was a well-defined elastic zone, which can be observed through the high values of κ.

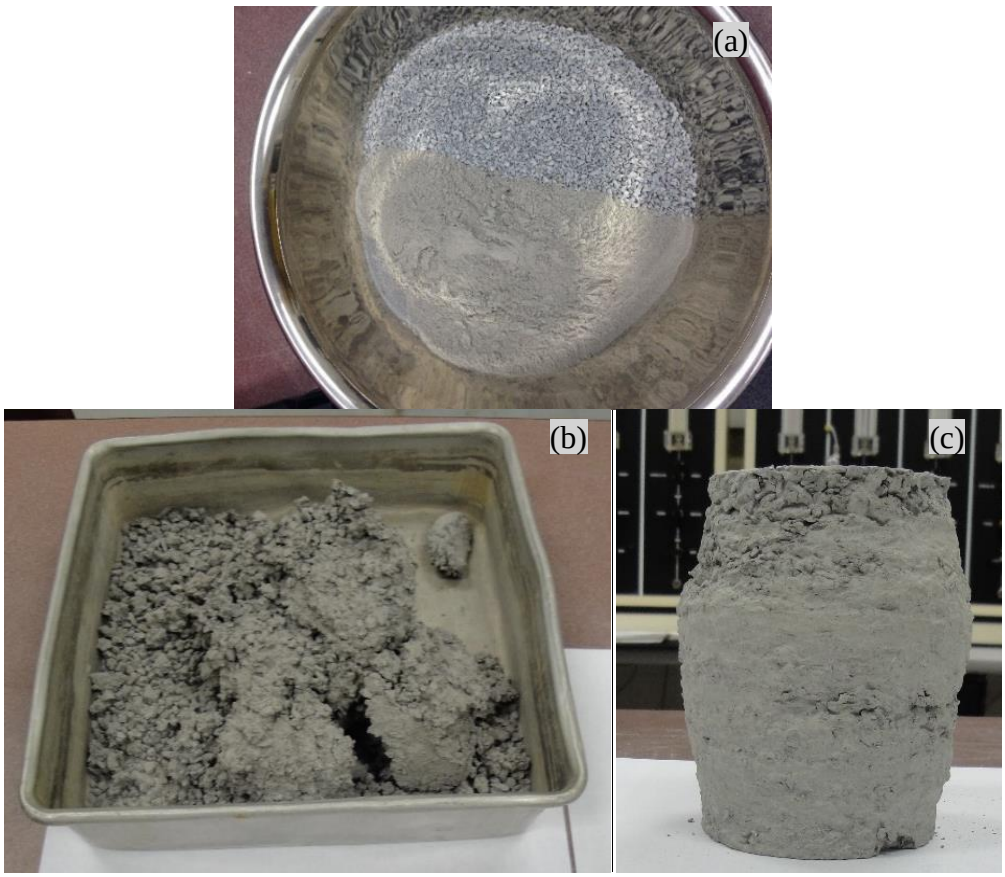

Figure 5.18. Crushed shale (a) before being compacted and (b) after being tested, when consolidated at low pressure or durable shales, and (c) when consolidated at high pressure or non-durable shales.

5.2.1.4. Influence of soaking time in consolidation parameters.

Figures 5.19a and 5.19b show the variation of ι and κ with soaking time of Type 1 and Type 2 compacted shales. Grundy and Carbondale showed an increase in the value of ι, while Fort Payne, Tradewater, and Bull Fork showed a small decrease in ι. Carbondale and Tradewater showed an increase in the value of κ with soaking time; Bull Fork and Fort Payne showed a decrease in the value of κ, and Grundy did not present important changes. The compacted shales that show destructuration during consolidation presented the highest values of ι and κ. κ was higher than ι as expected because ι represents the elastic behavior before to lose structure and κ after lose structure.

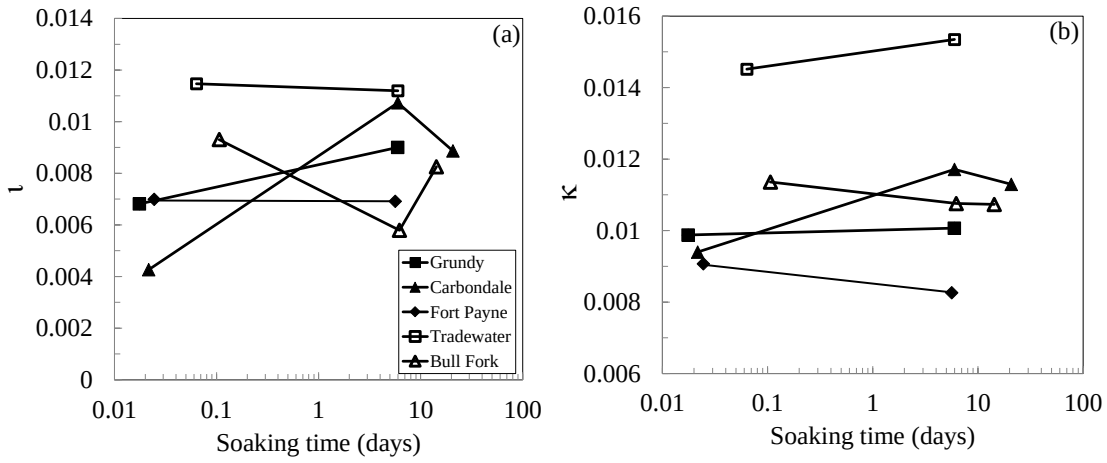

Figure 5.19. Variation of ι and κ with soaking time.

Figure 5.20a shows the variation of λ_{ncl} with soaking time of Type 1 compacted shales. Carbondale was the only compacted shale that had changes in the values of λ_{ncl} with soaking time, but without any pattern. The other compacted shales presented minimum changes. Figure 5.20b shows λ_{str} and λ_{dstr} for Type 2 compacted shales. As expected, λ_{dstr} was higher than λ_{str}. Similar to Type 1 compacted shales, there was not important change with soaking time.

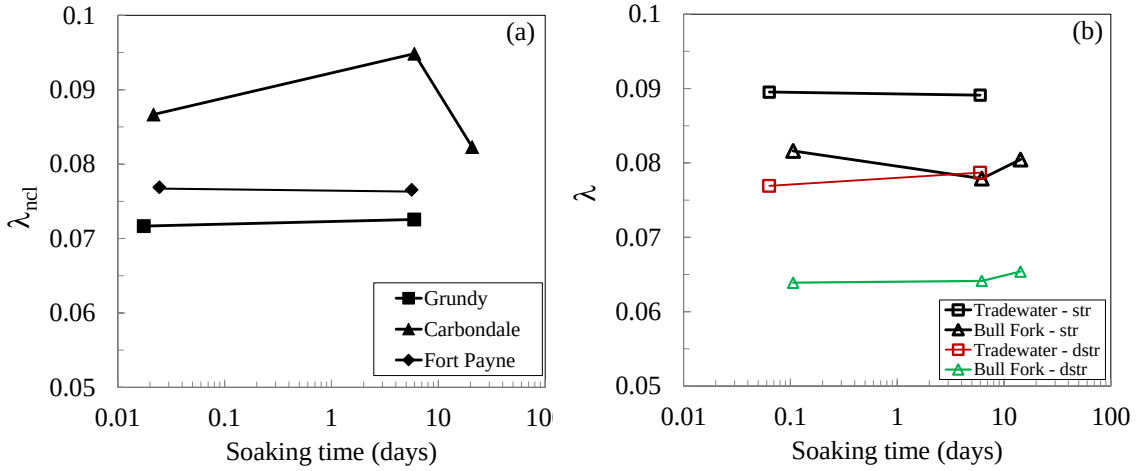

Figure 5.20. Variation of (a) Type 1 compacted shale λ_{ncl} and (b) Type 2 compacted shale λ_{str} and λ_{dstr}.

Figure 5.21 shows the variation of p'_y with soaking time of Type 1 and Type 2 compacted shales. Grundy, Carbondale, and Bull Fork showed a decrease in the value of p'_y. Fort Payne increased and Tradewater did not change in the value of p'_y. With the information

collected during this research, it was not possible to find a clear relationship between the IC curve parameters and soaking time.

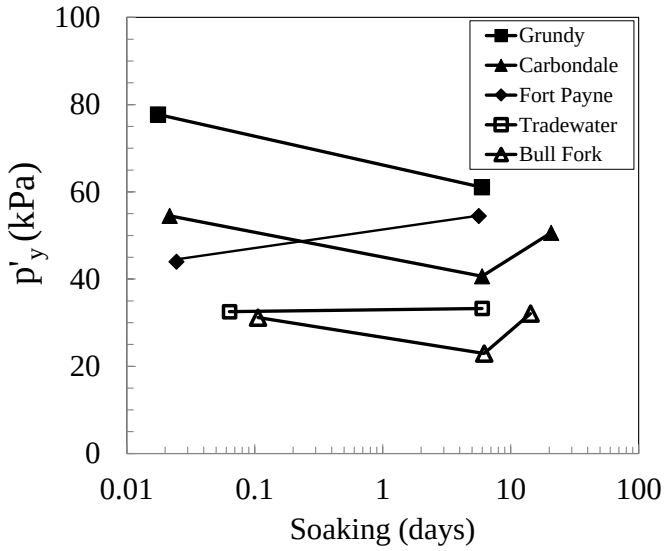

Figure 5.21. Variation of p'_y with soaking time.

5.2.1.5. Influence of mineralogy in consolidation parameters

The causes of the difference in the behavior between the Type 1 and Type 2 compacted shales were explored in mineralogical content and geological classification. Fort Payne, a Type 1 compacted shale, and Bull Fork, a Type 2 compacted shale, classified as marlstone, while the other three shales classified as mudstone. There was not observed any difference in mineralogical content that can be explained the difference in the behavior between Type 1 and Type 2 compacted shales.

Figures 5.22a to 5.22d show the variation of ι, κ, λ_{ncl}, and p'_y with the (Ch+I)/K ratio. The graphs show high dispersion. Figure 5.23a to 5.23d show the variation of ι , κ, λ_{ncl}, and p'_y with fine size quartz. Because ι and p'_y depend on the initial structure of the compacted shales, the high dispersion on figures was anticipated. The graphs show that the consolidation properties are not related with the total content of clay minerals. Another observation is that Type 1 copated shales (Grundy, Carbondale, and Fort Payne) had lower values of ι than Type 2 compacted shales (Tradewater and BullFork).

However, it was expected a more clear relationship between compression and swelling indexes, because they are properties of the material; therefore, they should depends on

the type of clays. It is necessary to perform more experiments with more shales in order to have more information and do better inferences.

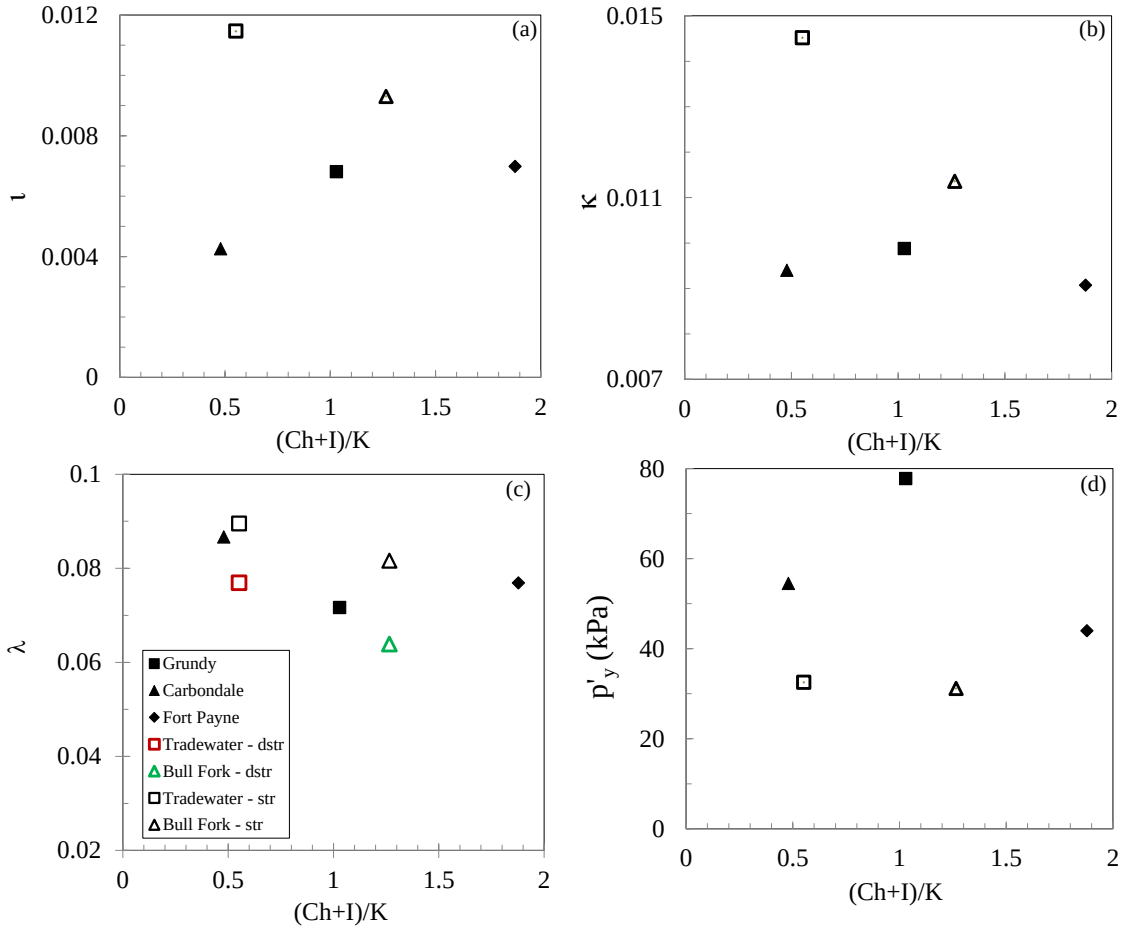

Figure 5.22. Variation of ι , κ, λ_{ncl}, and p'_y with (Ch+I)/K ratio.

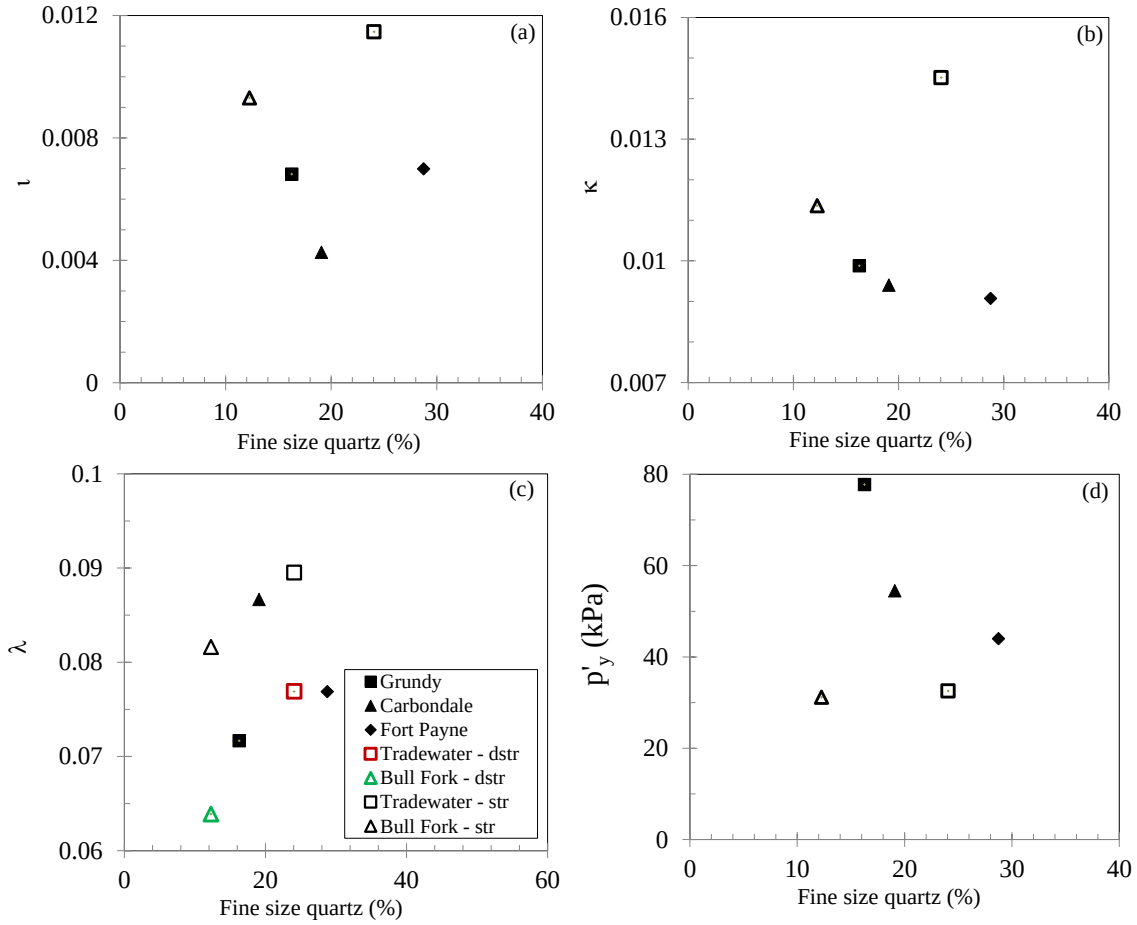

Figure 5.23. Variation of ι , κ, λ_{ncl}, and p'_y with total clay mineral content.

5.2.1.6. Influence of index properties and durability on consolidation parameters

Figures 5.24a to 5.24d show the variation of ι with A_c, S_{jar}, $Id_{(2)}$, and LSI. The parameters in the graphs are at zero soaking time. Even though the trends are not clear; it can be observed that ι increased with A_c and decreased with durability. The figures show that Type 1 copated shales (Grundy, Carbondale, and Fort Payne) had lower values of ι than Type 2 compacted shales (Tradewater and BullFork) as was prebiously mentioned. The dispersion in the figures show that ι is not entirely explained by index properties and durability. ι represents the initial elastic path of the sample before to lose structure; therefore, it is possible that ι is related with the initial structure of compacted shales.

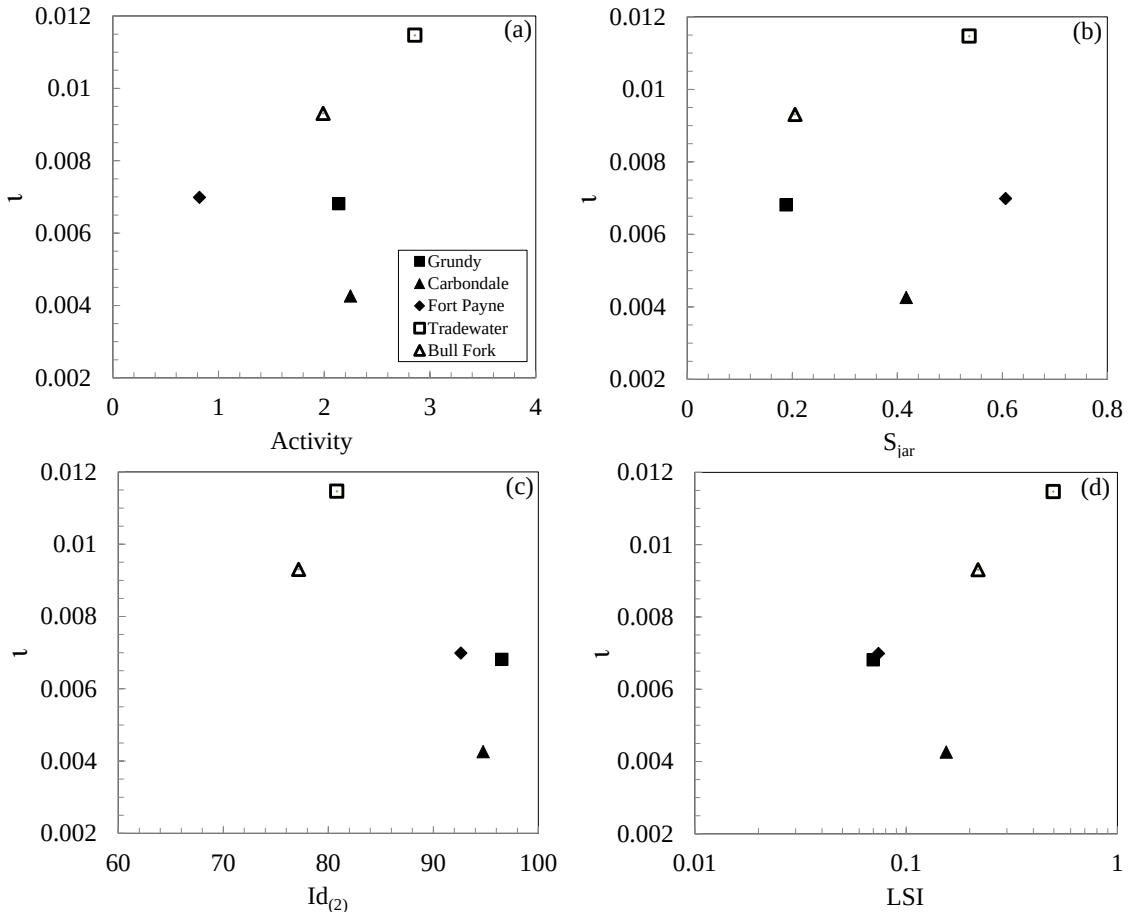

Figure 5.24. Variation of ι with (a) activity, (b) jar index, (c) durability index, and (d) LSI.

Figures 5.25a to 5.25e show the variation of κ with A_c, S_{jar}, $Id_{(2)}$, and LSI. κ was higher with higher A_c and low durability. The figures show that Type 1 copated shales (Grundy, Carbondale, and Fort Payne) had lower values of κ than Type 2 compacted shales (Tradewater and BullFork) as was prebiously mentioned. Type 2 compacted shales had higher values of κ than the Type 1 compacted shales. κ has two meanings: in the first, κ describes how much of the sample will swell when the soil is unloaded. This swelling behavior is a function of the index properties, and thus of the mineralogy. Soils composed of high plasticity clays will swell more than those soils composed of low plasticity clays or sands that will not swell at all, with κ being virtually zero. In the second meaning, κ describes how much elastic deformation is recoverable when the soil is unloaded. Soils with more clay content can hold more elastic deformations than sands. When the reload

starts, κ makes the soil follow an elastic path until the soil reaches the pressure at which the soil was unloaded. The dispersion in the figures show that κ is not entirely explained by index properties and durability.

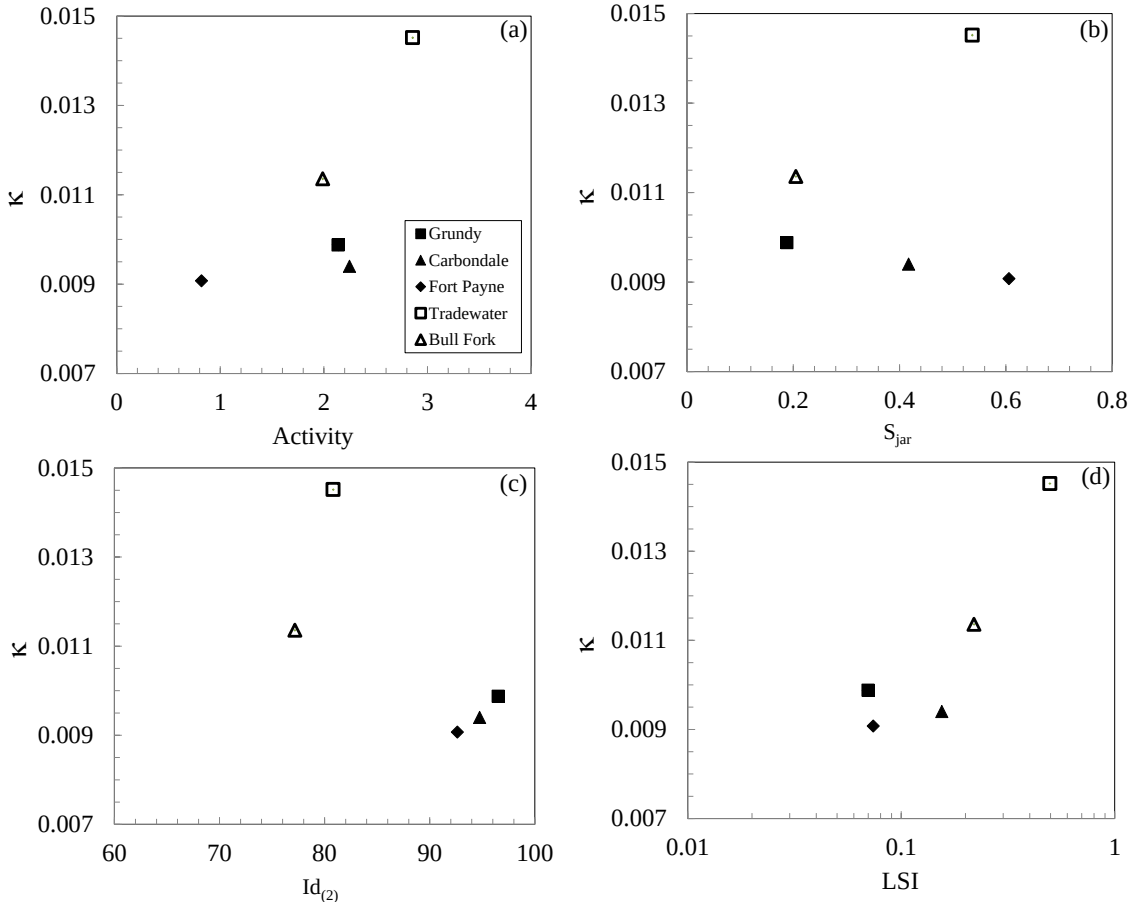

Figure 5.25. Variation of κ with (a) activity, (b) jar index, (c) durability index, and (d) LSI.

Figures 5.26a to 5.26d show the variation of λ_{ncl} (Grundy, Carbondale, and Fort Payne) and λ_{str} and λ_{dstr} (Tradewater and Bull Fork) with A_c, S_{jar}, $Id_{(2)}$, and LSI. This figures show the λ_{dstr} of Type 2 compacted shales. The graphs show in general that λ_{ncl} increases with A_c and decreases with durability. λ_{ncl} is an elastic-plastic modulus that describes both elastic and plastic deformations held by the soil. The elastic deformations can be recovered, but the plastic deformations will not be recovered. Under this interpretation of λ_{ncl}, low plastic and durable shales will derivate in compacted shales with less permanent deformations than non-durable shales. The dispersion in the figures show that λ is not

entirely explained by index properties and durability.

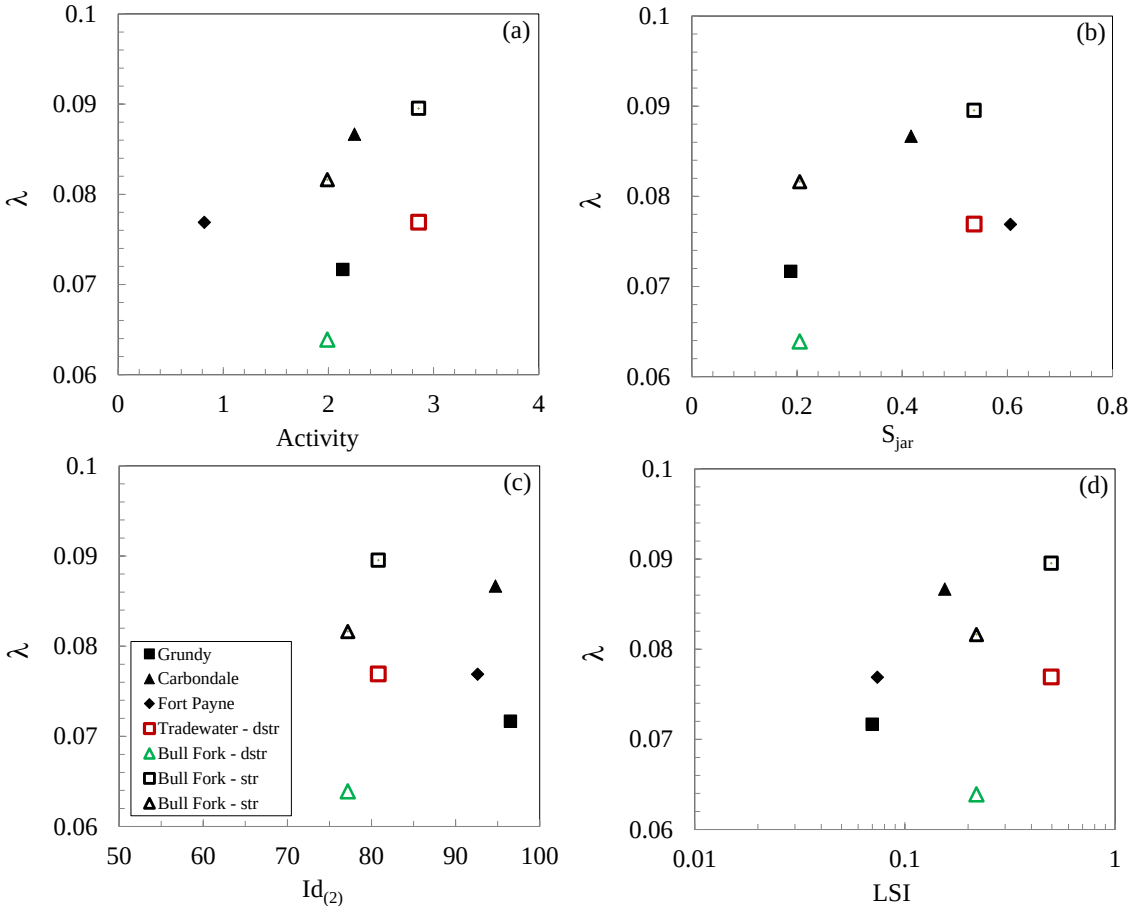

Figure 5.26. Variation of λ_{ncl} with (a) activity, (b) jar index, (c) durability index, and (d) LSI.

Figures 5.27a to 5.27d show the variation of p'_y with A_c, S_{jar}, $Id_{(2)}$, and LSI. The figures show that Type 1 copated shales (Grundy, Carbondale, and Fort Payne) had higher values of p'_y than Type 2 compacted shales (Tradewater and BullFork) as was prebiously mentioned. The dispersion in Figures 5.27a and 5.27b show that p'_y is not entirely explained by index properties and S_{jar}. Figures 5.27c and 5.27d show that both Type 1 and Type 2 compacted shales are in the same trend line, where p'_y increases with durability.

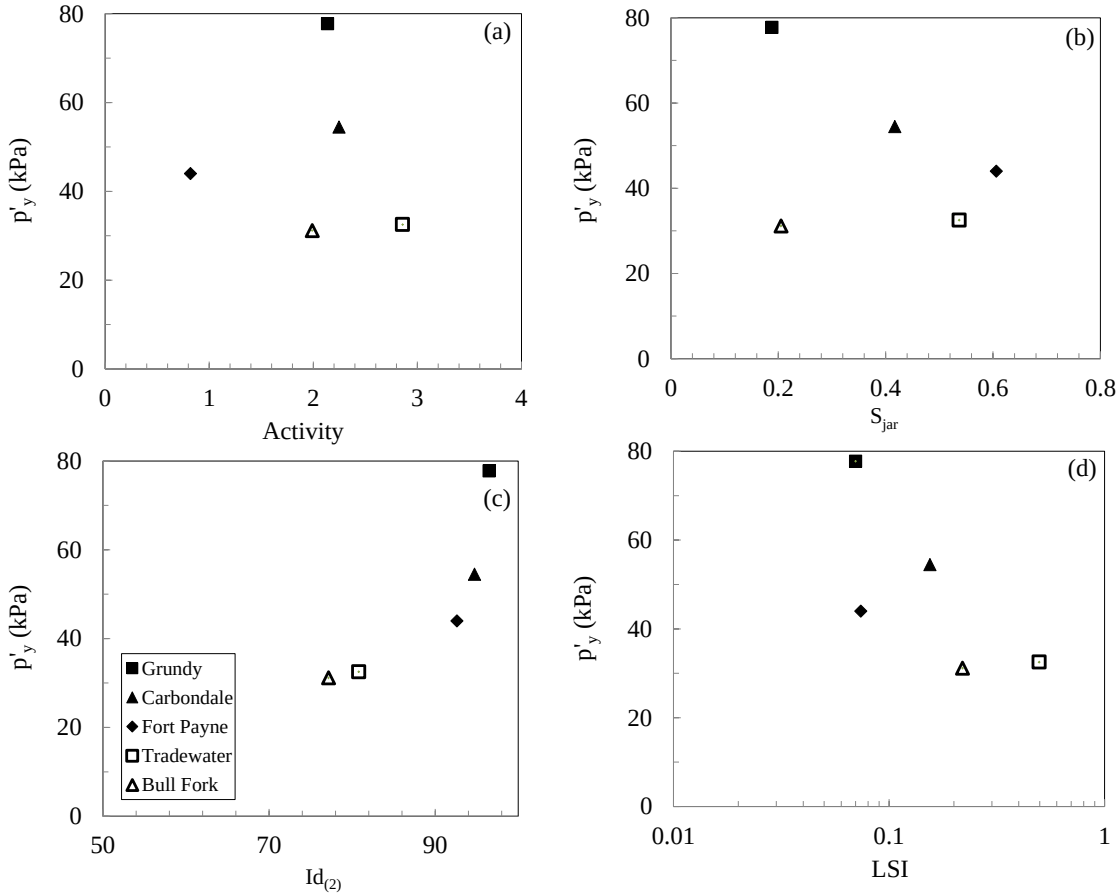

Figure 5.27. Variation of p'_y with (a) activity, (b) jar index, (c) durability index, and (d) LSI.

Two more particular characteristics of the compacted shales were the difference between ι and κ, where ι was much smaller than κ, and the fact that the initial elastic path had less curvature than the *url* path, as shown in Figures 5.15 and 5.17. This can change the interpretation of p'_y . The pressure when the elastic behavior finished at the beginning does not have the same meaning as the pressure when the *url* line returns to the *iso-ncl*. Therefore, p'_y is not the maximum past pressure related to the energy used to compact the sample; p'_y is a pressure at which a change of structure occurs. Otherwise, the change of slope when the specimen left the *url* to go to the *ncl* represents the change necessary for the elastic range to go to an elastic-plastic range. For clays it is clear that p'_y is the maximum load experienced by the sample in the past; for sands p'_y is an especially high pressure where the particles of sands start to fracture. One hypothesis of this research is that p'_y marks a change of structure due to the breaking of the particles for Type 1

compacted shales, and due to the breaking of the particles and cement for Type 2 compacted shales.

5.2.2. Undrained shear testing

The Type 1 and Type 2 compacted shales also exhibited different behavior during the shear. The following section presents in detail the shear phase characteristics of two CIU triaxial tests performed on a Type 1 and a Type 2 compacted shale. Bellow the experiments Carbondale20120711_0 and BullFork20120712_0 will be used to explain the typical examples of shear behavior of Type 1 and Type 2 compacted shales, respectively. Appendix I shows results of this experiments for each compacted shale.

5.2.2.1. Undrained shear in Type 1 compacted shales

Figures 5.28a and 5.28b show the stress paths of the CIU triaxial test Carbondale20120711_0 in p' – q and q - ε_q spaces. Figures 5.29 shows the stress path in e - p' space. Because the test was undrained, the void ratio did not change during the shear; therefore, the stress path in e - p' space was horizontal.

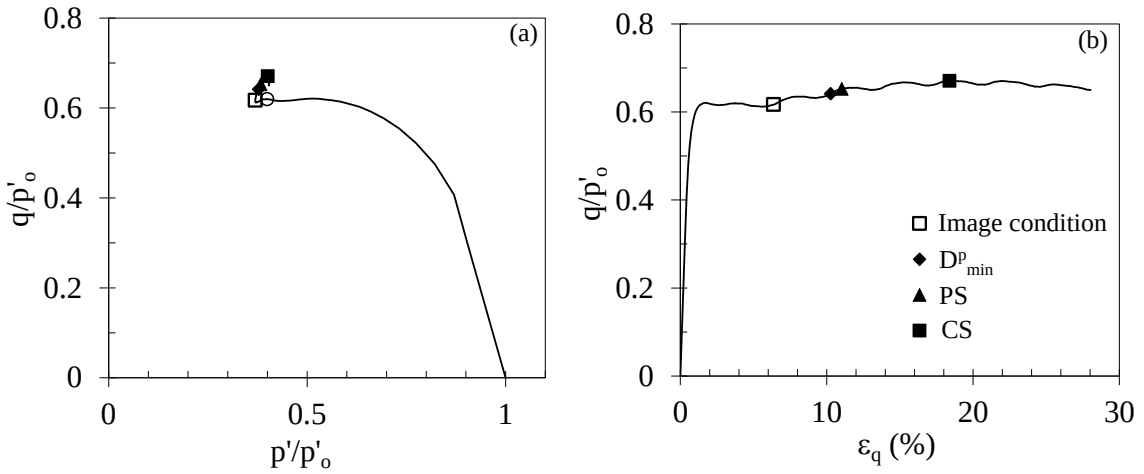

Figure 5.28. Stress path of the CIU triaxial test Carbondale20120711_0 in (a) normalized shear stress vs. normalized mean stress and (b) normalized shear stress vs. shear strain.

Figure 5.29 shows in detail the evolution of ψ during the shear in e – p' space. This experiment started in the current *iso-ncl* (R=1.0) with $\psi_o > 0$; ψ got smaller until it crossed the *csl* for first time where $\psi = 0$ changed sign and became negative, until it

reached the IC with $\psi < 0$, and returned again toward the *csl* where it finished with $\psi = 0$. The test was analyzed until ε_q = 28 percent.

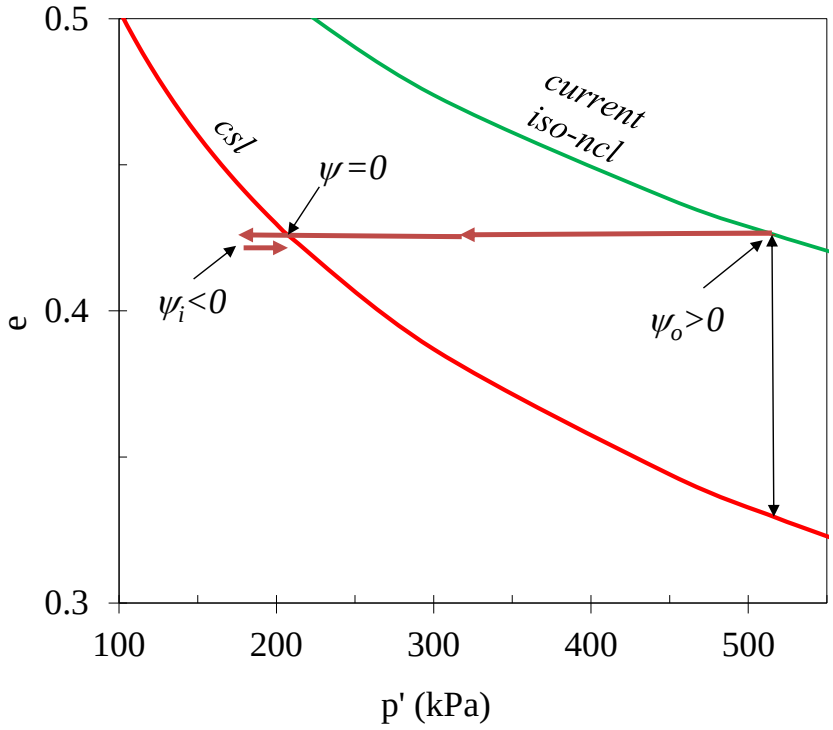

Figure 5.29. Stress path on *e* - *p*' space of the CIU triaxial test Carbondale20120711_0.

As expected for a test with $\psi_o > 0$, Figure 5.29 shows that the stress path in the *p*' - *q* space was toward the left. This is because the excess in pore pressure, Δu, was positive, as shown in Figure 5.30a. However, after Δu reached a maximum, $\Delta(\Delta u)$ changed from positive to negative, making the specimen dilate even though the specimen started with $\psi_o > 0$. After an additional shear, the sample reached a PS, where η was maximum, before CS, as shown in Figure 5.30b.

This change in Δu during the shear made the specimen go into some different particular points or stress conditions that characterized the behavior of the specimen. Figure 5.31 shows in detail the evolution of this test in the axes *p*' and $\dot{p}$' with ε_q.

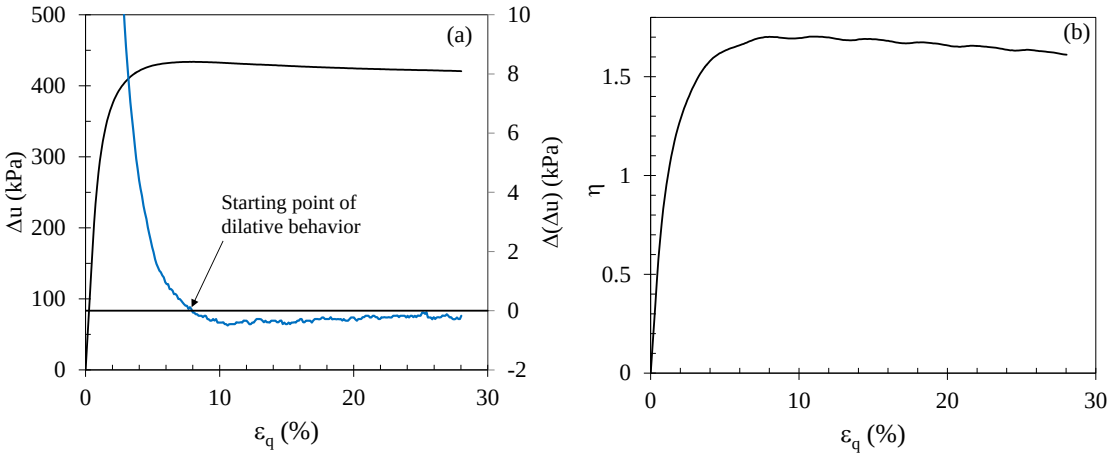

Figure 5.30. Variation of stress ratio and excess of pore pressure during the shear phase for the CIU triaxial test Carbondale20120711_0.

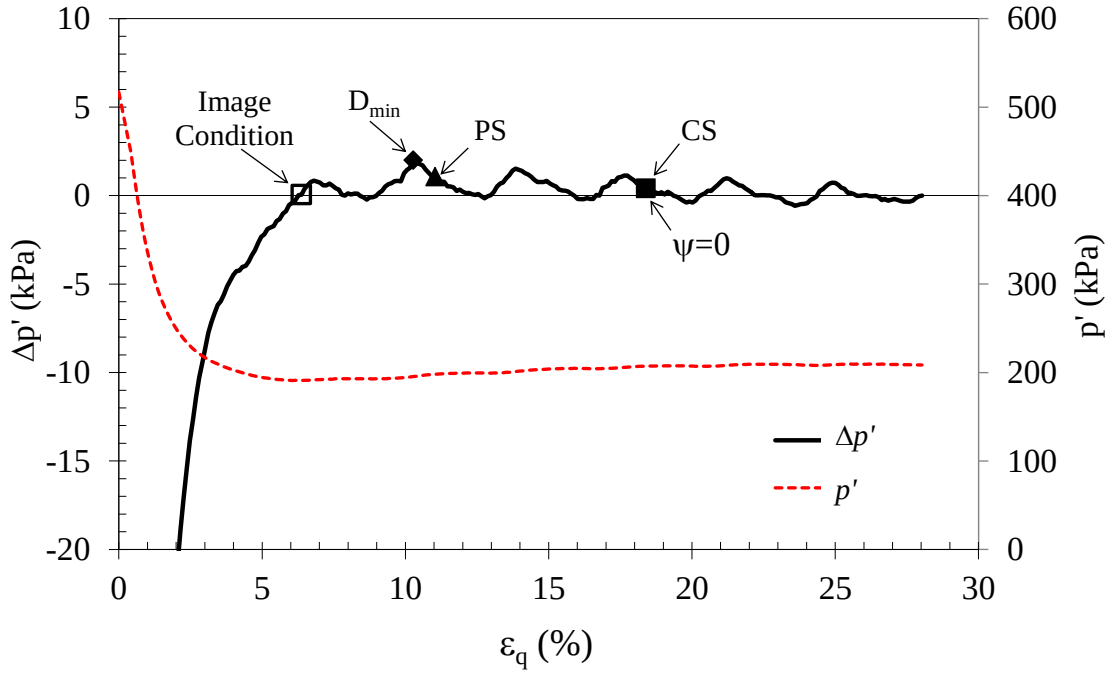

Figure 5.31. Change of the mean stress and the derivative of mean stress during the shear phase of the CIU triaxial test Carbondale20120711_0.

The shear started with $\psi_o > 0$. With the increment of η, the specimen tended to compress, as evidenced by the reduction of p' due to positive Δu. The specimen continued this reduction of effective mean stress until it reached a point at which the shear path crossed the *csl* in the e - p' space, but without being in the CS. At this point $\psi = 0$. This stress condition was reached when ε_q was 3.67 percent. This point is marked using an open

circle in Figures 5.28 and 5.31.

After the shear path crossed this point, ψ went from being positive to negative with the increase of η. The specimen continued with the same tendency to compress until it reached a condition where $p' = p'_{min}$, $\dot{p}' = 0$, and $\ddot{p}' \neq 0$. As was discussed in Chapter 2, this is the IC with $\eta = M_i$. In this stress condition $D^p = 0$ and $\dot{D}^p \neq 0$, and with additional shear it changed sign. It is important to emphasize that the IC happened slightly after $\Delta(\Delta u) = 0$ because the total stress path had a slope of 1/3. The IC was reached when ε_q = 6.37 percent. The IC is shown with an open square in Figures 5.28 and 5.31.

After the IC, the sample did not compress anymore. η continued to increase until the specimen reached a stress condition where $\dot{p}' = \dot{p}'_{max}$ and $\ddot{p}' = 0$. At this point $D^p = D^p{}_{min}$ (i.e. maximum dilatancy) because the test was undrained. This condition was at ε_q = 10.27 percent, and is displayed as a rhombus in Figures 5.28 and 5.31.

With some additional shear, η reached a maximum value, η_{max} or the PS condition. This condition was at ε_q = 11.03 percent. The PS is shown as a triangle in Figures 5.28 and 5.31. $D^p{}_{min}$ did not occur at the same time as the PS, but they occurred closely as shown in Figure 5.31. This phenomenon is equivalent with the observation made by Bolton (1986) regarding sands, in which the peak friction angle is the ultimate friction angle plus 0.8 times the maximum dilatancy (positive dilatancy for Bolton (1986) is negative dilatancy for this research).

After this point, the shear continued with the decrease of η until the specimen reached a point where the two axioms of the CS were satisfied: (1) p' is constant, $\dot{p}' = 0$, and $\ddot{p}' = 0$ (i.e. $D^p = 0$ and $\dot{D}^p = 0$) as shown in Figure 5.31 as a square, and (2) $\psi = 0$ as shown in Figures 5.29. In this point $\eta = M_{tc}$. The CS was reached when ε_q = 18.39 percent.

It was observed that after the CS condition was reached, η decreased but still satisfied the first axiom of the CS by a constant p' and $\dot{p}' = 0$, as shown in Figure 5.32. This means that the sample softened while in the CS condition and approached the residual condition

(i.e. residual shear strength) until the test was stopped at ε_q = 28 percent.

Table 5.6 shows the characteristics of the CIU triaxial tests of Carbondale compacted shale for specimens that were weathered over 0 days, 6 days, and 21 days (Carbondale20120711_0, Carbondale20121009_6, and Carbondale20120115_21), and consolidated at the same p'_o such that the specimen started with $\psi_o > 0$. The table shows another experiment in which the specimen was not weathered and that was performed starting with $\psi_o < 0$ (Carbondale20130213_0) to give a good definition of the *csl* in the *e* - *p*' space. The table also shows the void ration before the isotropic consolidation (e_{ini}), the void ration after the isotropic consolidation at which the shear started (e_o), the consolidation pressure associated with a loss of structure (p'_y), the consolidation pressure (p'_o), and the overconsolidation ratio (R).

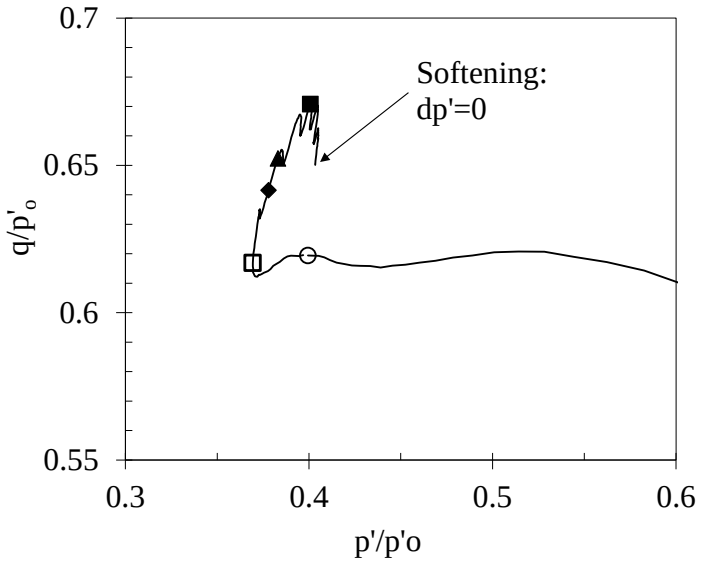

Figure 5.32. Softening behavior of the CIU triaxial test Carbondale20120711_0.

Table 5.6. Experiments performed in Carbondale compacted shale.

Experiment	Soaking time (days)	e_o	ψ_o	p'_y (kPa)	p'_o (kPa)	R
Carbondale20120711_0	0	0.43	0.10	517.05	517.05	1.0
Carbondale20121012_6	6	0.37	0.09	517.20	517.26	1.0
Carbondale20130113_20	21	0.40	0.08	517.11	517.11	1.0
Carbondale20130213_0	0	0.60	-0.17	48.57	6.48	7.5

5.2.2.2. Undrained shear in Type 2 compacted shales

Figures 5.33a and 5.33b show the results of the CIU triaxial test BullFork20120712_0 compacted shale. These figures show the stress path in p' - q and the q - ε_q spaces. Figure 5.34 shows the stress path in e - p' space. As can be observed in Figure 5.34, this experiment was performed with the specimen in an initial condition of $\psi_o > 0$ because the stress path was toward the left. The specimen started in a current *iso-ncl* (i.e. R=1.0) and there was no change in the void ratio during the shear because the shear was undrained. As with Type 1 compacted shales, the specimen showed dilatancy. Even though the specimen was shear until ε_q= 35 percent, it did not reach the CS. However, the experiment was analyzed until ε_q = 28 percent.

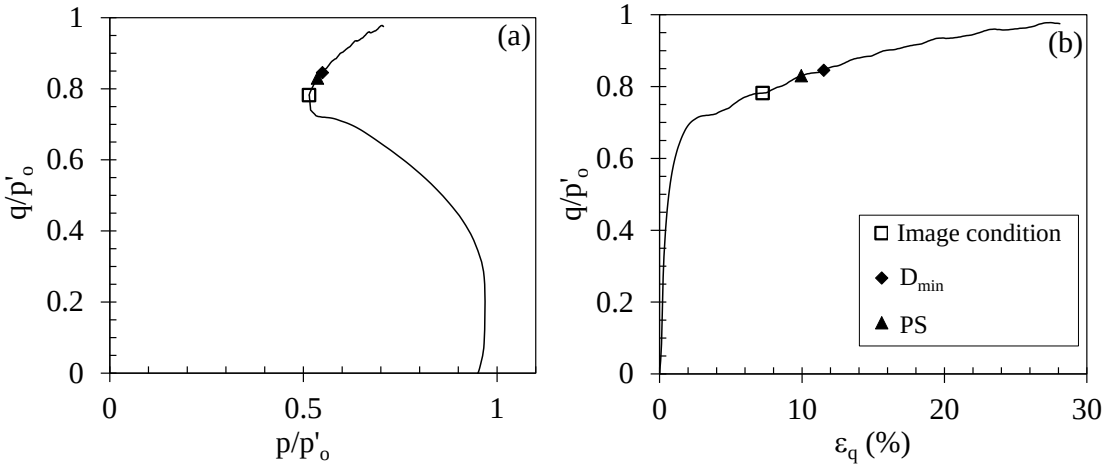

Figure 5.33. Stress path of the CIU triaxial test BullFork20120712_0 in (a) normalized shear stress vs. normalized mean stress and (b) normalized shear stress vs. shear strain.

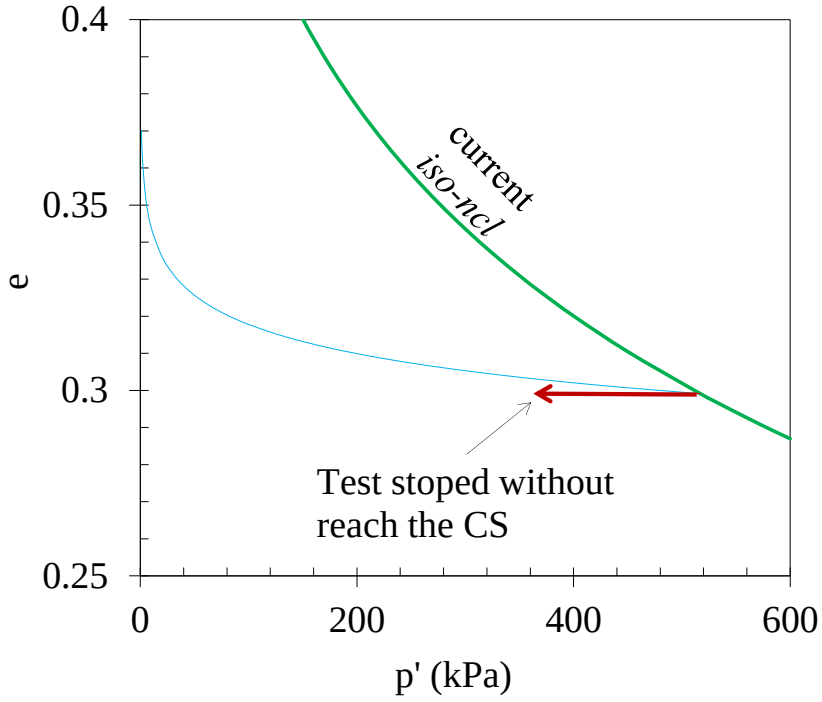

Figure 5.34. Stress path on *e* - *p*' space of the CIU triaxial test BullFork20120712_0.

Figures 5.35a and 5.35b show the change of Δu and η with ε_q. The characteristics of these curves were similar to those of the Type 1 compacted shale curve shown in Figure 5.30. When Δu reached a maximum, $\Delta(\Delta u)$ changed sign, making the specimen dilate even though the specimen started with $\psi_o > 0$. Due to the dilative behavior, the specimen experienced a PS when $\eta = \eta_{max}$.

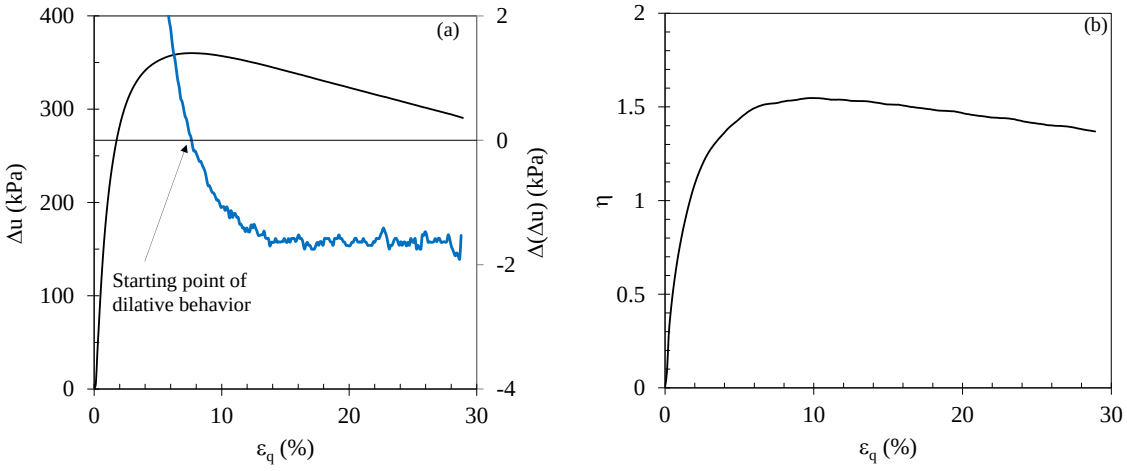

Figure 5.35. Change of stress ratio and excess in pore pressure in the experiment BullFork20120712_0.

During the shear the specimen went into different particular points or stress conditions that characterized the behavior of the specimen. Figures 5.33a, 5.33b, and 5.36 show in detail the evolution of the stress conditions during the shear. At the beginning of the shear, and with the increment of η, the specimen compress due to the increment in the excess of pore pressure. The location of the *csl* was unknown because the specimen did not reach the CS. Therefore, the point at which the stress path crossed the *csl* in $e - \ln(p')$ space could not be determined as shown in Figure 5.34.

With additional shear the IC was reached; therefore, $\eta = M_i$ when ε_q = 7.24 percent. This stress condition is shown with an open square in Figures 5.33 and 5.36.

Until the IC the sample was compressing all the time. In this stress condition $D^p = 0$, and with additional shear D^p changed from being positive to negative.

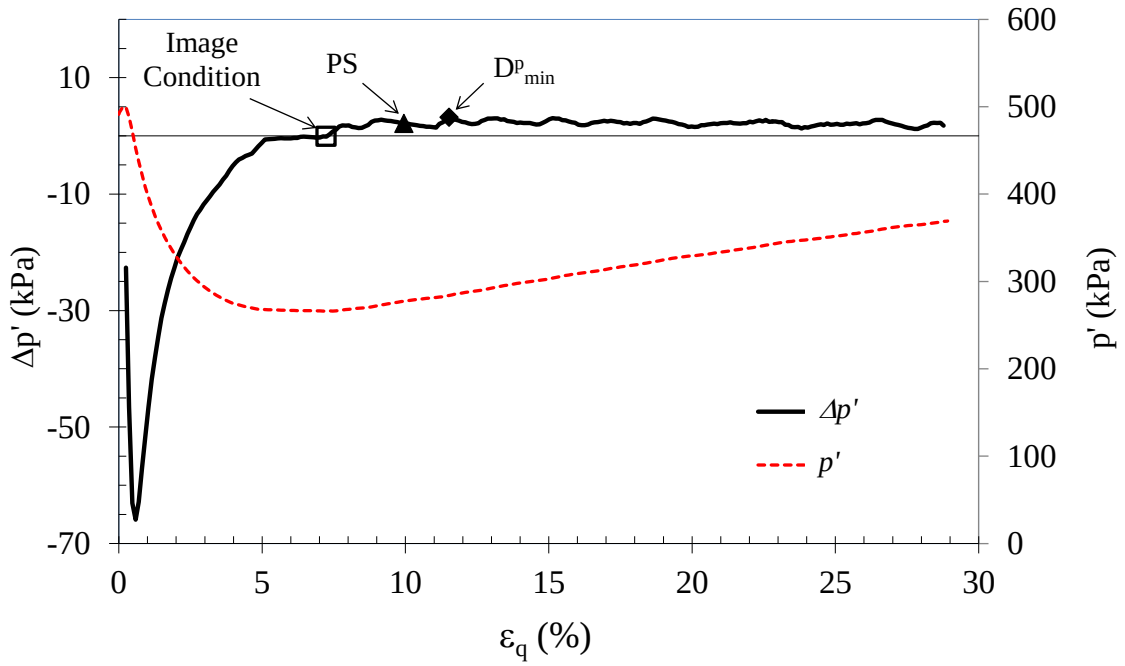

Figure 5.36. Change in mean stress and the derivative of mean stress during the shear phase of the CIU triaxial test BullFork20120712_0.

After the IC, η continued increasing until the specimen reached η_{max} or the PS. This condition was reached when ε_q = 9.94 percent. Figures 5.33 and 5.36 show the PS as a

triangle. From this point, η started to decrease until the specimen reached a stress condition where $\dot{p}' = \dot{p}'_{max}$ and $\ddot{p}' = 0$ (i.e. $D^p = D^p{}_{min}$). This condition was reached when ε_q = 11.52 percent. This stress condition is displayed as a rhombus in Figures 5.33 and 5.36. Unlike Type 1 compacted shales, Type 2 compacted shales reached the PS before $D^p{}_{min}$.

In addition, in Figure 5.36 it can be observed that after the point of minimum dilatancy, the shear continued following a steady state condition by which *p*' increased at the same rate; therefore, $\dot{p}' = constant \neq 0$. This steady state is named by Li (1997) as "undrained dilative shear failure." Eventually $\dot{p}'$ will be zero, since this steady state path in which *p*' increases indefinitely is impossible to follow because the sample would explode. Therefore, it is assumed that the Type 2 compacted shales should reach the CS at strains higher than 35 percent.

Table 5.7 presents the characteristics of the CIU triaxial tests performed on Bull Fork compacted shale. The specimens were weathered over 0 days, 6 days, and 14 days (BullFork20120712_0, BullFork20120907_6, and BullFork20121108_14), and consolidated at a p'_o such that the specimen started with $\psi_o > 0$. The table also shows the void ration before the isotropic consolidation (e_{ini}), the void ration after the isotropic consolidation at which the shear started (e_o), the consolidation pressure (p'_y), the pressure at which the shear started (p'_o), and *R*. It can be observed that all the specimens were practically NC.

Table 5.7. Characteristics of the CIU triaxial tests performed on Bull Fork compacted shale.

Experiment	Soaking time (days)	e_o	p'_y (kPa)	p'_o (kPa)	R
BullFork20120712_0	0	0.30	516.95	491.37	1.05
BullFork20120907_6	6	0.29	517.08	493.45	1.05
BullFork20121108_14	14	0.27	517.18	517.13	1.00

5.2.2.3. Influence of soaking time in shear behavior

The influence of the soaking time in the shear behavior was observed only for those compacted shales that were consolidated to $\psi_o > 0$. Figure 5.37 and Tables 5.8 to 5.11 show the stress paths and the results of the experiments on the Type 1 compacted shale Carbondale. The experiments in the graph are Carbondale20120711_0, Carbondale20121009_6, and Carbondale20120115_21. The data presented in the figure and the tables show that specimens that were soaked over more time (1) reached the IC at higher minimum mean stress, p'_{min}, (2) reached $D^p{}_{min}$ before η_{max}, (3) had lower η_{max} value and therefore lower ϕ'_p, and (4) reached the CS at higher q_c and p'_c. This implies that higher q_c with soaking time results in higher $\left(S_u / p'_o\right)_{\psi_o>0}$, as shown in Table 5.11.

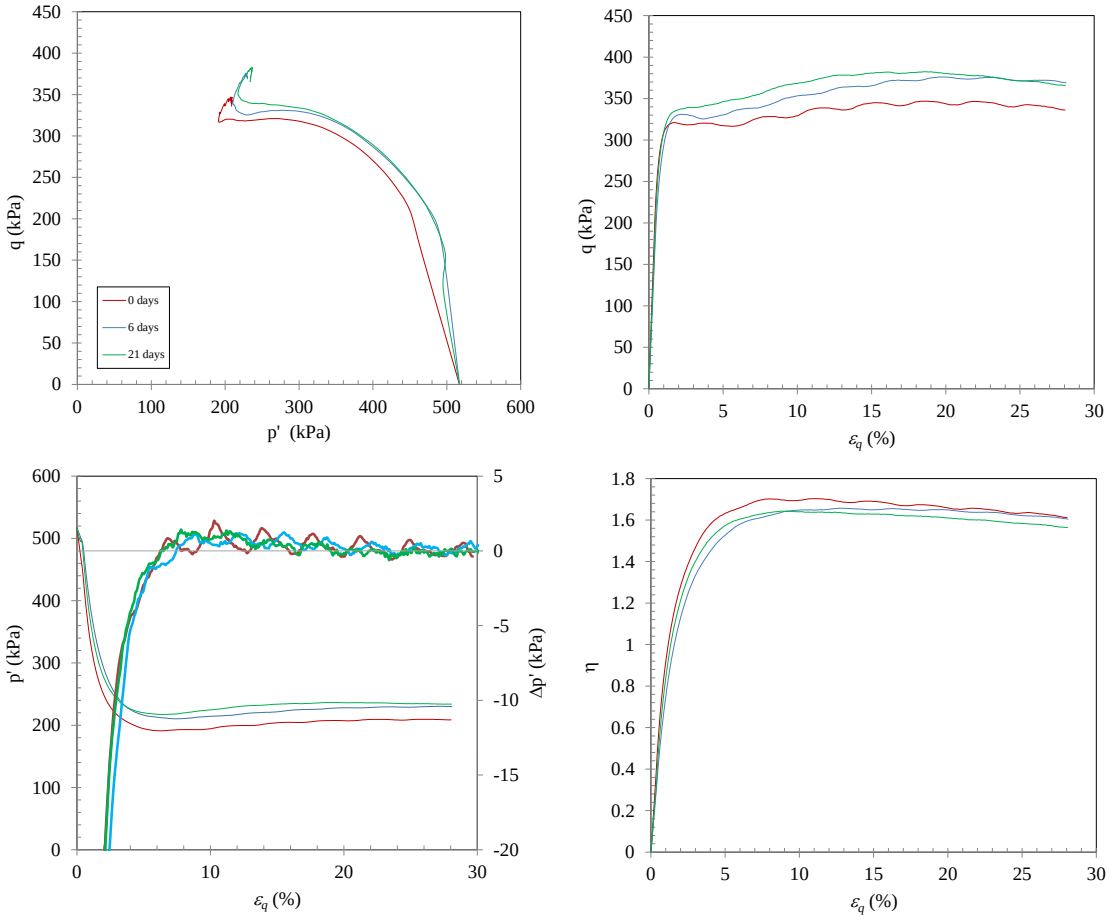

Figure 5.37. CIU triaxial tests on Carbondale compacted shale weathered over 0, 6, and 21 days.

Table 5.8. Characteristics of the image condition.

Experiment	q (kPa)	p' (kPa)	ε_q (%)	η
Carbondale20120711_0	319.0	191.0	6.4	1.67
Carbondale20121012_6	338.7	210.3	7.4	1.61
Carbondale20130113_20	350.1	217.3	6.4	1.61

Table 5.9. Characteristics at D^p_{min}.

Experiment	q (kPa)	p' (kPa)	ε_q (%)	η
Carbondale20120711_0	331.73	195.42	10.27	1.70
Carbondale20121012_6	367.54	222.63	15.45	1.65
Carbondale20130113_20	357.95	219.07	7.80	1.63

Table 5.10. Characteristics of the PS condition.

Experiment	q (kPa)	p' (kPa)	ε_q (%)	η	ϕ'_p
Carbondale20120711_0	337.3	198.1	11.0	1.70	41.6
Carbondale20121012_6	362.7	218.9	12.7	1.66	40.5
Carbondale20130113_20	364.2	221.7	8.7	1.64	40.2

Table 5.11. Characteristics of the CS condition.

Experiment	q (kPa)	p' (kPa)	ε_q (%)	M_c	Su/p'_o
Carbondale20120711_0	346.8	207.2	18.4	1.67	0.34
Carbondale20121012_6	376.0	228.0	19.9	1.65	0.36
Carbondale20130113_20	382.3	236.4	18.7	1.62	0.37

Figure 5.38 and Tables 5.12 to 5.14 show the stress paths and the results of the experiments BullFork20120712_0, BullFork20120907_6, and BullFork20121108_14 in the Type 2 compacted shale Bull Fork. The tests were analyzed until ε_q = 28 percent.

These stress paths show that the specimens that were soaked over more time (1) reached the IC at lower p'_{min}, and (2) had a higher η_{max} and therefore higher ϕ'_p; (3) D^p_{min} (also the beginning of steady state) was reached after η_{max}, with lower stress ratio and higher q and p', and (4) the value of q at ε_q = 28 percent was higher with soaking time. As mentioned

above, this kind of compacted shale did not reach the CS. The behavior of PS was opposite to that of Type 1 compacted shales; for Type 2 compacted shales the soaking increased shear strength, as shown in Table 5.13.

Table 5.12. Characteristics of the image condition.

Experiment	**q (kPa)**	**p' (kPa)**	**ε_q (%)**	**η**
BullFork20120712_0	404.1	266.1	7.2	1.52
BullFork20120907_6	383.6	256.1	5.3	1.50
BullFork20121108_14	428.6	276.2	6.5	1.55

Table 5.13. Characteristics of the PS condition.

Experiment	**q (kPa)**	**p' (kPa)**	**ε_q (%)**	**η_{max}**	**ϕ'_{max}**
BullFork20120712_0	429.3	277.3	9.9	1.55	37.9
BullFork20120907_6	424.8	270.3	9.5	1.57	38.5
BullFork20121108_14	453.5	284.2	9.1	1.60	39.1

Table 5.14. Characteristics at D_{min}.

Experiment	**q (kPa)**	**p' (kPa)**	**ε_q (%)**	**η**
BullFork20120712_0	437.0	284.0	11.5	1.54
BullFork20120907_6	445.1	286.8	12.4	1.55
BullFork20121108_14	492.7	313.3	13.6	1.57

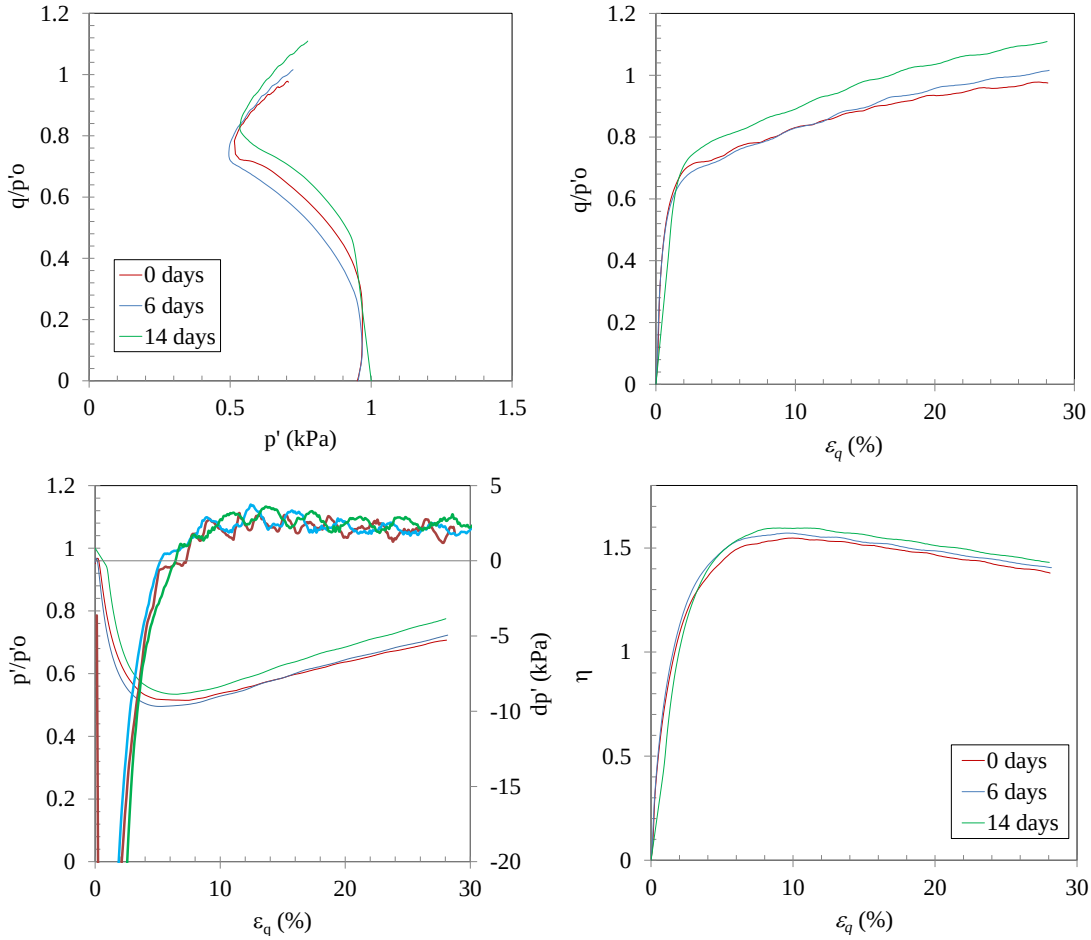

Figure 5.38. CIU triaxial tests on Bull Fork compacted shale weathered over 0, 6, and 14 days.

Figures 5.39 shows the variation of $(S_u/p'_o)_{\psi_o>0}$ with soaking time for those experiments that started the shear with $\psi_o > 0$. Figure 5.39 shows that $(S_u/p'_o)_{\psi_o>0}$ of Carbondale and Grundy compacted shales increases with soaking time. There is no clear trend regarding Fort Payne.

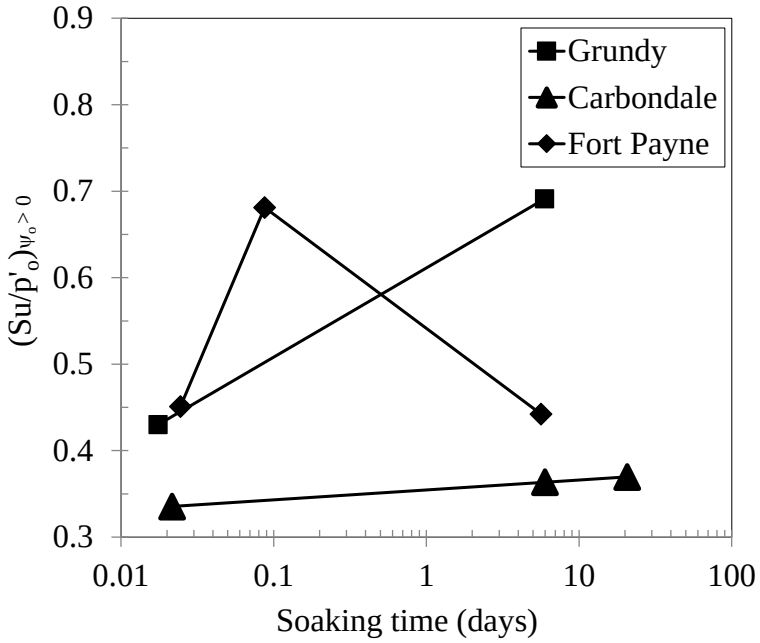

Figure 5.39. Variation of undrained shear strength with soaking time for experiments performed with $\psi_o > 0$.

Regardless of PS, figures 5.40a and 5.40b show the variation of η_{max} and D^p_{min} with soaking time for those compacted shales with $\psi_o > 0$. Figure 5.40a shows that Type 1 compacted shales suffer reduction of η_{max} with soaking time. However, Grundy compacted shale has an insignificant variation of η_{max} with soaking time. It can thus be interpreted that the soaking time made the Type 1 compacted shales behave more like a clay because loss peak strength. The Type 2 compacted shales demonstrate different behavior among them: Bull Fork increases and Tradewater reduces η_{max} with soaking time. It can also be observed in Figure 5.40a that the η_{max} of Type 2 compacted shales (the non-durable shales) is much smaller than the η_{max} of Type 1 compacted shales (the durable shales). This means that η_{max} is also a function of the durability. Regarding D^p_{min}, Figure 5.40b shows that there is not a clear trend between D^p_{min} and soaking time.

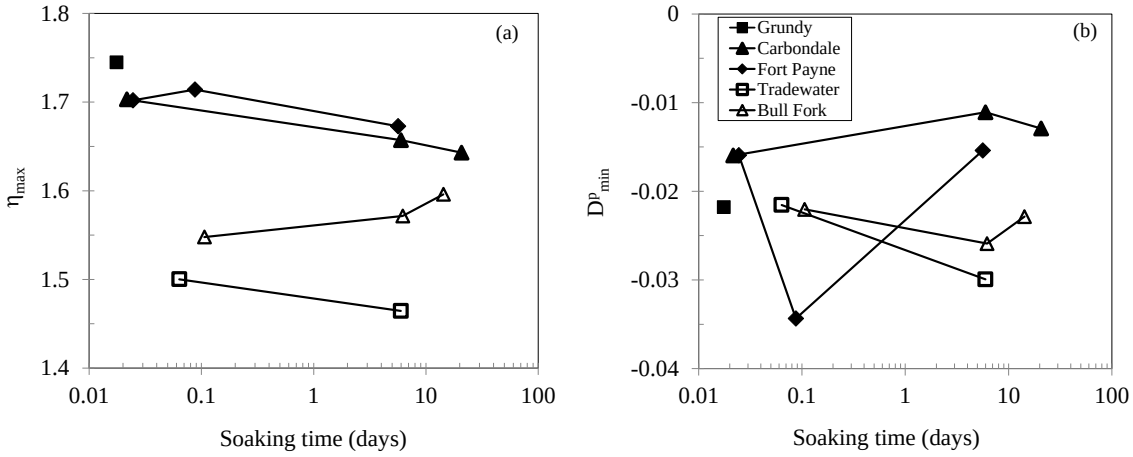

Figure 5.40. Change of (a) maximum stress ratio and (b) minimum plastic dilatancy with soaking time for experiments performed at $\psi_o > 0$.

CHAPTER 6

6. Critical State and Peak State

This chapter is divided into two sections. The first section shows the CS parameters obtained through the CIU experiments shown in the previous chapter. The influence of the mineralogical content and index properties on the CS is explored. The second section describes the behavior of the samples when they reached the PS.

6.1. Critical State parameters Type 1 compacted shales

Equation 2.13a defines the *csl* in an $e - q - p'$ space. The parameters of these equations are M_{tc}, λ_s and Γ. As was discussed in Chapter 2, M is a material property that depends on ϕ'_c and θ; therefore, the slope of Equation 2.13 will be referred to as M_{tc}.

Figures 6.1a and 6.1b show the points where the four specimens of Carbondale compacted shale reached the CS in $q - p'$ and $e - \ln(p')$ spaces. In Figure 6.1b, the solid black circles indicate where the shear started and the solid triangles where the CS was reached. The accurate definition of the *csl* indicates that it was unique regardless of the soaking time and ψ_o.

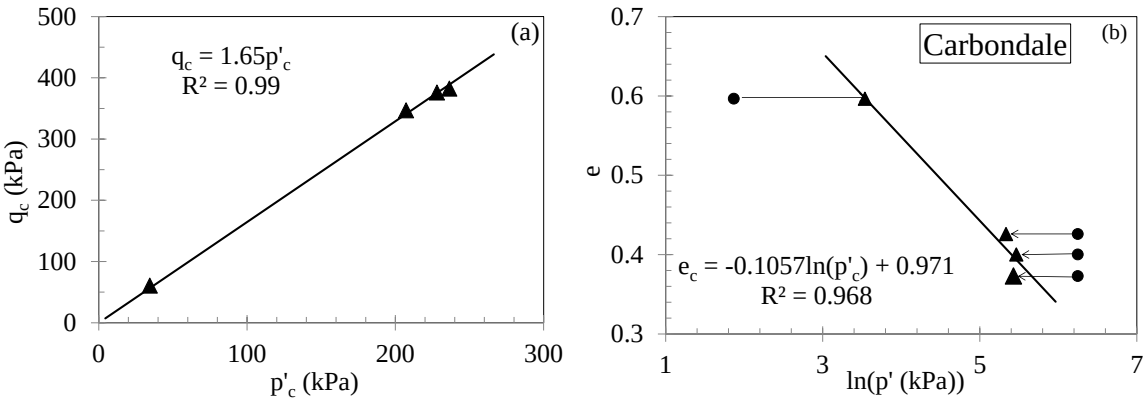

Figure 6.1. Critical state line for Carbondale compacted shale in (a) $q - p'$ space and (b) $e - \ln(p')$ space.

From Figures 6.1a and 6.1b, the CS parameters of Carbondale compacted shale are:

$M_{tc} = 1.65$

$\lambda_s = 0.1057$

$\Gamma = 0.97$

The following analysis is done with ϕ'_{cs} because it is a property of the material, unlike M_{tc} that is a function of the material and θ. Rewriting the Equation [2.14], ϕ'_{cs} was calculated by:

$$\sin\phi'_{cs} = \frac{3M_{tc}}{6+M_{tc}} \qquad [6.1]$$

In a similar way the CS parameters of Grundy and Fort Payne compacted shales were calculated as shown in Figures 6.2a to 6.2d. Table 6.1 summarizes the *csl* parameters for the Type 1 compacted shales.

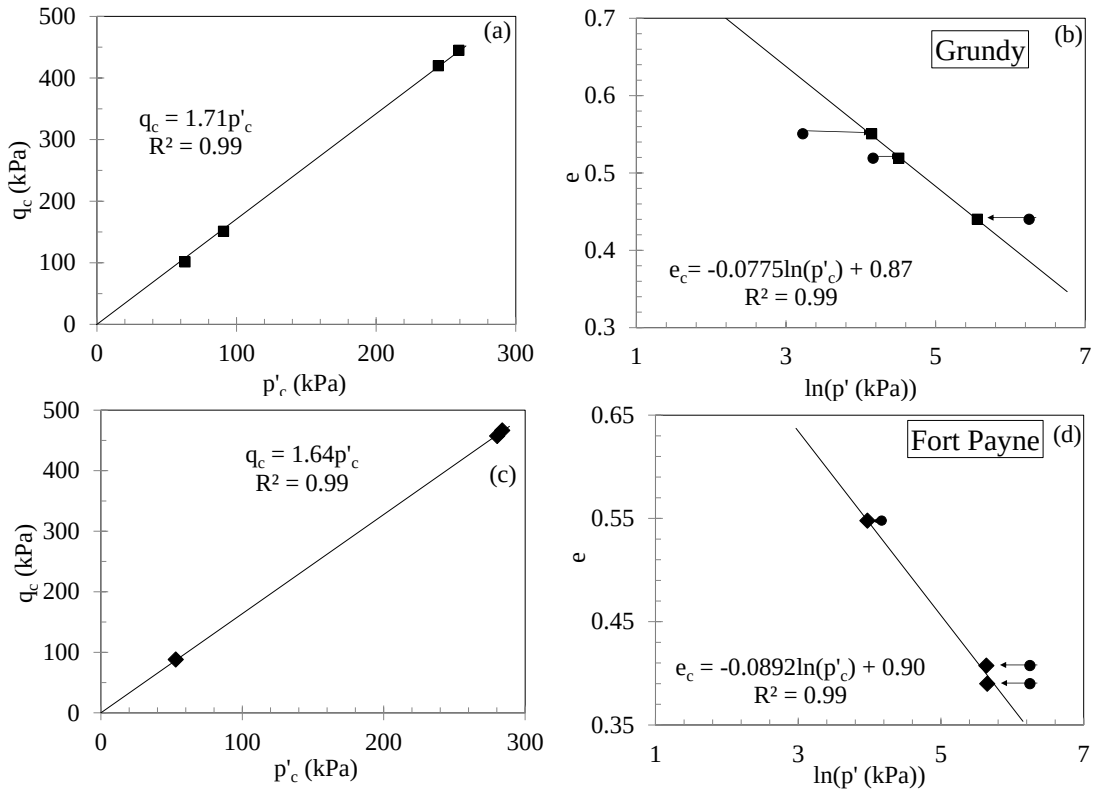

Figure 6.2. Critical state line for Grundy and Fort Payne compacted shale in (a) and (b) *q* - *p*' space and (b) and (c) *e* – ln(*p*') space.

As was discussed in Chapter 2, the undrained shear strength of clays is a specific condition of CS that is a function of the void ratio and R (i.e. stress state-dependent property).

Table 6.1. Critical state parameters of the Type 1 compacted shales.

Shale	M_{tc}	$\phi'_{(c)}$	Γ	λ_s
Grundy	1.71	41.7	0.870	0.0775
Carbondale	1.65	40.2	0.971	0.1057
Fort Payne	1.64	40.0	0.902	0.0892

Even though crushed shales classify as sands due to their GSD, they start to weather with the first contact with water. This caused the specimens exhibited apparent cohesion after the CIU tests finished, especially those compacted shales that were soaked more or consolidated to a higher pressure, as shown in Figure 5.18. Therefore, the undrained shear strength is a valid way to evaluate the shear strength of compacted shales under monotonic or undrained conditions. The normalized undrained shear strength, (S_u / p'_o) was calculated using Equation [2.17]:

$$\left(\frac{Su}{p'_o}\right) = \frac{q_{cs}}{2p'_o} \qquad [2.17]$$

The relationship between undrained shear strength and ψ_o was explored in Figure 6.3 because the concept of ψ_o takes into account *e* and the stress condition.

Such a high R^2 (99 percent), shown in Figure 6.3, has two meanings. The first meaning is that ψ_o and (S_u / p'_o) are collinear. The collinearity is due to the fact that both parameters are located over the same line, *csl*, as shown in Figure 6.4. ψ_o and (S_u / p'_o) are functions of e_o and p'_o; and S_u is also a function of e_o. Ideally, S_u is

$$S_u = \frac{M_{tc}}{2}\exp\left(\frac{\Gamma - e_o}{\lambda_s}\right) \qquad [2.16]$$

The word ideally is used because, as will been seen in Chapter 7, this equation did not produce good estimates of S_u.

However, they are parameters measured with the CIU triaxial test results in a completely different way, as shown in Equations [2.6] and [2.17]. Therefore, this high R^2 implies that the experiments were performed in a coherent way.

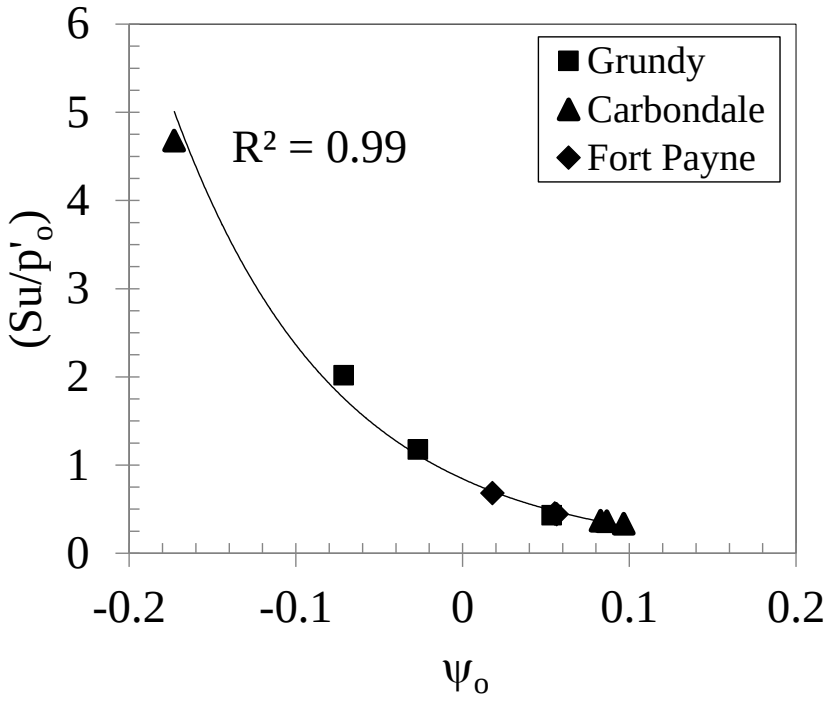

Figure 6.3. Variation of (S_u/p'_o) with initial state parameter for compacted shales.

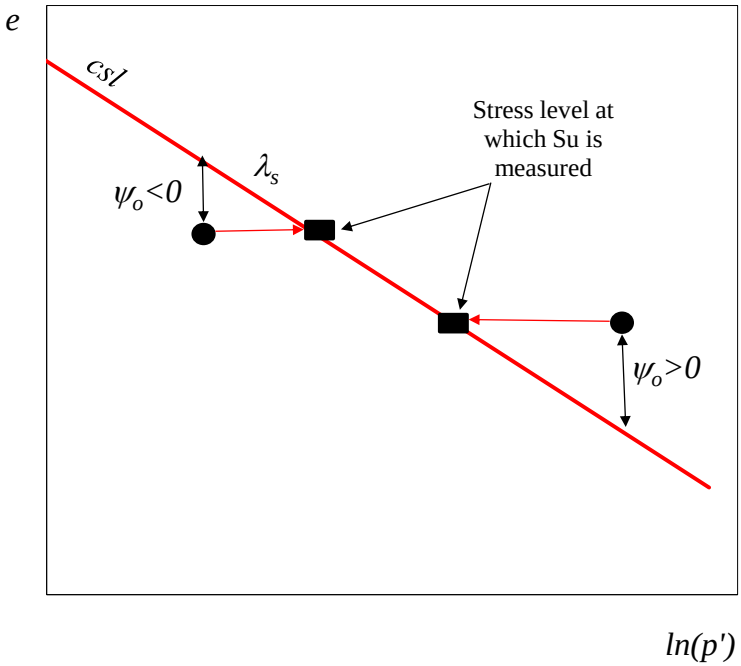

Figure 6.4. Stress level at which S_u measured.

The second meaning of this high R^2 is that ψ_o explains all the variability of (S_u/p'_o). The influence of R in (S_u/p'_o) need to be study in future research. From Figure 6.3, a

relationship to estimate the value of (S_u / p'_o) is proposed as:

$$\frac{S_u}{p'_o} = 0.8 \exp(-10.2\psi_o) \quad [6.2]$$

6.1.1. Influence of Mineralogy on CS parameters

The CS parameters to analyze are M_{tc}, λ_s, and Γ. Only Type 1 compacted shales reached the CS; therefore, only data from Grundy, Carbondale, and Fort Payne are analyzed below.

Figures 6.5a to 6.5f show the variation of ϕ'_{cs}, λ_s, and Γ with the (Ch+I)/K ratio and fine size quartz for the Type 1 compacted shales (Grundy, Carbondale, and Fort Payne). The graphs do not show a clear trend for any variables. It should be noted that there are only 3 shales that reached the CS; therefore, there is not enough data in order to infer about the relation of the CS parameters and mineralogical characteristics.

6.1.2. Influence of index properties and durability on critical state

Empirical relations that may be useful when inferring strength parameters of compacted shales for Type 1 and Type 2 compacted shales will also be proposed. The aim of these empirical relations is to use them as a tool to solve problems using advanced techniques or to give engineers a picture of the behavior of compacted shales.

6.1.2.1. Critical state friction angle

Table 6.1 shows that ϕ'_{cs} ranges between 40 and 41.7. Figure 6.6 shows the variation of ϕ'_{cs} with CF for weathered compacted shales by Bryson et al. (2012) and the compacted shales of this study.

As was already mentioned, CF is a parameter that is controlled by the energy used to crush the shales. The CF reported by Bryson et al. (2012) is a function of the weathering mechanisms suffered by the shales during years of weathering cycles. They took their shale samples from talus piles adjacent to highways in order to have representative weathered samples of the shales in the embankments after several years of construction.

Their samples classify as CL and ML with less than 15 percent of sand size.

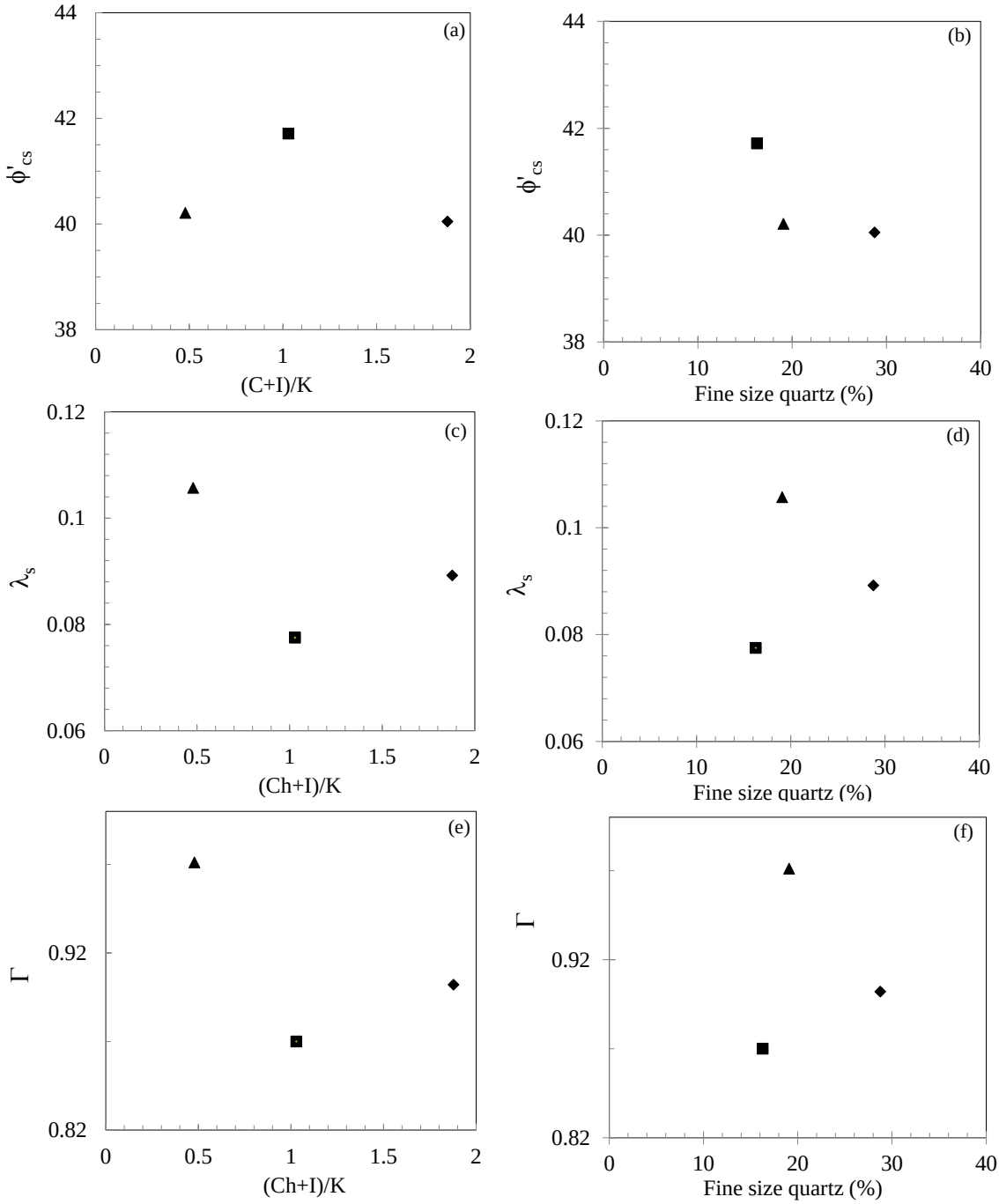

Figure 6.5. Variation of critical state friction angle with (Ch+I)/K ratio and fine size quartz.

Otherwise, the shales of this study were fresh outcrop samples that were crushed using a modified proctor hammer applying the same level of energy. These crushed samples

classify as SW-SC with less than 10 percent of silts. While there is not enough information, it is possible to infer that ϕ'_{cs} will not change with the GSD; either the sample comes from a talus pile or comes from an outcrop and is crushed. It is inferred that the friction goes through parallel curves of the same crushing energy or weathered time.

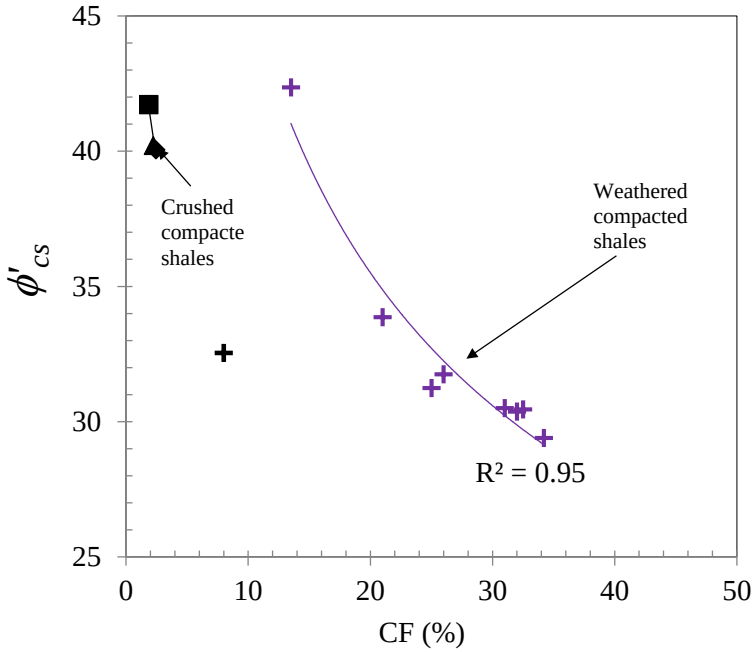

Figure 6.6. Variation of critical state friction angle with clay fraction after crushing.

The relation of ϕ'_{cs} with LL and PI was explored. Figure 6.7 shows the variation of ϕ'_{cs} with LL. Figure 6.7 includes friction angle of clays, silts, and shales from Stark and Eid (1997), Mesri and Cepeda (986), and Bryson et al. (2012). In the graph the compacted shales of this study are located in the area of low LL and high ϕ'_{cs}. A clear trend is observed in which soils with higher LL exhibit lower ϕ'_{cs}. The shales of this study had low LL because chlorite, illite, and kaolinite are not expansive minerals; eventually they start to weather and transform into expansive minerals.

Figure 6.8 shows the variation of ϕ'_{cs} with PI. The graph includes friction angles of clays, silts, and shales from Kennye (1959), Bjerrum and Simons (1960), Mesri and Cepeda-

Diaz (1986), Diaz Rodriguez et al. (1992), Mesri and Abdel-Ghaffar (1993), Terzaghi et al. (1996), Stark and Eid (1997), and Bryson et al. (2012). Even though the data are highly scattered, a trend is observed in which soils with higher PI exhibit lower ϕ'_{cs}.

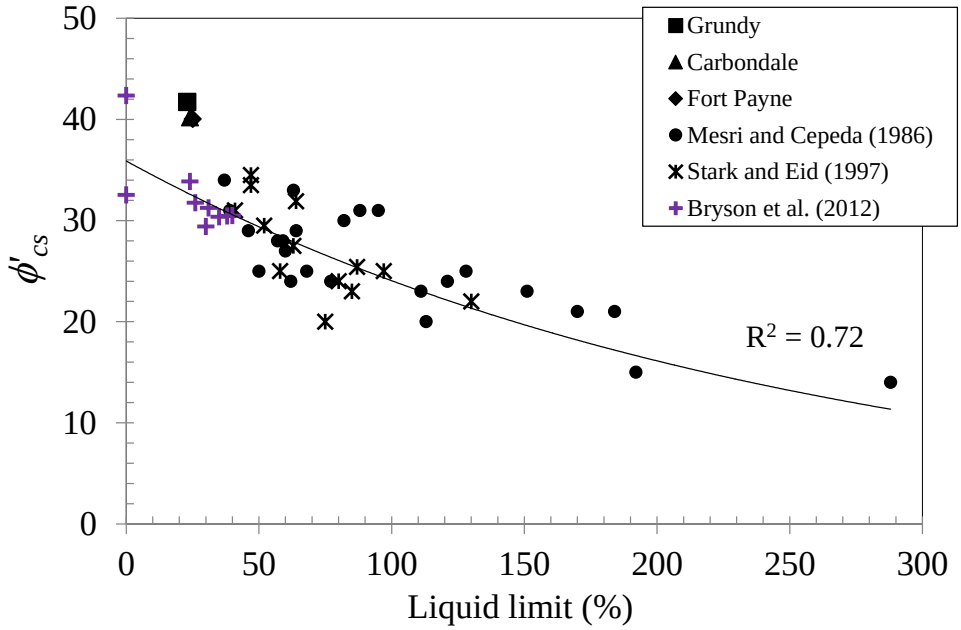

Figure 6.7. Variation of the critical state friction angle with liquid limit.

Figure 6.9 shows the variation of ϕ'_{cs} with A_c of clays, silts, and shales from Stark and Edid (1997), Mesri and Cepeda (1986), and Bryson et al. (2012). A clear pattern is observed in ϕ'_{cs} with PI and CF where ϕ'_{cs} decreased with PI and CF. However no pattern was observed with A_c.

Figures 6.10a and 6.10b show the variation of ϕ'_{cs} with $Id_{(2)}$ and LSI of the shales of this study. Figures 6.10a and 6.10b also show weathered shales by Bryson et al. (2012). The graphs demonstrate that the compacted shales constructed with more durable shales have high ϕ'_{cs}, and compacted shales constructed with less durable shales have low ϕ'_{cs}. The trend line followed by combining the data of this study and that from Bryson et al. (2012) is:

$$\phi'_{cs} = 31.13 * LSI^{-0.06} \qquad [6.3]$$

This equation is not recommended to use as an empirical equation because the few available data.

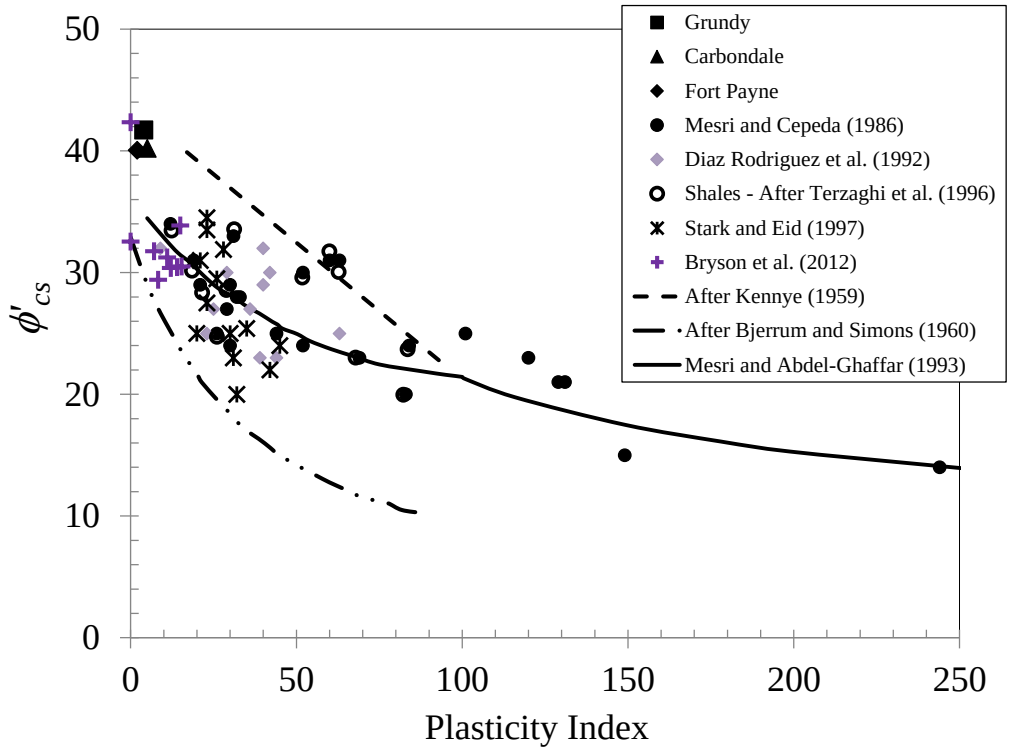

Figure 6.8. Variation of critical state friction angle with plasticity index.

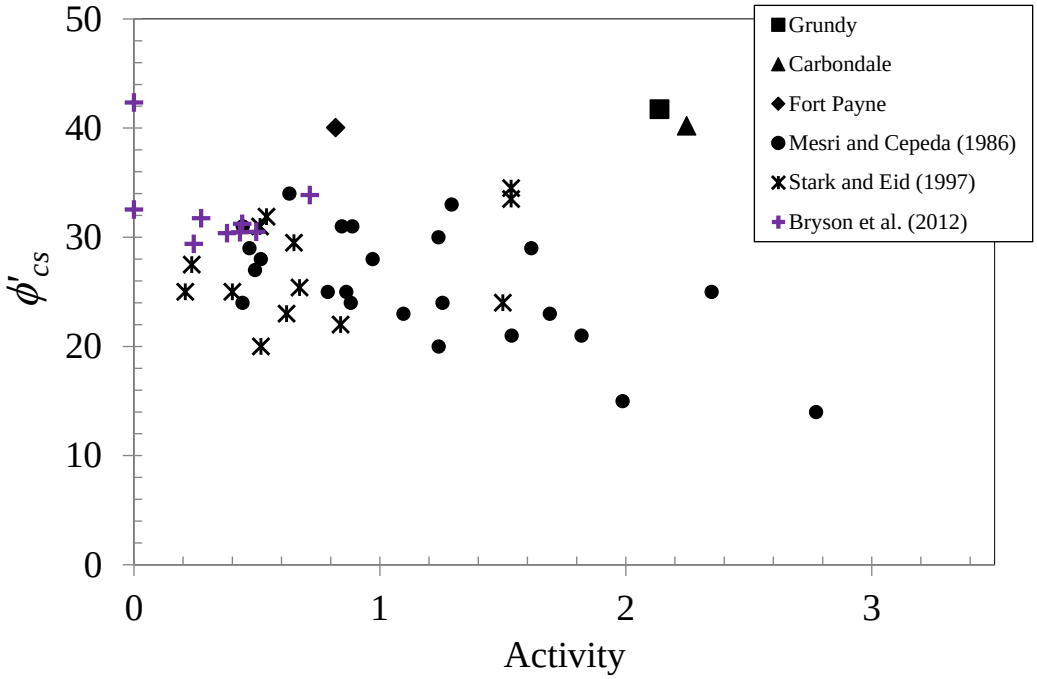

Figure 6.9. Variation of critical state friction angle with activity.

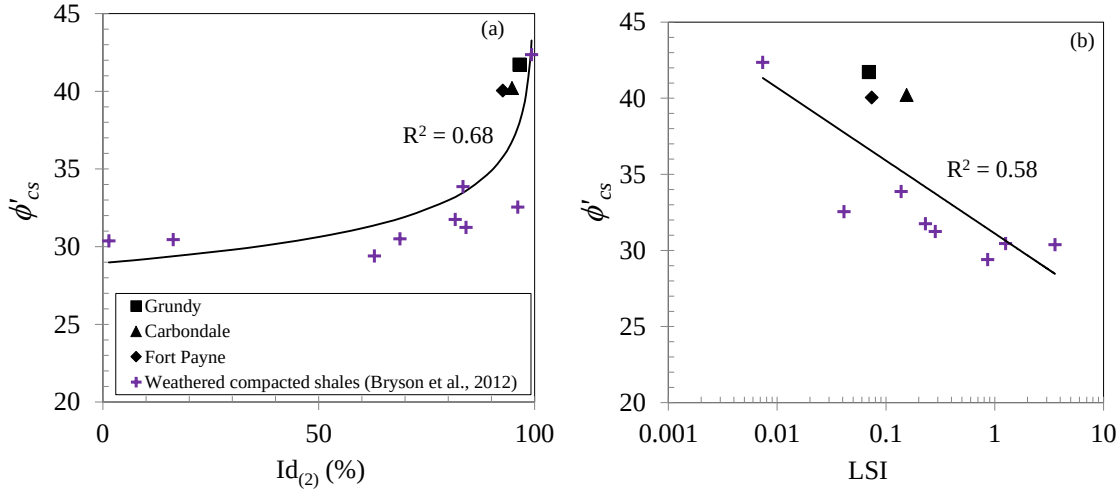

Figure 6.10. Variation of critical state friction angle with durability: (a) slake durability index and (b) loss slake index.

Even though there are only three points it is possible to observe in Figure 6.11 that exist a trend between ϕ'_{cs} and S_{jar}, where ϕ'_{cs} decreased with S_{jar}.

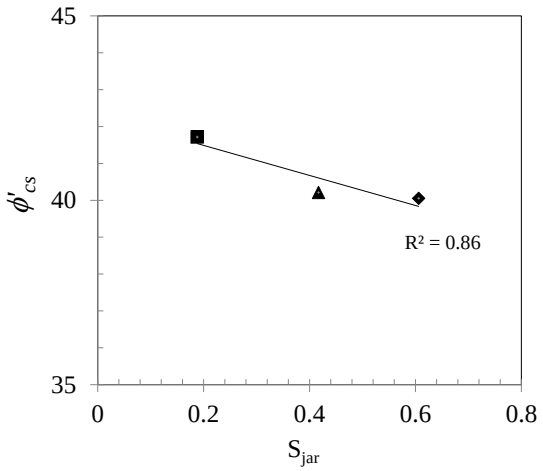

Figure 6.11. Variation of critical state friction angle with durability index S_{jar}.

6.1.2.2. Critical state parameters λs and Γ

Table 6.1 shows the values of λ_s and Γ for the Type 1 compacted shales. Table 6.1 shows that λ_s ranges between 0.0775 and 0.1057. According to Shuttle and Jefferies (2010), the typical values of λ_s are around 0.18 for clays, around 0.07 for silts, and between 0.014

and 0.03 for sands. Therefore, the magnitude of λ_s for the compacted shales of this study is inside the range of silts. Figures 6.11a to 6.11d shows the variation of λ_s with A_c, S_{jar}, $Id_{(2)}$, and LSI. There is no clear trend with A_c, S_{jar}, $Id_{(2)}$, but one with LSI with only 3 points, where λ_s increased with LSI.

Table 6.1 shows that Γ ranges between 0.8701 and 0.9021. According to Shuttle and Jefferies (2010), the typical values of Γ are around 2.7 for clays, around 1.1 for silt, and between 0.45 and 1.3 for sands. Therefore, the magnitude of Γ falls in the range of silts. Figures 6.12a to 6.12d shows the variation of Γ with A_c, S_{jar}, $Id_{(2)}$, and LSI. Similar to λ_s, Γ did not show a clear relationship with A_c, S_{jar}, and $Id_{(2)}$ is not observed. However, it was observed that Γ increased with LSI.

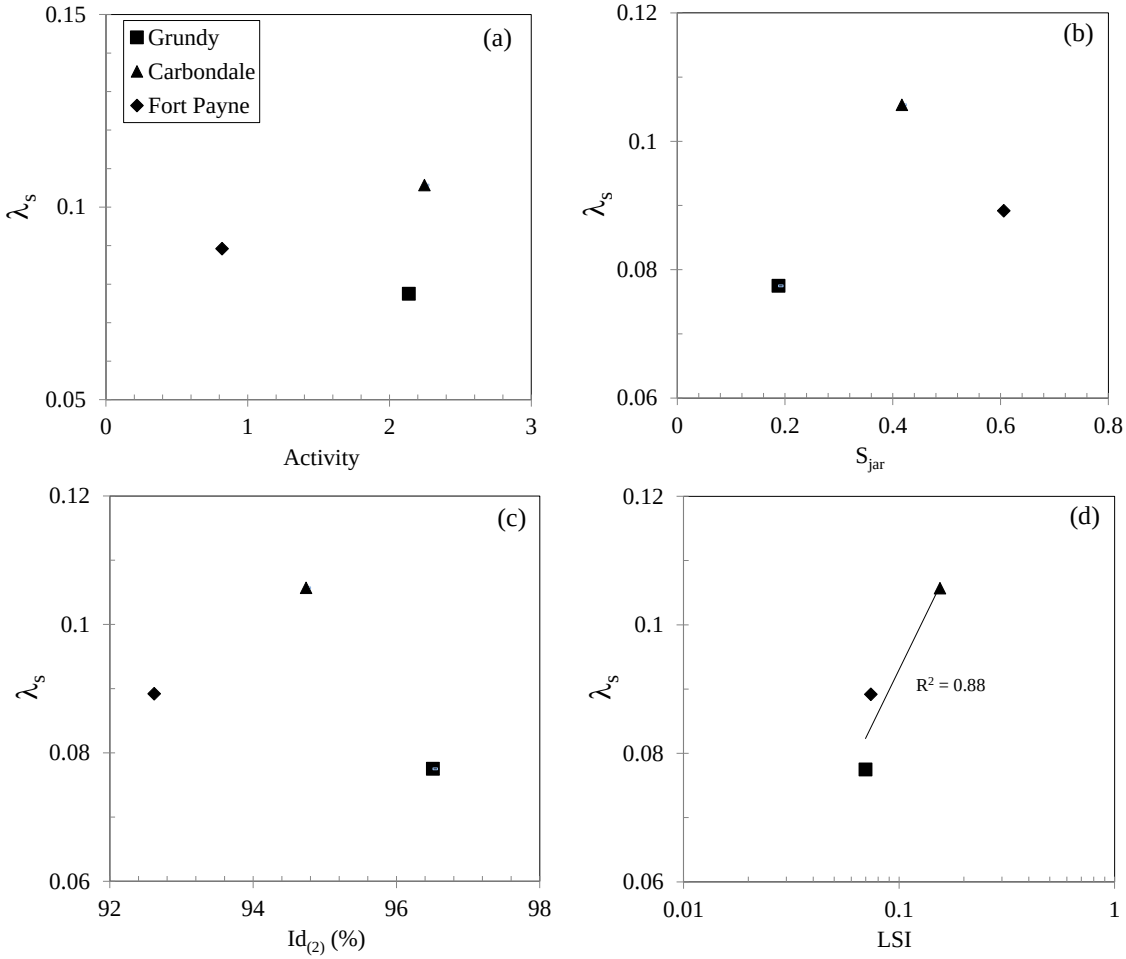

Figure 6.12. Variation of λ_s with A_c and durability indexes.

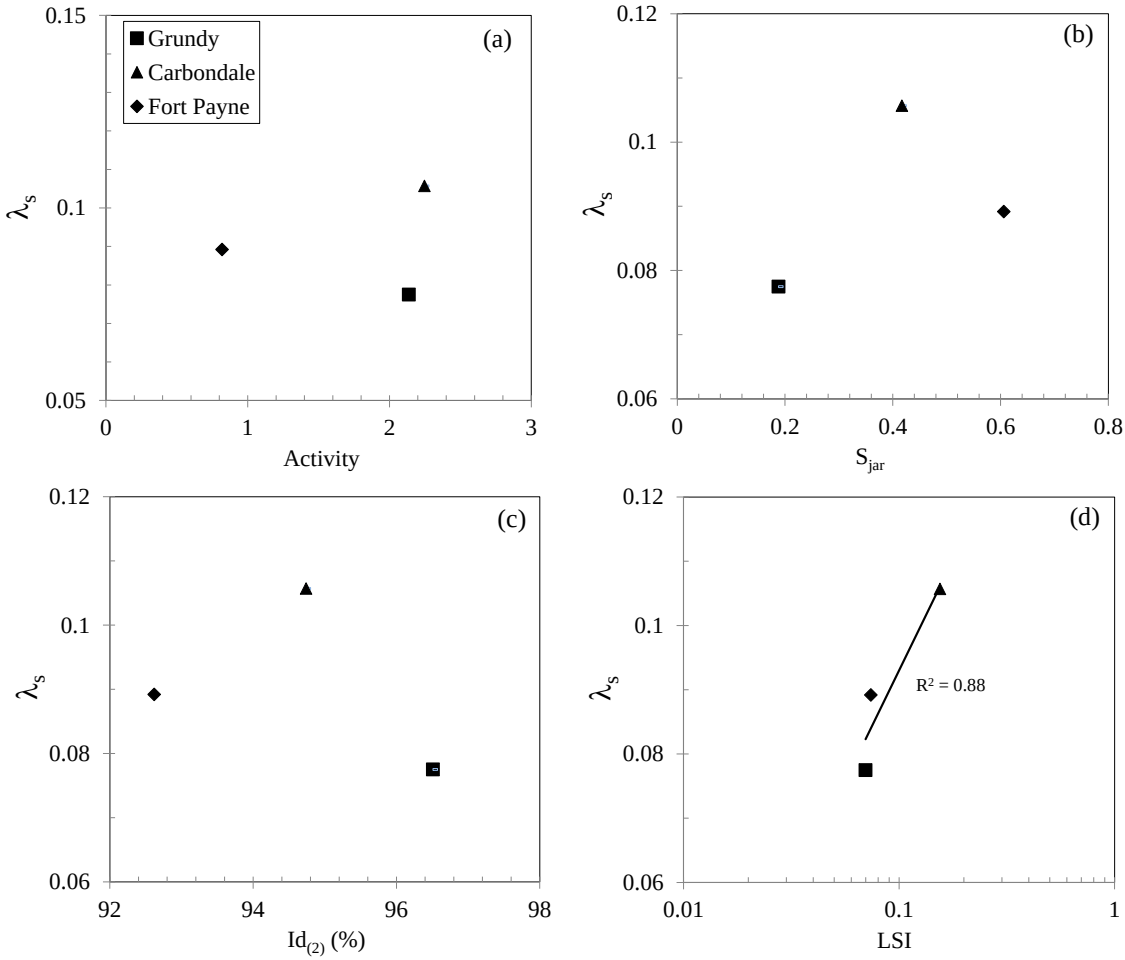

Figure 6.13. Variation of Γ with A_c and durability indexes.

6.2. Peak State parameters

This section describes the characteristic of PS of Type 1 and Type 2 compacted shales as well as the relationship between the NorSad parameters N and χ with ψ.

6.2.1. Maximum stress ratio and minimum dilatancy

In clays the dilatancy is related to *R*. For CC and MCC models, clays present negative dilatancy when *R* is greater than 2.72 and 2, respectively. Otherwise, the negative dilatancy in sands occurs due to a combination of high unit weight and low confining stress. For both clays and sands, high confining stress inhibits dilatancy.

It was observed that for compacted shales η_{max} and $D^p{}_{min}$ did not occurred at the same

time. Figure 6.14a shows that η_{max} occurred before D^p_{min} for Type 1 compacted shales; and η_{max} occurred after D^p_{min} for Type 2 compacted shales. Figure 6.14b shows that η at D^p_{min} was slightly close to η_{max} for almost all the specimens.

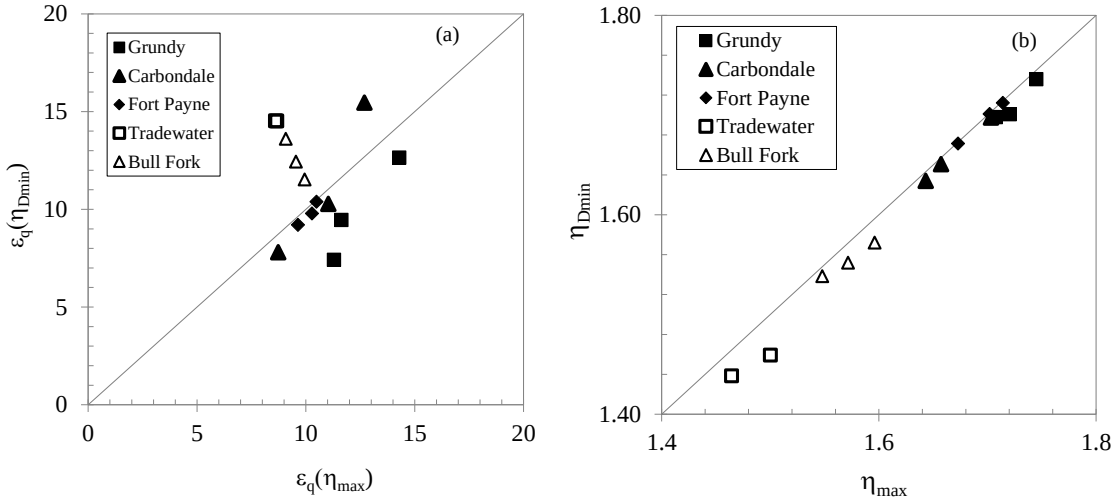

Figure 6.14. Comparison of stress ratio at the points of maximum stress ratio and stress ratio at minimum plastic dilatancy.

6.2.2. Parameter N

According to NorSand, the parameter N represent the slope of a straight line in a graph η_{max} versus D^p_{min}, as shown in Figure 2.5 (Jefferies and Been, 2006). Also represents the denominator in the Nova flow rule where μ = 1 - *N*. Figure 6.15 shows the plot η_{max} versus D^p_{min} of Type 1 and Type 2 compacted shales. It is possible to observe in the graph that there is no clear tendency between these two variables.

Given the observations that η_{max} and D^p_{min} did not occur at the same time, as shown in Figure 6.14b, in this study *N* has different meaning. If d^p is the difference between stress ratio at CS and PS:

$$d^p = M_{tc} - \eta_{max} \qquad [6.4]$$

and

$$D^{p}_{\min} = M_{tc} - \eta_{D^{p}_{\min}} \quad [6.5]$$

it is possible to define a parameter N of Equation [2.41] such as:

$$(1-N) = \frac{d^{p}}{D^{p}_{\min}} \quad [6.6]$$

Combining equations [6.9] and [6.11]:

$$D^{p}_{\min} = \frac{M_{tc} - \eta_{\max}}{1-N} \quad [2.41]$$

that is the same equation by Jefferies and Been (2006). *N* represents how far $\eta_{\max}$ and $D^{p}_{\min}$ occurs.

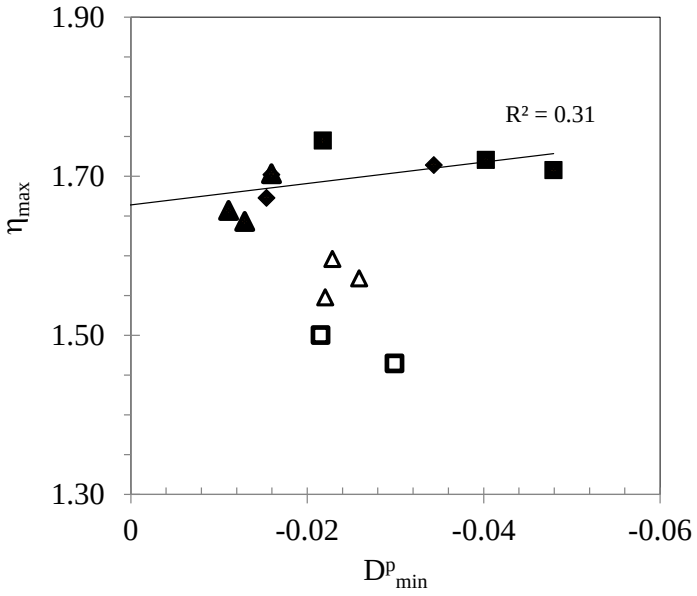

Figure 6.15. Variation of N with the state parameter at image condition.

It was searched if *N* varies with index properties, mineralogy, durability, estate parameter, etc, but clear relationships with this variables were not observed. Figure 6.16 shows the variation of *N* with ψ_i. It shows that *N* is not explained by ψ_i and has an average value of 0.23. According to Shuttle and Jefferies (2011), *N* varies between 028 and 0.41 for sands, silts, and clays. The experiment Carbondale121012_6 showed an unusual value of *N*. Nothing was found that can explain this high value of *N*. *N* = 0

implies that η_{max} and $D^p{}_{min}$ occurs at same time. For compacted shale, N is going to be interpreted as a measured of how far are η_{max} and $D^p{}_{min}$.

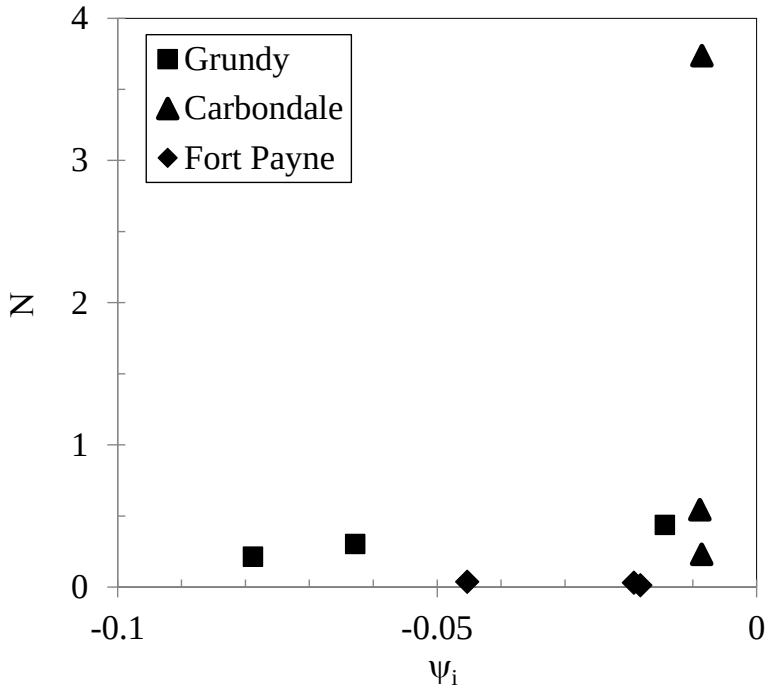

Figure 6.16. Variation of N with the state parameter at image condition.

From Equation 2.41, it is possible write this equation in the τ - σ space as:

$$\phi'_p = \phi'_{cs} + (1 - N)\alpha \qquad [6.7]$$

where 1 – N = 0.77 and α is the maximum dilatancy in τ - σ space.

Bolton (1986) studied the strength behavior of 17 different sands in axisymmetric and plane strain conditions at different densities and confining pressures. He found that the extra strength given by the dilatancy to the shear strength was:

$$\phi'_p = \phi'_{cs} + 0.8\alpha \qquad [6.8]$$

This equation confirms the results shown in Figure 6.14: the PS and the minimum dilatancy do not occur at the same time.

6.2.3. Parameter χ

The relationship between D^p_{min} and ψ_i is one of the key parts of the NorSand model because it links the current minimum possible dilatancy with the current IC by the constant of proportionality χ_{tc}, as shown in Equation [2.42] and Figure 2.6. χ is used to limit the internal cap for each increment in shear strain. In order to apply and explore the validity of the NorSand model in compacted shales, Figure 6.17 shows the variation of D^p_{min} with ψ_i of the CID triaxial tests of different types of sands by Jefferies and Been (2006) and the CIU triaxial tests of the compacted shales of this study. The figure shows that D^p_{min} of the compacted shales are inside the cloud of data by Jefferies and Been (2006), and, similarly with ψ_o, low ψ_i is associated with low values of D^p_{min}. It is also observed that Equation [2.42] applies to compacted shales by:

$$D^p_{min} = 0.67\psi_i \qquad [6.9]$$

where $\chi_{tc} = 0.67$.

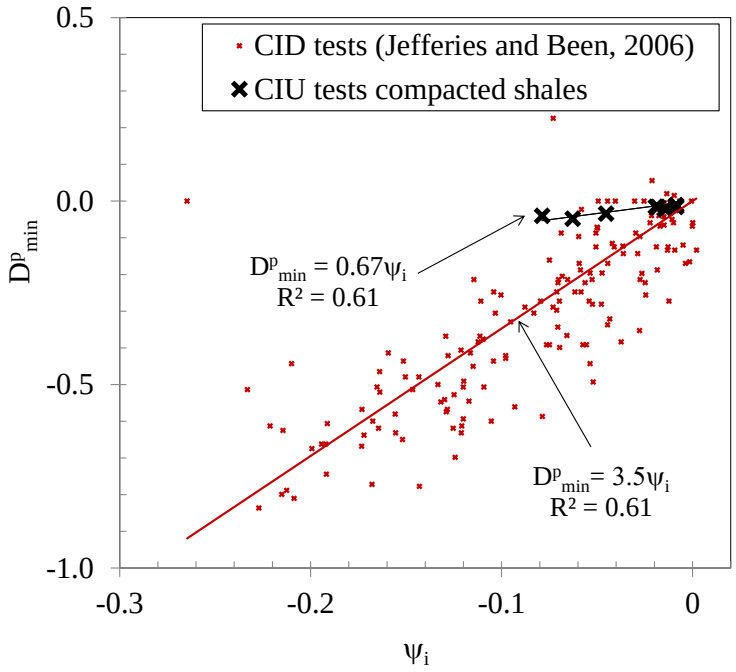

Figure 6.17. Variation of minimum dilatancy with state parameter at IC.

CHAPTER 7

7. Performance of CamClay, Modified CamClay, and NorSand models for compacted shales in Triaxial Compression

This chapter presents an analysis of the performance of the Critical State models CC, MCC, and NorSand used to predict shear behavior during the CIU triaxial test. In order to simulate a CIU triaxial test using CS models, it is necessary to solve Hooke's law, the flow rule, and the hardening rule together. This is difficult; therefore, the solution is achieved incrementally using an Euler scheme. Due to the fact that the shear phase of CIU triaxial tests is strain-controlled, the incremental solution is based on small increments of shear strain. The simulations were performed through a routine written in Visual Basic based in a routine by Shuttle and Jefferies (2010) download from (http://www.itasca-udm.com/pages/NorsandM.html). Appendix K shows the modified code.

The first section presents the performance of the models for Grundy, a Type 1 compacted shale, for which all the parameters are known. The second section shows the performance for Bull Fork, a Type 2 compacted shale.

7.1. Type 1 compacted shales

7.1.1. Input parameters

The mechanical properties of Type 1 compacted shales were calculated with the results of the CIU triaxial tests shown in Chapter 4. Table 5.1 shows the mechanical properties of Grundy compacted shale that were calculated in Chapter 5. The performance of the Critical State models on Type 1 compacted shales was evaluated through the results of the Grundy20120709_0 CIU triaxial test. This experiment was performed with R = 1.0 and ψ_o = 0.054. Table 7.1 shows the parameter used to do the simulations. It was found in Chapter 6 that χ_{tc} = 0.67, and the average value of N is 0.23. H, which depends on the fabric and ψ_o, was calculated by trial and error.

Table 7.1. Soil parameters of Grundy compacted shale.

Parameter	Value
λ_{ncl}	0.0717
κ	0.0099
G_{max}	45,133 kPa
ν	0.25
M_{tc}	1.71
Γ	0.87
λ_s	0.072
χ	0.67
N	0.23
H	Trial and error

7.1.2. Geometry of the critical state line in $e - p'$ space

$\lambda_s = \lambda_{ncl}$ in CC and MCC models and Γ is a function of the Flow Rule. For the CC model:

$$\Gamma = e_o + (\lambda_{ncl} - \kappa)\ln\left(\frac{p'_o}{\exp(1)}\right) + \kappa\ln(p'_o) \qquad [6.1]$$

and for the MCC model:

$$\Gamma = e_o + (\lambda_{ncl} - \kappa)\ln\left(\frac{p'_o}{2}\right) + \kappa\ln(p'_o) \qquad [6.2]$$

The NorSand model works with the "real" *csl*. Γ and λ_s should be estimated through the best fit line of at least three CS points in e – ln(p') space obtained from CIU or CID triaxial tests (see Figures 6.1 and 6.2). Figure 7.1 shows in space $e - p'$ the *csl* of the CC and MCC models, as well as the best fit *csl*. The figure also shows the undrained path of the experiment Grundy20120709_0. The Figure shows that the *csl* of CC and MCC models did not coincide with the "real" *csl*. One of the reasons for this is that these models assume a unique *ncl*; therefore, Γ will change with p'_o. This is wrong because Γ is a constant of the material.

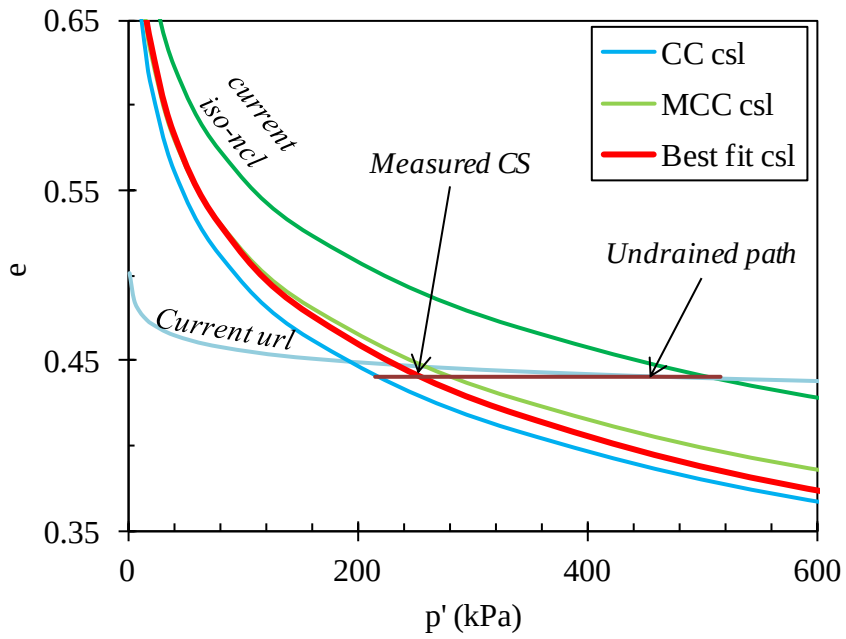

Figure 7.1. Critical state lines of the CC and MCC models and the best fit *csl* for Grundy compacted shale.

7.1.3. Performance of the CamClay and Modified CamClay models

Figures 7.2a to 7.2d show the stress path in q - p' space and the variation of q, Δu, and η with ε_q of the experiment Grundy20120709_0. The figures also show the test simulations using the CC and MCC models. The specimen had R = 1.0. The specimen started with positive increment in Δu, it arrived at the IC (i.e. p'_{min}) with the subsequent development of negative dilatancy until it reached the PS (i.e. η_{max}) before it reached the CS, where the specimen start to soften, as shown in Figures 7.2a and 7.2b. CC model reached the CS at ε_q = 2.94 percent and MCC model at ε_q = 2.68 percent, while the specimen reached the CS at ε_q = 18.75 percent. These differences are due to the fact that the CC and MCC models are unable to simulate negative dilatancy when R is smaller than 2.71 and 2, respectively. This occurs because the flow rule of CC and MCC are referenced to M_{tc} and also because the hardening of the yield loci is coupled with a unique *ncl*, which is not the case with compacted shales. Also, the CC and MCC models cannot soften as the specimen did during the experiment. Figures 7.2a and 7.2b also show that the stress paths of the CC and MCC models were different than the specimen stress path and CC model

underestimate q at the CS and MCC model overestimated q at the CS. Figure 7.2a shows that CC underestimate S_u and MCC overestimate S_u.

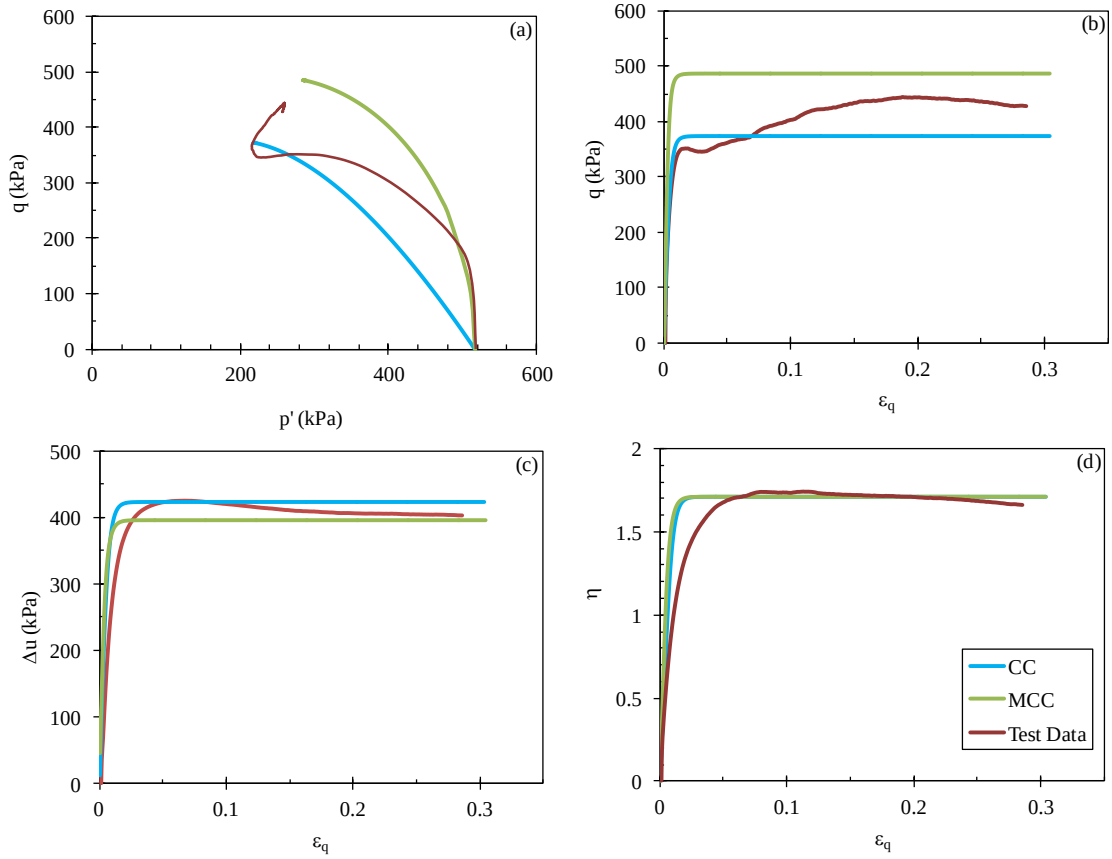

Figure 7.2. Stress paths of experiment Grundy20120709_0, CC, and MCC simulations.

7.1.4. Performance of NorSand model

The NorSand model was used to simulate the CIU triaxial tests of the compacted shales because this model has two characteristics: the flow rule is referenced to M_{tc} and it decouples the yield loci from the *ncl*. The second characteristic is important because it was found that compacted shales present infinite number of *ncl*.

Similar to Figures 7.2a to 7.2d, Figures 7.3a to 7.3d contrast the experiment Grundy20120709_0 with the NorSand simulations for values H equal to 110, 130, and 150.

The simulations showed the principal characteristics of the experiment: positive

increment of Δu, an IC, development of negative dilatancy, a PS, and finally the CS, as shown in Figures 7.3a to 7.2d. For the three simulations, D^p_{min} and the PS were reached at the same time, which is not the case with compacted shales.

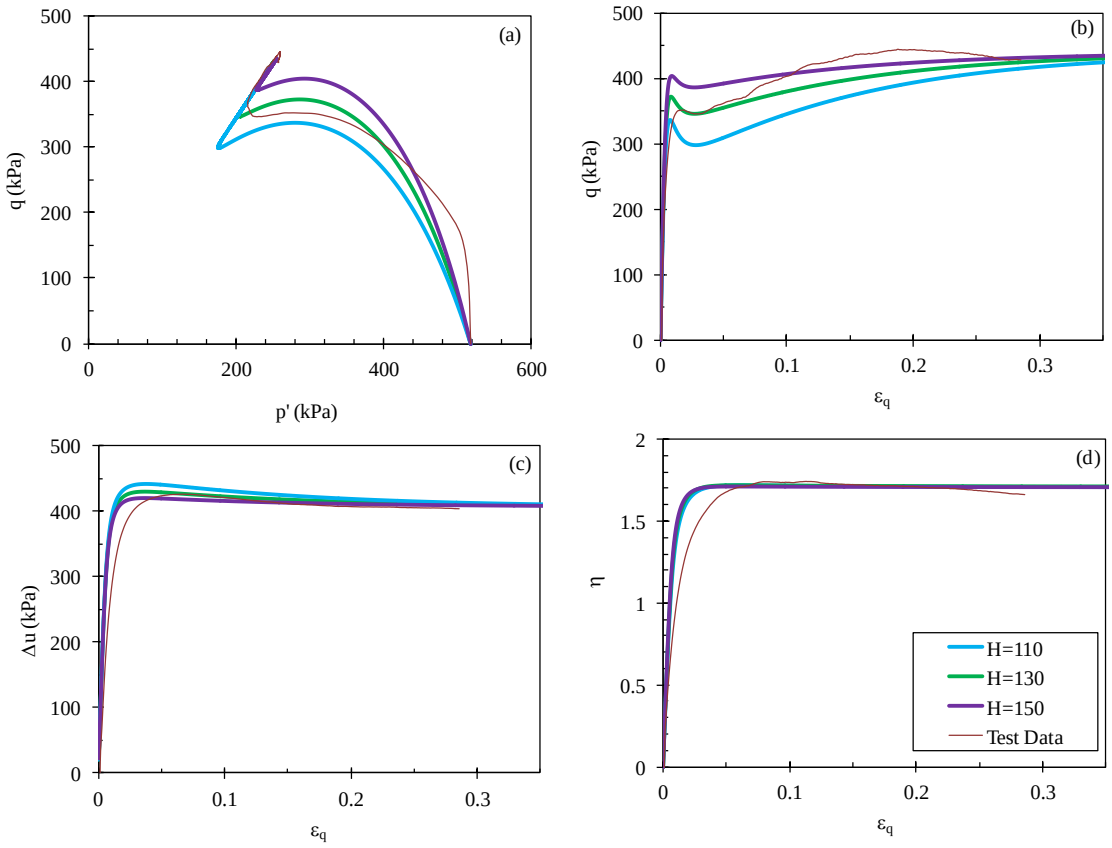

Figure 7.3. Stress paths of experiment Grundy20120709_0 and NorSand.

Figures 7.4a and 7.4b show the variation of M_i and ψ with ε_q for the three simulations. These graphs show how far each simulation had to go in order to reach the CS (i.e. $M_i = M_{tc}$ and $\psi = 0$). As shown in Figure 7.4a and 7.4b, the H=150 simulation reached the CS at ε_q = 29.39 percent. The H = 110 and H = 130 simulations did not reach the CS; however, they eventually will reach the CS, but with extremely high shear strains.

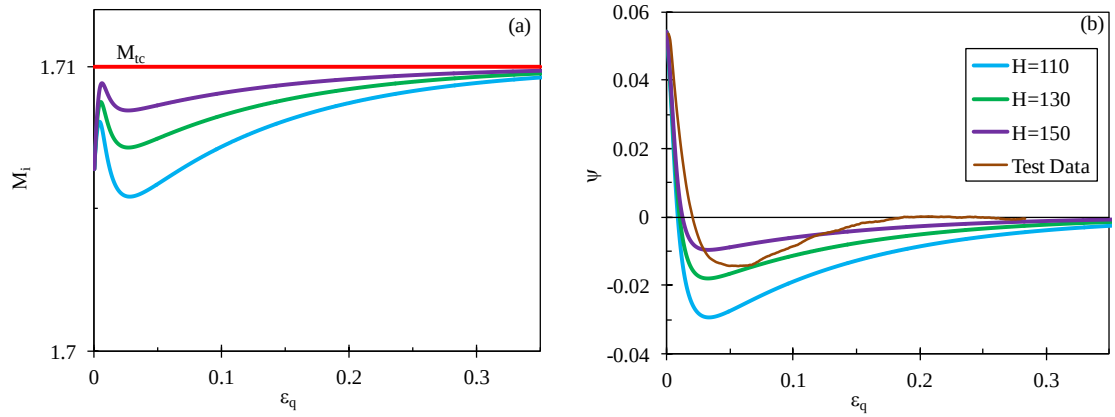

Figure 7.4. (a) Change of the image stress ratio and (b) variation of state parameter with shear strain.

7.2. Type 2 compacted shales

7.2.1. Input parameters

As was shown in Chapter 4, Type 2 compacted shales did not reach the CS. Therefore, all the parameters necessary to define the *csl* in $e - q - p'$ space were estimated by the empirical observationss shown in Chapter 4. ϕ'_{cs} was estimated with Equation [6.3] that relates the LSI durability index with ϕ'_{cs}. M_{tc} was calculated with Equation [2.14].

Figures 7.5a and 7.5b shows that λ_s and Γ were estimated following the trend lines showin in Figures 6.12 and 6.13, respectively.

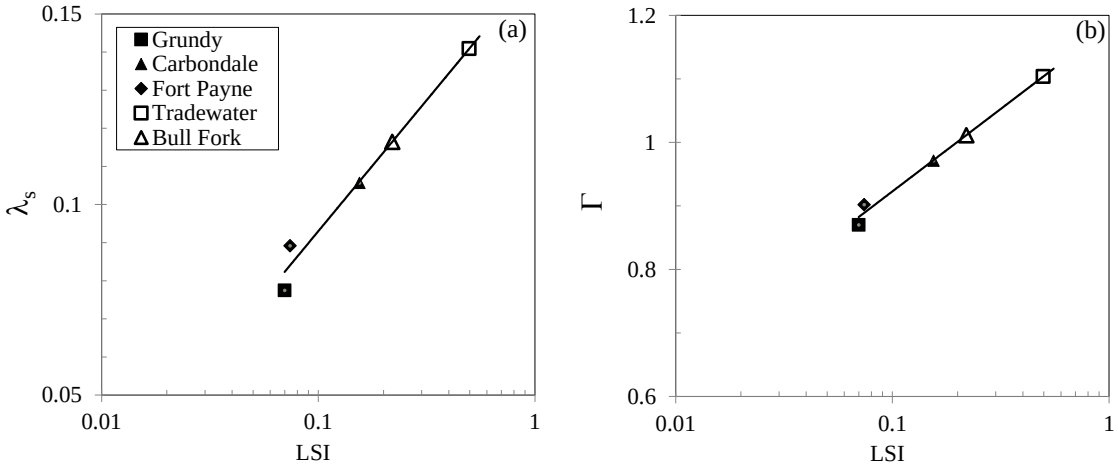

Figure 7.5. λ_s and Γ of experiment BullFork20120713_ 0.

Table 7.2 shows the *csl* parameter of the Type 2 compacted shales Tradewater and Bull Fork.

Table 7.2. Critical state line parameters of Type 2 compacted shales.

Shale	λ_s	Γ	ϕ'_{cs}	M_{tc}
Tradewater	0.1409	1.1037	32.46	1.31
Bull Fork	0.1164	1.0113	34.10	1.38

The performance of the Critical State models on Type 2 compacted shales was evaluated through the results of the CIU triaxial test BullFork20120713_ 0. This test was performed with R = 1.05. ψ_o was unknown because the specimen did not reach the CS. Table 7.3 shows the parameters that were used to do the simulations. Similar to Type 1 compacted shales, λ_{ncl} and κ were evaluated with the results of the isotropic consolidations; ν was assumed to be 0.25, and G_{max} was calculated using Equation [2.20b]. χ and N had the same value as the Type 1 compacted shales.

Table 7.3. Soil parameters of Bull Fork compacted shale.

Parameter	**Value**
λ_{ncl}	0.0639
κ	0.0114
G_{max}	35,472.64 kPa
ν	0.25
M_{tc}	1.38
Γ	1.01
λ_s	0.1164
χ	0.67
N	0.23
H	Trial an error

7.2.2. Performance of the CamClay and Modified CamClay models

Figures 7.6a to 7.6d show the test data of the experiment BullFork20120713_ 0, as well as the CC and MCC simulations in q - p' space and q, Δu, and η with ε_q.

Figures 7.6a and 7.6b show that the CC and MCC underestimated the shear strength. The CC reached the CS at ε_q = 4.37 percent and the MCC at ε_q = 4.09 percent, while the specimen did not reach the CS before ε_q = 30 percent, where the test stopped. The stress

path of the CC was under the stress path of the test data, and the MCC demonstrated a good simulation of the stress path until the IC. Neither simulation was dissimilar to the test data curve in Figure 7.6b. Figures 7.6a, 7.6b, and 7.6c show that the experiment reached the IC with the consecutive development of negative dilatancy and a PS. As was already mentioned, the CC and MCC are unable to model negative dilatancy when R is smaller than 2.71 and 2, respectively. Figure 7.6a shows that CC underestimate S_u and MCC overestimate S_u.

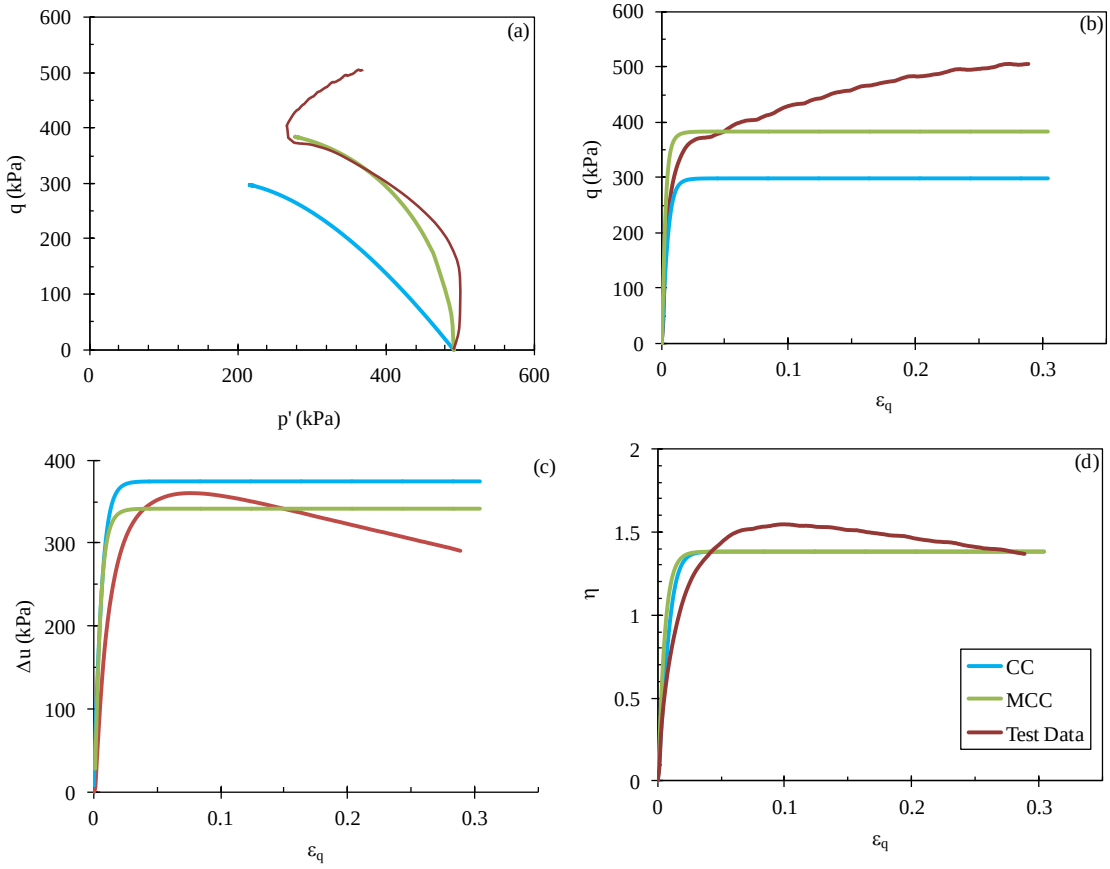

Figure 7.6. Stress paths of experiment BullFork20120713_ 0 and the CC and MCC models.

7.2.3. Performance of NorSand model

Elastic behavior was simulated in the same way as the CC and MCC models. Figures 7.7a to 7.7d show the test data of the BullFork20120713_ 0 experiment, as well as the simulation of the NorSand for H = 100, 125, and 150. The three simulations had an initial

increment in Δu, reached the IC, developed negative dilatancy, reached the PS, and did not reach the CS, as shown in Figures 7.7a to 7.7b. The three simulations represented these characteristics; however, $D^{p}_{\min}$ and the PS were reached at the same time, which is not the case with compacted shales. Figures 7.8a and 7.8b show the variation of M_i and ψ with shear strain. The figures show that the CS was not reached at ε_q = 35 percent, similar to the test data. The sample and simulations eventually will have to reach the CS at high shear strain.

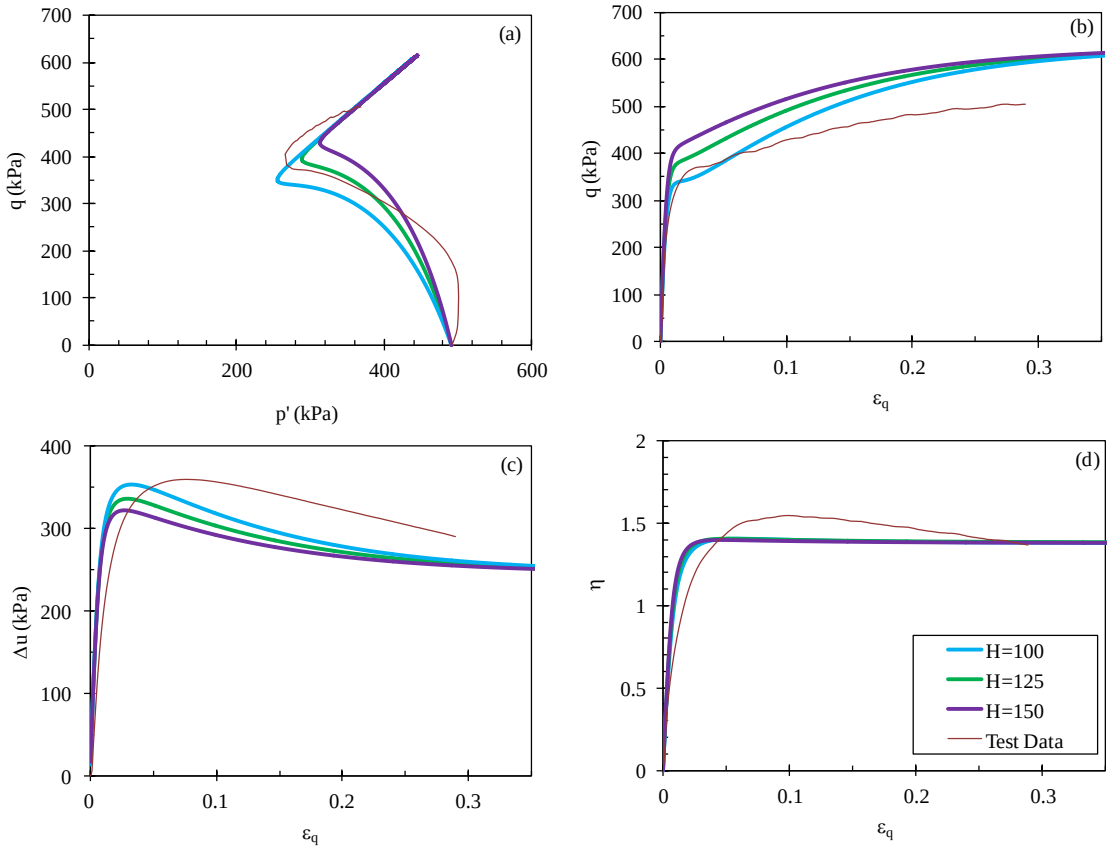

Figure 7.7. Stress paths of experiment BullFork20120713_ 0 and NorSand simulations for several values of H.

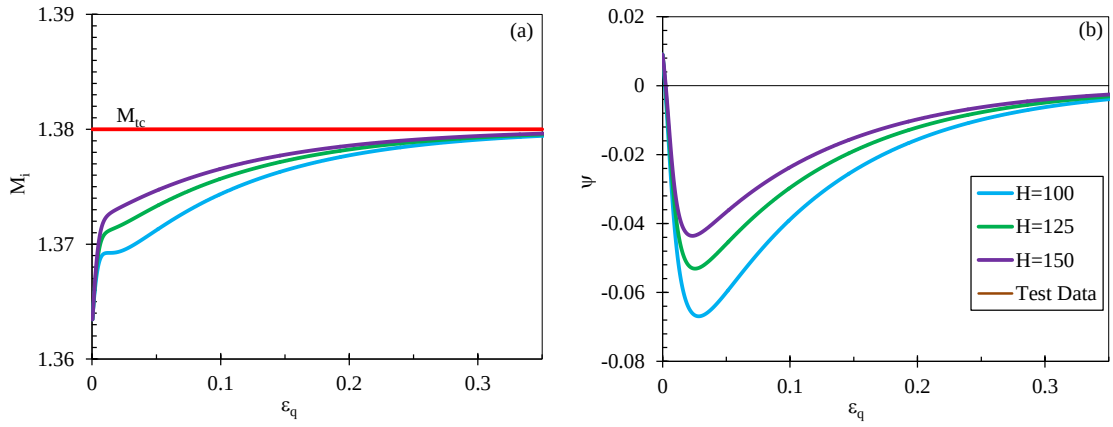

Figure 7.8. (a) Change of the image stress ratio and (b) variation of state parameter with shear strain.

7.3. Reasons the simulations do not model the test data

The differences between the simulations and the test data can be found in the characteristics of the models. Listed below are the sources of differences between simulations and real behavior.

7.3.1. Shear Modulus

The elastic component of the simulations was performed by calculating *K* and *G* with Equations [2.20a] and [2.20b], respectively. These equations made *K* and *G* linear functions of *p'*. Figures 7.9a to 7.9d show the variation of the K' and G with ε_q in a semilog scale for Grundy and Bull Fork compacted shales, respectively. The CC simulations have the form of the Modulus Reduction Curve, where *K* and *G* degrade with the increase in shear strain.

The CC simulations started with the modulus having maximum values, K_{max} and G_{max}, and degraded with the evolution of the undrained shear. When CS was reached, *K* and *G* became constant until the simulation was finished. However, the experiments displayed different behavior. The specimen showed reduction of K and G during the compression or decreasing of mean stress. When the specimen reached the IC, the specimen started to expand or increase the mean stress due to the fact that K and G are functions of *p'*; then, the specimen became more rigid. Also, for a given shear strain, the simulations had lower

K and *G* than the test data.

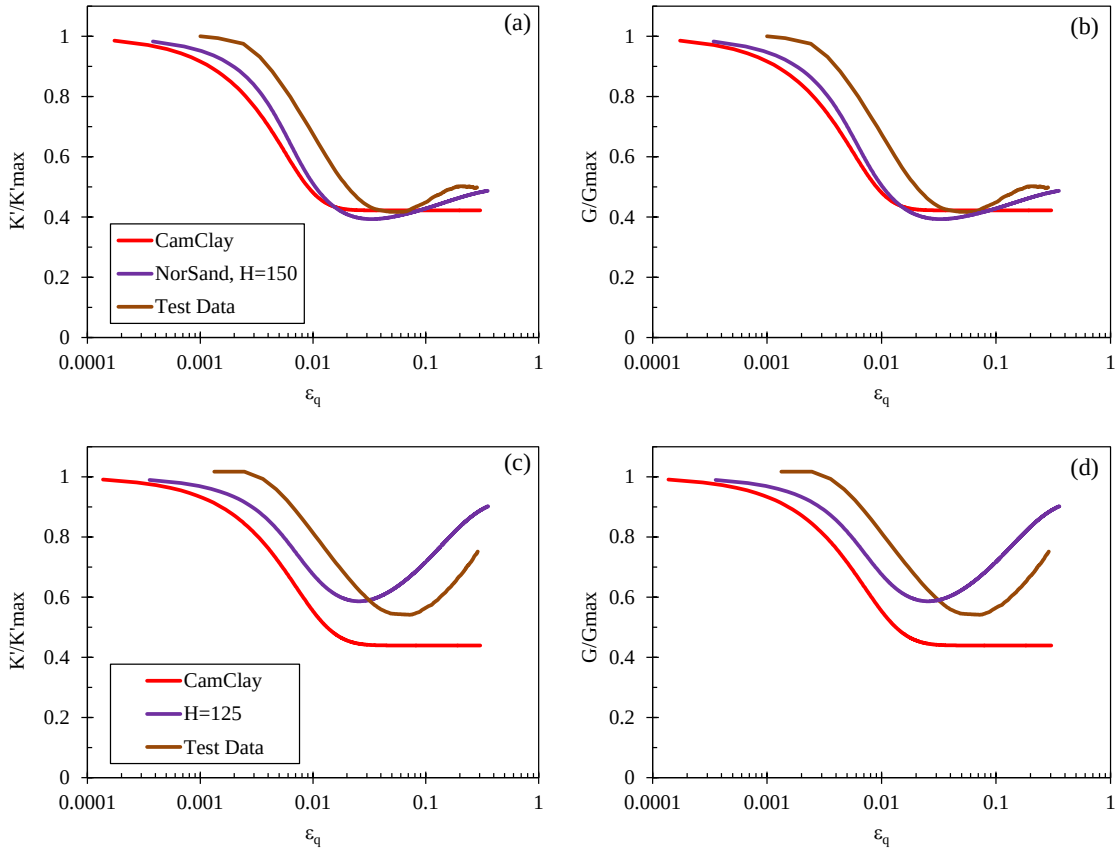

Figure 7.9. Grundy: variation of the (a) bulk modulus and (b) shear modulus with shear strain. Bull Fork: variation of the (c) bulk modulus and (d) shear modulus with shear strain.

7.3.2. Flow Rule

Figures 7.10 and 7.11 show the stress – dilatancy path of the experiments Grundy20120709_0 and BullFork20120713_ 0, respectively. The figures also show the stress – dilatancy paths of the CC, MCC, and NorSand simulations. Figures 7.10b and 7.11b show zooms of these paths in the area where the shear goes from the IC to the CS. It can be observed in the figures that the experiment had a path with a higher slope than the models, and the CC and MCC models did not reach η_{max}. The flow rule for compacted shales has to be changed in order to describe the stress – dilatancy paths shown in the figures. These changes will be discussed in Chapter 8.

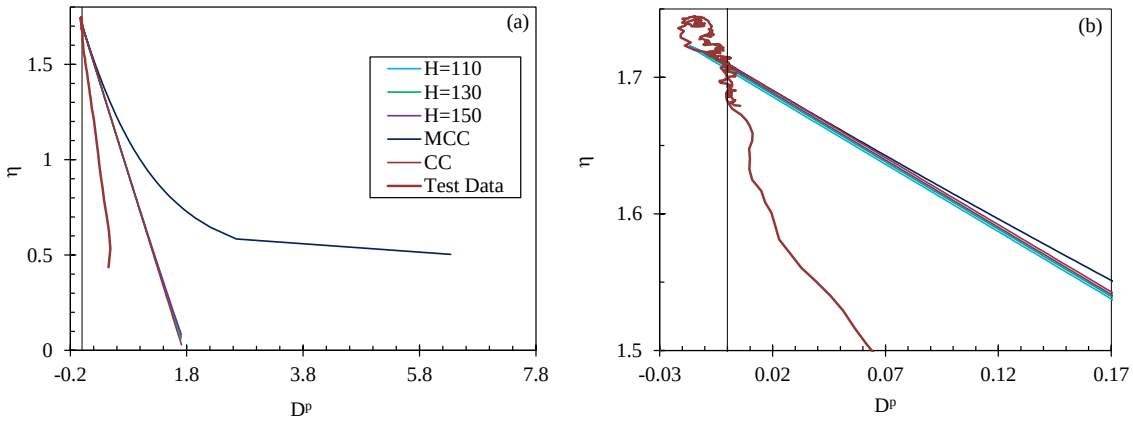

Figure 7.10. Stress – dilatancy path for CC, MCC, and NorSand simulations in comparison with the test data of Grundy20120709_0.

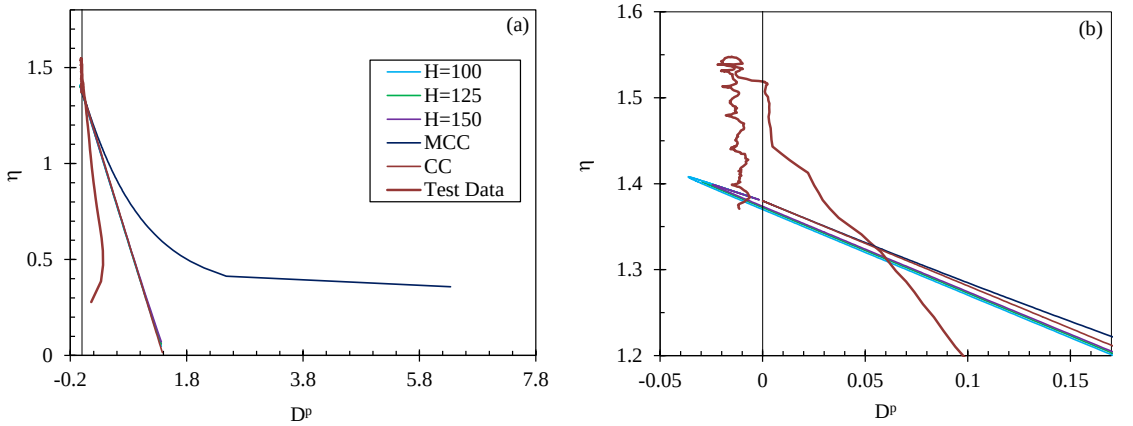

Figure 7.11. Stress – dilatancy path for CC, MCC, and NorSand simulations in comparison with the test data of BullFork20120713_ 0.

7.3.3. Hardening Rule

For NorSand, the hardening rule depends on the flow rule. Therefore, the shape of the yield loci and how it evolves with the shear are affected by the flow rule. Finally, H depends on the fabric and ψ_o. Additional research has to be done in order to gain a better understanding of the parameter H.

CHAPTER 8

8. Framework for modifications to NorSand constitutive model for compacted shales in Triaxial Compression

This chapter is divided into three sections. The first section analyzes the stress – dilatancy path of compacted shales and the implications in the shape that a flow rule of compacted shales should have. The section also explores the influence of the mineralogical content and index properties on the stress – dilatancy behavior. The second section presents a modification in the NorSand flow rule and how this modification changes the plastic potential, yield loci, and hardening rule. Finally the third section shows the simulations.

8.1. Stress-dilatancy relationship

As was shown in the previous chapter, Figures 7.11 and 7.12 demonstrated that the CC, MCC, and NorSand models did not follow the same stress-dilatancy path of Grundy120709_0 (a Type 1 compacted shale) and BullFork20120713_ 0 (a Type 2 compacted shale) experiments. Following is present an analysis of the stress – dilatancy path of Grundy compacted shales. The assumptions of the analysis are:

- Axisymmetric condition of stresses and strains
- Isotropic material
- Specimen is uniform and uniformly strained
- The shear modulus is $G = \frac{3(1-2\nu)}{2(1+\nu)} \frac{1+e}{\kappa} p'$

8.1.1. Stress-dilatancy path

The flow rule is a relationship that relates the change of the increment of plastic strains (i.e. dilatancy) with the change of stresses (i.e. stress ratio) as shear occurs. The form of this relationship for compacted shales was explored by analyzing two experiments with $\psi_o > 0$ and $\psi_o < 0$. The experiments were Grundy120709_0 with $\psi_o = 0.054$ and Grundy130425_0 with $\psi_o = -0.027$. Both specimens were soaked less than 1 day. In order

to calculate D^p for each point of the CIU triaxial tests, Equation [2.10] was rewritten incrementally as:

$$D^p = \frac{\Delta\varepsilon_p^p}{\Delta\varepsilon_q^p} \qquad [8.1]$$

The total volumetric strain in the CIU triaxial tests is zero; therefore, the plastic volumetric strain is equal to the elastic volumetric strain (Equation [2.22]). Consequently, from Equation [2.19a], the increment in plastic volumetric strain is:

$$\Delta\varepsilon_p^p = \frac{-\kappa}{1+e}\frac{\Delta p'}{p'} \qquad [8.2]$$

There is a complete isotropic consolidation test for each compacted shale with $\psi_o > 0$ such that κ was known for each particular specimen. On the other hand, the CIU triaxial tests were strain-controlled; therefore, the total shear strain was known. Hence, from Equation [2.19b] the increment in the plastic shear strain is:

$$\Delta\varepsilon_q^p = \Delta\varepsilon_q - \frac{\Delta q}{3G} \qquad [8.3]$$

where G is calculated using Equation [2.20b] assuming $\nu = 0.25$.

Figure 8.1a shows the stress-dilatancy path of two triaxial tests of Erka Sand by Jefferies and Been (2006). One test was performed on loose sand (i.e. $\psi_o = 0.067$) and the other on dense sand (i.e. $\psi_o = -0.18$). Figure 8.1b shows the stress-dilatancy paths of the two triaxial tests on Grundy compacted shale. The part of the curves at low η are not considered in the analysis because it is attributed to the rupture of asperities (Nova and Wood, 19790) and effects of initial fabric (Jefferies and Been, 2006). In Figure 8.1a it is observed that the loose sand compressed over the entire shear following a path with slope -1:1 until it reached the CS condition. The dense sand compressed in the first part of the test until it reached the IC where:

$$D^p = 0, \quad \dot{D}^p \neq 0, \quad \eta = M_i \qquad [8.4]$$

After the IC, and with an increase of η, the specimen expanded or "dilated" (i.e. $D^p < 0$) until it reached the PS condition at:

$$\eta = \eta_{max} \quad [8.5]$$

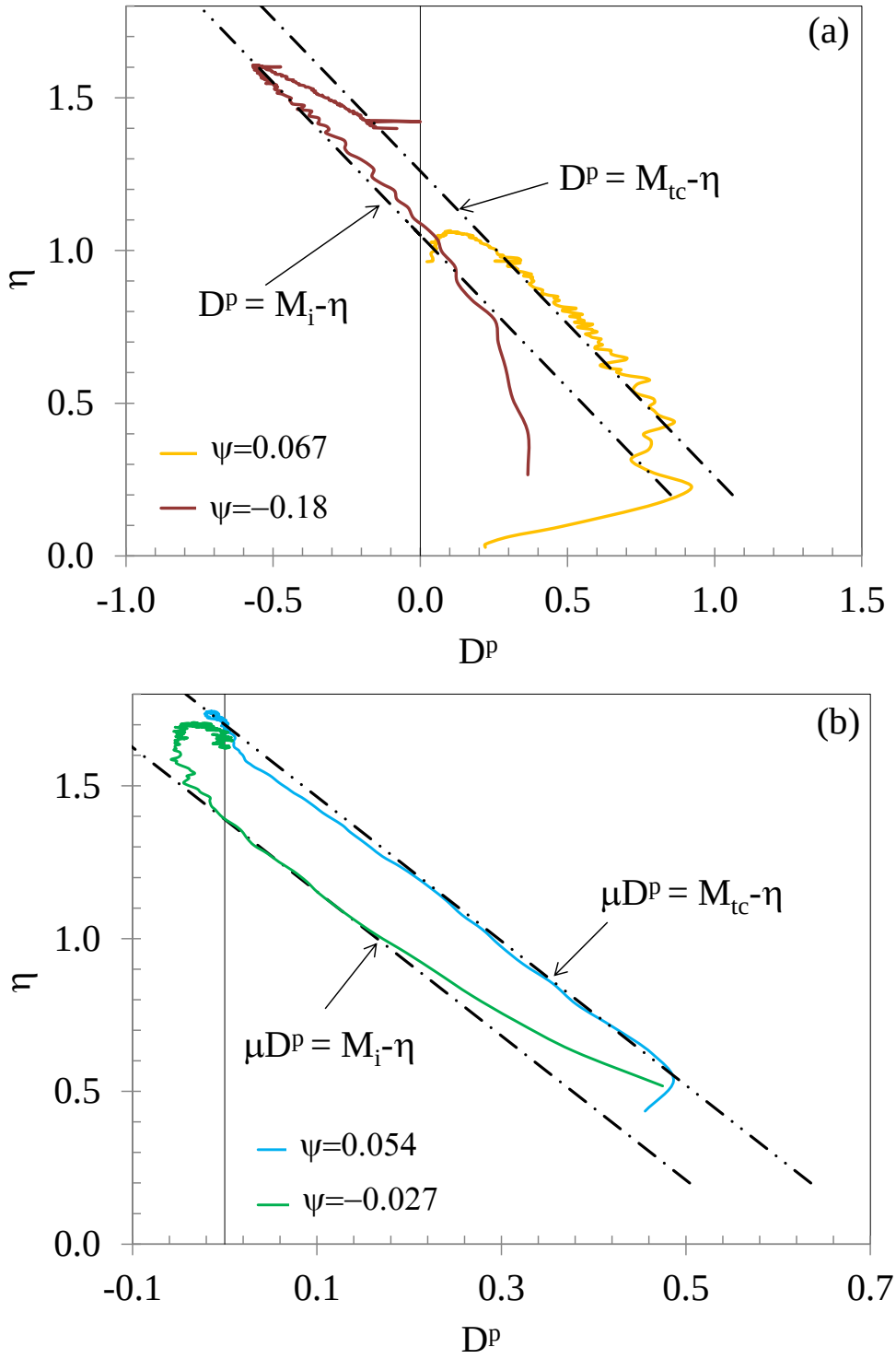

Figure 8.1. Stress–dilatancy paths of triaxial test of (a) Erka Sand by Jefferies and Been (2006) and (b) Grundy compacted shale.

In Figure 8.1a it is observed that the PS was reached at the same time as $D^p_{\min}$. With additional shear, the specimen suffered a decrease of η, going to the CS condition:

$$D^p = 0,\ \dot{D}^p = 0 \rightarrow \eta = M_{tc}, \qquad [8.6]$$

following the first and second axioms of the CS.

In a similar way, Figure 8.1b shows that both compacted shales ($\psi_o = 0.054$ and $\psi_o = -0.027$) compressed over the shear following two parallel paths with slope -μ:1. These paths continued until they reached the IC given in Equation [8.4]. With additional shear, they dilated until they reached a condition where:

$$D^p = D^p_{\min} \qquad [8.7]$$

Additional shear was required to reach the PS (Equation [8.5]), as shown in Figure 8.1b. After the PS, the compacted shale specimens decrease in η, going to the CS.

All the Type 1 compacted shales softened after they reached the CS, as shown in Figures 5.32 and 8.1b. Erka Sand shown in Figure 8.1a and all the Type 2 compacted shales did not reach the CS during the experiments; therefore, it was not possible to observe softening. Appendix J shows the stress – dilatancy paths of the five compacted shales.

8.1.2. Flow rule for compacted shales

Figure 8.1a shows that the stress-dilatancy path of Erka sand has the form of the NorSand flow rule:

$$D^p = M_i - \eta \qquad [2.38]$$

The stress-dilatancy path shown in Figure 8.1b indicates that compacted shales have the following flow rule:

$$D^p = \frac{M_i - \eta}{\mu} \qquad [8.8]$$

where μ is the slope of the stress-dilatancy path and μ is assumed to be a property of the material such that when it is one, Equation [8.8] converges to the NorSand flow rule shown in Equation [2.38].

This flow rule is a Nova Type flow rule similar to the original NorSand model by Jefferies (1993) with the difference that in Equation [8.8] the parameter M is not a true material property but is an image of M_{tc}, M_i. Table 8.1 shows the average μ values of the compacted shales of this study.

Table 8.1. Values of μ.

Shale	μ
Grundy	2.4
Carbondale	2.5
Fort Payne	3.4
Tradewater	2.0
Bull Fork	3.0

This flow rule for compacted shales implies that the work – energy equilibrium is:

$$q\dot{\varepsilon}_q^p + p'\dot{\varepsilon}_p^p = M_{tc} \mid \dot{\varepsilon}_q^p \mid + \mathrm{P}p' \mid \dot{\varepsilon}_p^p \mid \qquad [8.9]$$

where μ = 1 – P. The left part of equation represents only the plastic work because the elastic work is recoverable. The right part of the equation represents the energy dissipated throgh friction ($M_{tc} \mid \dot{\varepsilon}_q^p \mid$). The additional portion of energy $\mathrm{P}p' \mid \dot{\varepsilon}_p^p \mid$ is interpretated as the energy required to provide apparent cohesion to the compacted shale after the triaxial test is finished (Collins, 2005). The absolute value in the strain component of $\mathrm{P}p' \mid \dot{\varepsilon}_p^p \mid$ is due to P is less than 1, as can be deduced from Table 8.1. This interpretation of P can be observed in the fact that the test started with a specimen with characteristics of sand and finish with a well formed specimen with apparent cohesion, as shown in Figure 5.18.

8.1.3. Influence of mineralogy and index properties in μ

As was previously discussed, the (Ch+I)/K ratio can be used as a parameter to describe the characteristics of crushed shales: an increase in (Ch+I)/K implies an increase in A_c because typically chlorite and illite have a higher PI than kaolinite. Figures 8.2a to 8.2d show the variation of μ with (Ch+I)/K, fine size quartz, A_c, and S_{jar}. The high R^2 of the graphs demonstrates that much of the variability of μ is explained by the mineralogical characteristics (Ch+I)/K and fine size quartz, and by A_c. This relationship has two

complementary interpretations. The first one is that the form of the flow rule is a property of the material, which also affects the form of the plastic potential and the yield loci. The second interpretation is that shales with high (Ch+I)/K, low fine size quartz, and low A_c had higher μ; therefore, the dilatancy due to the increment of the shear stress is lower. Compacted shales with lower μ dilate more under a given increment in the shear. The relation between μ and durability was explored in Figure 8.2d, but a clear trend was not observed.

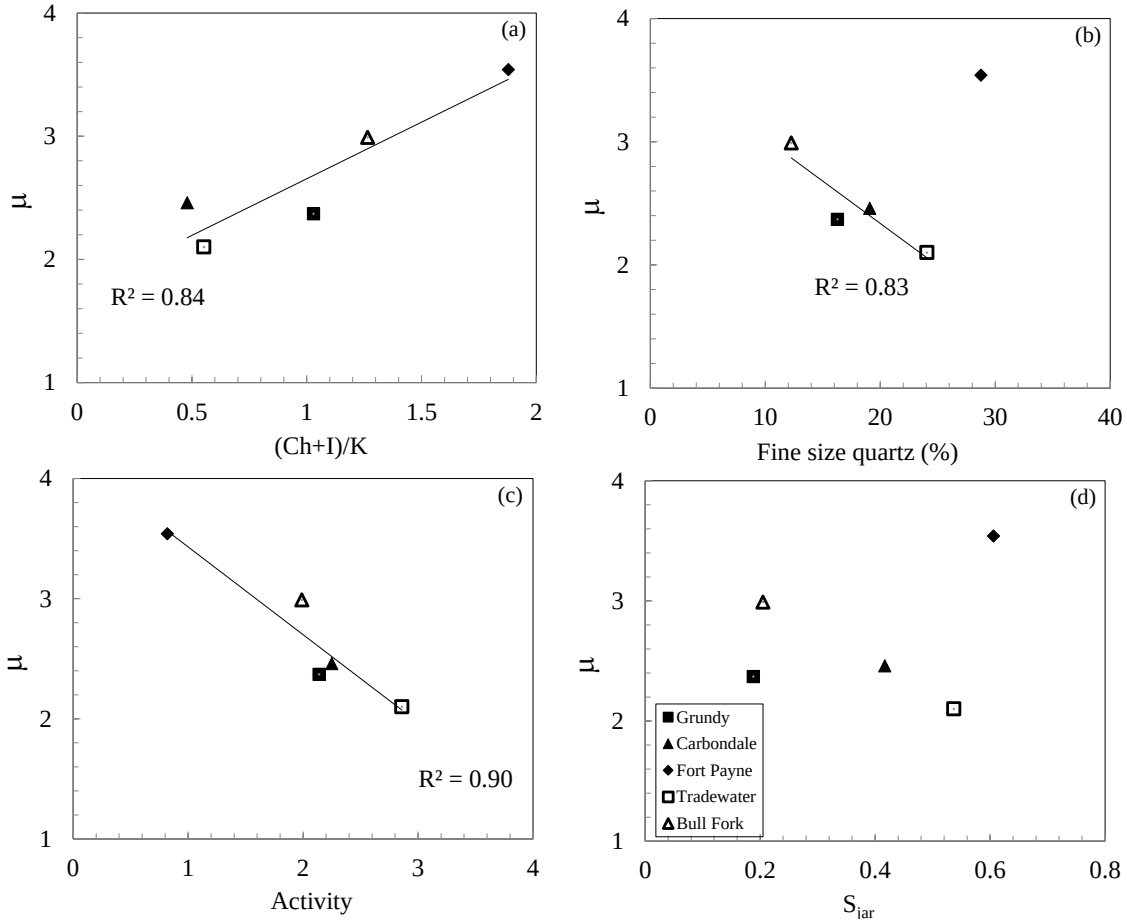

Figure 8.2. Variation of μ with (a) (Ch+I)/K ratio, (b) fine size quartz, (c) activity, and (d) S_{jar}.

Finally, Table 8.1 shows that μ was greater than 1 for all compacted shales. Therefore, it is assumed that $\mu > 1$. When $\mu = 1$, the flow rule converges to NorSand and CC flow rules. Understand the convergence to CC is easier because it is expected that clays have high A_c. However, A_c is a parameter that does not make sense for application to clean sands.

8.2. Equations of the modified model

For this research it was assumed that the elastic behavior described by CS theory is accurate. Regarding the plastic behavior, the change in the form of the flow rule was necessary in order to be coherent with the actual behavior that the compacted shales showed.

8.2.1. Flow rule

Equation [8.8] shows the form of the more appropriate flow rule for compacted shales. Figure 8.4 shows the simulation of the stress-dilatancy path for different values of μ using the flow rule of Equation [8.8] and assuming M_i = 1.7. Figure 8.4 shows that when μ = 1, the stress-dilatancy path converges to the NorSand flow rule. The figure shows that when μ = 1 (NorSand), the change in plastic dilatancy with the evolution of the shear is higher than the plastic dilatancy when μ > 1. Because the compacted shales of this study presented μ > 1, it is concluded that the dilatancy was much smaller than the dilatancy that a sand can present under the same shear conditions.

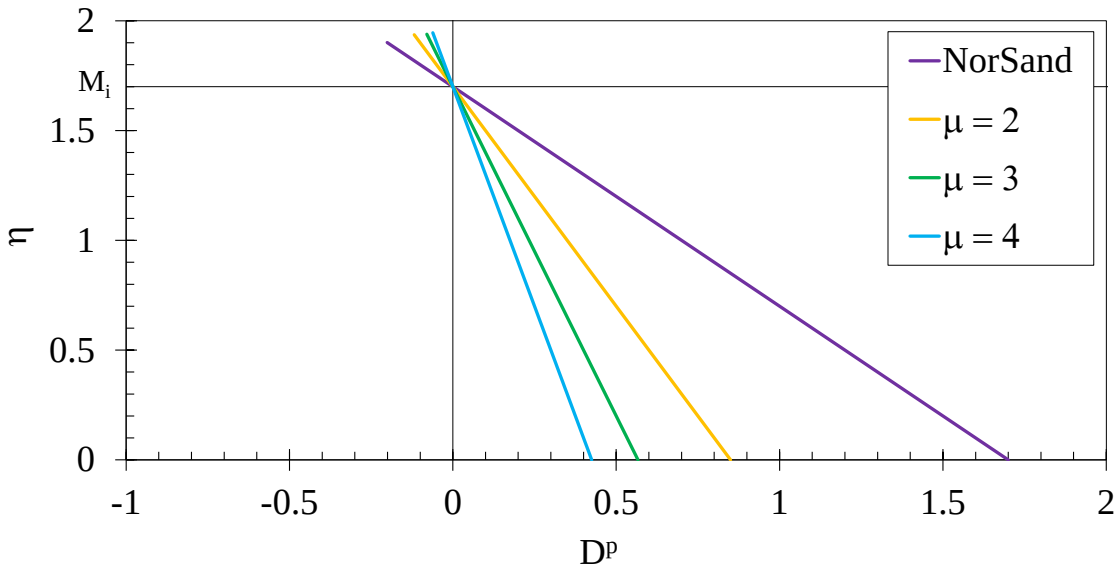

Figure 8.3. Flow rule of Equation [8.8] for different values of μ.

8.2.2. Plastic potential and yield locus

Assuming that for compacted shales the flow rule is associated (i.e. the postulate of

normality applies), the equation that controls the change of stresses during the shear is:

$$\frac{1}{\mu}\frac{q}{p'}-\frac{\dot{q}}{\dot{p}'}=\frac{M_i}{\mu} \qquad [8.10]$$

Solving Equation 8.10 with the border condition $\eta = M_i$ when $p' = p'_i$, the plastic potential - yield locus is:

$$g = f = \eta - \frac{M_i}{1-\mu}\left[1-\mu\left(\frac{p'}{p'_i}\right)^{\frac{1-\mu}{\mu}}\right]=0 \qquad \text{if } \mu > 1 \qquad [8.11a]$$

$$g = f = \eta - M_i\left(1-\ln\left(\frac{p'}{p'_i}\right)\right)=0 \qquad \text{if } \mu = 1 \qquad [8.11b]$$

8.2.2.1. Stress ratio at image condition

Replacing Equation [2.41] and [8.8], the stress ratio at IC is:

$$M_i = M_{tc} + \left(\mu - (1-N)\right)D^p_{\min} \qquad [8.12]$$

From equation [2.42]

$$M_i = M_{tc} + \left(\mu - (1-N)\right)\chi_{tc}\psi_i \qquad [8.13]$$

Assuming a symmetric behavior between $\psi_i < 0$ and $\psi_i > 0$:

$$M_i = M_{tc} - \left(\mu - (1-N)\right)\chi_{tc}\,|\psi_i| \qquad [8.14]$$

When $\mu = 1$, then:

$$M_i = M_{tc} - N\chi_{tc}\,|\psi_i| \qquad [2.44]$$

Which is the expression for the stress ratio at IC of NorSand. Equation [8.14] shows that M_i depends on ψ_i.

8.2.2.2. Limit of the internal cap

The limit of the internal cap for each yield locus is given by $D^p_{\min}$ at any p'_i. As shown in Figure [6.14], the stress ratio at $D^p_{\min}$ was smaller than $\eta_{\max}$, because they did not occur

at the same time. Therefore, solving η_{max} from Equation [2.41]:

$$\eta_{max} = M_{tc} - (1-N)D_{min}^{p} \qquad [8.15]$$

Replacing [8.15] in [8.11a] and [8.11b] when $\eta = \eta_{max}$

$$\left(\frac{p'_i}{p'}\right)_{max} = \left[\frac{1}{\mu} - \frac{(1-\mu)}{\mu}\left(\frac{M_{tc} - (1-N)D_{min}^{p}}{M_i}\right)\right]^{\frac{-\mu}{1-\mu}} \quad \text{if } \mu > 1 \qquad [8.16a]$$

$$\left(\frac{p'_i}{p'}\right)_{max} = \exp\left(\frac{M_{tc} - (1-N)D_{min}^{p}}{M_i} - 1\right) \quad \text{if } \mu = 1 \qquad [8.16b]$$

Replacing Equation [2.42] and [8.14] in [8.16a] and [8.16b], the limit of the internal cap is:

$$\left(\frac{p'_i}{p'}\right)_{max} = \left[\frac{1}{\mu} - \frac{(1-\mu)}{\mu}\left(\frac{M_{tc} - (1-N)\chi_{tc}\psi_i}{M_{tc} - (\mu - (1-N))\chi_{tc}|\psi_i|}\right)\right]^{\frac{-\mu}{1-\mu}} \quad \text{if } \mu > 1 \qquad [8.17a]$$

$$\left(\frac{p'_i}{p'}\right)_{max} = \exp\left(\frac{M_{tc} - (1-N)\chi_{tc}\psi_i}{M_{tc} - (\mu - (1-N))\chi_{tc}|\psi_i|} - 1\right) \quad \text{if } \mu = 1 \qquad [8.17b]$$

Equation [8.17b] is different from the NorSand internal cap (Equation [2.43]) because the stress ratio at D_{min}^{p} is the same as η_{max} for NorSand model. Due to the second Axiom, when the CS is reached, $\psi_i = 0$ and therefore $M_i = M_{tc}$, then:

$$\left(\frac{p'_i}{p'}\right)_{max} = 1 \qquad [8.17c]$$

This means that the internal cap at CS is limited by the mean stress at CS, fulfilling the first axiom that forces the model to reach a constant mean stress. Equation [8.17c] is important because is impossible to have expansion or compression indefinitely.

Figures 8.5a and 8.5b show the yield loci of Equation [8.11] for different values of μ, given $\psi_i = 0.1$ and $M_i = 1.85$ and $\psi_i = -0.1$ and $M_i = 1.85$, respectively.

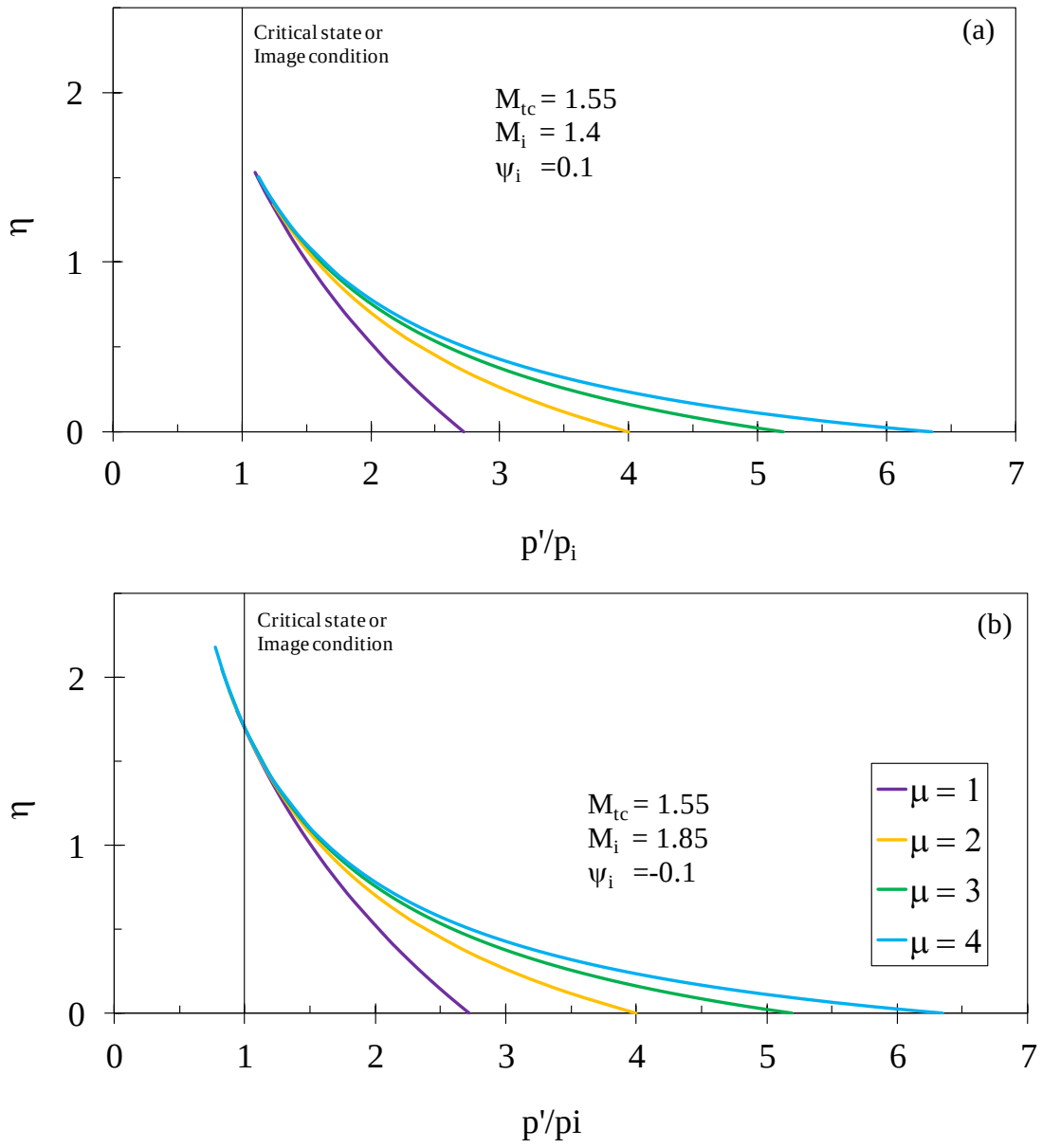

Figure 8.4. Family of yield loci as a function of μ.

When μ is higher, the curvature of the yield loci is higher. When $\psi_i > 0$, $M_i < M_{tc}$ and $\left(\frac{p'_i}{p'}\right)_{max} > 1$. Therefore, the yield locus contract toward IC or CS, the specimen has not crossed the IC and has positive dilatancy. In this case, if the shear increases, the soil either can cross the IC or can arrive at the CS. When $\psi_i < 0$, $M_i > M_{tc}$ and $\left(\frac{p'_i}{p'}\right)_{max} < 1$.

Therefore, the yield locus expand toward the CS and the specimen has negative dilatancy.

Figure 8.5 shows the same yield loci as Figure 8.4 but in the space q/p'_y vs. p'/p'_y. Figure 8.5 shows that when $\mu = 1$ (i.e. NorSand), the yield locus is bigger in comparison to the yield locus when $\mu = 4$. Therefore, the NorSand model allows more elastic deformation than the model with $\mu = 4$.

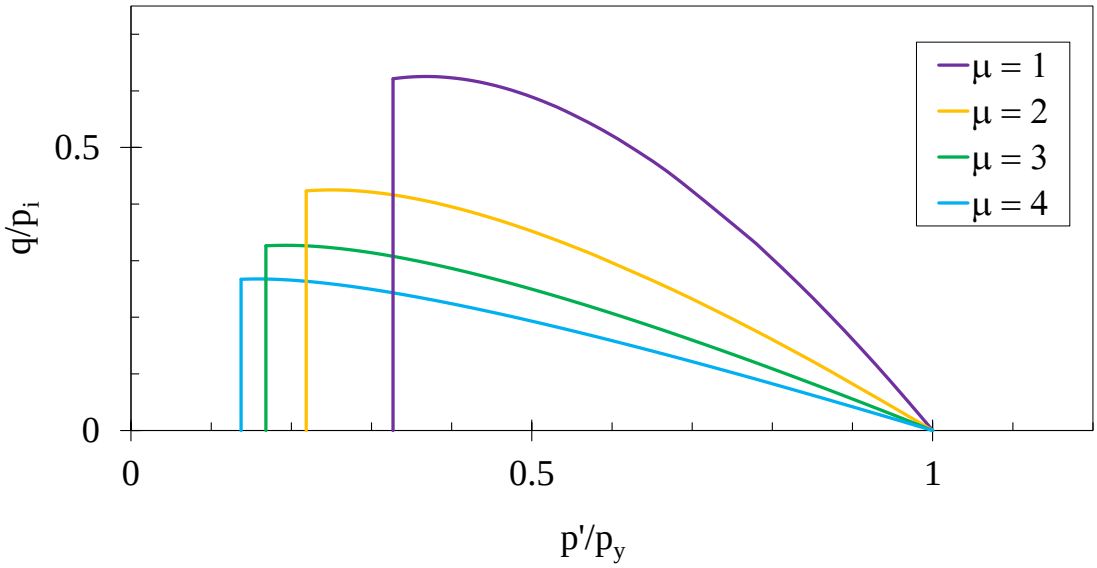

Figure 8.5. Family of yield loci as a function of μ.

8.2.3. Hardening rule

Evidence indicating that the form of the NorSand hardening and softening rules should be modified was not found. NorSand hardens and softens through the change in shear strain following the second axiom of CS, and is a function of the soil fabric through the parameter *H*. Compacted shales cannot harden by the volumetric strain because of the evidence of infinite *ncl*; therefore, hardening and *ncl* are decoupled. It is important to note that the performed experiments in this research were not designed to observe the behavior of the hardening rule and internal cap softening rules. It is necessary to perform additional experiments designed in such a way to permit the evaluation of the performance of the hardening and softening rules of the CS theory.

In this research, the hardening rule and internal cap softening are the same as NorSand:

$$\frac{\dot{p}'_i}{p'_i} = H\left(\frac{p'}{p'_i}\right)^2\left(\left(\frac{p'_i}{p'}\right)_{max} - \frac{p'_i}{p'}\right)\dot{\varepsilon}_q^p \qquad [2.46]$$

and

$$\frac{\dot{p}'_i}{p'} = \frac{H}{2}\,|\,\dot{\varepsilon}_q^p\,| \qquad [2.47]$$

The only change in the hardening rule was due to the new expression of $\left(\frac{p'_i}{p'}\right)_{max}$ given in Equation [8.18].

8.3. Simulations

The simulations were performed through a routine written in Visual Basic based in a routine by Shuttle and Jefferies (2010) download from (http://www.itasca-udm.com/pages/NorsandM.html). Appendix K shows the modified code.

Two simulations are presented: one with ψ_o = 0.054 (Grundy20120709_0), and the other with ψ_o = -0.027 (Grundy20130425_0).

Figures 8.6a to 8.6d show the stress path in q - p' space and the variation of q, Δu, and η with ε_q of the experiment Grundy20120709_0 and the simulation with the new model. The figures show that the new model simulates properly all the characteristics of the experiment, especially the excess of pore pressure, as shown in Figure 8.6c. Figure 8.7a shows a comparison between the stress – dilatancy path of the experiment and the simulation. Figure 8.7b shows a detail of this path at high stress ratio. This figure shows that the stress – dilatancy path is simulated with precision by the new model. Finally, after the IC, the change of q with ε_q is slightly inaccurate, as shown in Figures 8.6a and 8.6b.

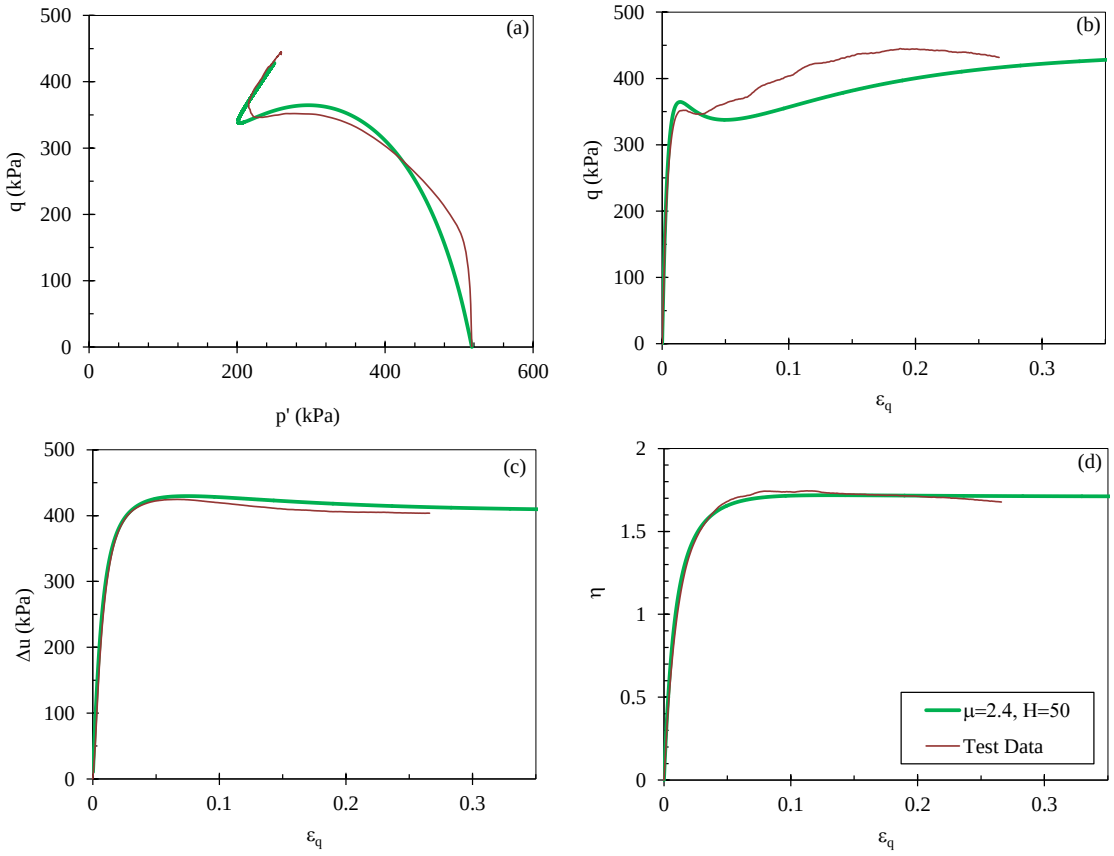

Figure 8.6. Stress path of experiment Grundy20120709_0 and simulation with the new model (R = 1.0 and ψ_o = 0.054).

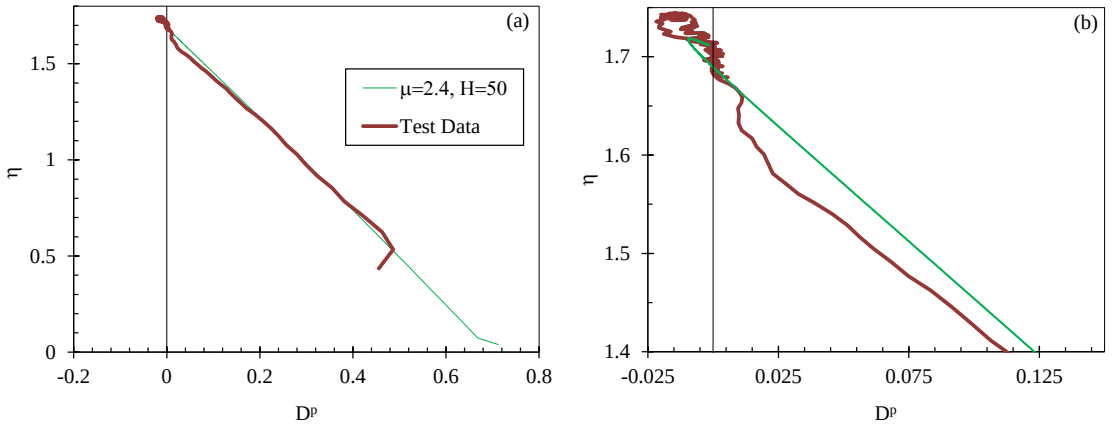

Figure 8.7. Stress – dilatancy path of experiment Grundy20120709_0 and simulation with the new model (R = 1.0 and ψ_o = 0.054).

Figures 8.8a to 8.8d show the stress path in q - p' space and the variation of q, Δu, and η with ε_q of the experiment Grundy20130425_0 and the simulation with the new model.

The figures show that the simulations are similar to the test data with some few

differences. Figure 8.8c that the new model simulates in an accurate way the excess of pore pressure during the first 0.5 percent of the shear strain.

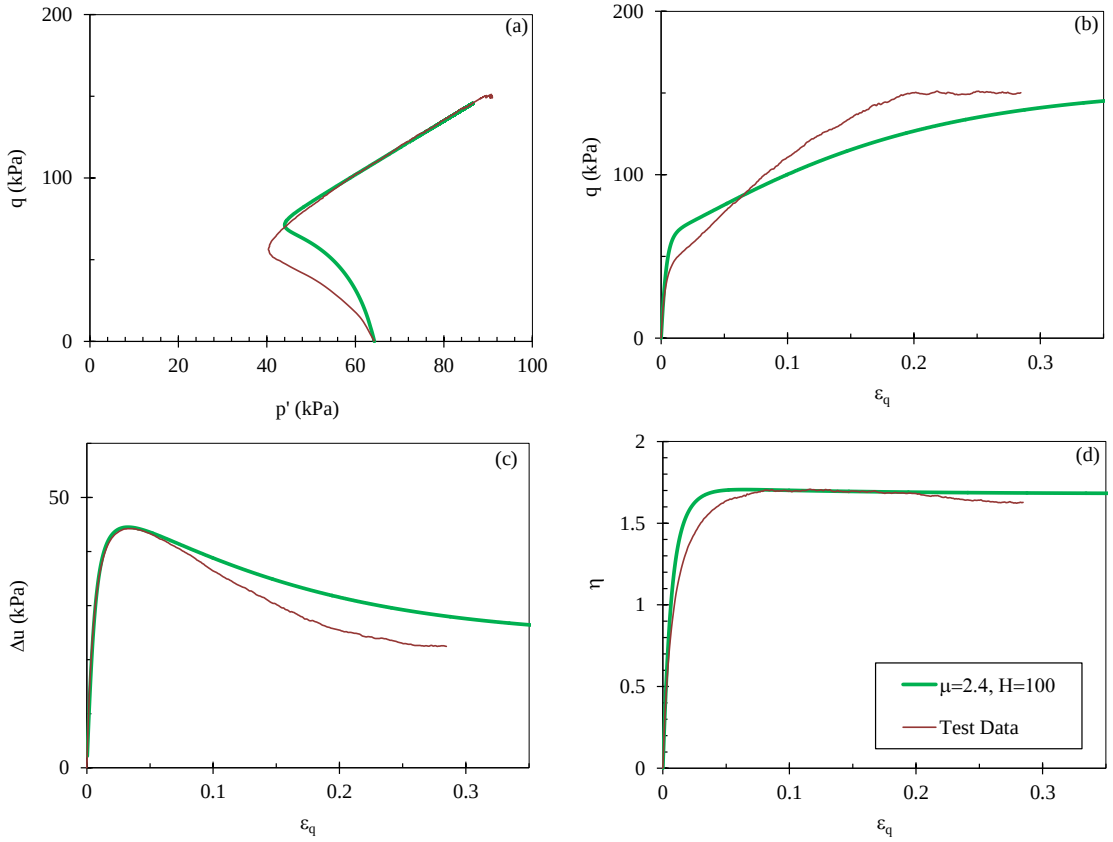

Figure 8.8. Stress path of experiment Grundy20130425_0 and simulation with the new model(R = 1.0 and ψo = -0.027).

The reason why there are some differences between the test data and the simulations when $\psi_o < 0$ must to be found in Figure 8.9. Figure 8.9a shows the stress – dilatancy path of the experiment and the simulation. Figure 8.9b shows in detail these paths at high stress ratio. When $\psi_o < 0$, the stress – dilatancy path of the simulation is parallel to the test data but the model overestimate the stress ratio at IC. This occurred because Equation [8.14] attaches the evolution of the shear to M_{tc}. Additional research has to be done in order to arrive at a better form of Equation [8.14] to do a better simulation of the stress – dilatancy paths when $\psi_o < 0$.

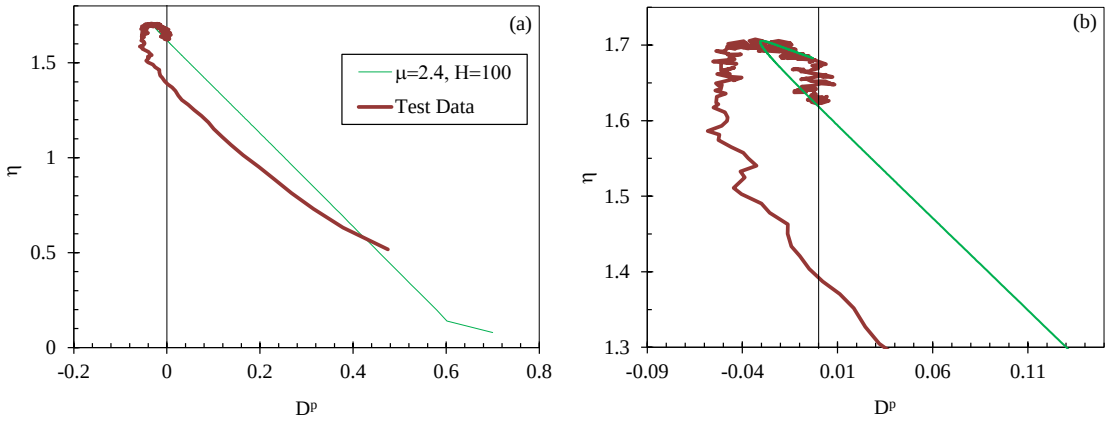

Figure 8.9. Stress – dilatancy path of experiment Grundy20130425_0 and simulation with the new model (R = 1.0 and ψo = 0.054).

.

CHAPTER 9

9. Conclusions

9.1. Novel contribution

The novel contribution of this research is the development of a constitutive model to characterize the behavior of compacted shales, something that had not been attempted before.

- It was found that the flow rule that controls the plastic behavior of compacted shales has the form:

$$D^p = \frac{M_i - \eta}{\mu} \qquad [8.8]$$

where μ is a parameter that correlates with (Ch+I)/K and A_c. When μ = 1, this flow rule converges to the NorSand flow rule. M_i is an operating friction ratio for a given particular yield surface given by:

$$M_i = M_{tc} - \left(\mu - (1-N)\right)\chi_{tc}\,|\psi_i| \qquad [8.14]$$

This is a Nova Type flow rule similar to the original NorSand flow rule by Jefferies (1993) with the difference that for him M was conceived to be a true material property.

- Unlike NorSand model, it was found that N does not have the same interpretation as μ. It was found that $D^p_{\min}$ and $\eta_{\max}$ did not occur at the same time. Here, N is presented as a parameter that describes how far they occurred:

$$(1-N) = \frac{d^p}{D^p{}_{\min}} \qquad [6.11]$$

where d^p is the difference between the stress ratio at CS and PS:

When N = 0, $D^p_{\min}$ and $\eta_{\max}$ occurred at the same time. It was found that N is independent of the state parameter and has an average value of 0.23.

- Assuming an associated flow rule, the plastic potential is the same as the yield loci and have the form:

$$g = f = \eta - \frac{M_i}{1-\mu}\left[1-\mu\left(\frac{p'}{p'_i}\right)^{\frac{1-\mu}{\mu}}\right] = 0 \qquad \text{if } \mu > 1 \qquad [8.11a]$$

$$g = f = \eta - M_i\left(1-\ln\left(\frac{p'}{p'_i}\right)\right) = 0 \qquad \text{if } \mu = 1 \qquad [8.11b]$$

- The limit of the internal cap is:

$$\left(\frac{p'_i}{p'}\right)_{\max} = \left[\frac{1}{\mu} - \frac{(1-\mu)}{\mu}\left(\frac{M_{tc} - (1-N)\chi_{tc}\psi_i}{M_{tc} - (\mu - (1-N))\chi_{tc}\,|\psi_i|}\right)\right]^{\frac{-\mu}{1-\mu}} \text{ if } \mu > 1 \qquad [8.17a]$$

$$\left(\frac{p'_i}{p'}\right)_{\max} = \exp\left(\frac{M_{tc} - (1-N)\chi_{tc}\psi_i}{M_{tc} - (\mu - (1-N))\chi_{tc}\,|\psi_i|} - 1\right) \qquad \text{if } \mu = 1 \qquad [8.17b]$$

where $\chi_{tc} = 0.67$. At the CS the limit of the internal cap is:

$$\left(\frac{p'_i}{p'}\right)_{\max} = 1 \qquad [8.15]$$

- The normailized undrainde shear strength, $\left(S_u / p'_o\right)$ was a function of the state parameter with the form.

$$\frac{S_u}{p'_o} = 0.8\exp(-10.2\psi_o) \qquad [6.2]$$

9.2. Conclusions

- One of the five shales of this study classify as a mudstone, two as calcareous mudstone, and two as Marlstone.
- It was found that (chlorite + illite) have an inverse relationship with kaolinite, in which (chlorite + illite) decrease as kaolinite increases. This is due to the initial mineralogical characteristics of the deposited sediments and the mineralogical transformations during the diagenesis.

- It was found that the ratio (chlorite + illite)/kaolinite and fine size quartz explain the activity of crushed samples of shales. This is due to shales with high content of quartz and low proportion of chlorite and illite have lower clay faction after crushing.
- No clear relationship between consolidation and shear parameters with soaking time was found. This can be due to the fact that tap water was used to perform the CIU triaxial tests and the samples were not soaked enough time. Therefore, dispersion of the clay minerals of the shale particles occurred at such a low rate, that it was not possible to observe the effect of weathering in the mechanical behavior of compacted shales.
- Two different types of behavior were observed. The first type (Type 1 compacted shales) had a convex consolidation curve, which reached the CS during the shear. They were the most durable shales. These shales were Grundy, Carbondale, and Fort Payne. The second type (Type 2 compacted shales) had concave curve, which did not reach the CS. They were the softest shales. These shales were Bull Fork and Tradewater. A concave curve indicates that there is cement that was broken apart after a given p'_y. The samples were well graded sands; therefore, the cement that was broken was the cement of each shale particle.

  The mineralogical content was analyzed in order to find the reason for the difference between these two types of shales. However, differences were not found. Bull Fork was a marlstone with 45 percent calcite and 15 percent dolomite, and there was no evidence of the presence of organic matter. Tradewater was a calcareous mudstone with 4 percent calcite and 12 percent siderite with evidence of the presence of organic matter. It is assumed that Bull Fork is cemented by the carbonate minerals, and it is assumed that the cement in Tradewater is due to the chelation of the organic matter. It is necessary to do additional research in order to observe the influence of mineralogy and fabric in the behavior of compacted shales.
- It was observed that the isotropic consolidation curves did not reach a unique normally consolidated line. Therefore, an infinite number of normally consolidated lines do exist.

- It was necessary to decouple the yield loci from the normally consolidated lines due to the fact that a unique normally consolidated line was not observed.
- Empirical evidence showed that the plastic behavior of compacted shales is controlled by a Nova type flow rule. This flow rule was a function of (Ch+I)/K, fine size quartz content and A_c. This means that the form of the flow rule is a property of the material, which also affects the form of the plastic potential and the yield loci.
- Due to the evidence of the existence of infinite *ncl*, the hardening rule of NorSand is adequate to describe the hardening in compacted shales. However, additional experiments should be designed in such a way that the hardening rule can be evaluated in compacted shales.

9.3. Future research

- It is necessary to carry out theoretical research in order to understand the meaning of m and P, and how much energy is spent to give apparent cohesion to the samples after the triaxial tests finished and the loads are relaxed.
- It is necessary to perform additional experimental research to find if N is a constant or if it depends on other variables such as state, overconsolidation ratio, etc.
- It is necessary to carry out additional experimental research in order to evaluate the performance of the NorSand hardening rule in compacted shales. The hardening constant, H, appears to depend on the initial state and the micro fabric.
- It is necessary to perform consolidated drained triaxial tests in order to evaluate if the shape of the flow rule found in this research is the same under drained conditions.
- The code used to do the simulations has to be extended to be applied under other conditions such as overconsolidation ratios greater than 1 and drained conditions.
- It is necessary to perform bender element tests in order to study the elastic behavior of compacted shales.

APPENDIX A

MINERALOGY TESTS

PRETREATMENT OF SHALES SAMPLES

Dissolution of carbonates, pyrite, iron oxides, organic matter:

Carbonates, pyrite, iron oxides, and organic matter cement and aggregate clay minerals and prevent their dispersion. Therefore, these minerals should be removed in order to facilitate fractionation. These pretreatment was performed following the procedure given by Jackson (1969) and Kunze and Dixon (1985). Air-dried crushed samples passed through a No. 200 (fine-size) were used to perform the experiments. Figure A1 show this samples.

Figure A1. Air-dried crushed samples passed through No. 200 sieve.

Carbonates removal

An initial evaluation of the presence of carbonates was performed pouring some drops of hydrochloric acid (HCl) over the samples. The hydrochloric acid reacted with carbonates producing carbon dioxide (CO_2), water (H_2O) and calcium chloride ($CaCl_2$). Figure A2 shows that the Carbondale shale did not react with hydrochloric acid, therefore this shale does not have carbonates. The figure also shows that Grundy shale reacted with hydrochloric acid, and therefore it has carbonates.

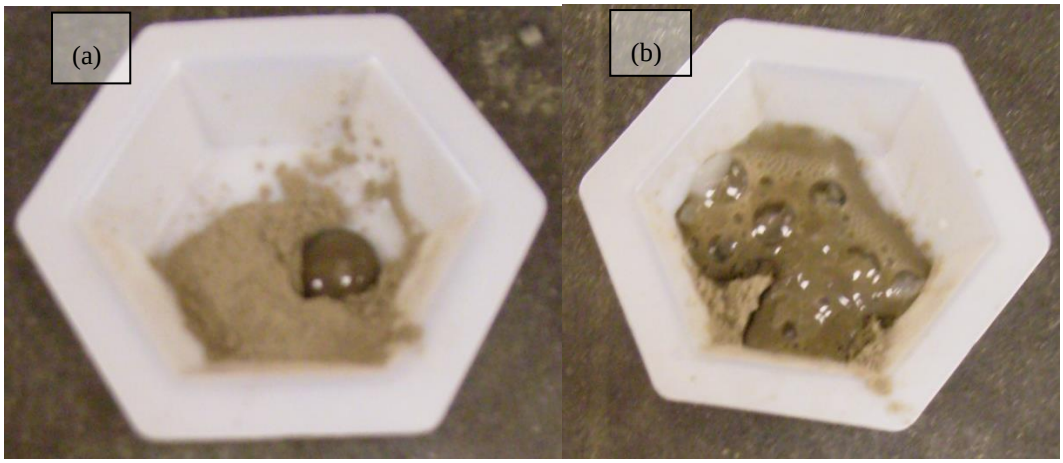

Figure A2. Reaction to HCl; (a) Carbondale and (b) Grundy.

Carbonates were dissolved using a pH 5N sodium acetate (NaOAc) buffer solution because it dissolves the carbonates and prevents pH drops. It is used a buffer solution because acids cause clay dissolution. During all the pretreatment tests, multivalent cations such as Ca^{2+} and Mg^{2+} were replaced by Na^{+} because multivalent cations cause flocculation and Na^{+} tends to cause dispersion (Reeves et al., 2009). It was observed that during the test some samples presented a dark brown or black supernatant with a texture of rubber. It was assumed that during the dissolution of the carbonates with sodium acetate the organic matter segregated from the other minerals going to the supernatant. Figure A3 shows this material.

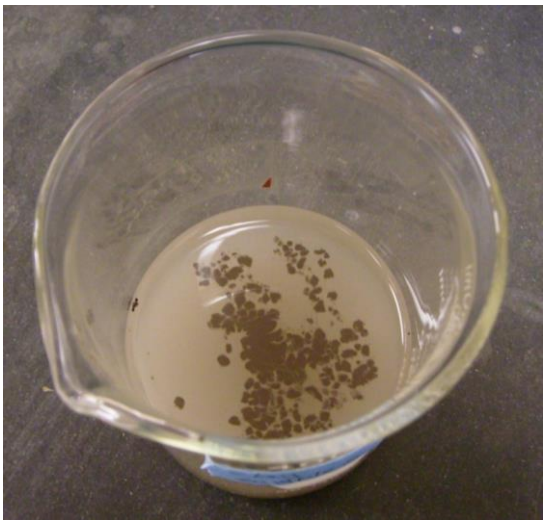

Figure A3. Organic matter supernatant during the treatment with sodium acetate.

Finally, after the dissolution of carbonates was finished, the excess of Ca^{2+} and Mg^{2+} was removed. Figure A4 shows the appearance of the samples reacting with the sodium acetate. Figure A4a shows that Tradewater did not react with sodium acetate, which implies that there were no carbonates in this shale. Figure A4b show that Fort Payne shale reacted with sodium acetate, which means that there were carbonates in this shale.

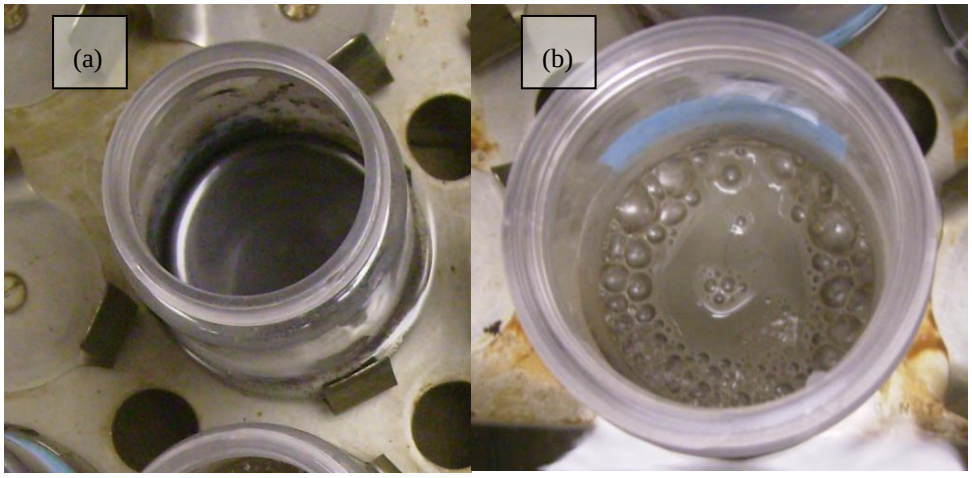

Figure A4. Reaction to sodium acetate. (a) Tradewater and (b) Fort Payne.

Pyrite removal:

Hydrogen peroxide (H_2O_2) was used to remove pyrite and organic matter. Hydrogen peroxide is a strong oxidizer that oxidizes pyrite and organic matter. The oxidation of pyrite produces sulfuric acid (H_2SO_4), water, and iron oxides. The oxidation of organic matter produces carbonic acid (H_2CO_3), carbonic dioxide, and water. The reaction was done using the same sodium acetate used in the carbonates removal phase, because it buffers the pH at a value at which hydrogen peroxide has maximum efficiency, and prevents the damage of clay minerals (Lagaly et al., 2006). Figure A5 shows the characteristics of this reaction in the Fort Payne sample. It can be observed in the figure that this reaction was very strong. Figure A6 shows the appearance of the supernatant after one night of reaction.

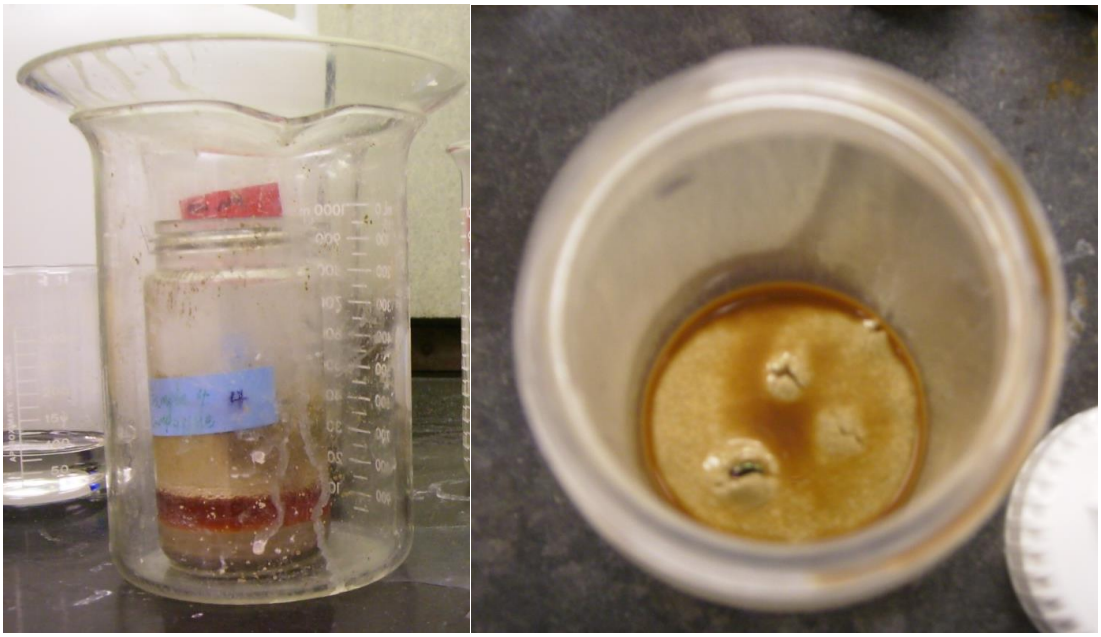

Figure A5. Reaction to hydrogen peroxide for the Fort Payne shale.

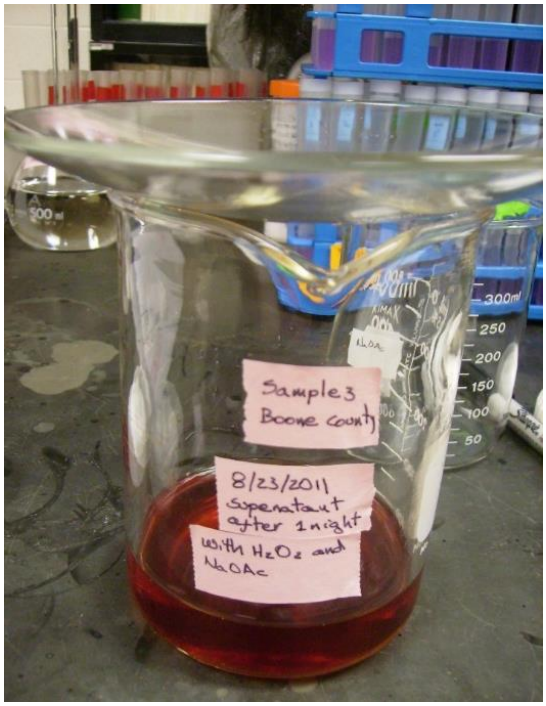

Figure A6. Supernatant formed after one night of reaction with hydrogen peroxide for the Bull Fork shale.

Iron oxides removal:

Even though all the shale samples of this study were dark colored, pretreatment was performed in order to remove iron oxides. In the event that iron oxides were present, they were removed using Na dithionite, Na citrate, and Na bicarbonate. Na dithionite was used to reduce the solutions that made the iron oxides more soluble. Then, Na citrate chelated the iron that was available in the solution. Finally, sodium bicarbonate buffered the solution and did not let the pH drop, protecting the clay minerals. Figure A7 shows the appearance of the sample after this treatment.

Figure A7. Reaction to iron oxides removal procedure for the carbondale shale.

Removal of residues:

After the above procedures were completed, the residues were washed out of the solution using a pH 5 NaOAc and N NaCl. The salt NaCl was used to flocculate the clays and made it easier to wash the samples (Jackson, 1969). Figure A8 shows the appearance of the sample after being washed.

Figure A8. Removal of residues for the Grundy and Tradewater shales.

Soil fractionation:

After the pretreatments were done, the result was a group of samples saturated with Na^+. The objective of the fractionation was to separate the clay actual size portion of each shale sample. The procedure given by Jackson (1969) was followed for the fractionation. A pH 10 sodium carbonate (Na_2CO_3) solution was poured on the sample. The sample was shaken for 1 hour to produce dispersion and was passed through a 50 micrometer sieve as shown Figure A9. The passing material was washed with more sodium carbonate solution and centrifugated (Figure A10), and the supernatant was recollected. This procedure was repeated until a clear supernatant was obtained. Finally the supernatant was oven dried at 40°C (Figure A11).

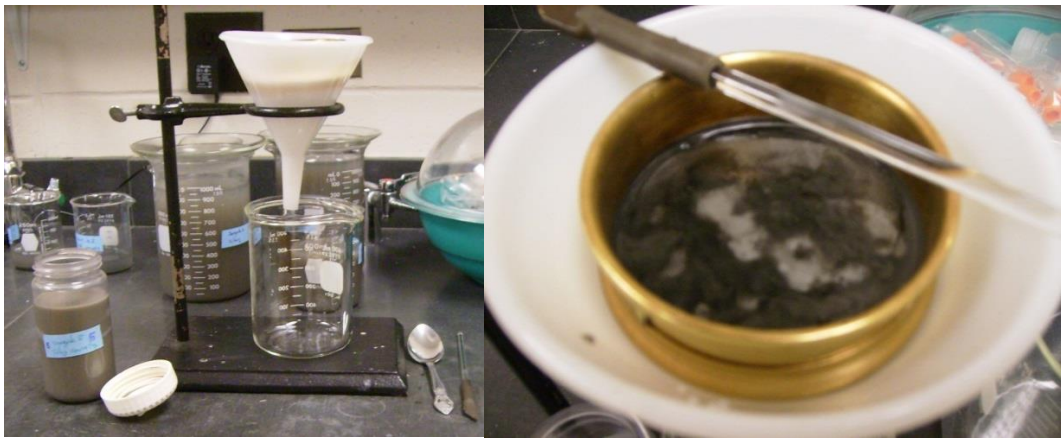

Figure A9. Sieving the samples through a 50 micrometer sieve.

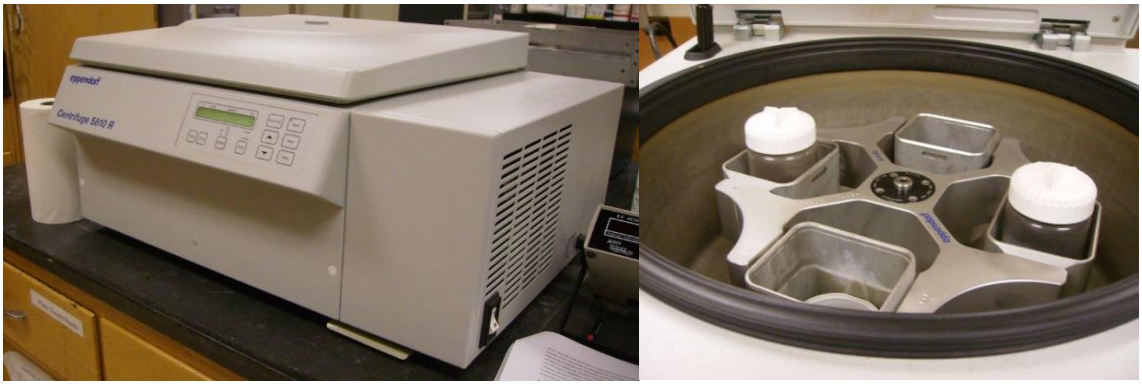

Figure A10. Centrifuge used to do the experiments.

Figure A11. Supernatant that contained the clay in suspension in the oven at 40°C.

After the pretreatment finished, the result was a powder of clay size material that was used to perform the XRD test. Figure A14 shows these samples.

Figure A14. Sample after the pretreatment.

Preparation of the XRD slides:

After the pretreatment and fractionation, the slides for the XRD test were done. The procedure by Jackson (1969), Drever (1973), and Karathanasis and Hajek (1981) was followed to do the slides. Two Mg-saturated and one K-saturated slides were done. One of the Mg slides was put inside a closed box with glycerol and left for 24 hours. These slides were used to run the first XRD tests. The scan range was 2° to 60° at 1°/minute and a step size of 0.1°. After the test with the K-saturated slide was finished, this slide was heated over one night at 100°C and the test was run again. This slide was heated again at 300°C over one night, and the test was run again. Finally, the slide was heated at 550°C over one night and the test was run again. Figure 3.16 shows the appearance of one of the slides.

Figure A15. Slide with sample after pretreatment used to run the XRD test.

Cation exchange capacity:

The CEC was measured following the instructions by Sposito (1989). This method is based on displace native cations by an index cation. The index cation is displaced by another cation. Then, the moles of the displaced index cation represents the moles of exchangeable surface charge per unit mass of sample Jackson (1956).

To remove the native cations by Ca2+, the index cation, one gram of the sample passed through a No. 200 sieve was washed with 0.5 M CaCl2 and *0.005 M CaCl2* solutions, then centrifugated at 8000 rpm for 10 minutes three times and five times respectively. The sample was then saturated with Ca2+. In order to replace the Ca2+ by Mg2+, the sample was washed four times with 0.5 M MgCl2 and centrifugated the same way. This is measured by atomic absorption spectroscopy (AAS). The initial weight of the sample, the weight of the sample and intersititial solution after saturation with Ca2+, and weight of the dry sample after the procedure was finished were taken. Then the CEC was calculated by:

$$CEC = \frac{Weight\ of\ interstitial\ Ca^{2+}}{\left(200.4\frac{mg}{cmol}\right)Weight\ of\ the\ sample} \qquad [A1]$$

APPENDIX B

XRD TEST ON CLAY FRACTION SAMPLES WITH PRETREATMENT

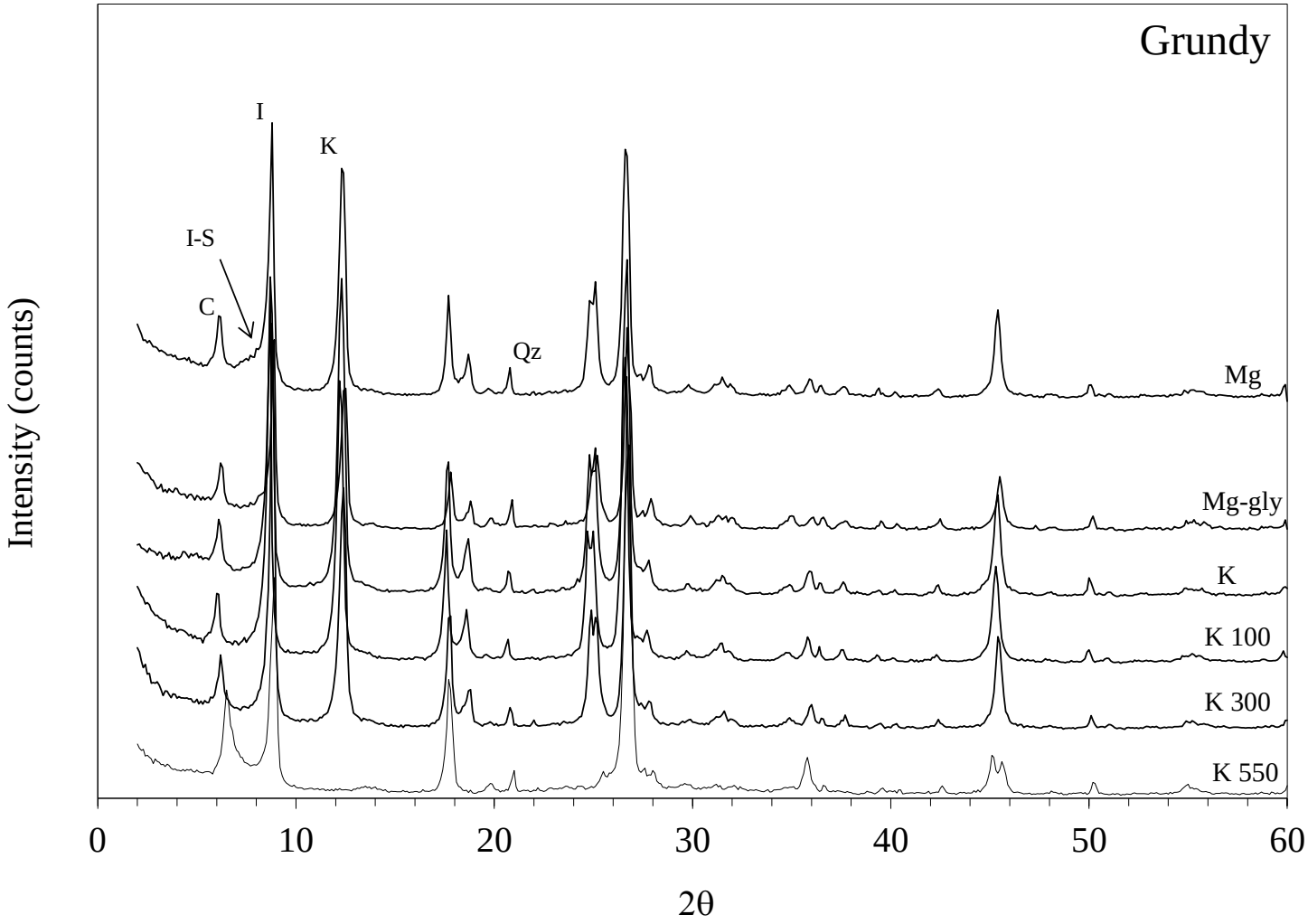

Figure B1. Grundy shale (Ch=chlorite, I-S=mixed layer illite-smectite, I=Illite, K= kaolinite, Qz=quartz).

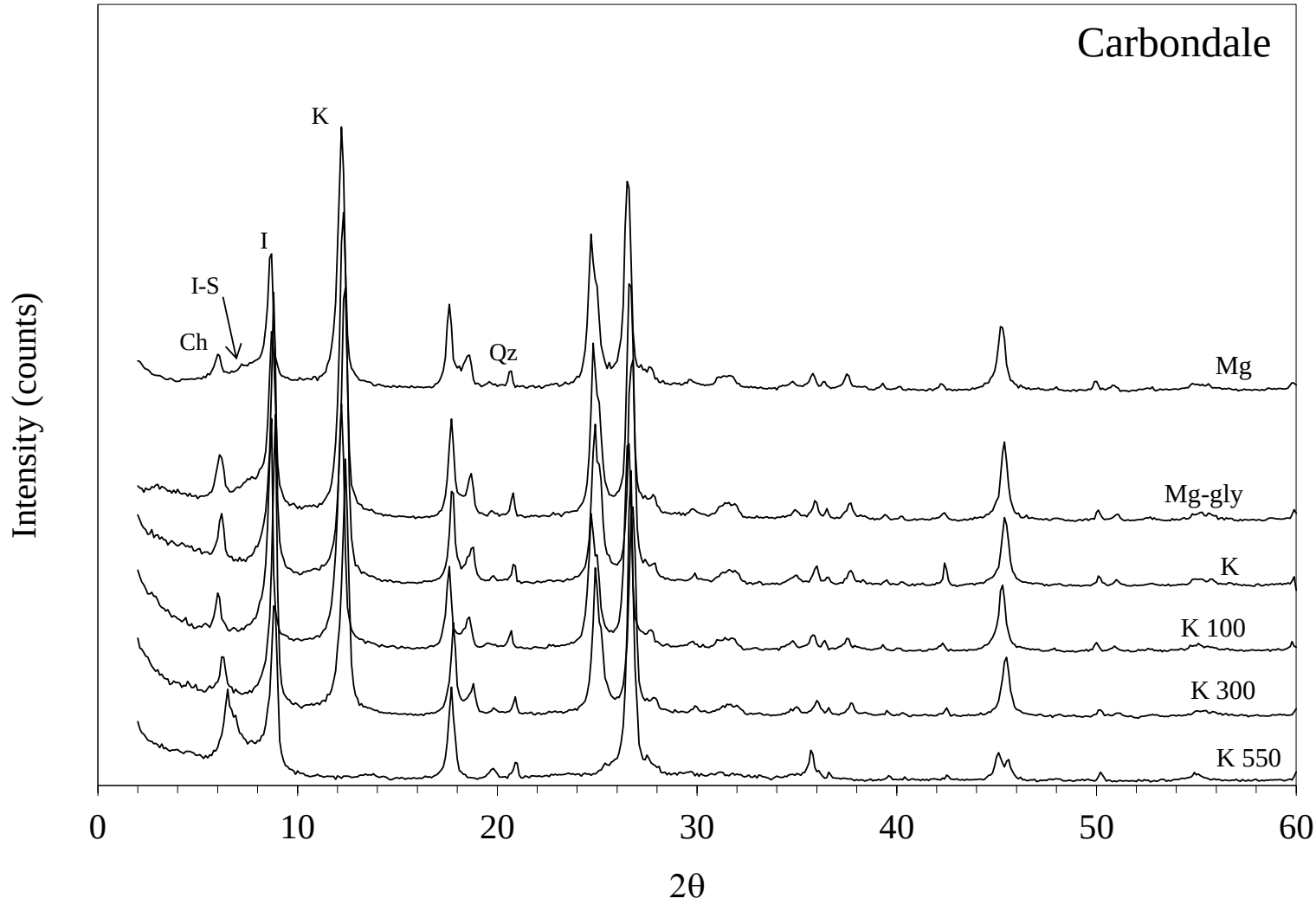

Figure B2. Carbondale shale (Ch=chlorite, I-S=mixed layer illite-smectite, I=Illite, K= kaolinite, Qz=quartz).

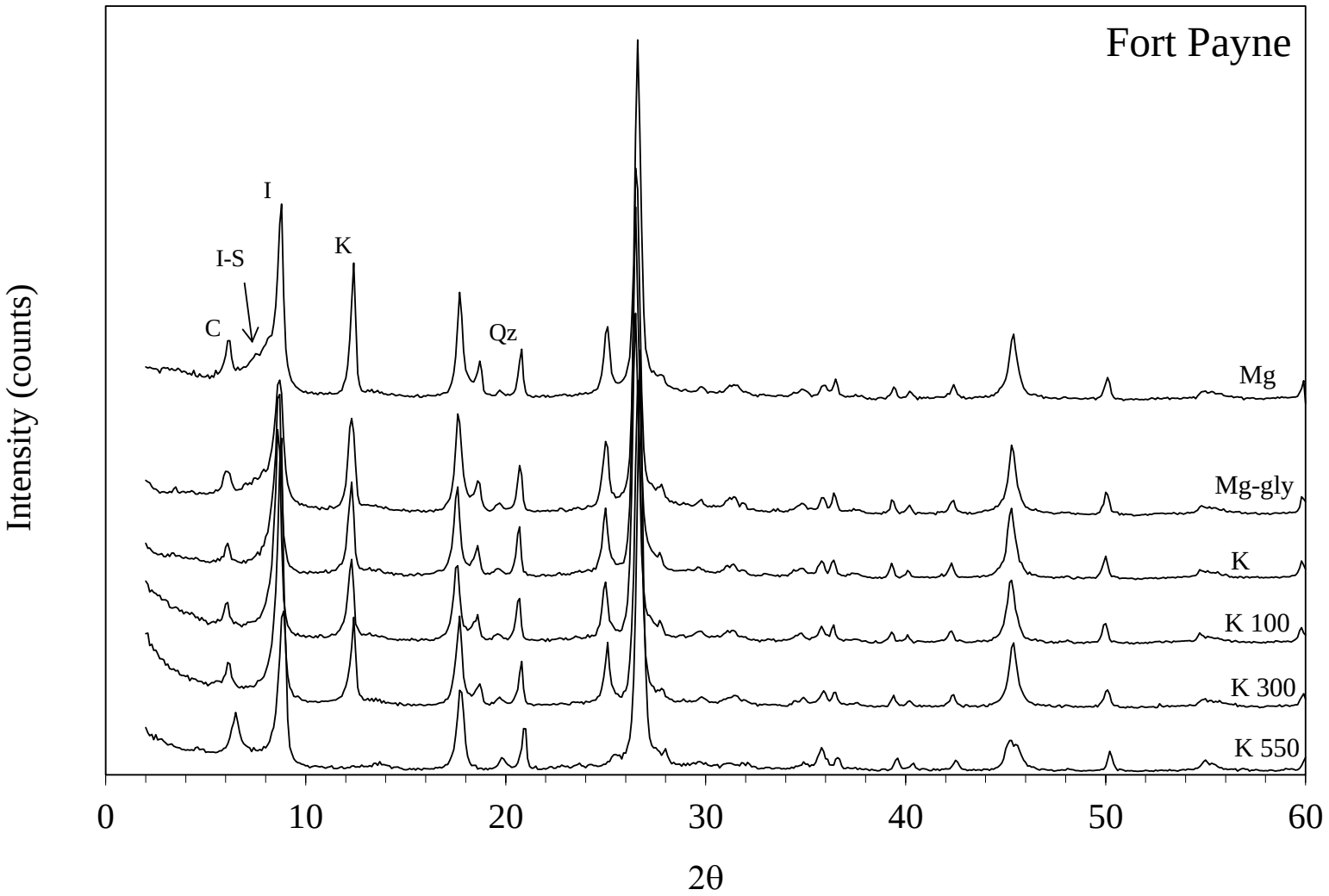

Figure B3. Fort Payne shale (Ch=chlorite, I-S=mixed layer illite-smectite, I=Illite, K= kaolinite, Qz=quartz).

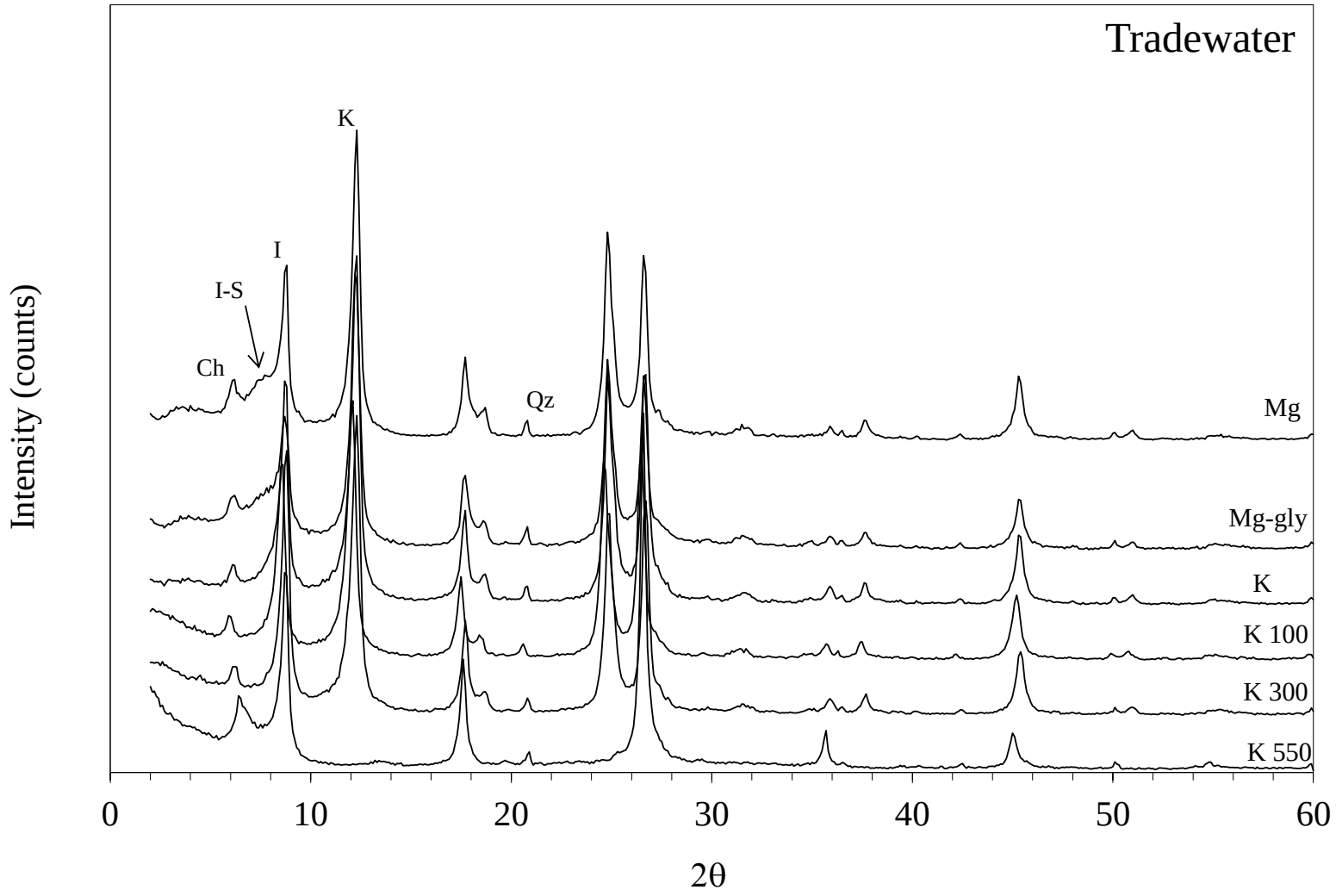

Figure B4. Tradewater shale (Ch=chlorite, I-S=mixed layer illite-smectite, I=Illite, K= kaolinite, Qz=quartz).

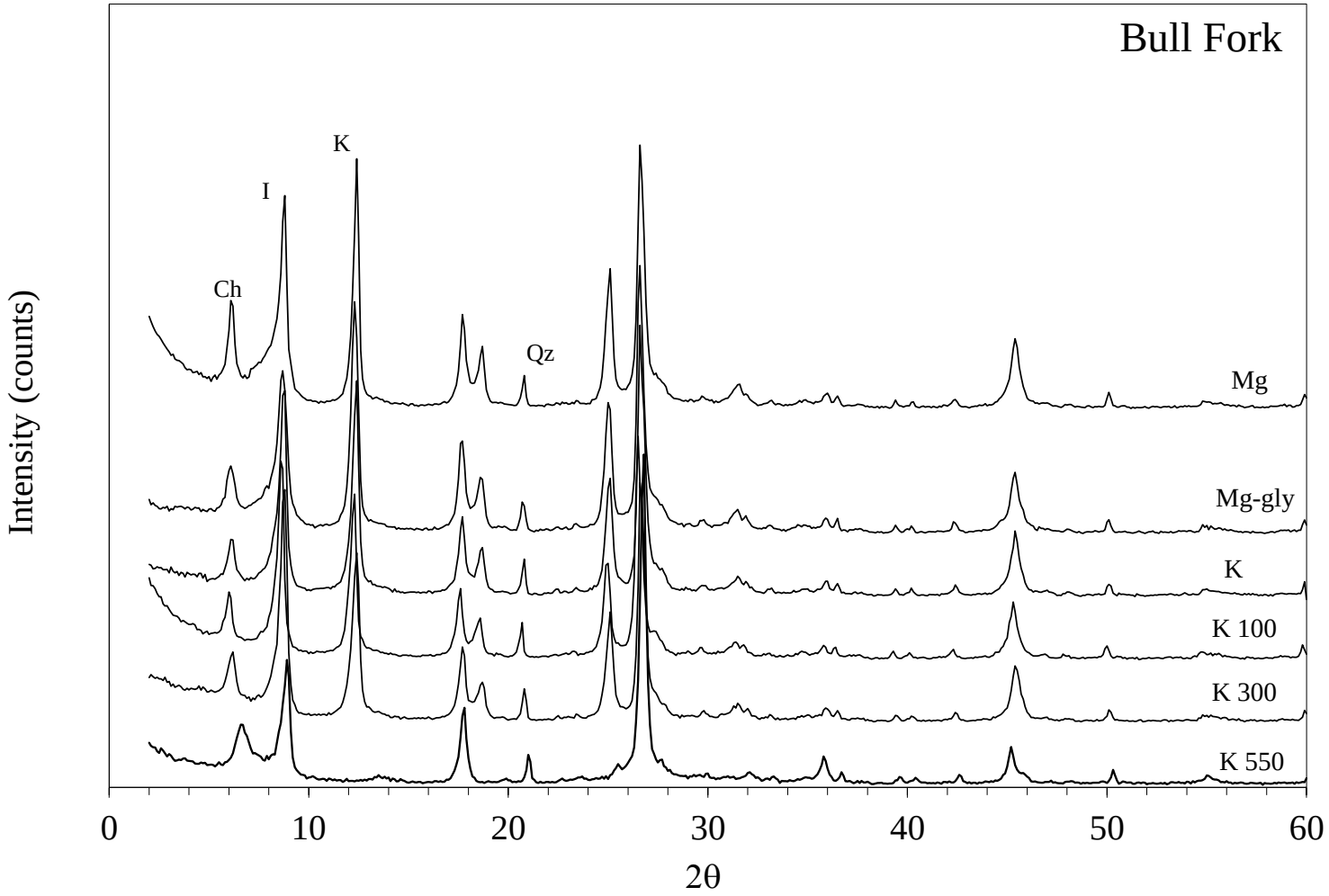

Figure B5. Bull Fork shale (Ch=chlorite, I-S=mixed layer illite-smectite, I=Illite, K= kaolinite, Qz=quartz).

APPENDIX C

TGA AND DTG PATTERNS FINE SAMPLES

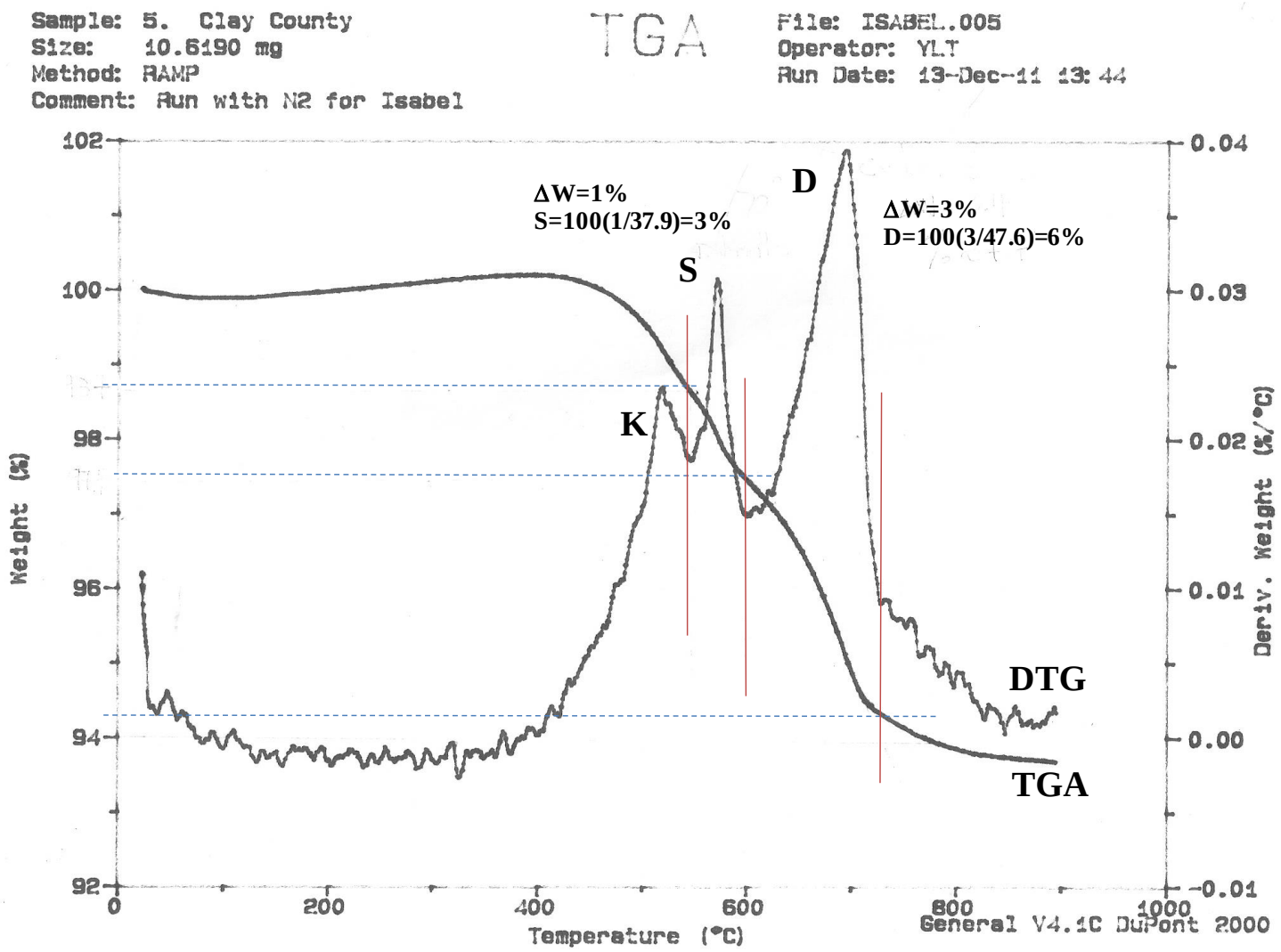

Figure C1. Grundy shale (K=kaolinite, S = siderite, D= dolomite).

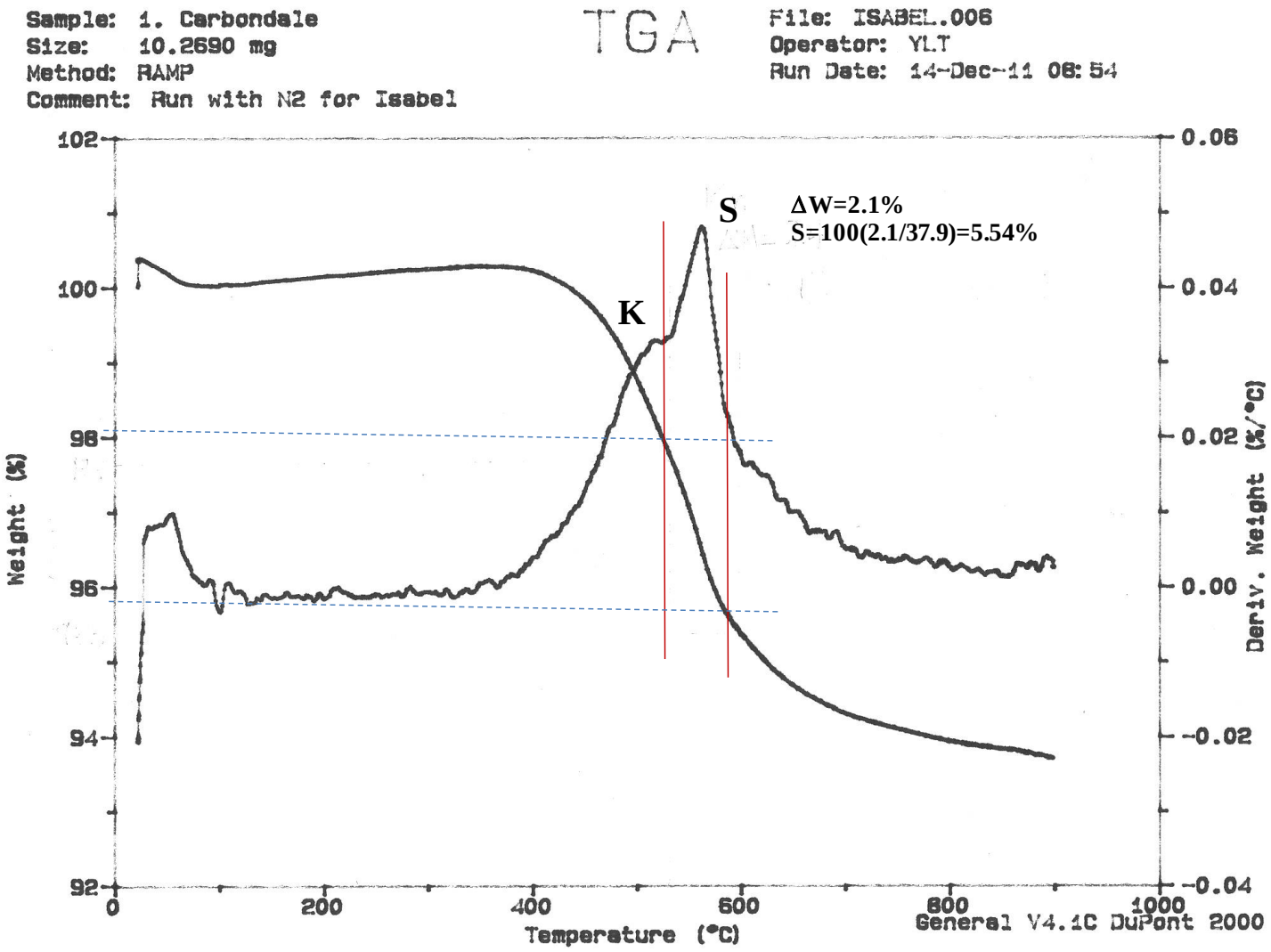

Figure C2. Carbondale shale (K=kaoinite).

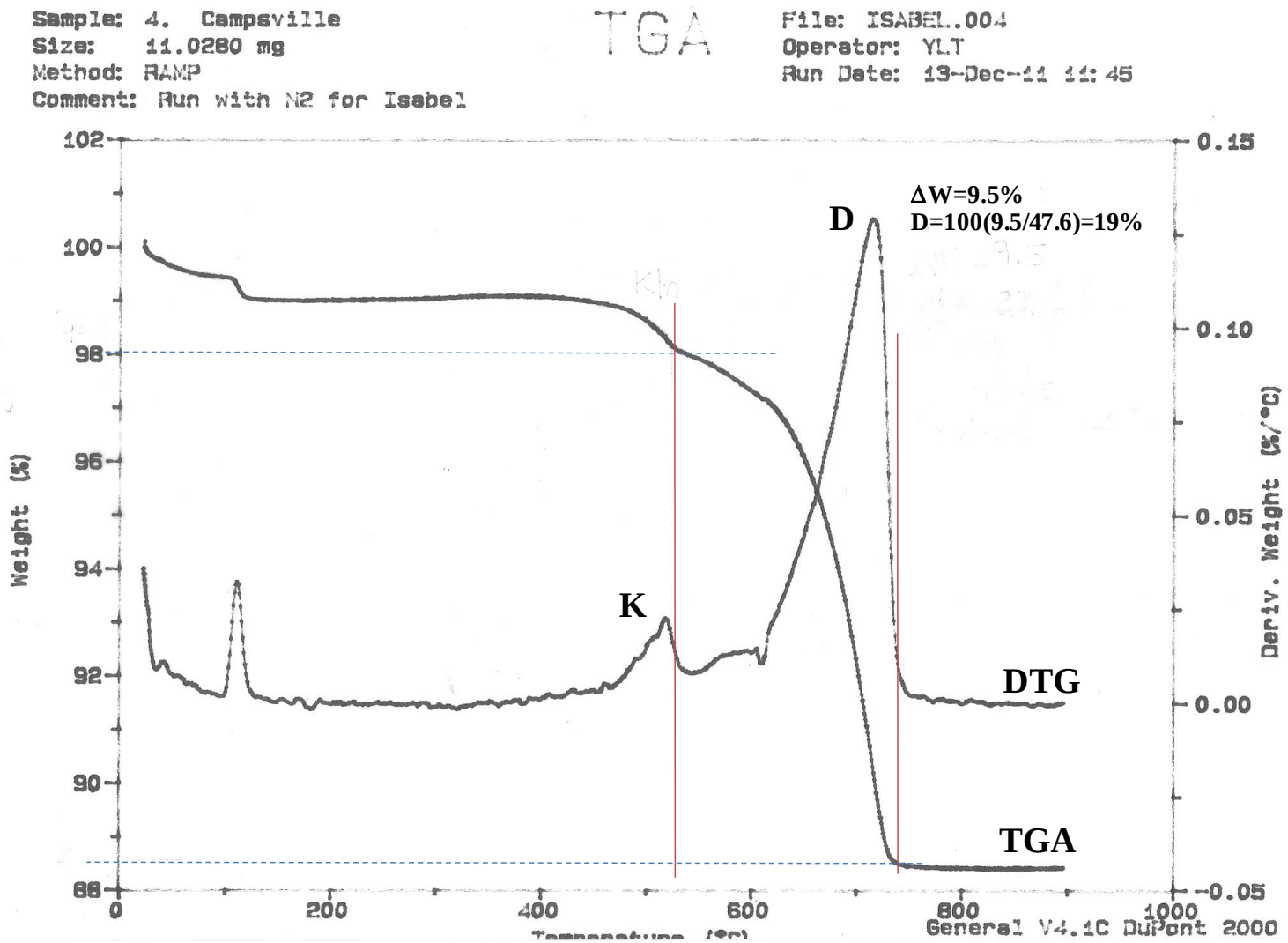

Figure C3. Fort Payne shale (K=kaolinite, D= dolomite).

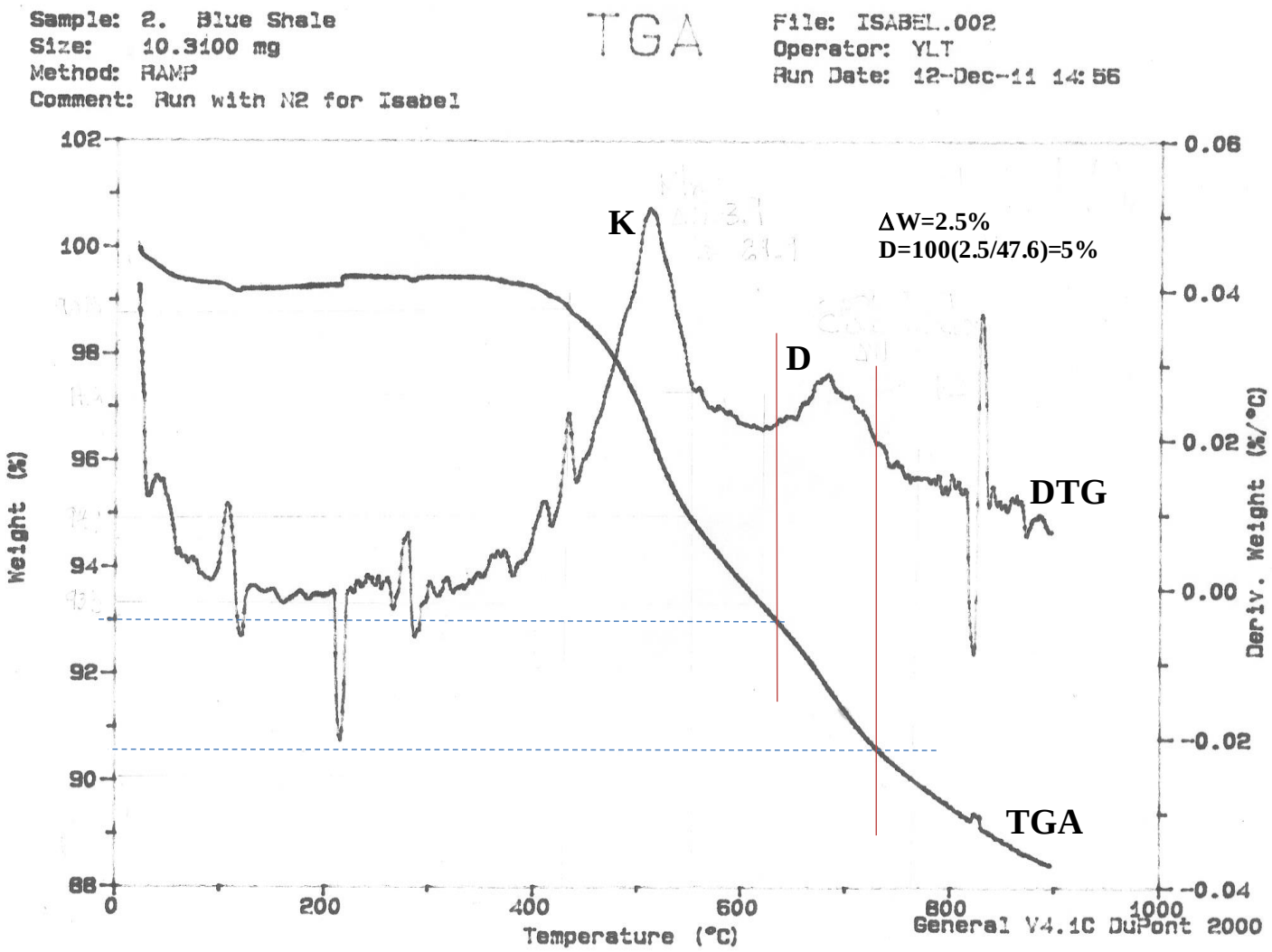

Figure C4. Tradewater shale (K=kaolinite, D= dolomite).

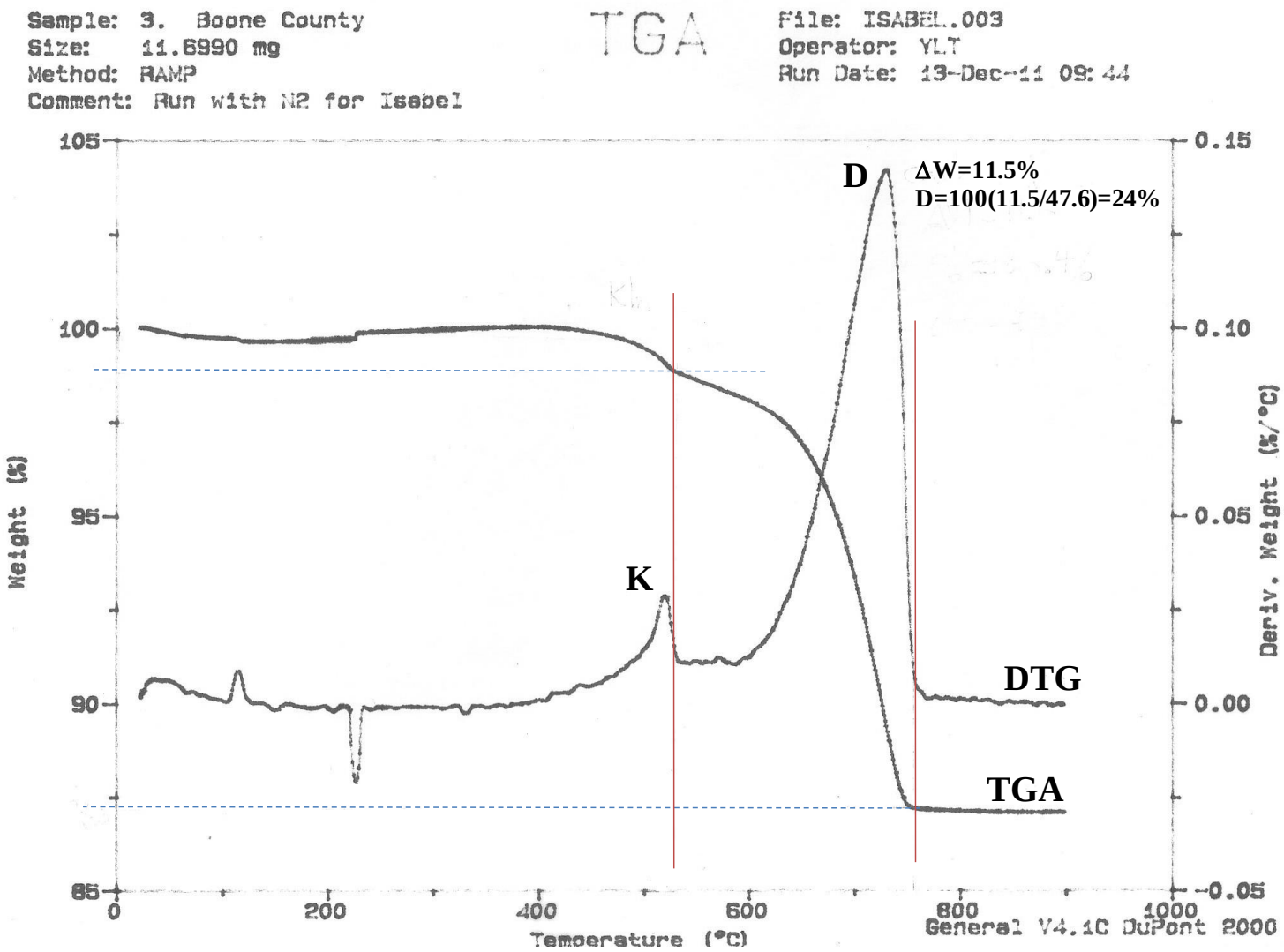

Figure C5. Bull Fork shale (K=kaolinite, D= dolomite).

APPENDIX D

XRD TEST ON FINE FRACTION SAMPLES WITHOUT PRETREATMENT

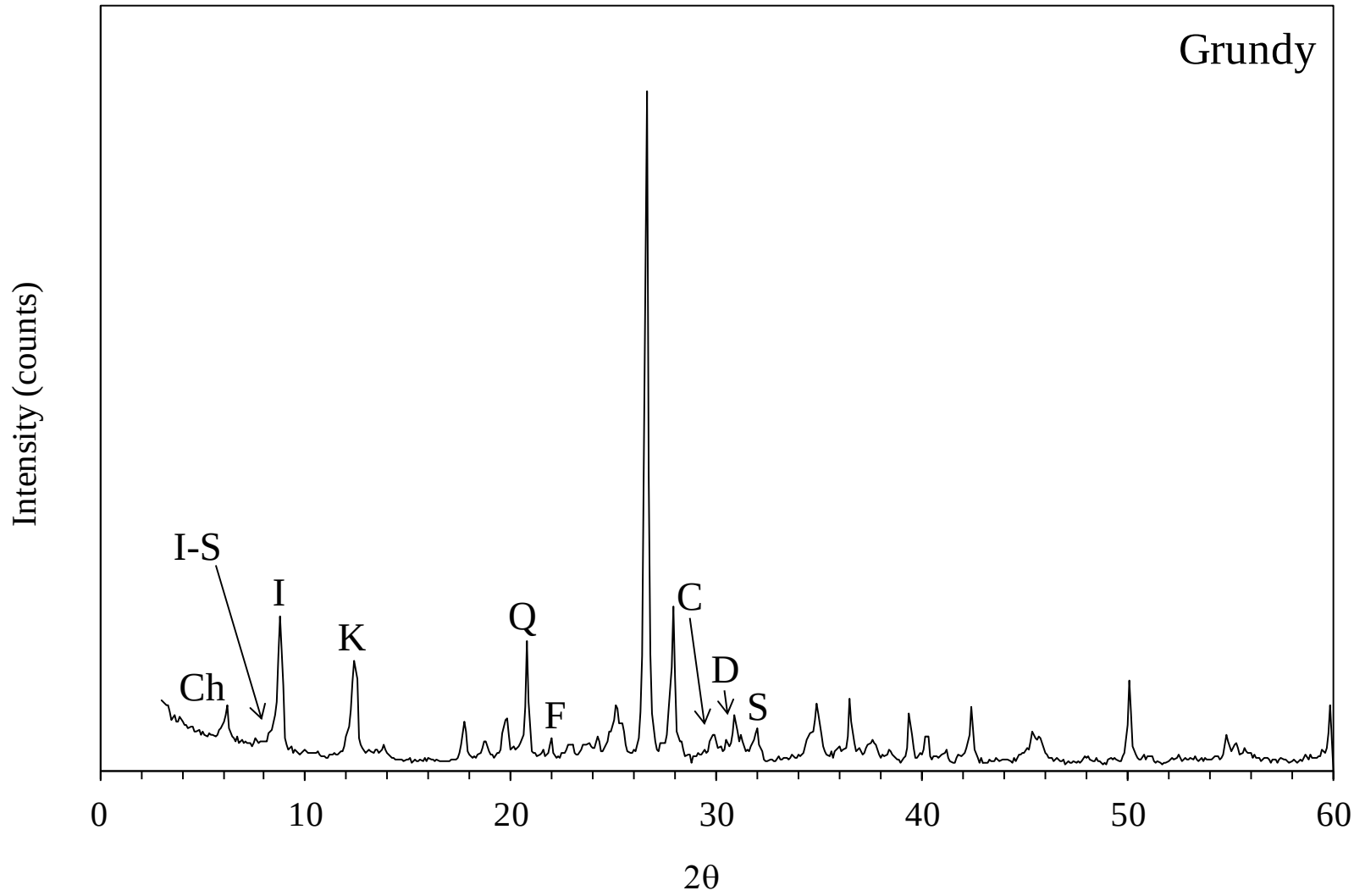

Figure D1. Grundy shale (Ch=chlorite, I-S=mixed layer Illite-smectite, I=Illite, K=kaolinite, Q=quartz, F=feldspar, C=calcite, D=dolomite, and P=pyrite).

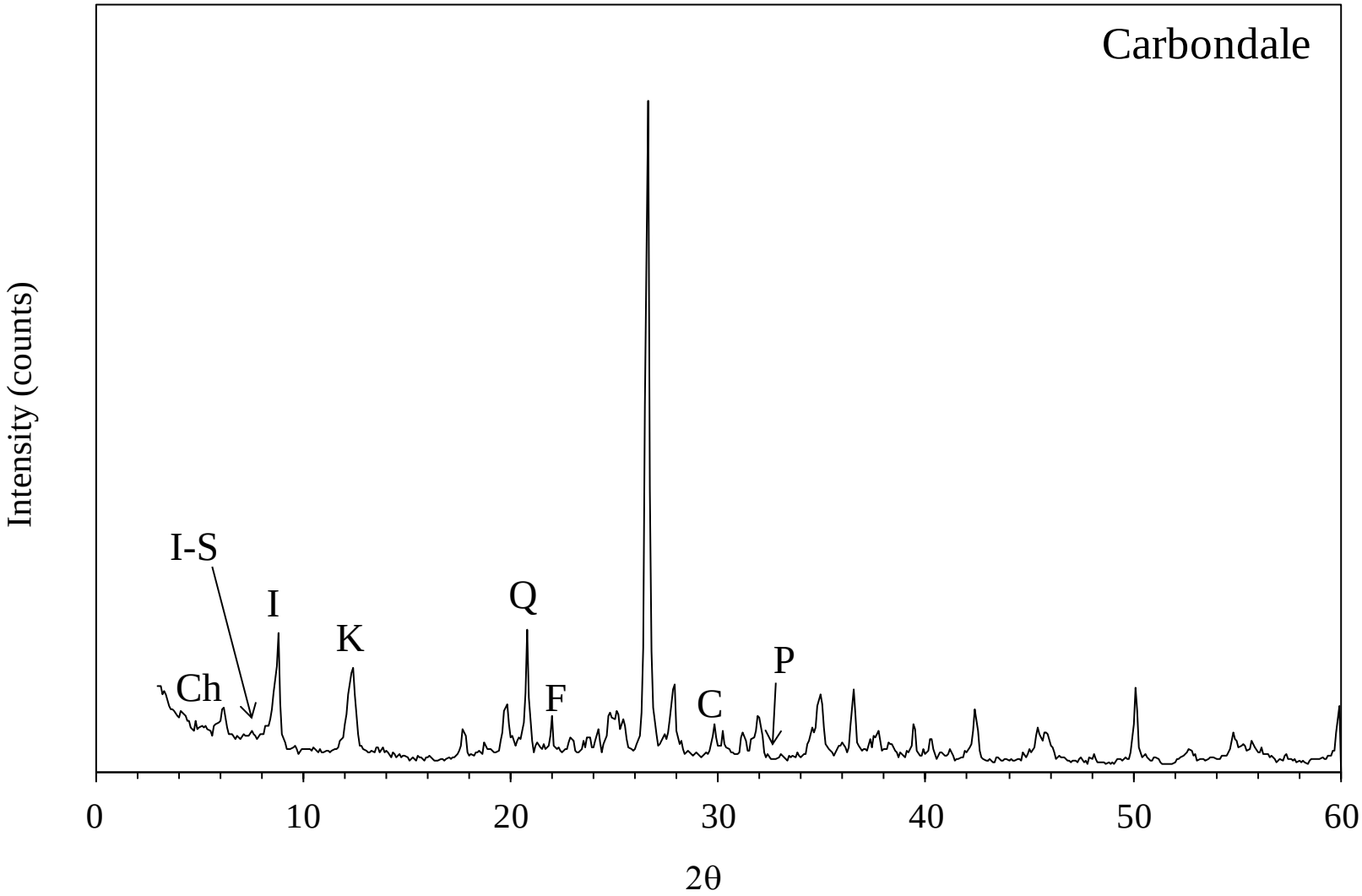

Figure D2. Carbondale shale (Ch=chlorite, I-S=mixed layer Illite-smectite, I=Illite, K=kaolinite, Q=quartz, F=feldspar, C=calcite, D=dolomite, and P=pyrite).

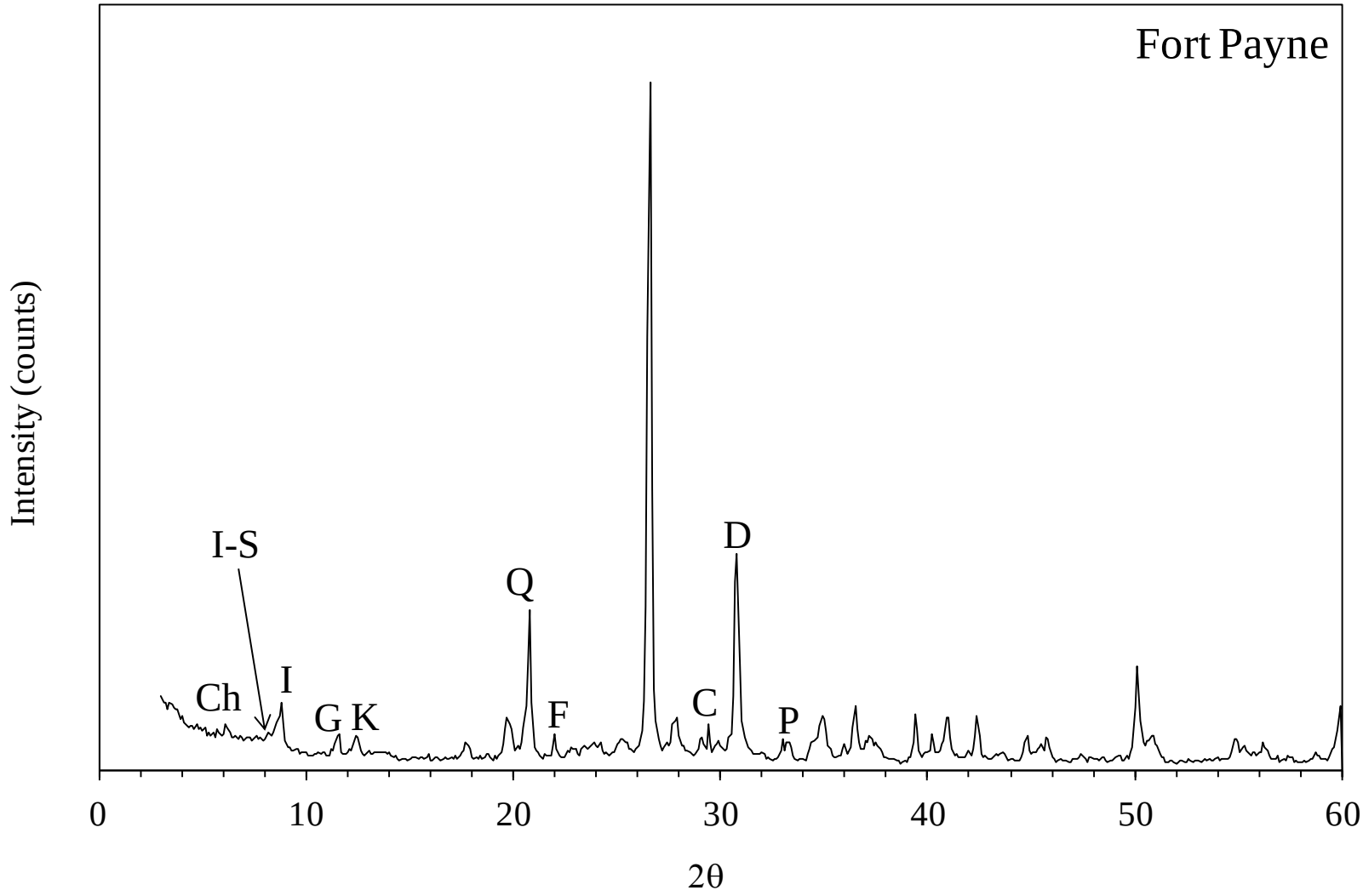

Figure D4. Fort Payne shale (Ch=chlorite, I-S=mixed layer illite-smectite, I=illite, G=Gypsum, K=kaolinite, Q=quartz, F=feldspar, C=calcite, D=dolomite, and P=pyrite).

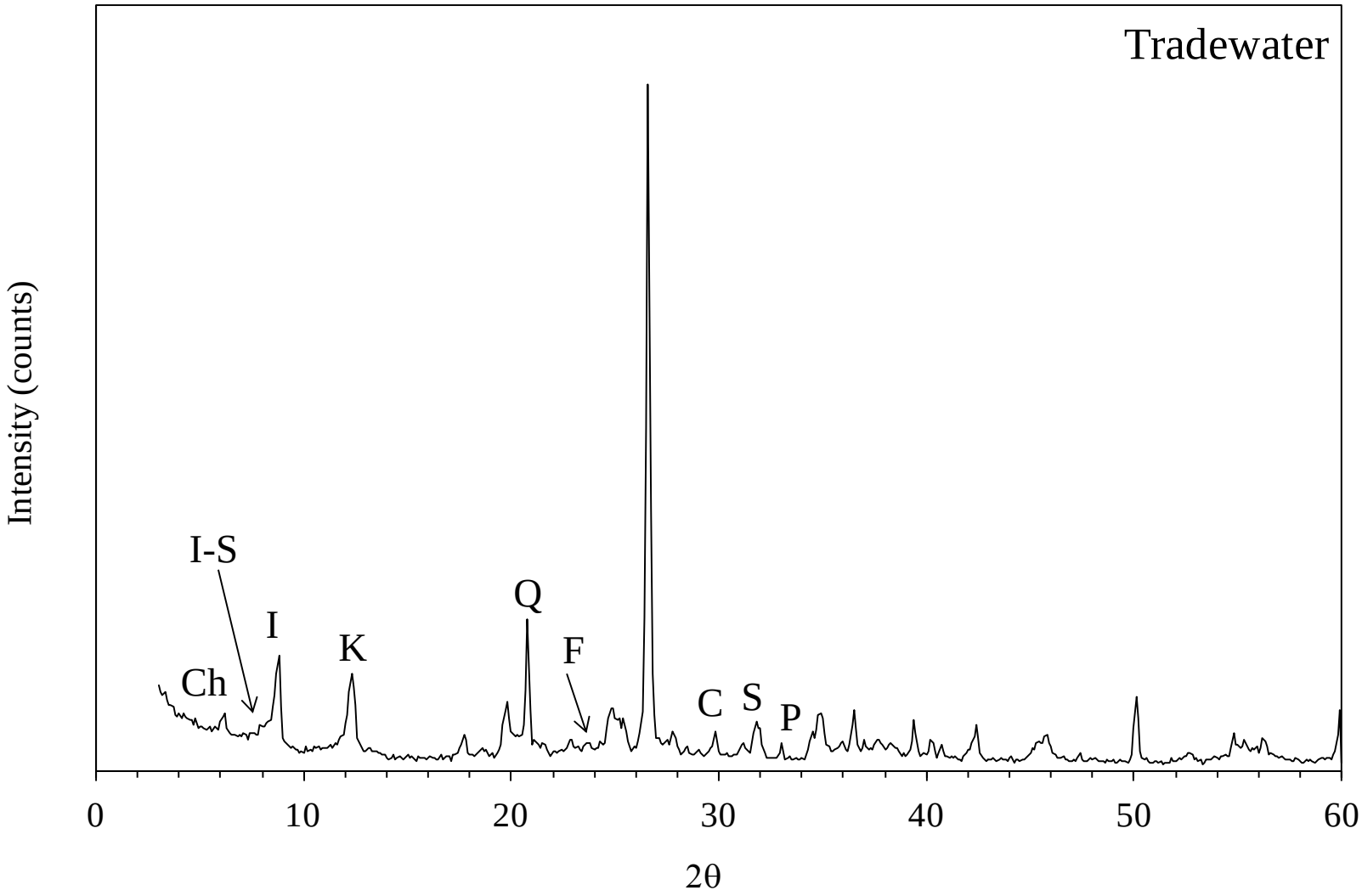

Figure D5. Tradewater shale (Ch=chlorite, I-S=mixed layer illite-smectite, I=Illite, K=kaolinite, Q=quartz, F=feldspar, C=calcite, S=siderite, and P=pyrite).

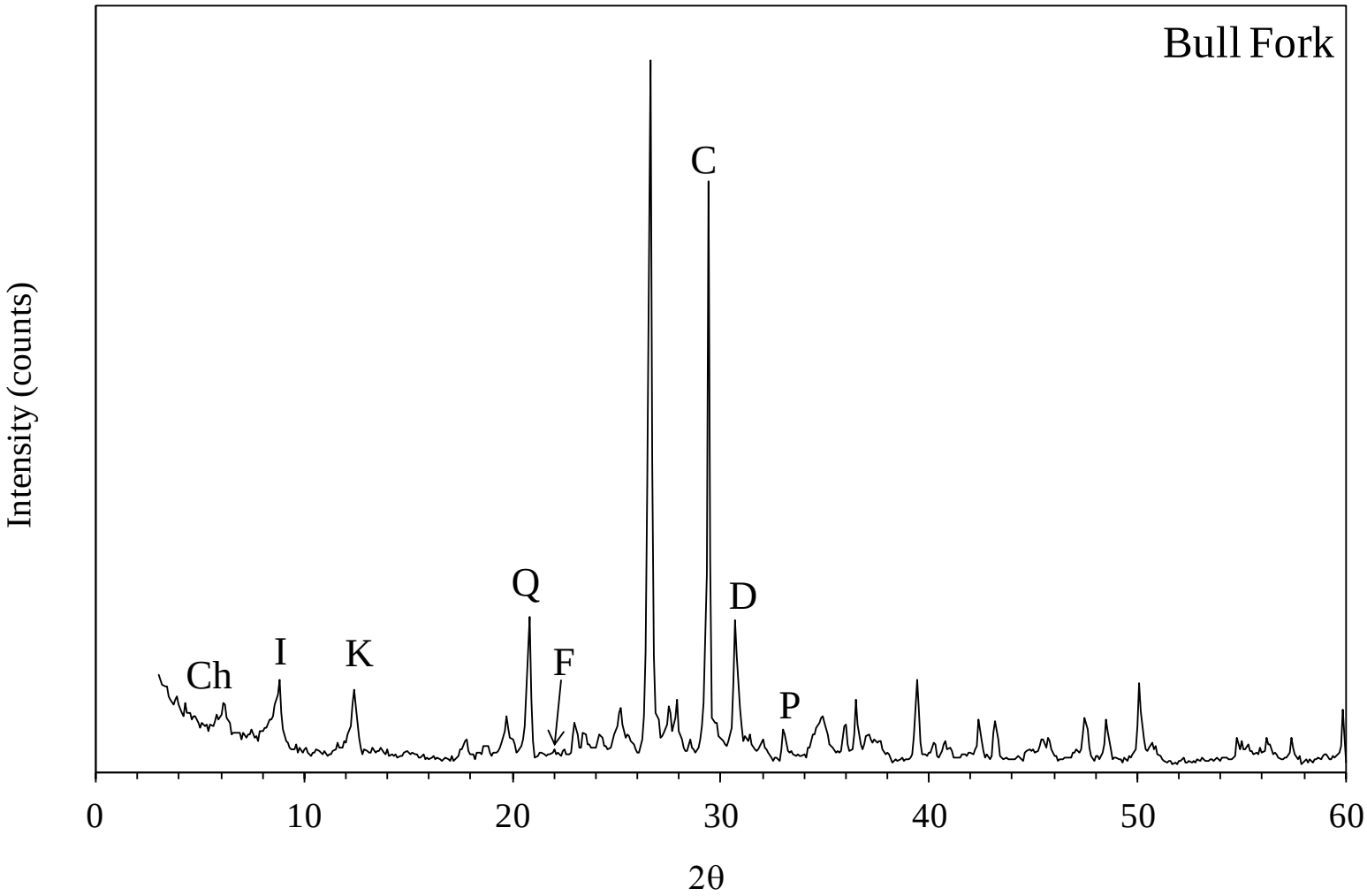

Figure D5. Bulk Fork shale (Ch=chlorite, I=Illite, K=kaolinite, Q=quartz, F=feldspar, C=calcite, and P=pyrite).

APPENDIX E

SAMPLE PREPARATION

This appendix shows the tools and procedure followed to crush the shale samples recollected in field to reduce them to size smaller than gravel. The samples were procedure:

a) Reduce the sample size with a Jaw crusher:

b) Take the portion of the sample that passed through and eight mm (0.315 in) and retained in No. 4 (4.76 mm = 0.187 in) sieves.

c) Weight 1000 grams of sample:

d) Place the sample in a Proctor mold and crushed it using a modified proctor hammer:

e) Crush the sample for 100 blows:

The sample recollected in this way was used to perform the Index, Mineralogical and Mechanical tests.

The energy used to crush the sample was:

$$E = \frac{N_{blows} \times W_{hammer} \times H_{drop}}{V_{mold}} = \frac{100 \times 4.54kgf \times 0.457m}{944cm^3} = 2{,}155kNm/m^3$$

where N_{blows} is the number of blows, W_{hammer} is the weight of the hammer, H_{drop} is the height of drop of hammer and V_{mold} is the volume of the mold.

APPENDIX F

GRAIN SIZE DISTRIBUTION

After the sample was crushed, the grain size distribution, GSD of the sample was calculated performing the Particle-Size Analysis test following the ASTM standard D422. The sieve analysis was performed using the Nos. 4, 10, 40, 200 and Pan sieve sizes as shown Figure 3.3c. When the test finished, the different grain sizes were stored in separate d boxes. The pictures show the sample before and after be sieved:

The hydrometer tests were performed with samples that passed the No. 200 sieve size:

HYGROSCOPIC MOISTURE CONTENT ALL SHALE SAMPLES

Hygroscopic moisture content							
Soil Mechanics laboratory							
June 18 - June 19 / 2012							
Material pass No. 200							
Grundy				**Carbondalle**			
Container ID:	#9	Brum #4	D25	Container ID:	1	8	11
Mass of container (g)	24.28	32.34	31.85	Mass of container (g)	31.78	31.57	31.63
Mass of air dry soil + container (g):	63.61	65.66	61.84	Mass of air dry soil + container (g):	76.61	56.24	64.67
Mass of oven dry soil + container (g):	63.38	65.46	61.65	Mass of oven dry soil + container (g):	76.23	56.03	64.38
Mass of moisture (M_w) (g):	0.23	0.2	0.19	Mass of moisture (M_w) (g):	0.38	0.21	0.29
Mass of dry soil (M_{ds}) (g):	39.1	33.12	29.8	Mass of dry soil (M_{ds}) (g):	44.45	24.46	32.75
Moisture content (ω): %	0.588	0.604	0.638	Moisture content (ω): %	0.855	0.859	0.885
Moisture content (w): %	**0.610**			**Moisture content (w): %**	**0.866**		
Fort Payne				**Tradewater**			
Container ID:	125	330X8	A	Container ID:	GroupC#1	B1-5pa	BB-top
Mass of container (g)	31.7	31.85	24.98	Mass of container (g)	24.41	31.82	32.1
Mass of air dry soil + container (g):	54.89	53.46	52.24	Mass of air dry soil + container (g):	58.69	72.4	62.19
Mass of oven dry soil + container (g):	54.53	53.14	51.83	Mass of oven dry soil + container (g):	58.25	71.9	61.78
Mass of moisture (M_w) (g):	0.36	0.32	0.41	Mass of moisture (M_w) (g):	0.44	0.5	0.41
Mass of dry soil (M_{ds}) (g):	22.83	21.29	26.85	Mass of dry soil (M_{ds}) (g):	33.84	40.08	29.68
Moisture content (ω): %	1.577	1.503	1.527	Moisture content (ω): %	1.300	1.248	1.381
Moisture content (w): %	**1.536**			**Moisture content (w): %**	**1.310**		
Bull Fork							
Container ID:	W	C	II				
Mass of container (g)	18.17	31.66	31.5				
Mass of air dry soil + container (g):	49.06	60.16	66.2				
Mass of oven dry soil + container (g):	48.74	59.85	65.83				
Mass of moisture (M_w) (g):	0.32	0.31	0.37				
Mass of dry soil (M_{ds}) (g):	30.57	28.19	34.33				
Moisture content (ω): %	1.047	1.100	1.078				
Moisture content (w): %	**1.075**						

HYDROMETER TEST

GRUNDY

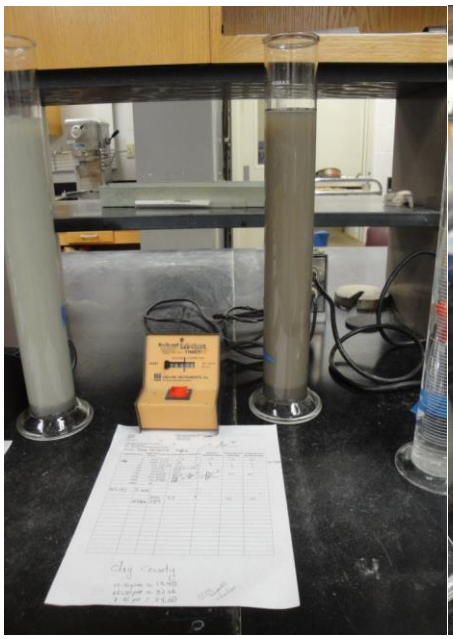

Weight air-dry sample pass No. 200 (g)	50
Hygroscopic moisture content (%)	0.61
1+ω	1.0061
Hygroscopic moisture correction factor	0.9939
Weight of solids - W (g)	49.70

Temperature (°C)	20
K = f(Gs, T°) (Table 3)	0.0133
a =f(Gs) (Table 1)	0.98

Reading time		Elapsed time	Elapsed time	Actual hydrometer reading	Effective depth	Diameter of particle	Percentage remaining in suspension	Percentage sedimented
t (min)	Date	day	min	R	L (cm)	D (mm)	P (%)	(%)
		0.00000	0.0			0.0740	100.00	0.0
2	6/15/2012	0.00139	2.0	38	10.070	0.0298	75.09	24.91
5	6/15/2012	0.00347	5.0	32	11.053	0.0198	63.23	11.86
15.3	6/15/2012	0.01063	15.3	30	11.381	0.0115	59.28	3.95
30	6/15/2012	0.02083	30.0	22	12.692	0.0086	43.47	15.81
60	6/15/2012	0.04167	60.0	21	12.856	0.0062	41.50	1.98
104	6/15/12 2:01 PM	0.07222	104.0	17	13.511	0.0048	33.59	7.90
250	6/15/12 4:27 PM	0.17361	250.0	15	13.839	0.0031	29.64	3.95
	6/15/12 6:05 PM	0.24167	348.0	13	14.167	0.0027	25.69	3.95
	6/16/12 2:16 PM	1.08236	1558.6	10	14.659	0.0013	19.76	5.93
	6/17/12 6:42 PM	2.26708	3264.6	9	14.823	0.0009	17.78	1.98
	6/18/12 10:50 AM	2.93931	4232.6	8	14.987	0.0008	15.81	1.98
	6/19/12 11:28 AM	3.96569	5710.6	8	14.987	0.0007	15.81	0.00
	6/20/12 12:28 PM	5.00736	7210.6	8	14.987	0.0006	15.81	0.00
	6/21/12 2:20 PM	6.08514	8762.6	7	15.150	0.0006	13.83	1.98
	6/22/12 2:14 PM	7.08097	10196.6	7	15.150	0.0005	13.83	0.00

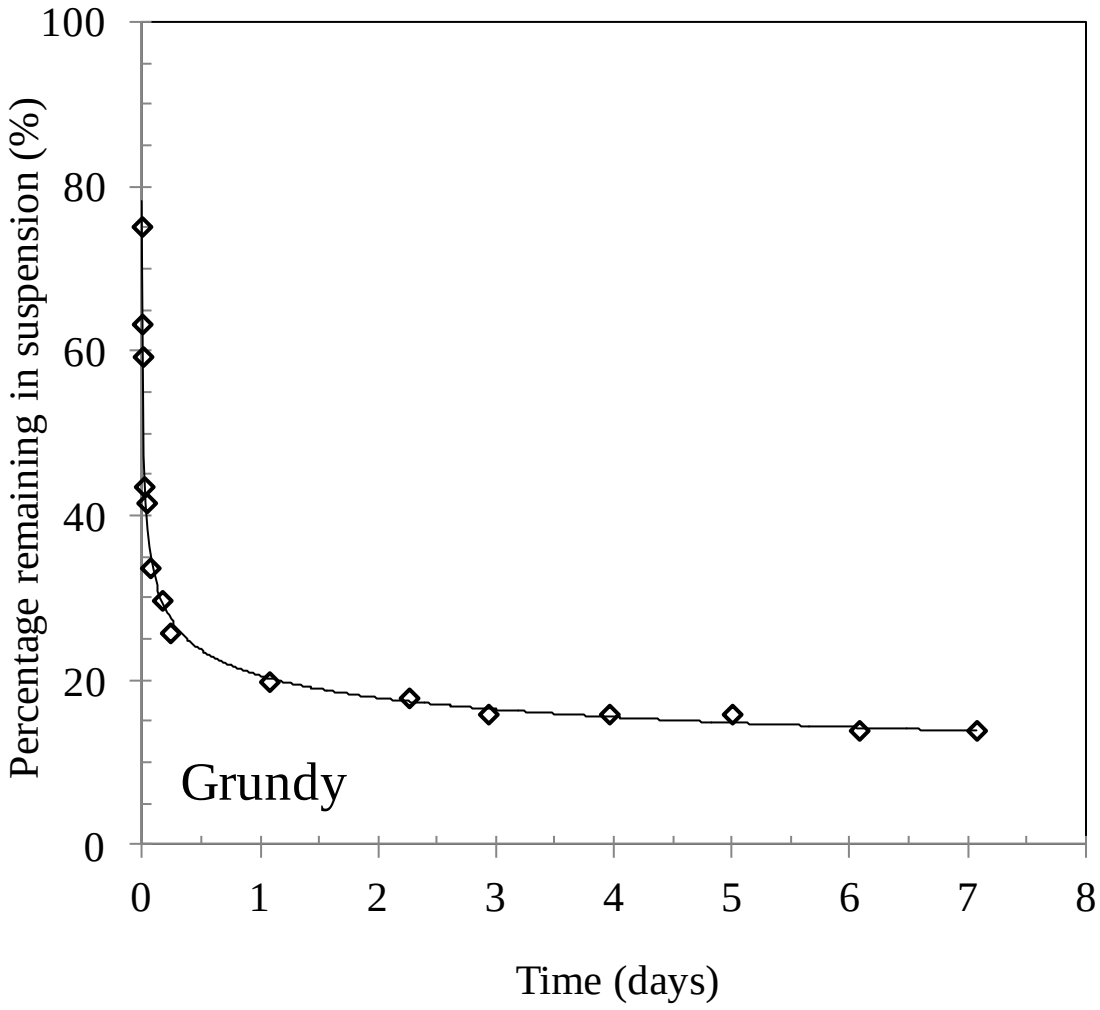
100
80
60
40
20
0
Percentage remaining in suspension (%)
Grundy
0
1
2
3
4
5
6
7
8
Time (days)

CARBONDALE

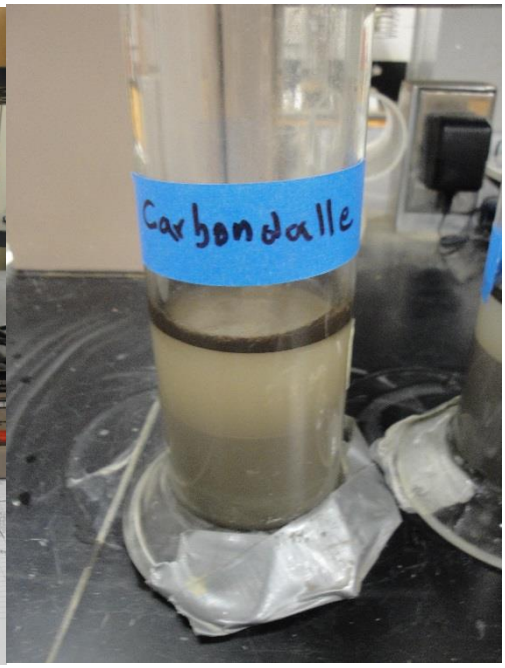

Weight air-dry sample pass No. 200 (g)	50
Hygroscopic moisture content (%)	0.87
1+ω	1.0087
Hygroscopic moisture correction factor	0.9914
Weight of solids - W (g)	49.57

Temperature (°C)	20
K = f(Gs, T°) (Table 3)	0.0132
a =f(Gs) (Table 1)	0.98

Reading time		Elapsed time	Elapsed time	Actual hydrometer reading	Effective depth	Diameter of particle	Percentage remaining in suspension	Percentage sedimented
t (min)	Date	day	min	R	L (cm)	D (mm)	P (%)	(%)
0	6/15/2012	0.00000	0.00			0.0740	100	0.0
148	6/15/2012	0.00171	2.47	44	9.128	0.0254	86.6	13.4
260	6/15/2012	0.00301	4.33	39	9.943	0.0200	76.8	23.2
300	6/15/2012	0.00347	5.00	38	10.106	0.0187	74.8	25.2
900	6/15/2012	0.01042	15.00	32	11.084	0.0113	63.0	37.0
1460	6/15/2012	0.01690	24.33	29	11.573	0.0091	57.1	42.9
1820	6/15/2012	0.02106	30.33	28	11.736	0.0082	55.1	44.9
3360	6/15/2012	0.03889	56.00	23	12.551	0.0062	45.3	54.7
3600	6/15/2012	0.04167	60.00	23	12.551	0.0060	45.3	54.7
8700	6/15/2012	0.10069	145.00	21	12.877	0.0039	41.3	58.7
9999	6/15/2012	0.11573	166.65	19	13.203	0.0037	37.4	62.6
5460	6/15/2012	0.17892	257.65	18	13.366	0.0030	35.4	64.6
8027	6/16/12 2:18 PM	1.13336	1632.03	12	14.344	0.0012	23.6	76.4
0850	6/17/12 6:53 PM	2.32433	3347.03	10	14.670	0.0009	19.7	80.3
8847	6/18/12 10:59 AM	2.99516	4313.03	10	14.670	0.0008	19.7	80.3
7710	6/19/12 11:40 AM	4.02363	5794.03	8	14.996	0.0007	15.8	84.2
7359	6/20/12 12:34 PM	5.06113	7288.03	8	14.996	0.0006	15.8	84.2
947	6/21/12 2:34 AM	5.64447	8128.03	8	14.996	0.0006	15.8	84.2
6366	6/22/12 2:18 PM	7.13336	10272.03	8	14.996	0.0005	15.8	84.2

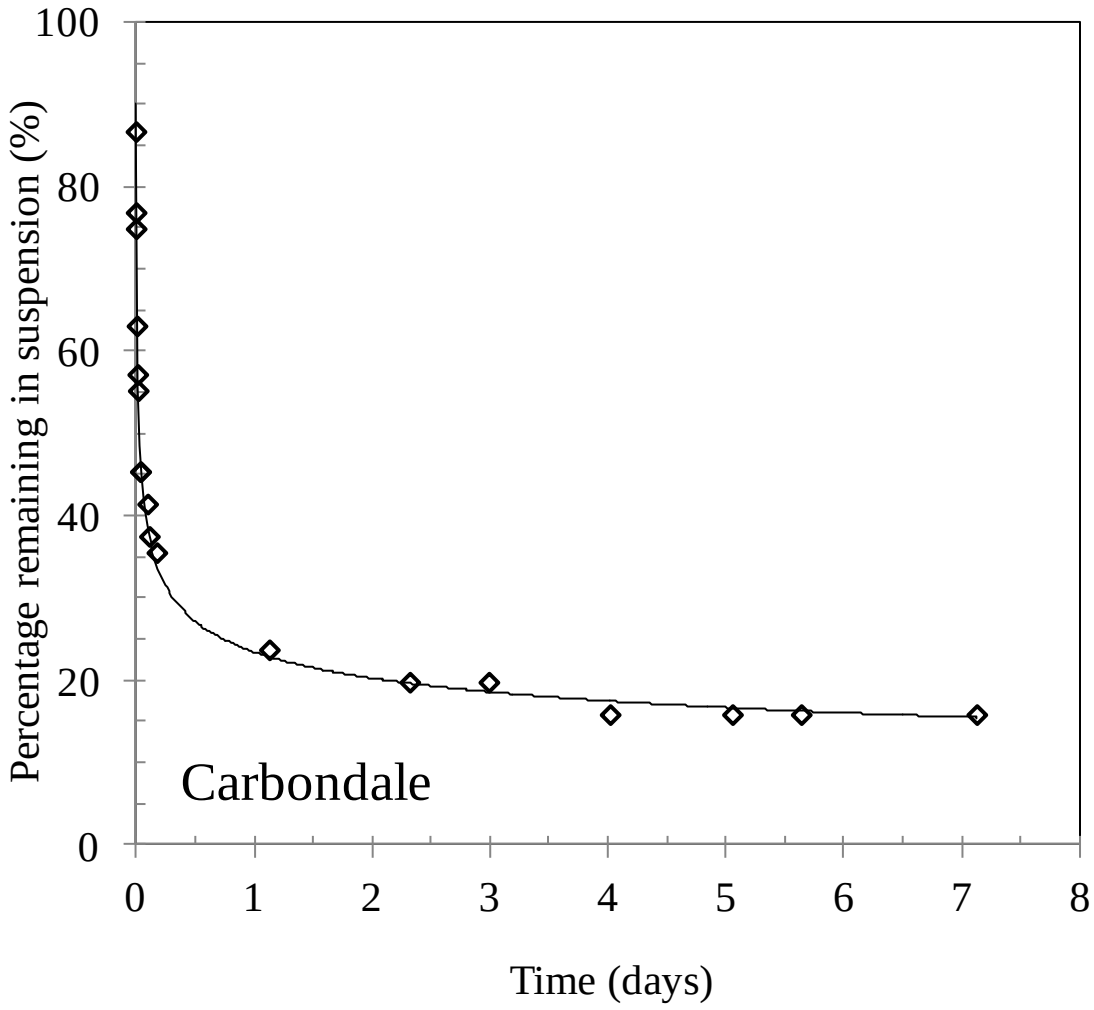
100
80
60
40
20
0
Percentage remaining in suspension (%)
Carbondale
0
1
2
3
4
5
6
7
8
Time (days)

FORT PAYNE

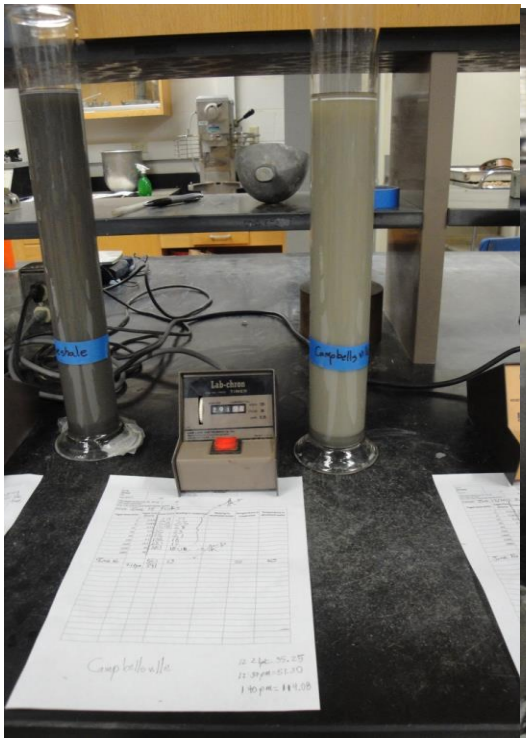

Weight air-dry sample pass No. 200 (g)	50
Hygroscopic moisture content (%)	1.54
1+ω	1.0154
Hygroscopic moisture correction factor	0.9849
Weight of solids - W (g)	49.24

Temperature (°C)	20
K = f(Gs, T°) (Table 3)	0.0137
a =f(Gs) (Table 1)	1.00

Reading time		Elapsed time	Elapsed time	Actual hydrometer reading	Effective depth	Diameter of particle	Percentage remaining in suspension	Percentage sedimented
t (min)	Date	day	min	R	L (cm)	D (mm)	P (%)	(%)
		0.00000	0.0			0.0740	100.00	0.0
2.19	6/15/2012	0.00152	2.2	40	9.742	0.0289	81.39	18.61
5.05	6/15/2012	0.00351	5.1	34	10.725	0.0200	69.18	12.21
14	6/15/2012	0.00972	14.0	28	11.709	0.0125	56.97	12.21
30	6/15/2012	0.02083	30.0	24	12.364	0.0088	48.83	8.14
58	6/15/2012	0.04028	58.0	22	12.692	0.0064	44.77	4.07
132	6/15/12 1:58 PM	0.09167	132.0	19	13.184	0.0043	38.66	6.10
253	6/15/12 3:59 PM	0.17569	253.0	18	13.348	0.0031	36.63	2.03
383	6/15/12 6:09 PM	0.26597	383.0	16	13.675	0.0026	32.56	4.07
591	6/16/12 2:09 PM	1.09867	1582.1	13	14.167	0.0013	26.45	6.10
	6/17/12 6:48 PM	2.29242	3301.1	11	14.495	0.0009	22.38	4.07
	6/18/12 10:55 AM	2.96394	4268.1	11	14.495	0.0008	22.38	0.00
	6/19/12 11:35 AM	3.99172	5748.1	10	14.659	0.0007	20.35	2.03
	6/20/12 12:32 PM	5.03131	7245.1	10	14.659	0.0006	20.35	0.00
	6/21/12 2:32 PM	6.11464	8805.1	10	14.659	0.0006	20.35	0.00
	6/22/12 2:16 PM	7.10353	10229.1	9	14.823	0.0005	18.31	2.03

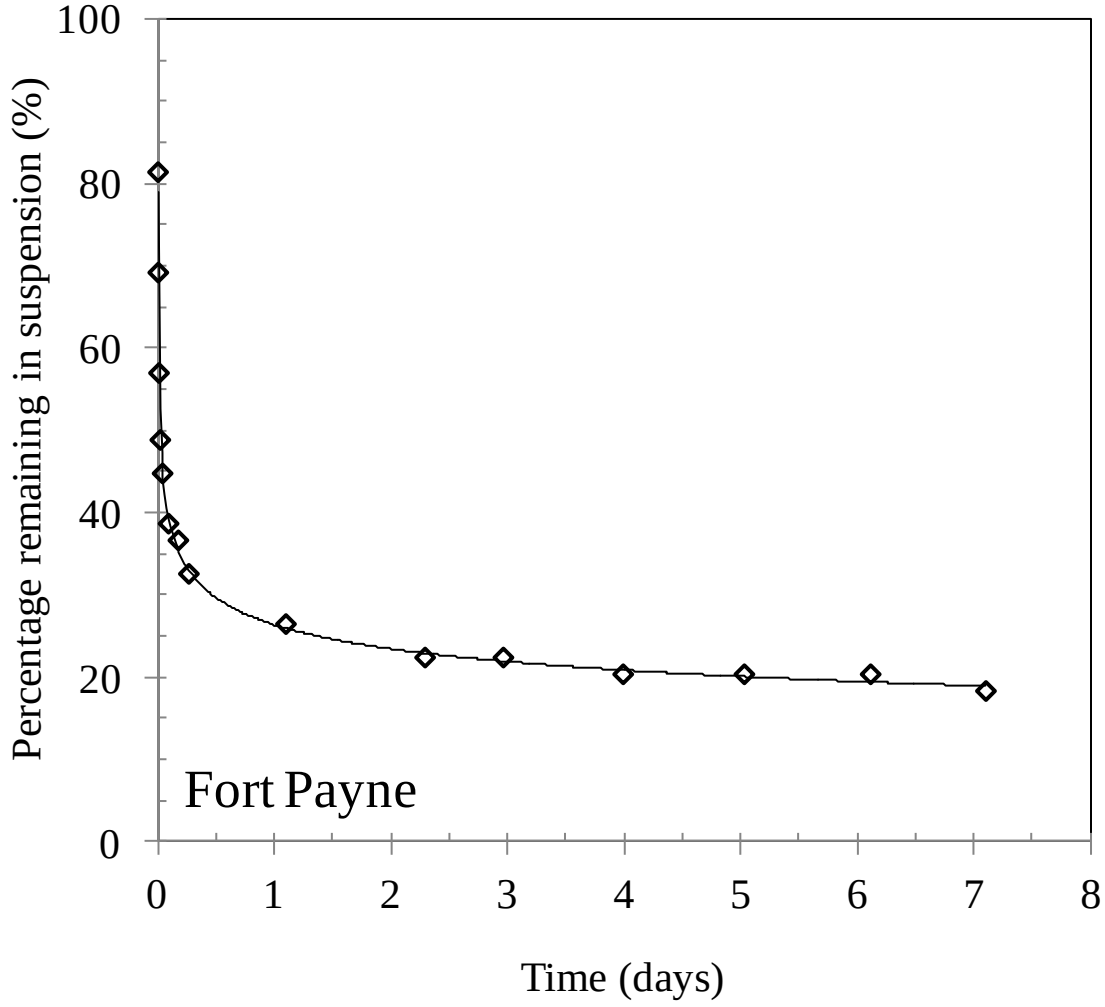
Percentage remaining in suspension (%)
100
80
60
40
20
0
0
1
2
3
4
5
6
7
8
Time (days)
Fort Payne

TRADEWATER

Weight air-dry sample pass No. 200 (g)	50
Hygroscopic moisture content (%)	1.31
1+ω	1.013
Hygroscopic moisture correction factor	0.9871
Weight of solids - W (g)	49.35

Temperature (°C)	20
K = f(Gs, T°) (Table 3)	0.0135
K = f(Gs, T°) (Table 3)	0.0133
a =f(Gs) (Table 1)	0.99
a =f(Gs) (Table 1)	0.98

If Gs=2.75

If Gs=2.68, a=0.99 and P=102.7%

If Gs=2.75, then a=0.98

Change 51 for 2.75

Reading time		Elapsed time	Elapsed time	Actual hydrometer reading	Effective depth	Diameter of particle	Percentage remaining in suspension	Percentage sedimented
t (min)	Date	day	min	R	L (cm)	D (mm)	P (%)	(%)
		0.00000	0.0			0.0740	100	0.0
2	6/15/2012	0.00139	2.0	50	8.103	0.0267	99.3	0.7
5	6/15/2012	0.00347	5.0	46	8.758	0.0175	91.3	8.7
14.4	6/15/2012	0.01000	14.4	39	9.906	0.0110	77.4	22.6
28	6/15/2012	0.01944	28.0	35	10.561	0.0081	69.5	30.5
61	6/15/2012	0.04236	61.0	31	11.217	0.0057	61.6	38.4
142	6/15/2012	0.09861	142.0	25	12.200	0.0039	49.6	50.4
250	6/15/2012	0.17361	250.0	23	12.528	0.0030	45.7	54.3
399	6/15/2012	0.27708	399.0	20	13.020	0.0024	39.7	60.3
	6/16/2012	1.10896	1596.9	15	13.839	0.0012	29.8	70.2
	6/17/12 6:50 PM	2.30340	3316.9	12	14.331	0.0009	23.8	76.2
	6/18/12 10:57 AM	2.97493	4283.9	11	14.495	0.0008	21.8	78.2
	6/20/12 12:33 PM	5.04160	7259.9	11	14.495	0.0006	21.8	78.2
	6/21/12 2:33 PM	6.12493	8819.9	11	14.495	0.0005	21.8	78.2
	6/22/12 2:17 PM	7.11382	10243.9	10	14.659	0.0005	19.9	80.1

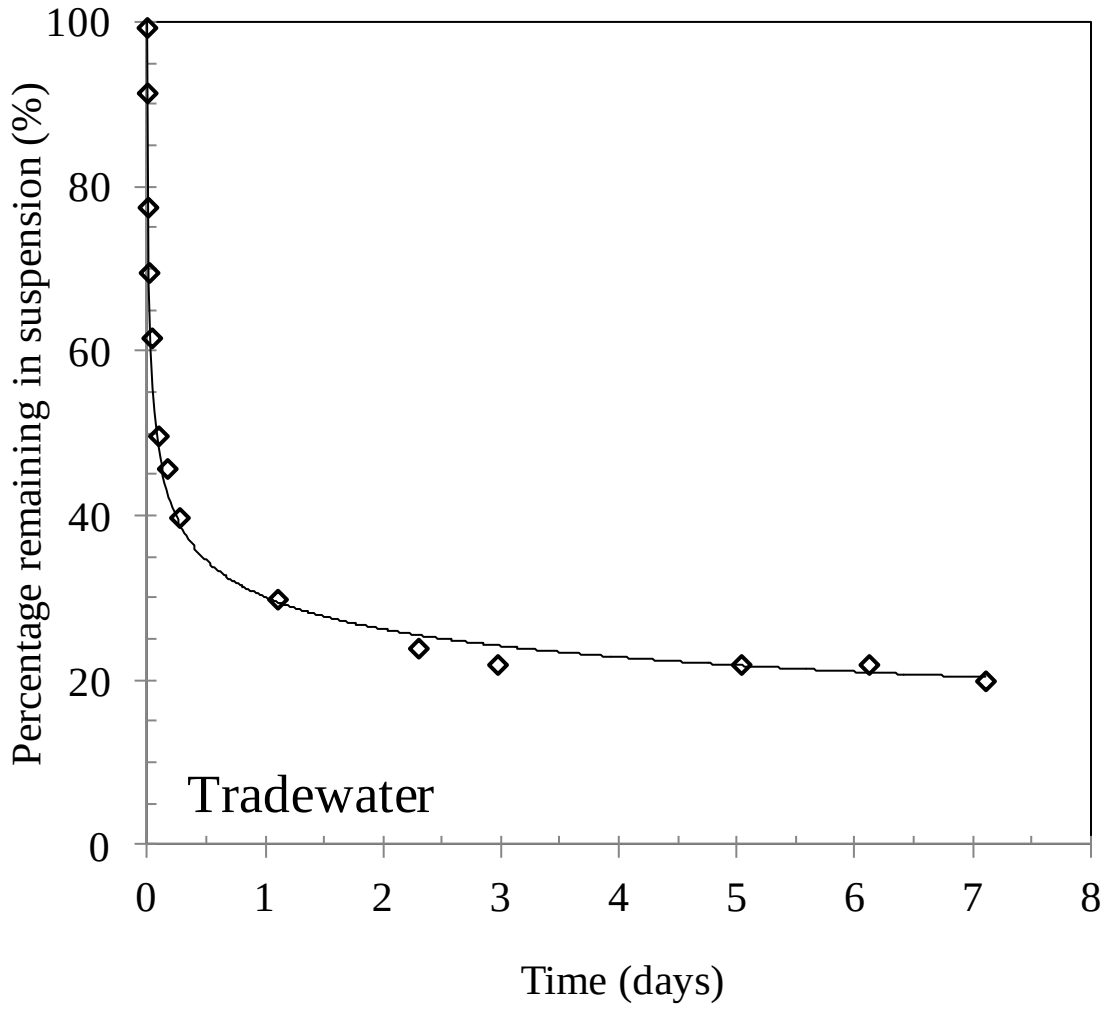
Percentage remaining in suspension (%)
100
80
60
40
20
0
0
1
2
3
4
5
6
7
8
Time (days)
Tradewater

BULL FORK

Weight air-dry sample pass No. 200 (g)	50
Hygroscopic moisture content (%)	1.07
1+ω	1.0107
Hygroscopic moisture correction factor	0.9894
Weight of solids - W (g)	49.47

Temperature (°C)	20
K = f(Gs, T°) (Table 3)	0.0137
a =f(Gs) (Table 1)	1.00

Reading time		Elapsed time	Elapsed time	Actual hydrometer reading	Effective depth	Diameter of particle	Percentage remaining in suspension	Percentage sedimented
t (min)	Date	day	min	R	L (cm)	D (mm)	P (%)	(%)
		0.00000	0.0			0.0740	100.00	0.0
2	6/15/2012	0.00139	2.0	47	8.594	0.0283	95.01	4.99
5	6/15/2012	0.00347	5.0	41	9.578	0.0189	82.88	12.13
15	6/15/2012	0.01042	15.0	35	10.561	0.0115	70.75	12.13
30.9	6/15/2012	0.02146	30.9	32	11.053	0.0082	64.69	6.06
37.5	6/15/2012	0.02604	37.5	31	11.217	0.0075	62.67	2.02
60	6/15/2012	0.04167	60.0	28	11.709	0.0060	56.60	6.06
115	6/15/12 1:59 PM	0.07986	115.0	25	12.200	0.0044	50.54	6.06
250	6/15/12 4:14 PM	0.17361	250.0	21	12.856	0.0031	42.45	8.09
362	6/15/12 6:06 PM	0.25139	362.0	20	13.020	0.0026	40.43	2.02
	6/16/12 2:16 PM	1.09132	1571.5	15	13.839	0.0013	30.32	10.11
	6/17/12 6:45 PM	2.27812	3280.5	13	14.167	0.0009	26.28	4.04
	6/18/12 10:53 AM	2.95035	4248.5	13	14.167	0.0008	26.28	0.00
	6/19/12 11:29 AM	3.97535	5724.5	12	14.331	0.0007	24.26	2.02
	6/20/12 12:30 PM	5.01771	7225.5	12	14.331	0.0006	24.26	0.00
	6/21/12 2:31 PM	6.10174	8786.5	11	14.495	0.0006	22.24	2.02
	6/22/12 2:14 PM	7.08993	10209.5	11	14.495	0.0005	22.24	0.00

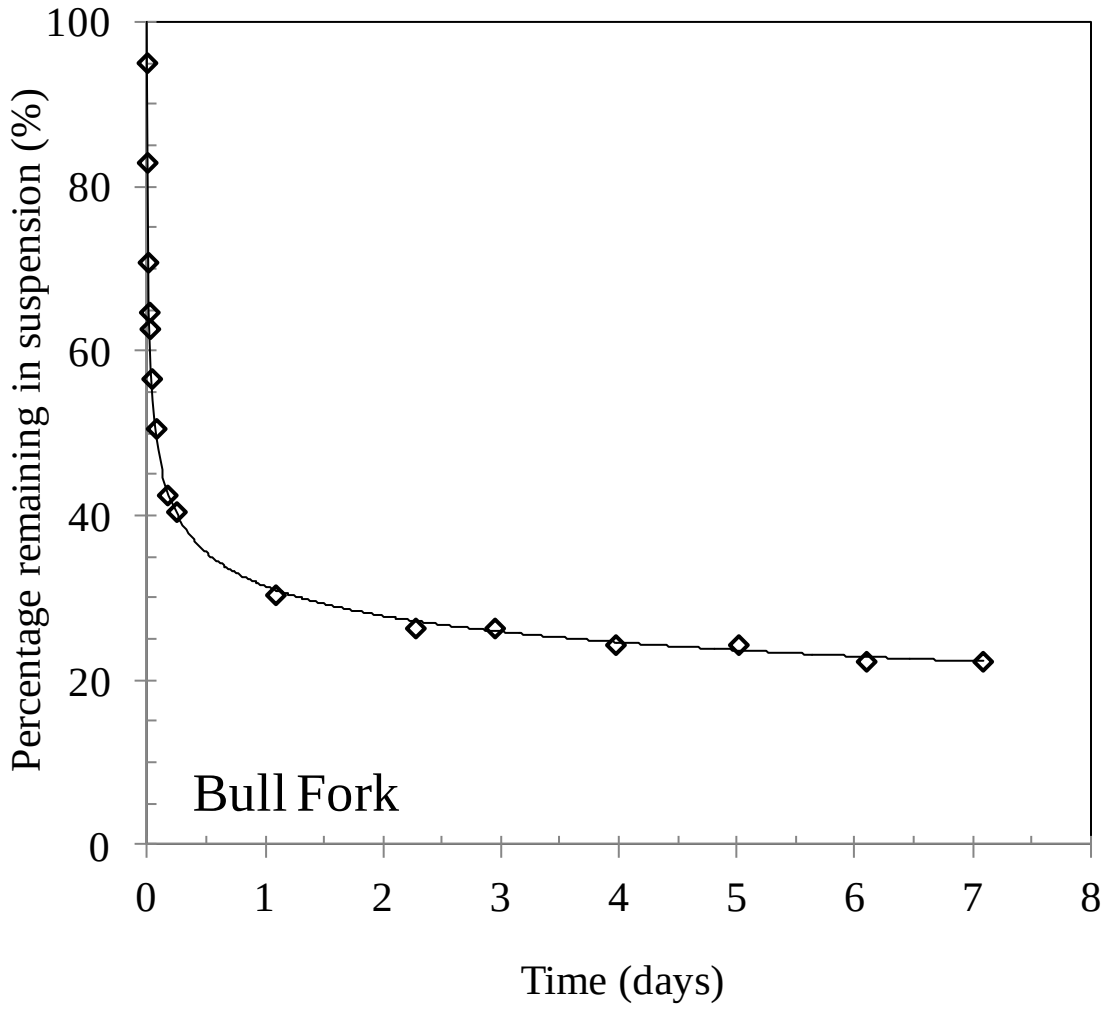
100
80
60
40
20
0
Percentage remaining in suspension (%)
Bull Fork
0
1
2
3
4
5
6
7
8
Time (days)

HYDROMETER GRAPHS ALL THE SHALE SAMPLES

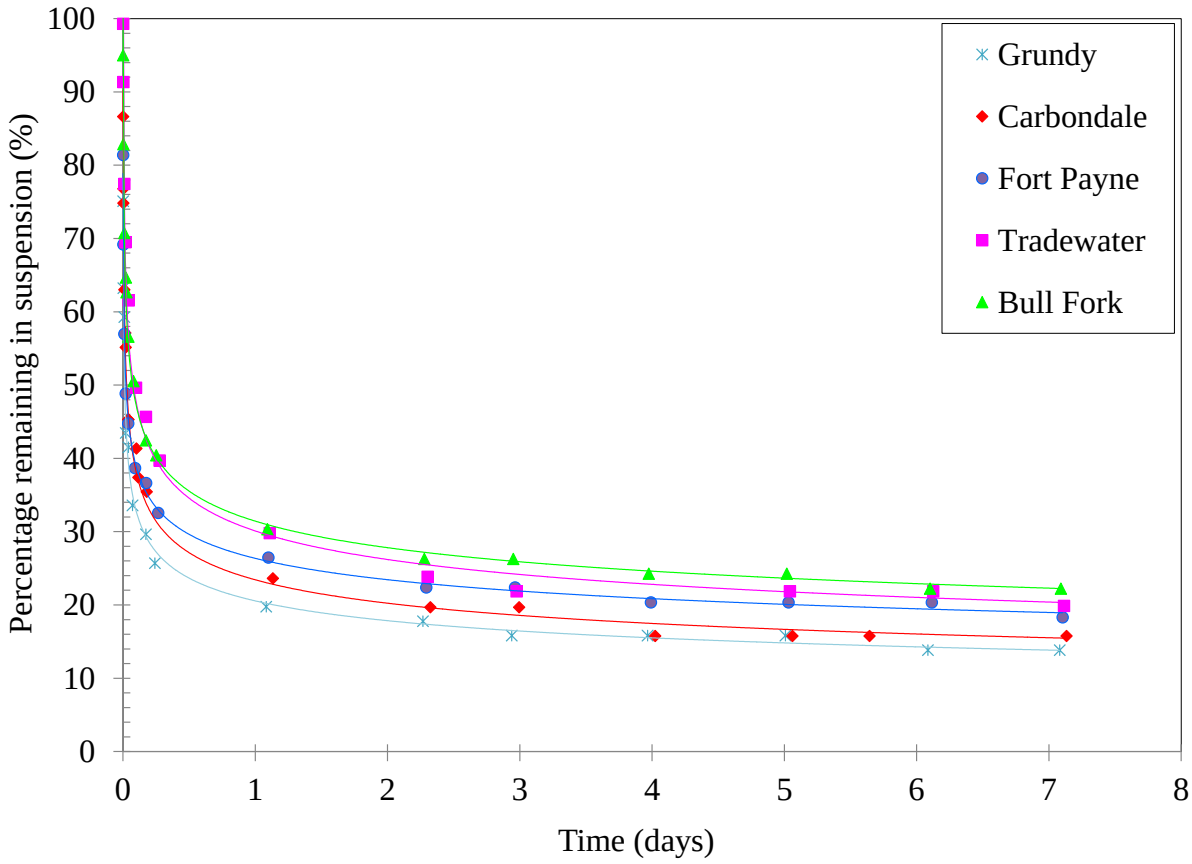

APPENDIX G

GRAIN SIZE DISTRIBUTION SPECIMENS FOR CIU TRIAXIAL TESTS

GRUNDY

GRAIN SIZE DISTRIBUTION			
ASTM	D 422		
Sample:	**Grundy**	Gs	2.74
D_{60} (mm)	2.84	Cu	19.06
D_{30} (mm)	1.25	Cc	3.68
D_{10} (mm)	0.15	CF	1.87

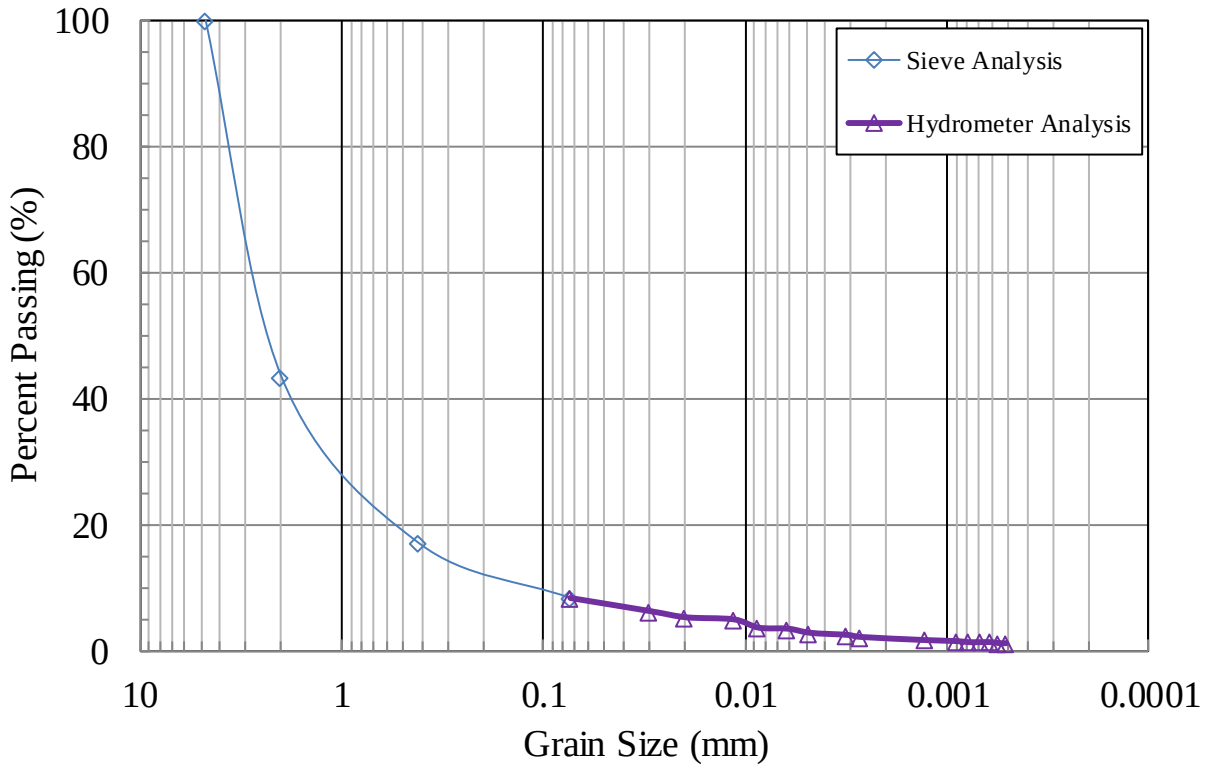

Sieve Designation	Sieve size (mm)	Grams retained	Cumulative mass retained	Grams passing	% Passing	% Retained
No. 4	4.76	0.0	0.0	985.84	100.0	0.0
No. 10	2.00	558.84	558.84	427.00	43.3	56.7
No. 40	0.42	259.31	818.15	167.69	17.0	26.3
No. 200	0.074	86.69	904.84	81.00	8.2	8.8
Pan	-	81.00	**985.84**	0.0	0.0	8.2
		985.84				

CARBONDALE

GRAIN SIZE DISTRIBUTION			
ASTM	D 422		
Sample:	**Carbondale**	Gs	2.77
D_{60} (mm)	2.85	Cu	19.00
D_{30} (mm)	1.26	Cc	3.71
D_{10} (mm)	0.15	CF	2.23

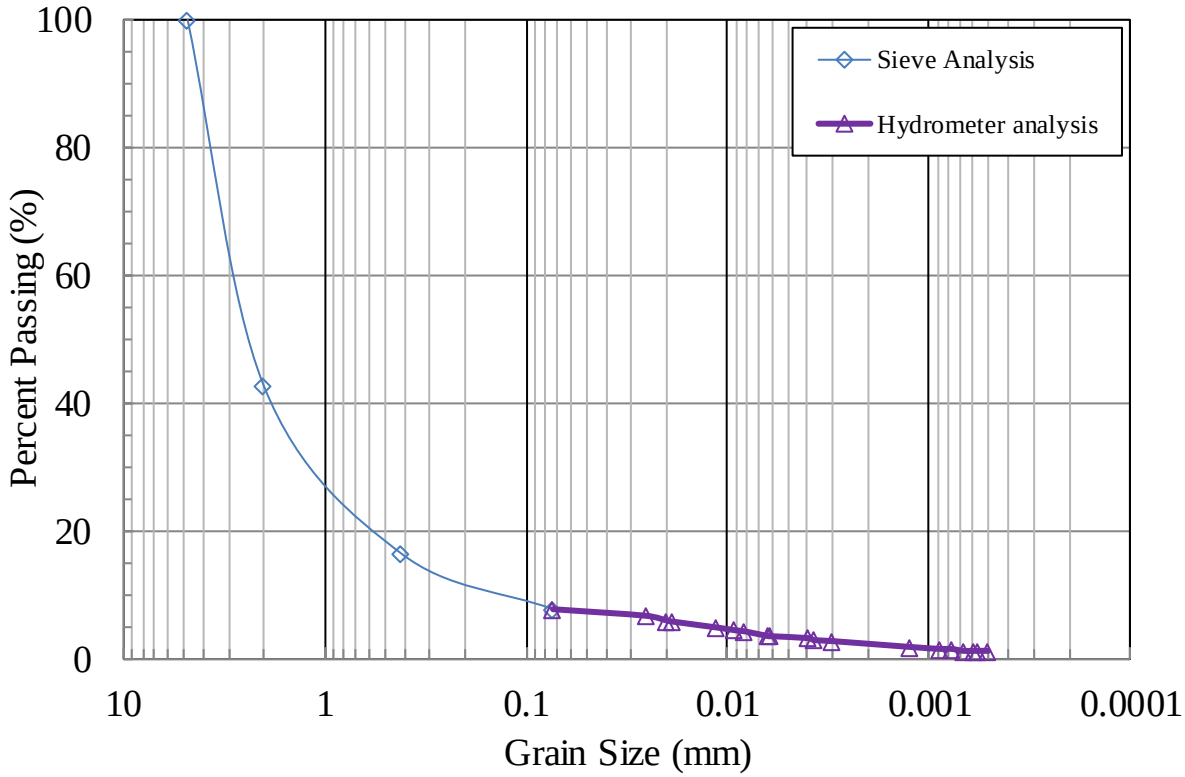

Sieve Designation	Sieve size (mm)	Grams retained	Cumulative mass retained	Grams passing	% Passing	% Retained
No. 4	4.76	0.0	0.0	985.84	100.0	0.0
No. 10	2.00	564.42	564.42	421.41	42.7	57.3
No. 40	0.42	258.45	822.87	162.97	16.5	26.2
No. 200	0.074	86.63	909.50	76.34	7.7	8.8
Pan	-	76.34	**985.84**	0.0	0.0	7.7
		985.84				

FORT PAYNE

GRAIN SIZE DISTRIBUTION			
ASTM	D 422		
Sample:	**Fort Payne**	Gs	2.64
D_{60} (mm)	2.46	Cu	19.68
D_{30} (mm)	0.90	Cc	2.63
D_{10} (mm)	0.13	CF	2.44

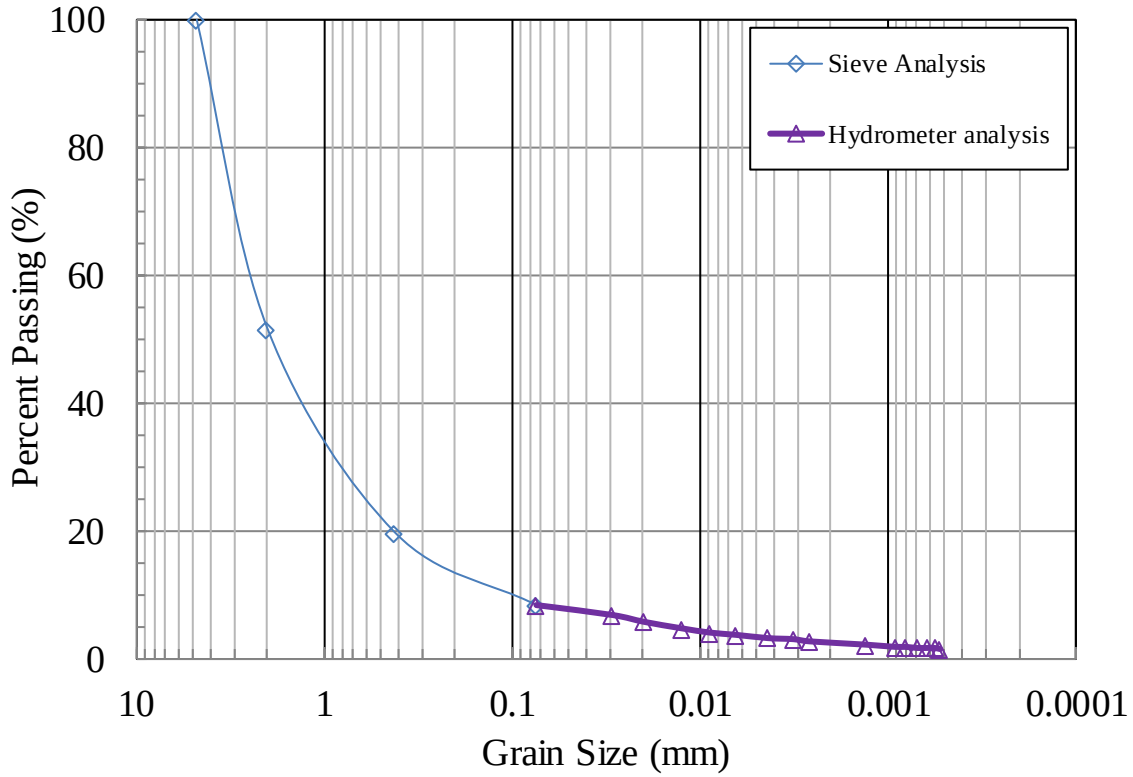

Sieve Designation	Sieve size (mm)	Grams retained	Cumulative mass retained	Grams passing	% Passing	% Retained
No. 4	4.76	0.0	0.0	985.84	100.0	0.0
No. 10	2.00	477.67	477.67	508.17	51.5	48.5
No. 40	0.42	314.83	792.50	193.34	19.6	31.9
No. 200	0.074	112.51	905.01	80.83	8.2	11.4
Pan	-	80.83	**985.84**	0.0	0.0	8.2
		985.84				

TRADEWATER

GRAIN SIZE DISTRIBUTION			
ASTM	D 422		
Sample:	**Tradewater**	Gs	2.68
D_{60} (mm)	2.55	Cu	20.40
D_{30} (mm)	0.93	Cc	2.68
D_{10} (mm)	0.13	CF	2.80

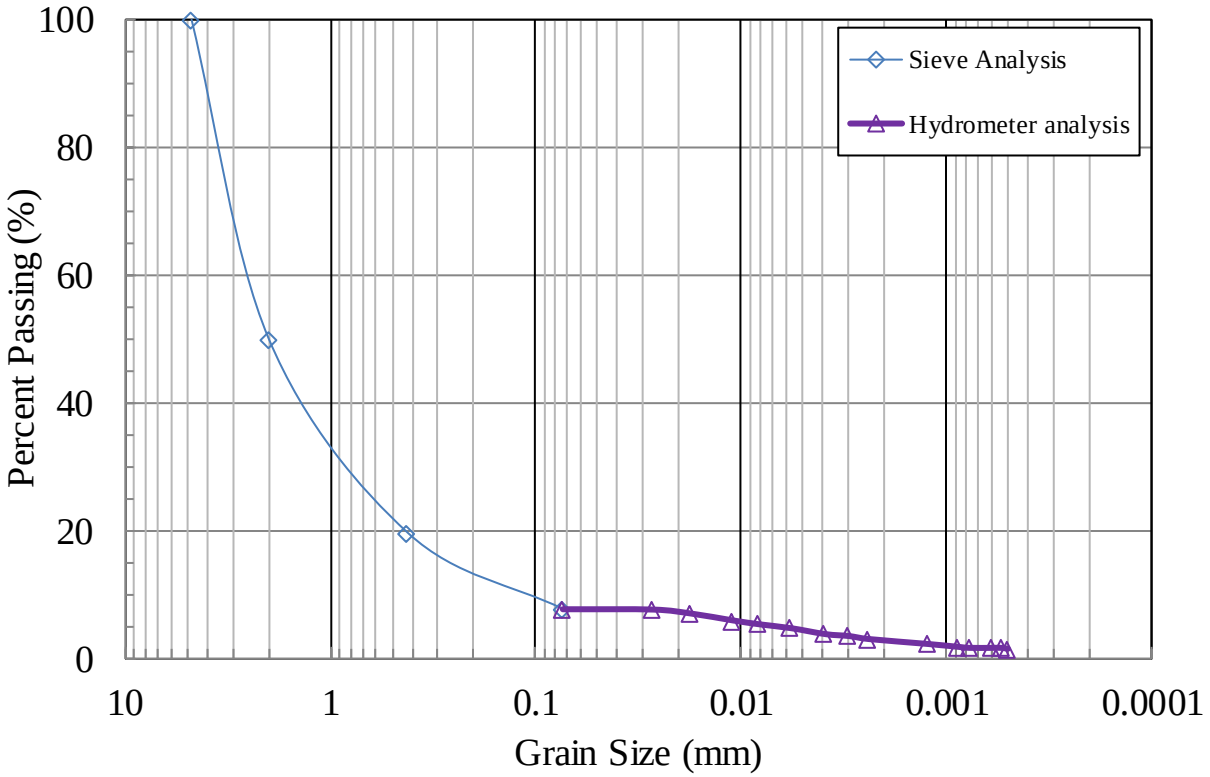

Sieve Designation	Sieve size (mm)	Grams retained	Cumulative mass retained	Grams passing	% Passing	% Retained
No. 4	4.76	0.0	0.0	985.84	100.0	0.0
No. 10	2.00	493.19	493.19	492.65	50.0	50.0
No. 40	0.42	299.48	792.67	193.17	19.6	30.4
No. 200	0.074	117.21	909.88	75.96	7.7	11.9
Pan	-	75.96	**985.84**	0.0	0.0	7.7
		985.84				

BULL FORK

GRAIN SIZE DISTRIBUTION			
ASTM	D 422		
Sample:	**Bull Fork**	Gs	2.65
D_{60} (mm)	2.23	Cu	27.81
D_{30} (mm)	0.73	Cc	2.95
D_{10} (mm)	0.08	CF	3.52

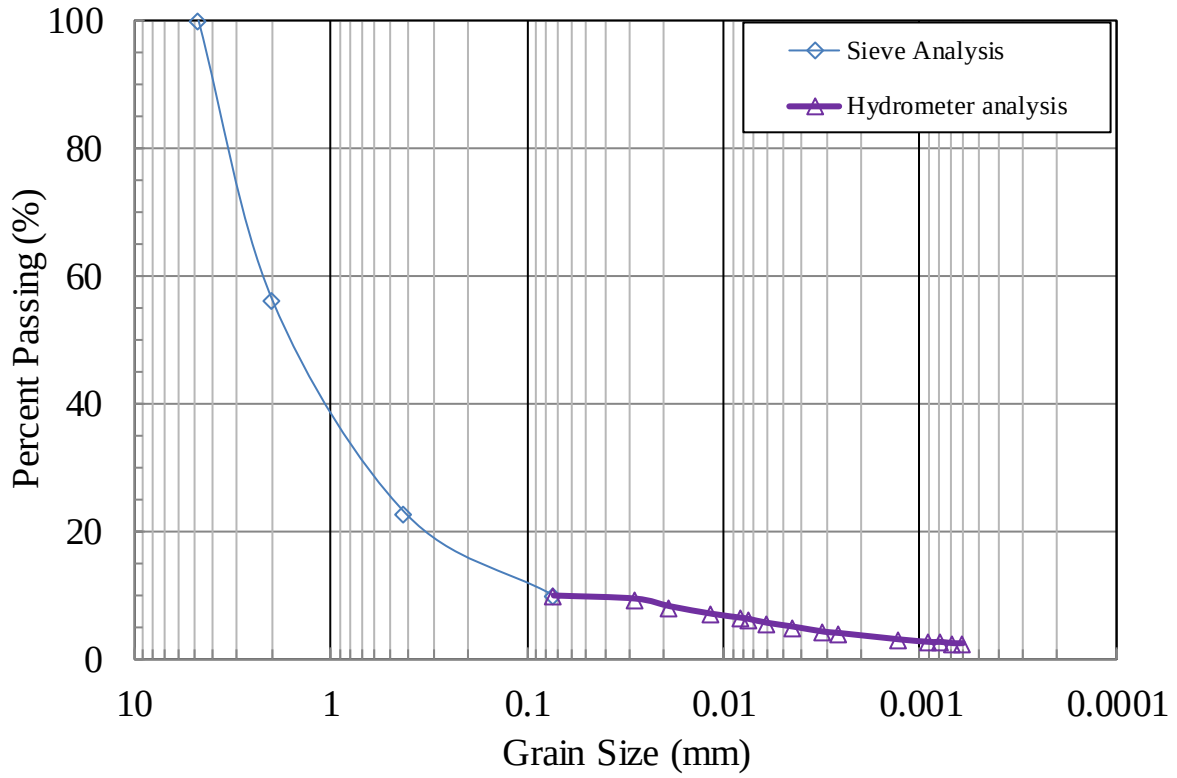

Sieve Designation	Sieve size (mm)	Grams retained	Cumulative mass retained	Grams passing	% Passing	% Retained
No. 4	4.76	0.0	0.0	985.84	100.0	0.0
No. 10	2.00	432.84	432.84	553.00	56.1	43.9
No. 40	0.42	329.33	762.18	223.66	22.7	33.4
No. 200	0.074	126.97	889.15	96.69	9.8	12.9
Pan	-	96.69	985.84	0.0	0.0	9.8
		985.84				

APPENDIX H

CIU TRIAXIAL TESTING PROCEDURE

This appendix shows the tools used and procedures followed to perform the CIU triaxial experiments.

Triaxial equipment:

The consolidated undrained triaxial compression (CIU) tests with pore pressure measurements were performed following ASTM D4767. All triaxial tests were carried out using Geocomp Triaxial testing machine Load Trac-II/Flow Trac-II system. This system fully automates a triaxial test of a soil specimen. The system consists of a LoadTrac-II load frame, two FlowTrac-II flow pumps for controlling volume and pressure for the cell and specimen, a computer with a network card for test control and data acquisition, and Microsoft Windows application software, called TRIAXIAL, for controlling a test and creating a report of the results.

Figure G1. Picture of the Geocomp machine.

After a soil specimen is in place and the test conditions selected, the system runs the entire triaxial test automatically. The test data is stored in a file for reduction and analysis of the results. The system can perform isotropic and anisotropic consolidations tests as well as undrained and drained triaxial tests. The tests can be performed stress or strain controlled. Figure 3.12 shows the The GeoComp machine system Load Trac-II. The procedure followed to make the specimen is presented below.

1. A pedestal with a base and a top cap of 70 mm diameter is shown:

2. Prepare the tools that will be used to make the specimens are shown below:

3. Clean and dry carefully the triaxial cell, the pedestal and all the tubes.

4. Apply vacuum grease to the base cap of the cell pedestal and the top cap:

5. Put a dry porous stone and filter paper over the base cap of the pedestal:

6. Place the membrane and secure the membrane with the O-rings. Put one O-ring in the ridge along the circumference of the base cap. Put the second O-ring below the ridge at the base of the base cap:

7. Put the split cylinder mold on the base cap, connect to vacuum and adjust the membrane in the mold:

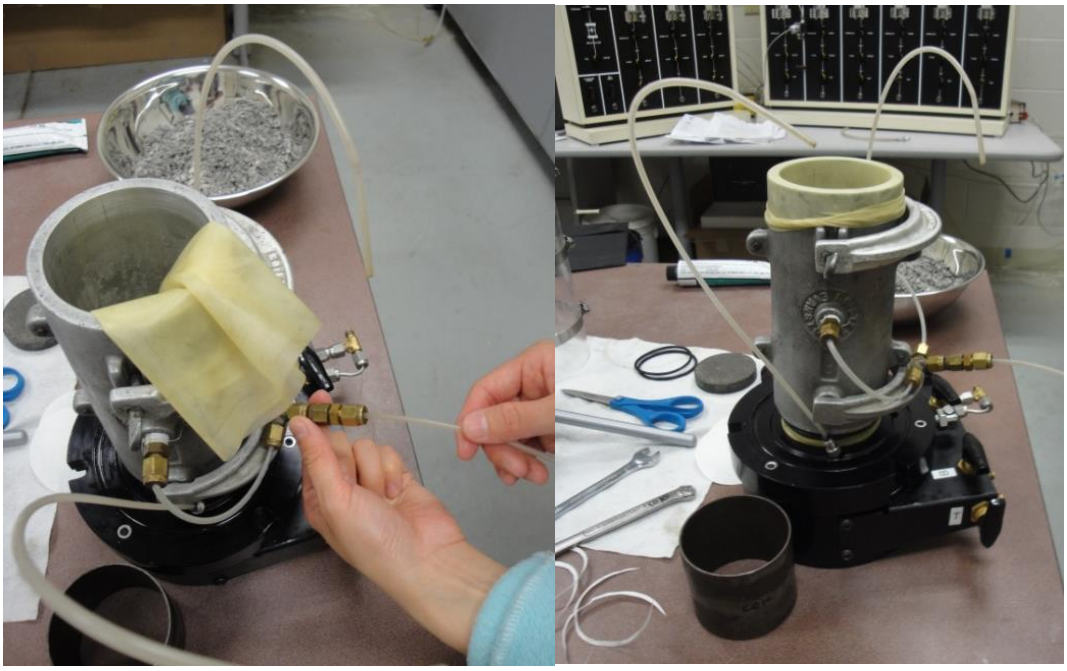

8. Separate the crushed shale in sizes in portions with the sizes Pan, retained No. 200 sieve size, retained No. 40 sieve size, retained No. 10 size – passed No. 4 sieve size:

9. Weight and mix each portion in order to reach the target GSD and pouring inside the mold.

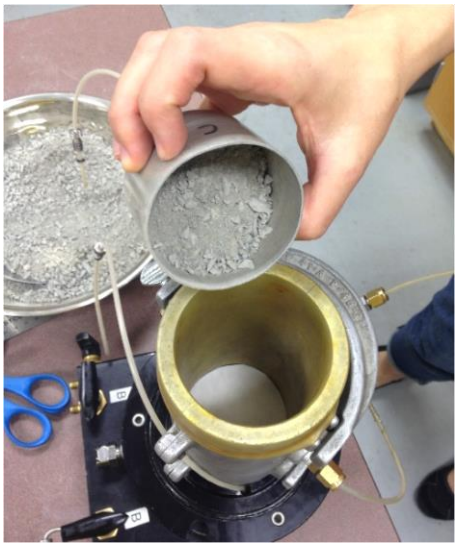

10. Compact the crushed shale inside the mold using a hammer of 838 g:

11. Place the dry filter paper and the dry porous stone:

12. Place the top cap:

13. Fold down the membrane over the top cap and place one o-ring on the ridge of the top cap and the other o-ring above the ridge.


14. Adjust the membrane in the top cap and open the split mold:


15. Take the dimensions of the specimen:

16. Place the chamber over the triaxial cell pedestal, leaving the vacuum, and fill the cell with tap water.

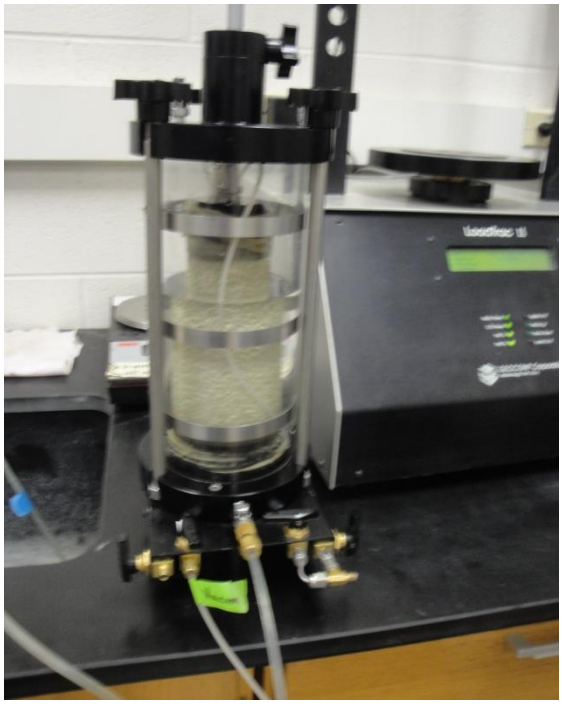

17. Place the triaxial cell on LoadTrac II. Connect the chamber with the cell pressure pump applying a pressure between 20.68 kPa to 34.47 kPa (3 psi to 5 psi). Closing bottom and top specimen valves, disconnect the vacuum and connect the specimen with the pore pressure pump in the bottom valve. Connect a top specimen valve with an open tube, such that the specimen at the top be at atmospheric pressure:

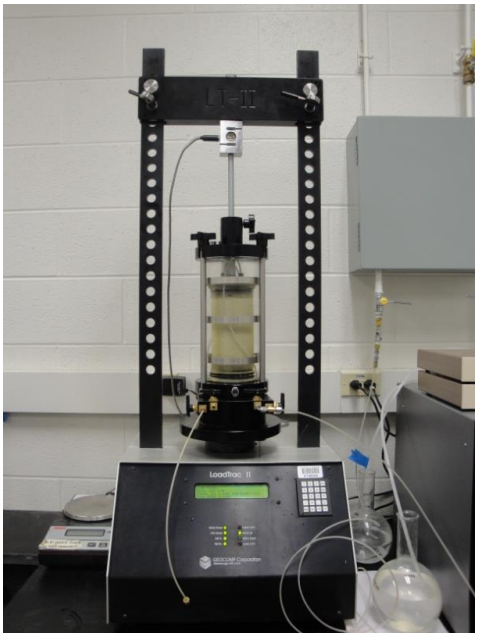


18. In this moment the specimen is dry and ready to start the test.

19. Because the specimen had to be soaking during different periods of time, the procedure to do the test had some differences with respect to the standard instructions followed for CIU triaxial tests. The procedure to follow is presented below:

a. Fill the Project and Specimen menus with the relevant information about the specimen.

b. Go to the Read Table menu. This menu controls the reading schedule to register the data of the steps of Initialization, Saturation, Consolidation and Shear. The reading table of Initialization, Saturation and Consolidation was “controlling time” and the reading table was controlling strain. These were the reading schedules:

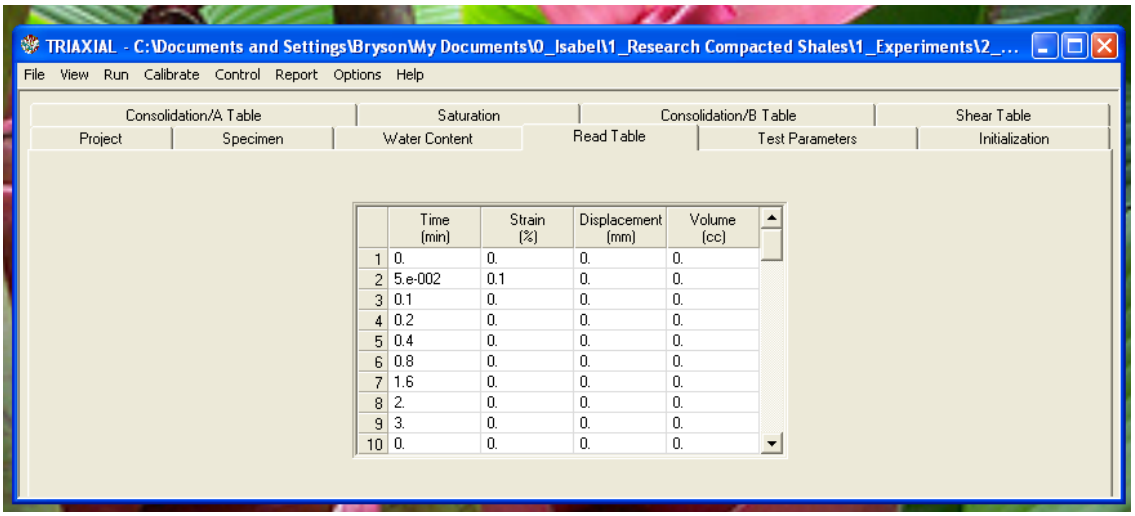

c. Go to Initialization menu. This menu sets the initial cell and specimen pressure, the stress rate, and the duration of the socking. One target of this step was that the cell pressure to be 20.68 kPa (3 psi) and the specimen pressure to be 13.79 kPa (2 psi); therefore, the effective stress of the specimen was 6.89 kPa (1 psi). The duration of this menu depended on the target soaking times (i.e. zero, six, 12 or 20 days):

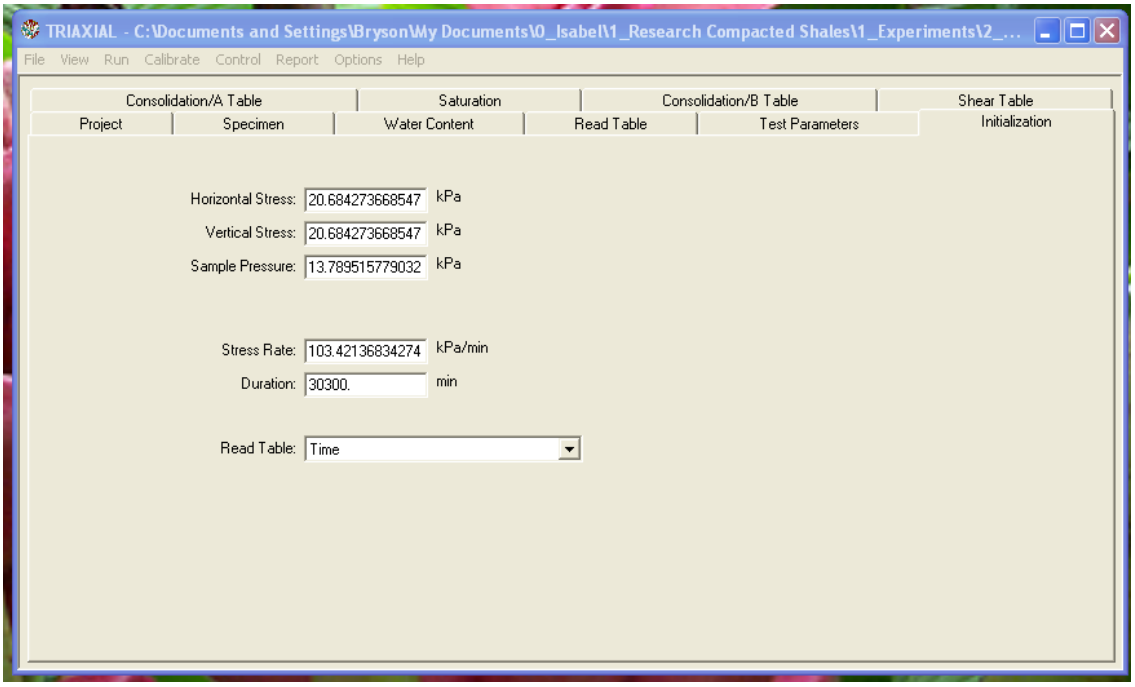

d. Go to Saturation menu. This menu controls the saturation of the specimen. The targets of this step were: the specimen remained with an effective stress of 6.89 kPa (1 psi); the B were greater than 0.95; and the cell pressure be at the end of the saturation between 68.95 kPa (10 psi) to 482.63 kPa (70 psi):

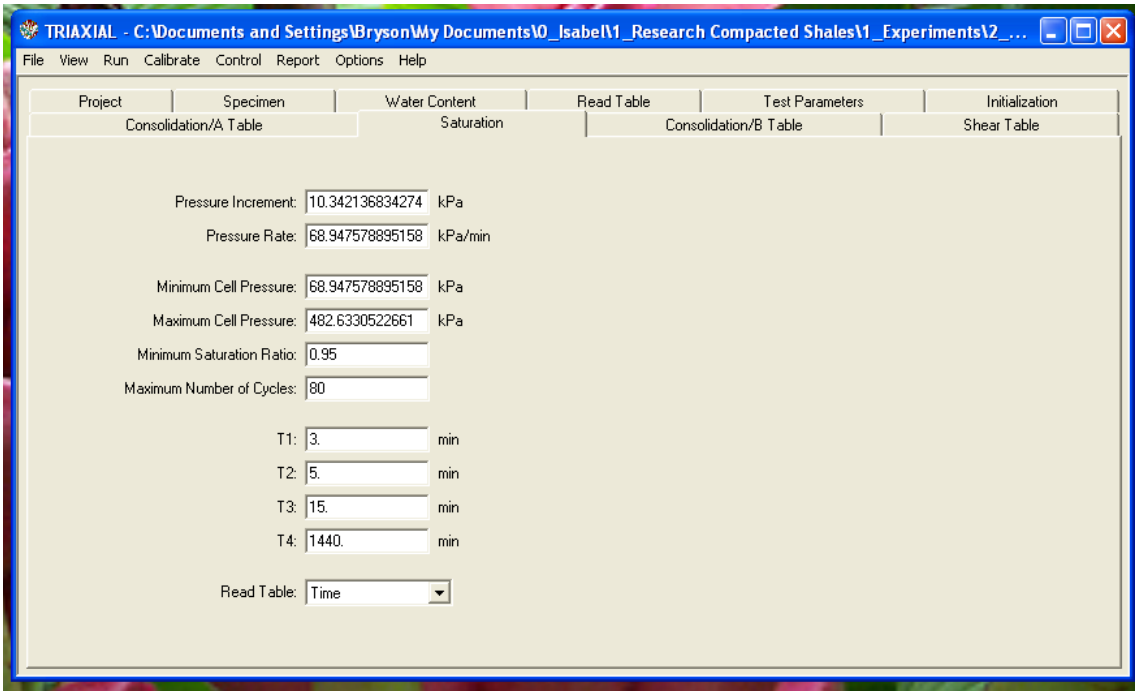

e. Go to Consolidation menu. This menu controls how the consolidation was performed. An initial increment of the effective stress of 6.89 kPa (1 psi) to 344.73 kPa (50 psi) was applied. An unload to 68.95 kPa (10 psi) and reload of 517.11 kPa (75 psi) were applied. The IC was performed by controlling the cell pressure. The cell pressure was incremented continually at a low rate of 1.38 kPa/min. The increment in the pressure of the cell was small enough that the specimen had time to dissipate the increment in the pore pressure produced in the specimen and the increment in the effective stress was the same as the increment in the total stress. This is the table:

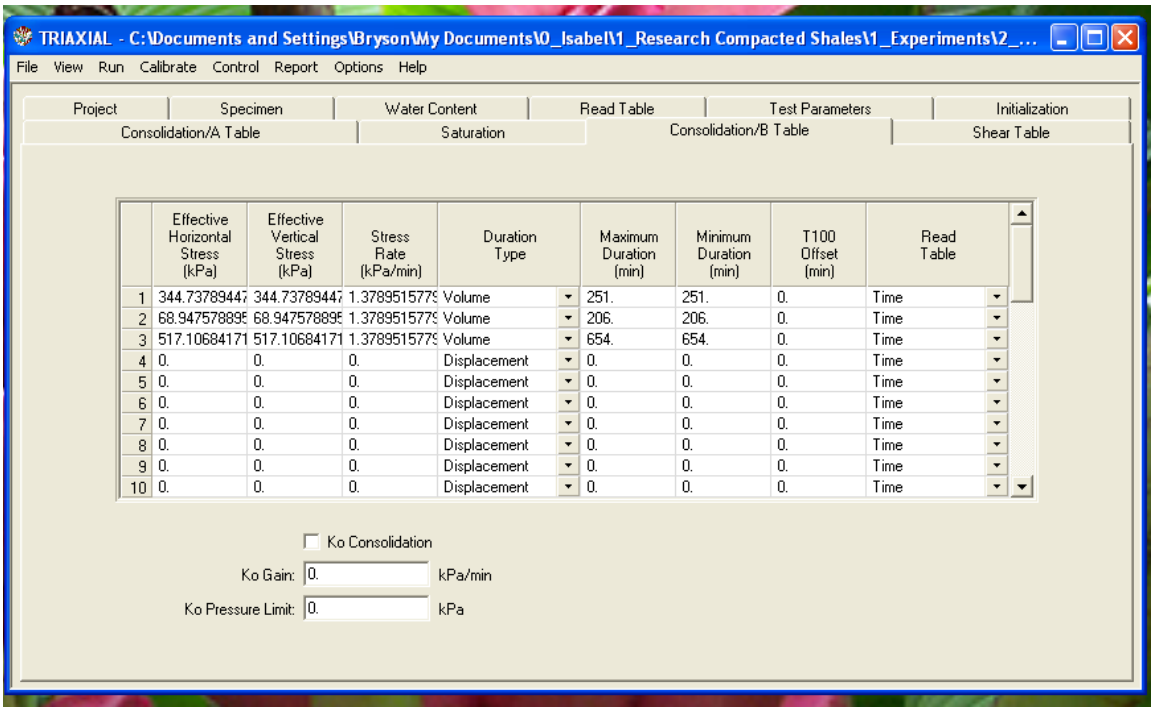

f. Go to the Shear menu. This menu controls the shear. It has the possibility to be drained or undrained, and isotropic or anisotropic. The objective of this step was to shear the specimens under undrained condition controlling the strain. The Axial displacement was at a rate of 0.2%/min until the specimen reached an axial strain of 30 percent:

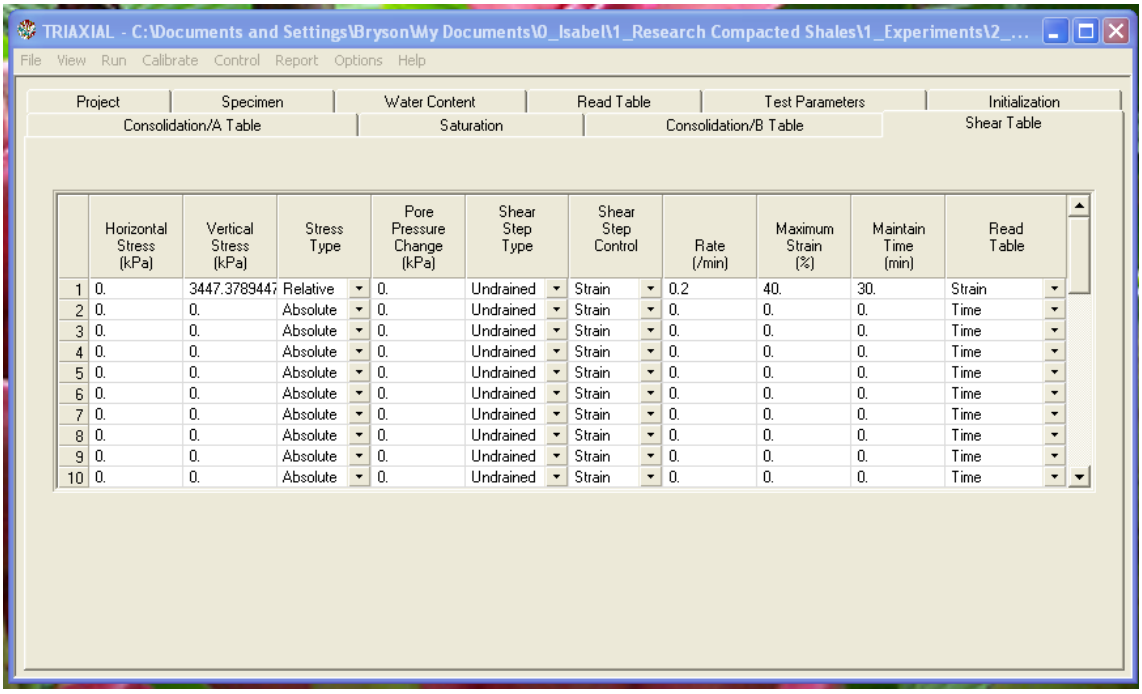

	Horizontal Stress (kPa)	Vertical Stress (kPa)	Stress Type	Pore Pressure Change (kPa)	Shear Step Type	Shear Step Control	Rate (/min)	Maximum Strain (%)	Maintain Time (min)	Read Table
1	0.	3447.3789447	Relative	0.	Undrained	Strain	0.2	40.	30.	Strain
2	0.	0.	Absolute	0.	Undrained	Strain	0.	0.	0.	Time
3	0.	0.	Absolute	0.	Undrained	Strain	0.	0.	0.	Time
4	0.	0.	Absolute	0.	Undrained	Strain	0.	0.	0.	Time
5	0.	0.	Absolute	0.	Undrained	Strain	0.	0.	0.	Time
6	0.	0.	Absolute	0.	Undrained	Strain	0.	0.	0.	Time
7	0.	0.	Absolute	0.	Undrained	Strain	0.	0.	0.	Time
8	0.	0.	Absolute	0.	Undrained	Strain	0.	0.	0.	Time
9	0.	0.	Absolute	0.	Undrained	Strain	0.	0.	0.	Time
10	0.	0.	Absolute	0.	Undrained	Strain	0.	0.	0.	Time

20. After configuring the software, it was started:

    a. The software gives the option to fill the pumps. However, this option was not selected because the specimen was flooded during 3 pump cycles. Also, the software gives the option to adjust the Piston. This option was chosen. This procedure was followed because the objective was to register all the process of flooding.

    b. Open the bottom valve that is connected to the specimen pressure pump and the top valve that is connected to air. This started pumping water into the specimen through the bottom valve. Because the specimen was under vacuum, when the top valve was open the volume of the specimen changed. For Type 1 shales the flooding took 1 hour, and for Type 2 shales the flooding took more time.

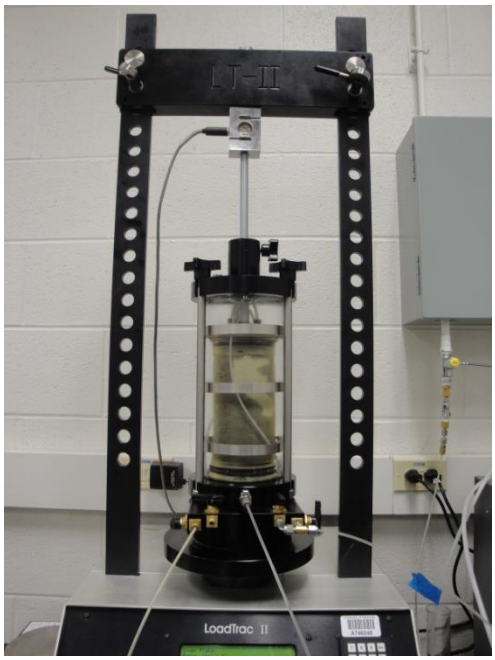

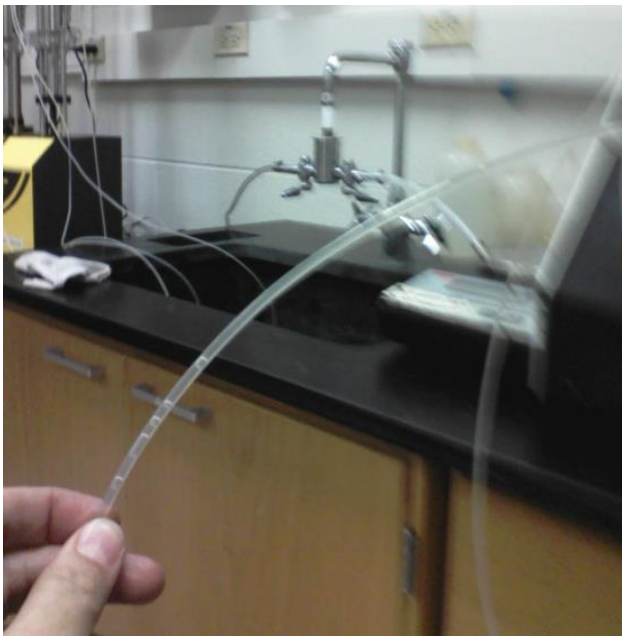

c. After flooding during 3 pump cycles, the top valve was closed and the specimen was left soaking during the times that were scheduled. From this point, the software took control of the test:

d. When the test finished the specimen had this appearance:

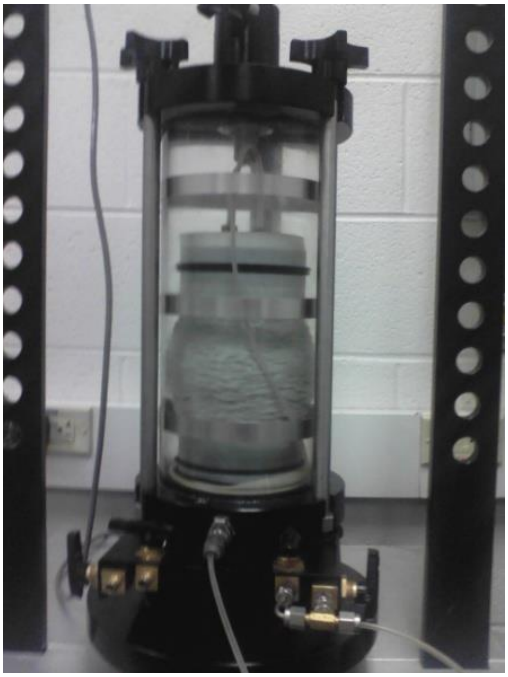

e. The specimen was unmounted and the moisture content of the specimen was calculated:

APPENDIX I

STRESS PATH

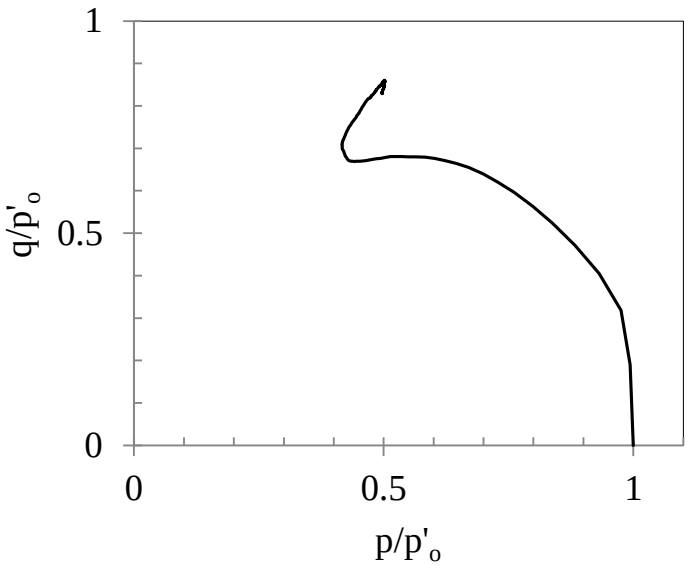
1
0.5
0
0
0.5
1
q/p'o
p/p'o

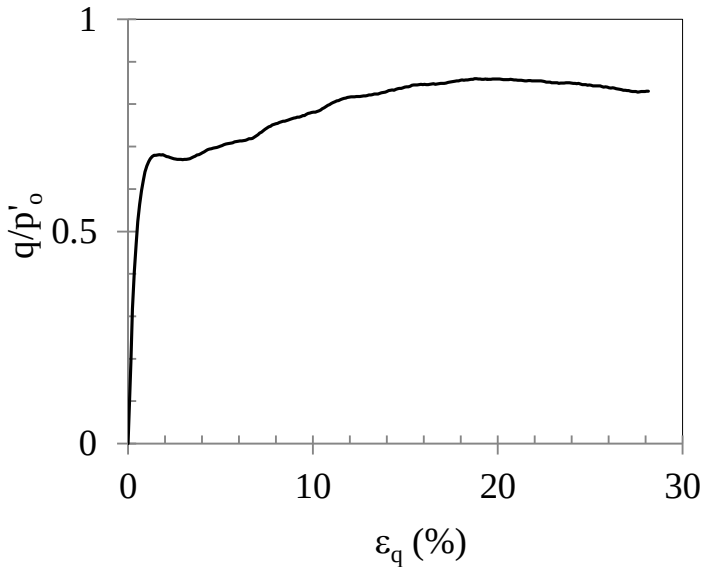
1
0.5
0
0
10
20
30
q/p'o
εq (%)

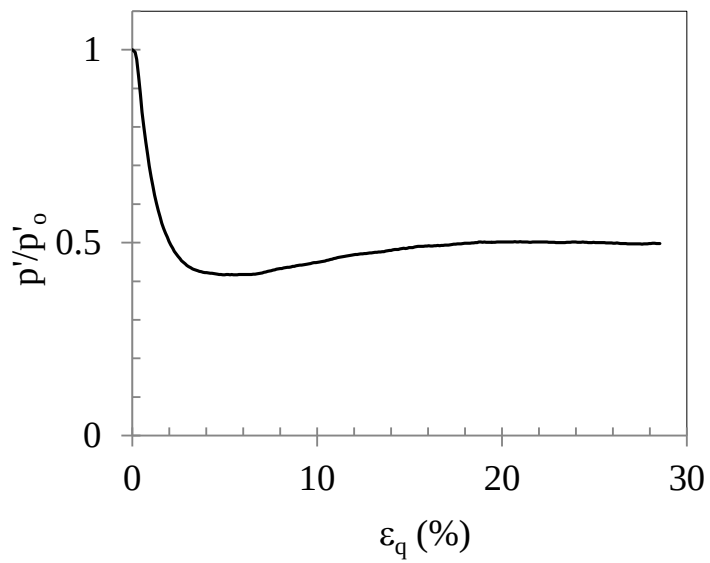
1
0.5
0
0
10
20
30
p'/p'o
εq (%)

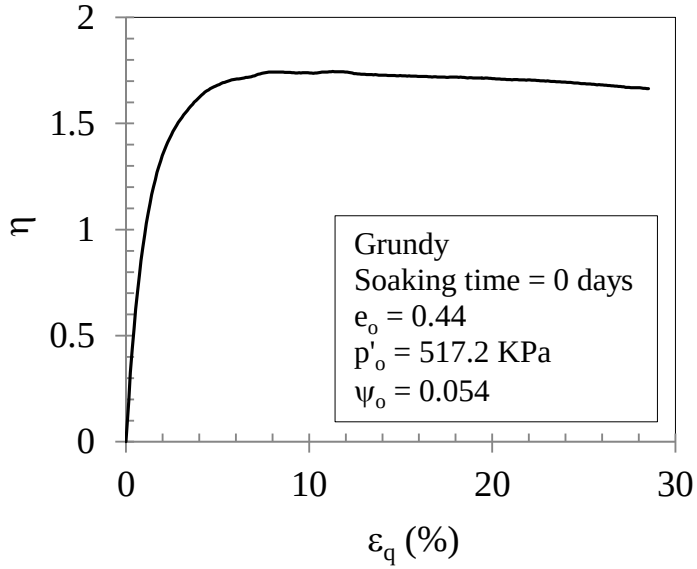
2
1.5
1
0.5
0
0
10
20
30
η
εq (%)
Grundy
Soaking time = 0 days
eo = 0.44
p'o = 517.2 KPa
ψo = 0.054

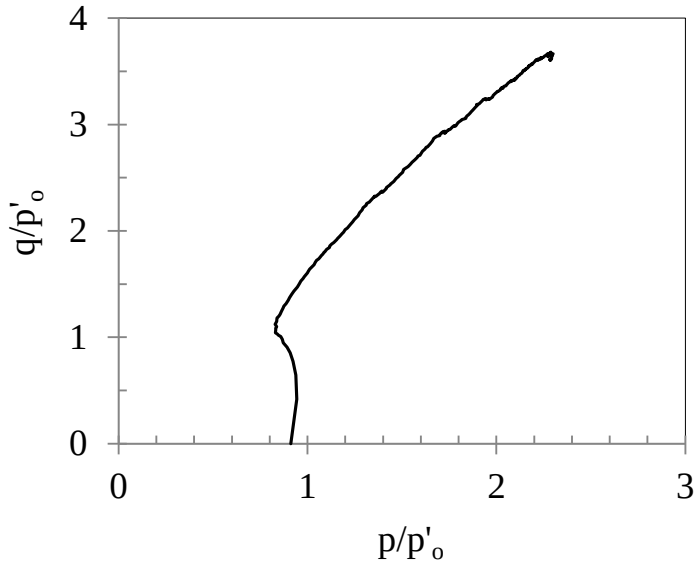
4
3
2
1
0
q/p'o
0
1
2
3
p/p'o

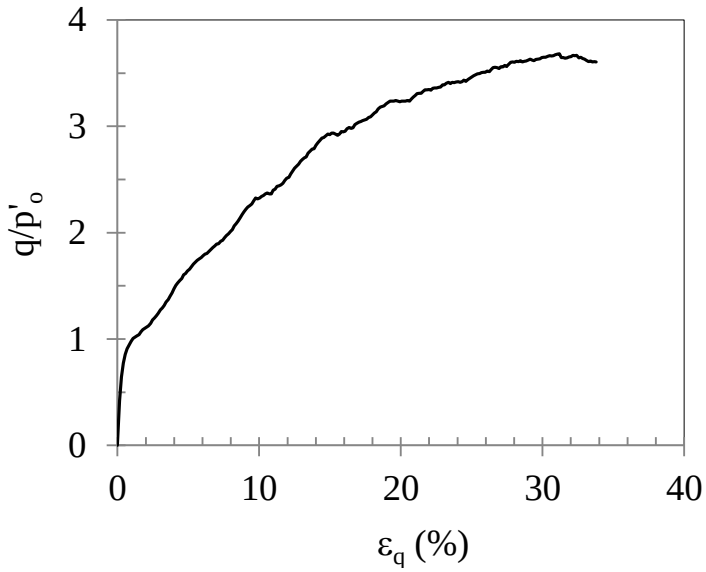
4
3
2
1
0
q/p'o
0
10
20
30
40
εq (%)

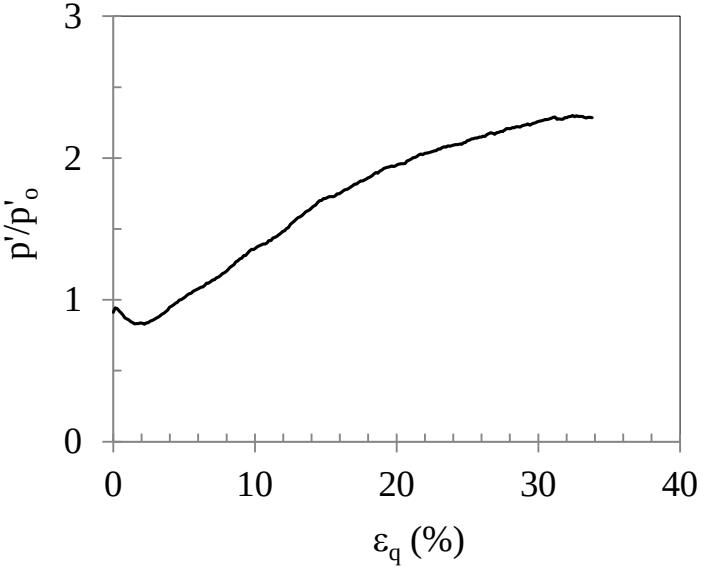
3
2
1
0
p'/p'o
0
10
20
30
40
εq (%)

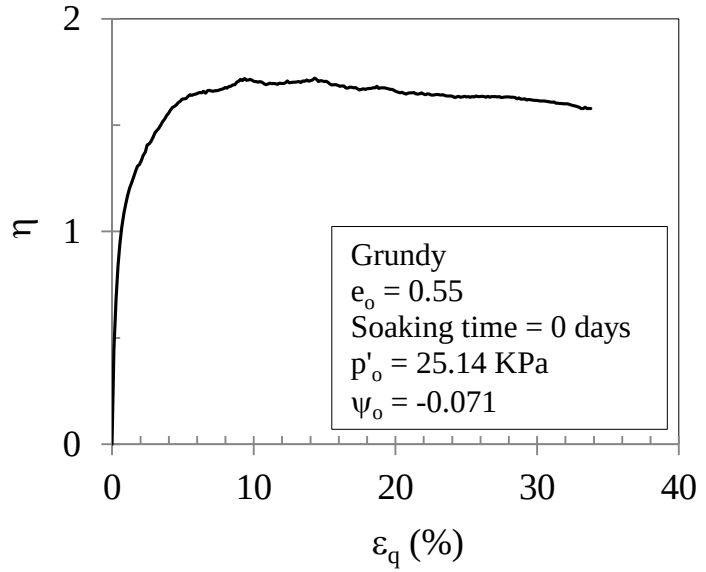
2
1
0
η
0
10
20
30
40
εq (%)
Grundy
eo = 0.55
Soaking time = 0 days
p'o = 25.14 KPa
ψo = -0.071

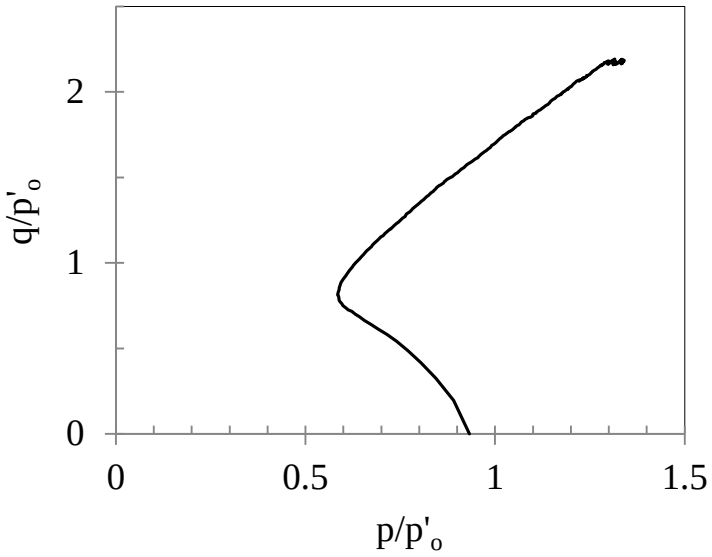
q/p'o
p/p'o
0
0.5
1
1.5
0
1
2

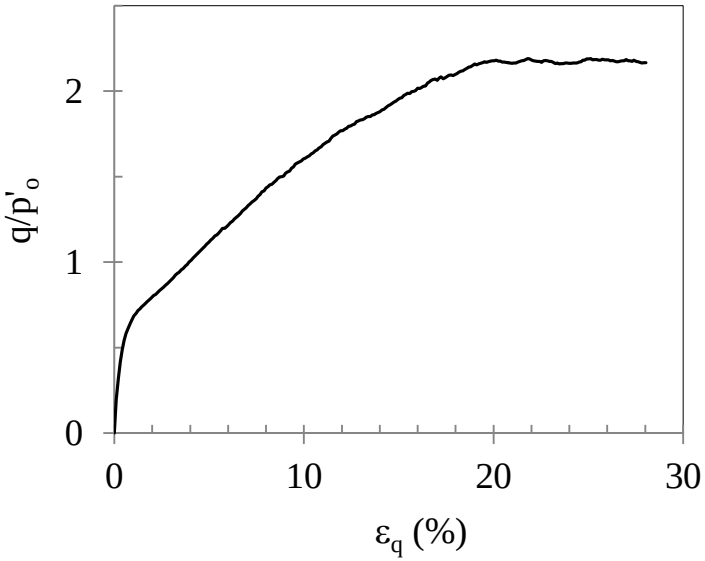
q/p'o
εq (%)
0
10
20
30
0
1
2

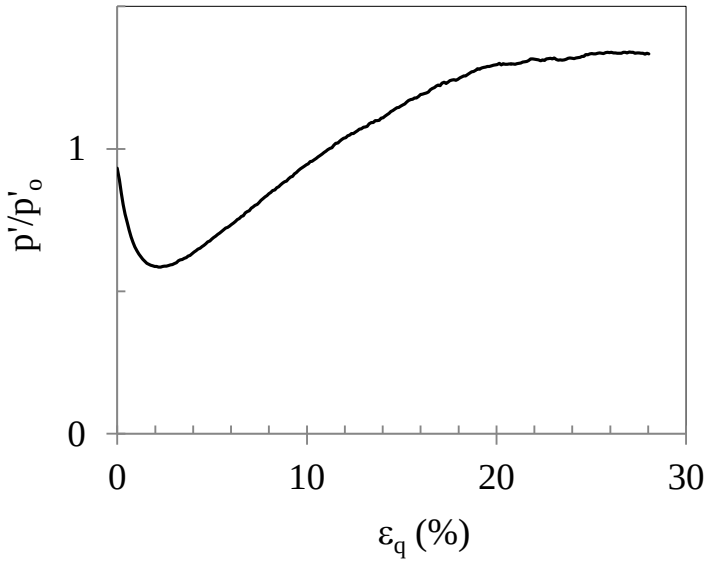
p'/p'o
εq (%)
0
10
20
30
0
1

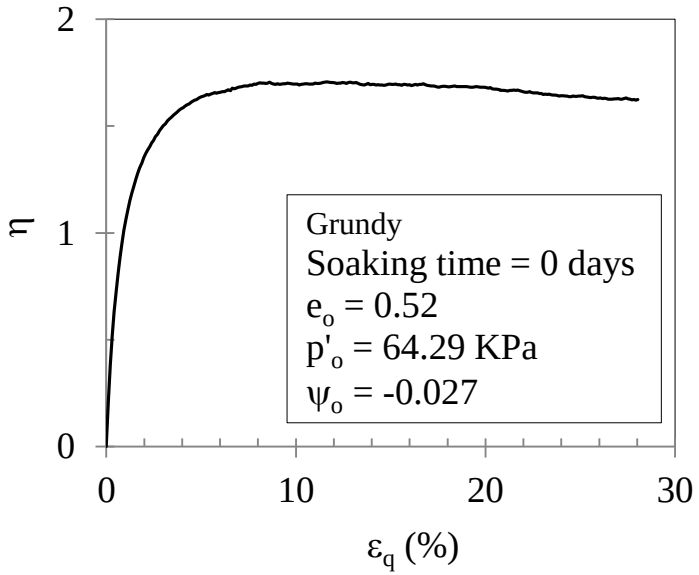
η
εq (%)
0
10
20
30
0
1
2
Grundy
Soaking time = 0 days
eo = 0.52
p'o = 64.29 KPa
ψo = -0.027

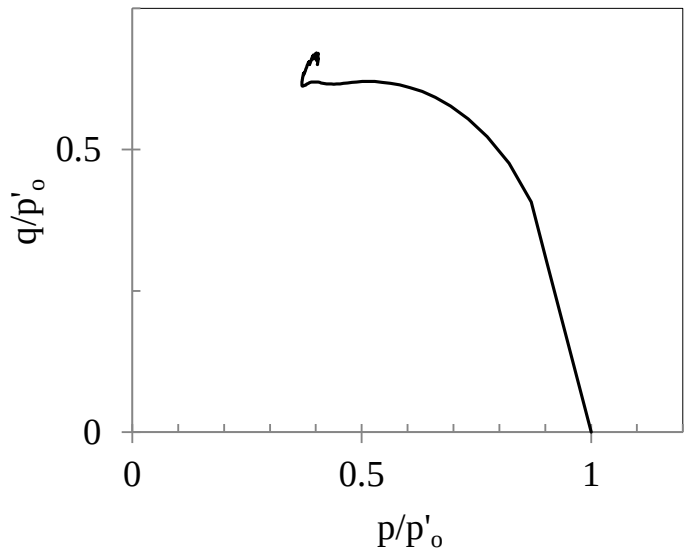
q/p'o
0.5
0
0
0.5
1
p/p'o

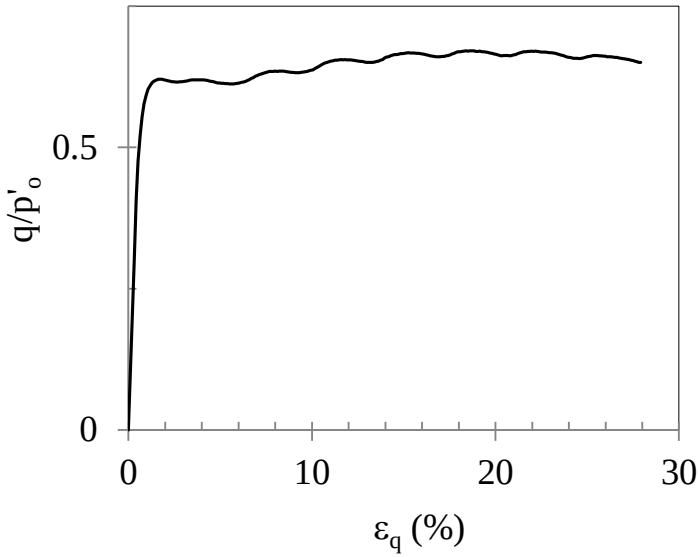
q/p'o
0.5
0
0
10
20
30
εq (%)

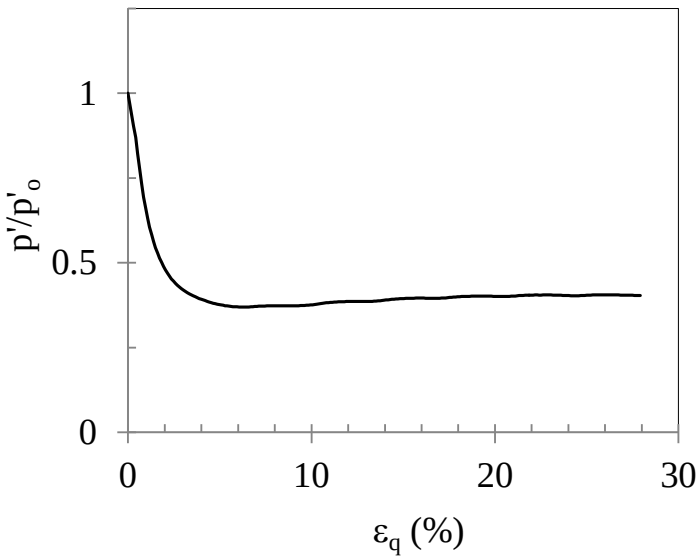
p'/p'o
1
0.5
0
0
10
20
30
εq (%)

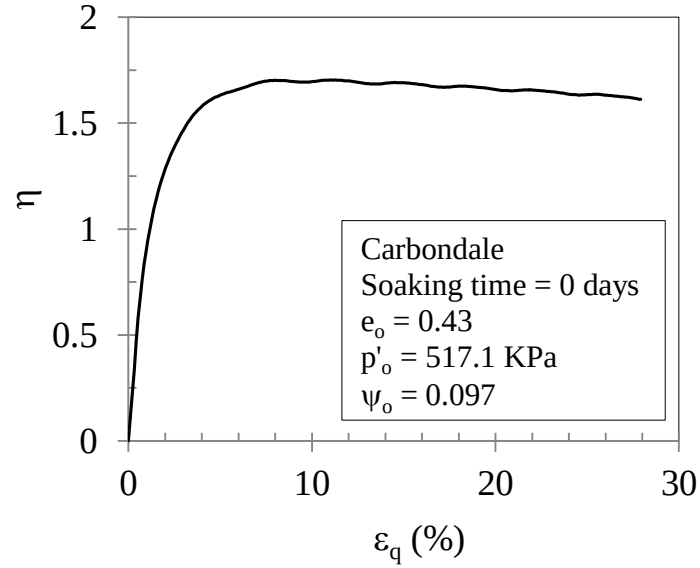
η
2
1.5
1
0.5
0
0
10
20
30
εq (%)
Carbondale
Soaking time = 0 days
eo = 0.43
p'o = 517.1 KPa
ψo = 0.097

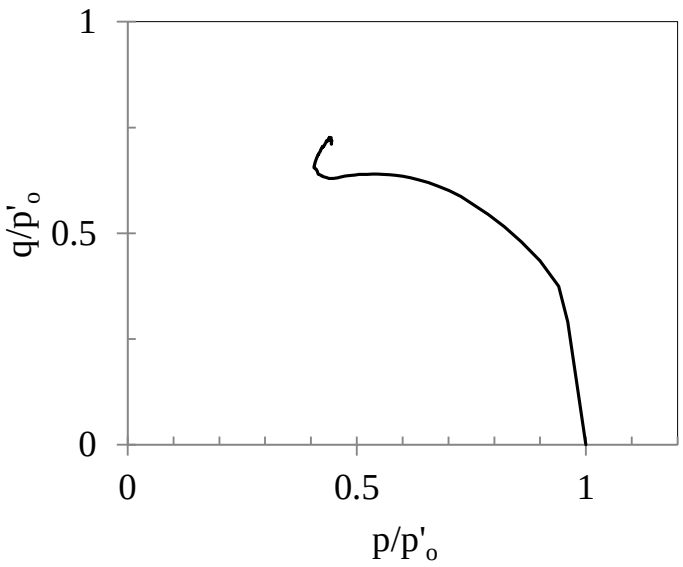
1
0.5
0
q/p'o
0
0.5
1
p/p'o

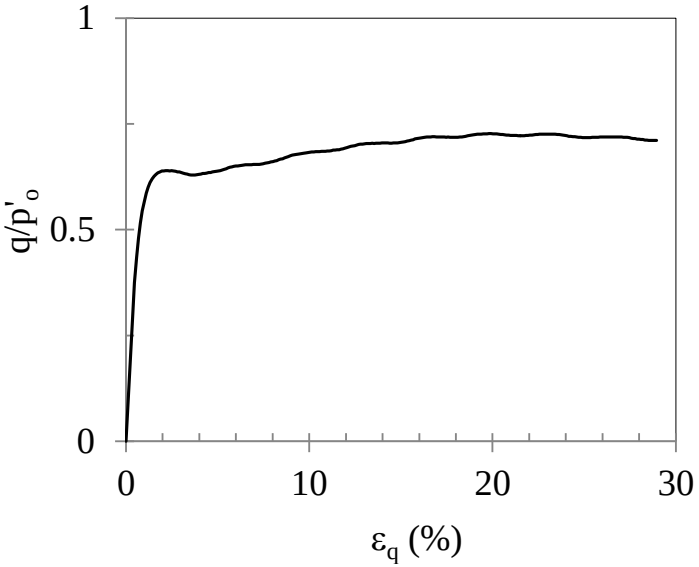
1
0.5
0
q/p'o
0
10
20
30
εq (%)

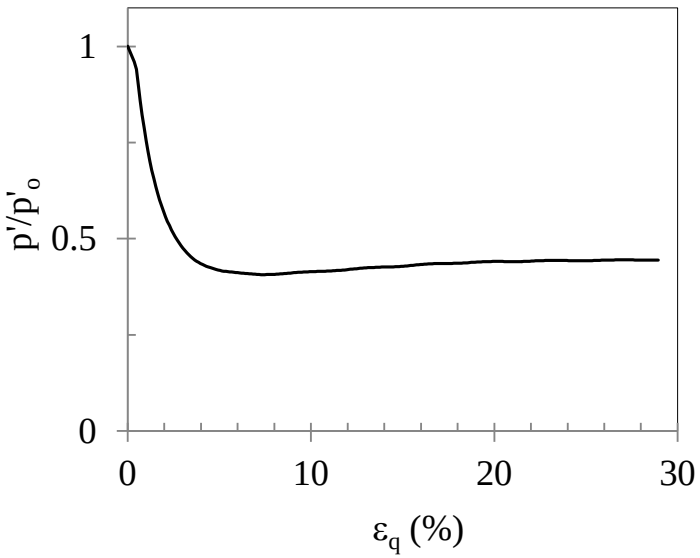
1
0.5
0
p'/p'o
0
10
20
30
εq (%)

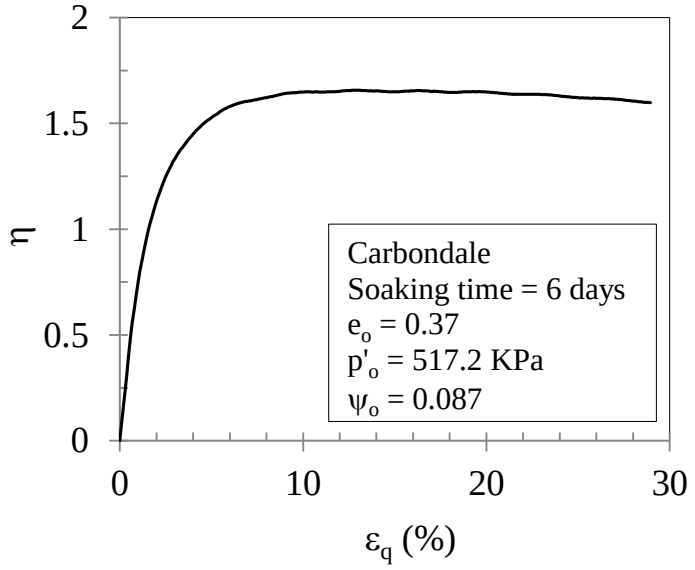
2
1.5
1
0.5
0
η
0
10
20
30
εq (%)
Carbondale
Soaking time = 6 days
eo = 0.37
p'o = 517.2 KPa
ψo = 0.087

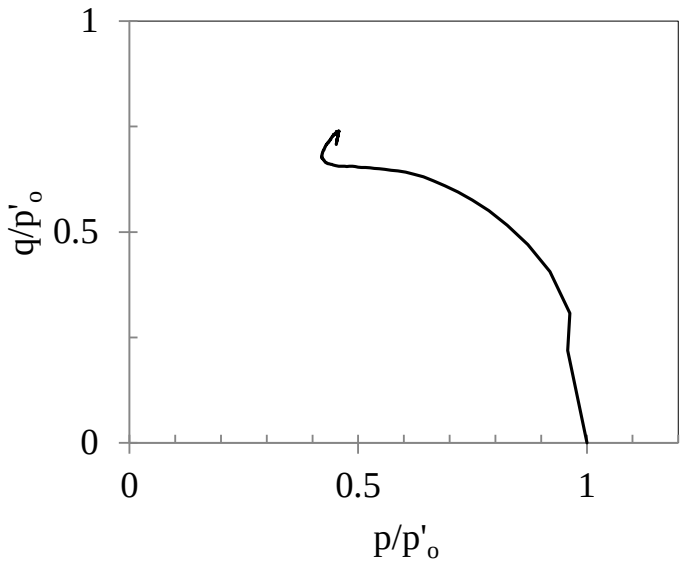
1
0.5
0
q/p'o
0
0.5
1
p/p'o

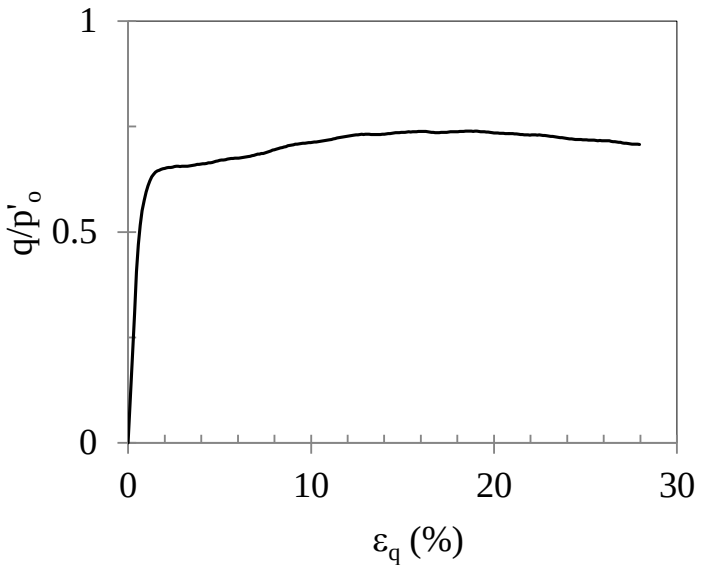
1
0.5
0
q/p'o
0
10
20
30
εq (%)

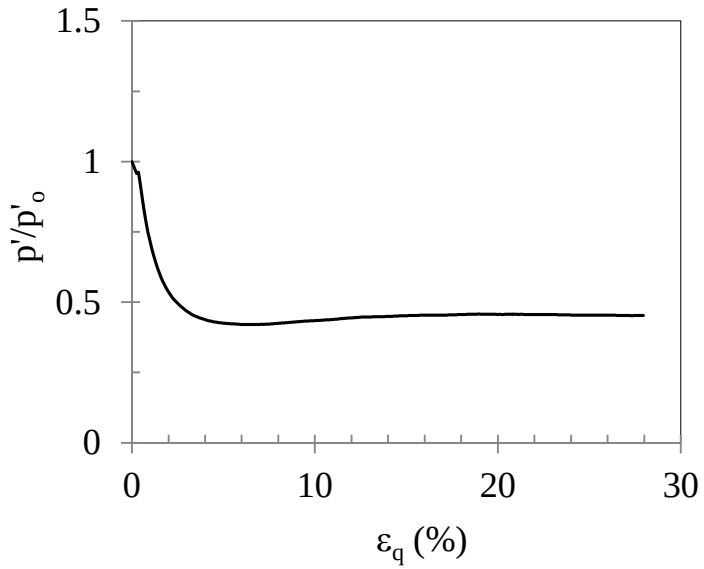
1.5
1
0.5
0
p'/p'o
0
10
20
30
εq (%)

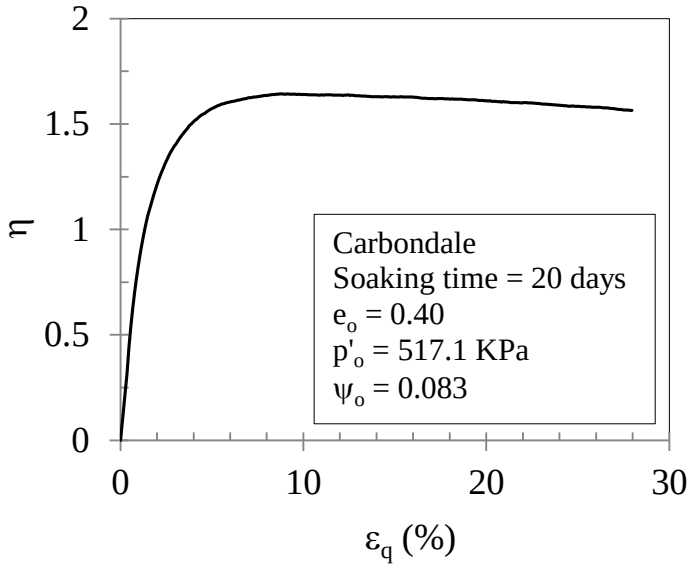
2
1.5
1
0.5
0
η
0
10
20
30
εq (%)
Carbondale
Soaking time = 20 days
eo = 0.40
p'o = 517.1 KPa
ψo = 0.083

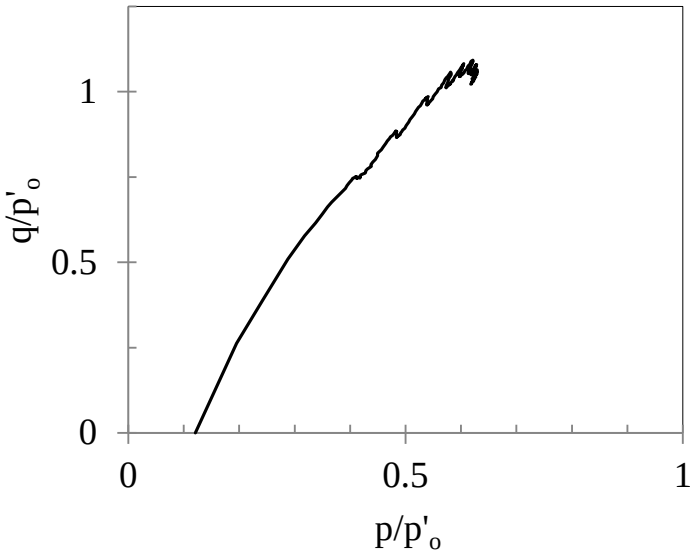
q/p'o
1
0.5
0
0
0.5
1
p/p'o

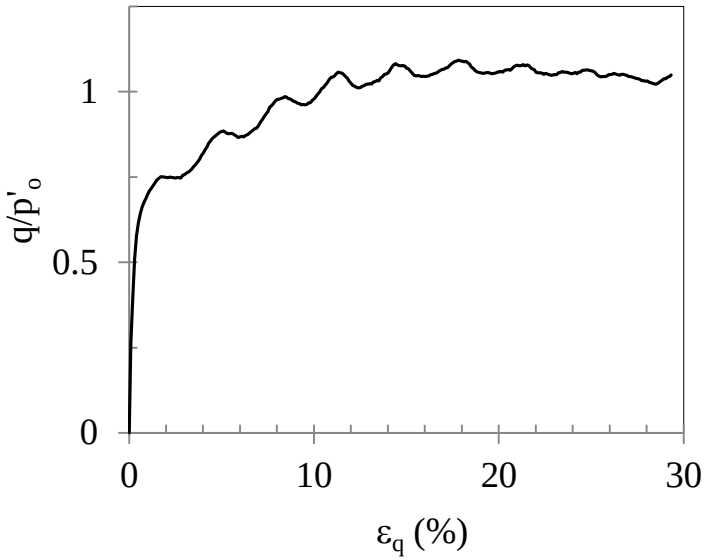
q/p'o
1
0.5
0
0
10
20
30
εq (%)

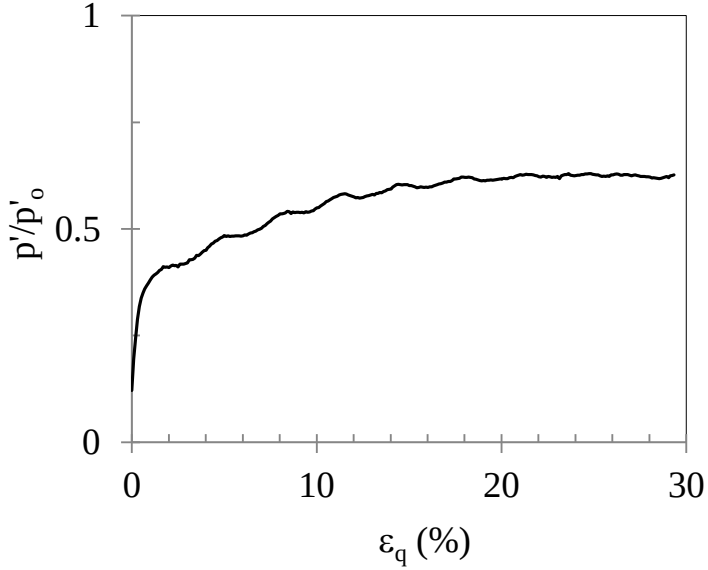
p'/p'o
1
0.5
0
0
10
20
30
εq (%)

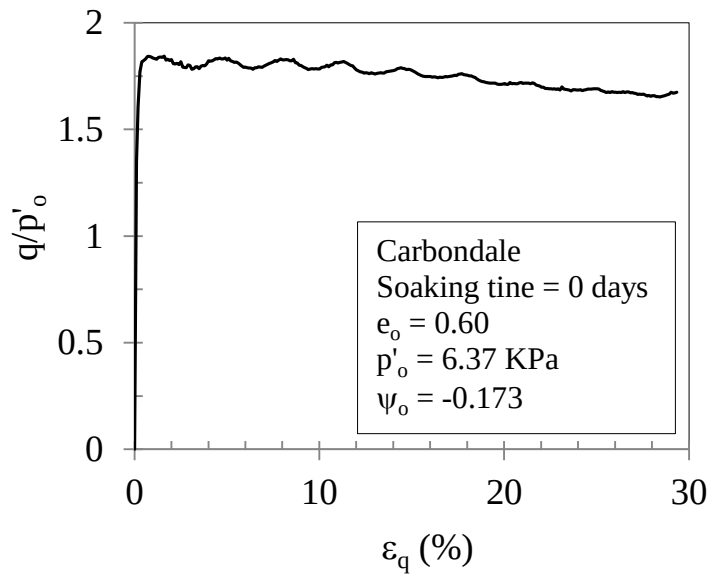
q/p'o
2
1.5
1
0.5
0
0
10
20
30
εq (%)
Carbondale
Soaking tine = 0 days
eo = 0.60
p'o = 6.37 KPa
ψo = -0.173

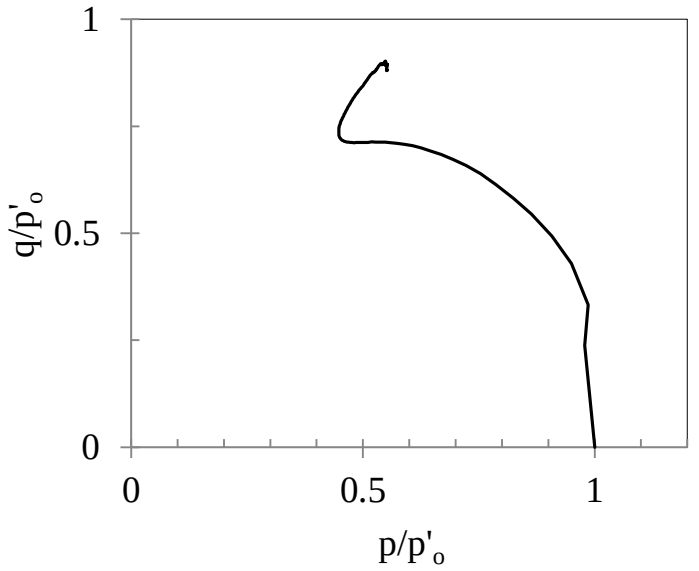
1
0.5
0
q/p'o
0
0.5
1
p/p'o

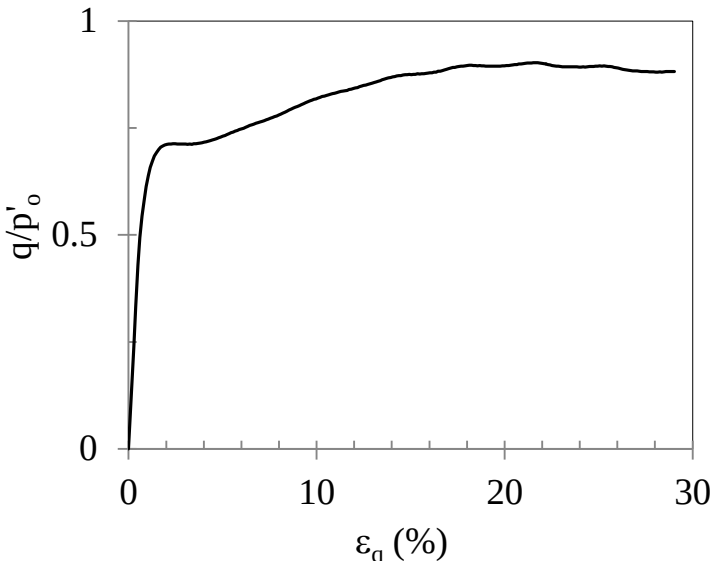
1
0.5
0
q/p'o
0
10
20
30
εa (%)

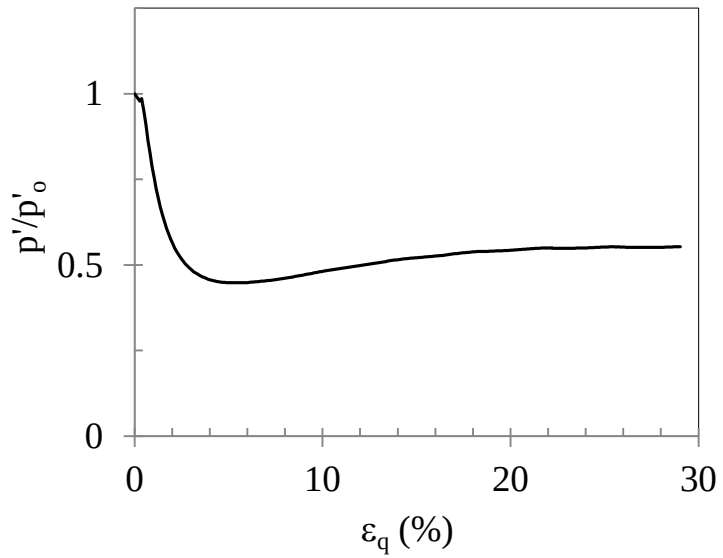
1
0.5
0
p'/p'o
0
10
20
30
εq (%)

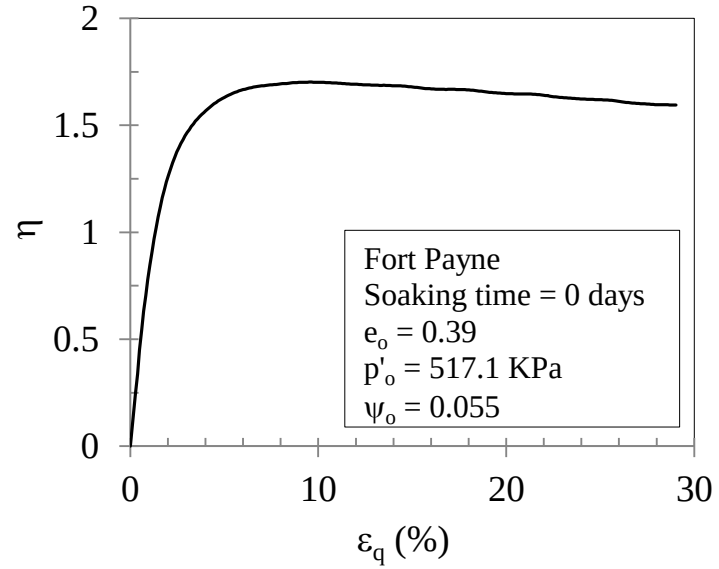
2
1.5
1
0.5
0
η
0
10
20
30
εq (%)
Fort Payne
Soaking time = 0 days
eo = 0.39
p'o = 517.1 KPa
ψo = 0.055

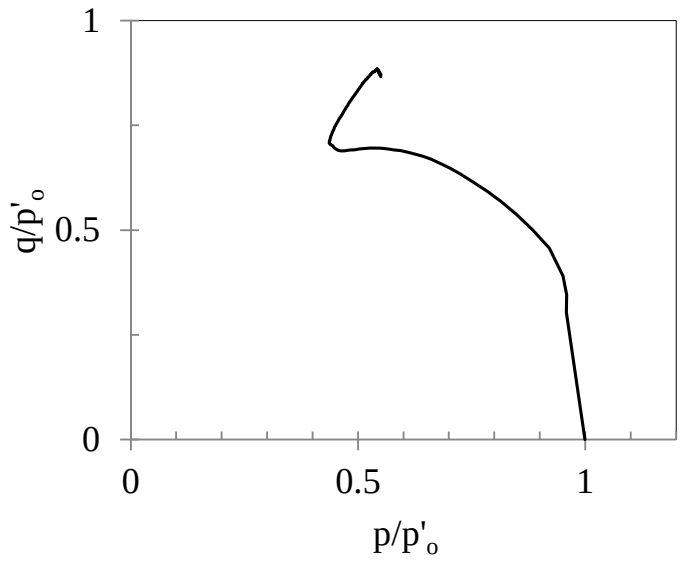
1
0.5
0
q/p'o
0
0.5
1
p/p'o

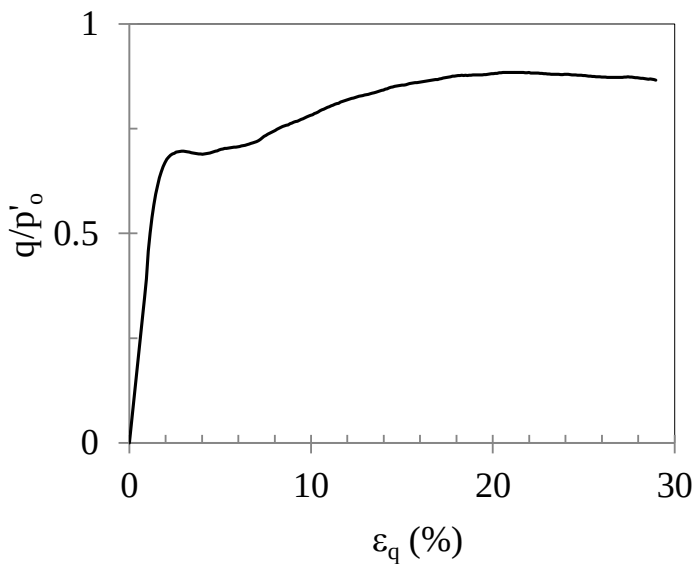
1
0.5
0
q/p'o
0
10
20
30
εq (%)

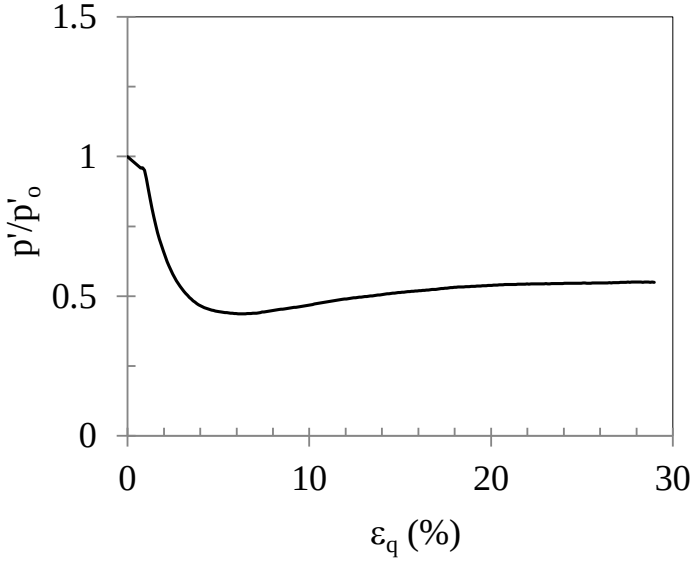
1.5
1
0.5
0
p'/p'o
0
10
20
30
εq (%)

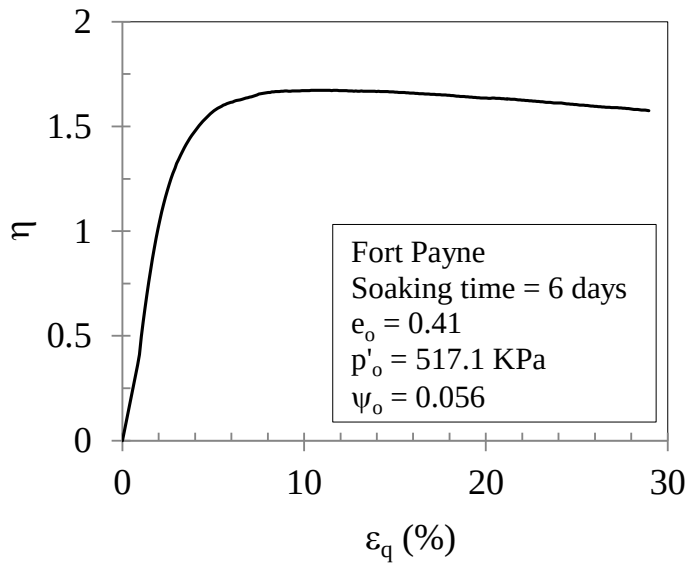
2
1.5
1
0.5
0
η
0
10
20
30
εq (%)
Fort Payne
Soaking time = 6 days
eo = 0.41
p'o = 517.1 KPa
ψo = 0.056

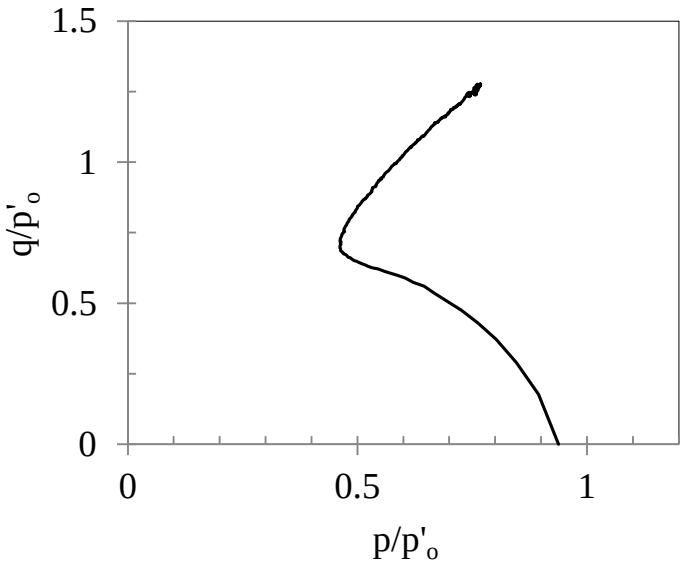
1.5
1
0.5
0
q/p'o
0
0.5
1
p/p'o

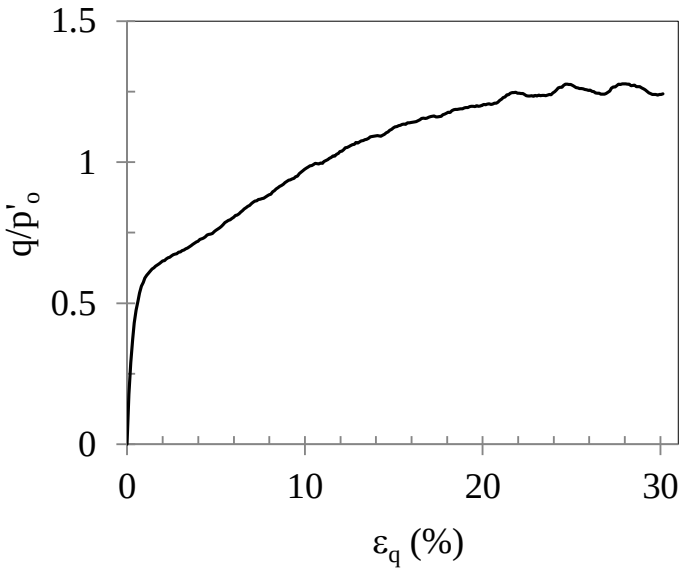
1.5
1
0.5
0
q/p'o
0
10
20
30
εq (%)

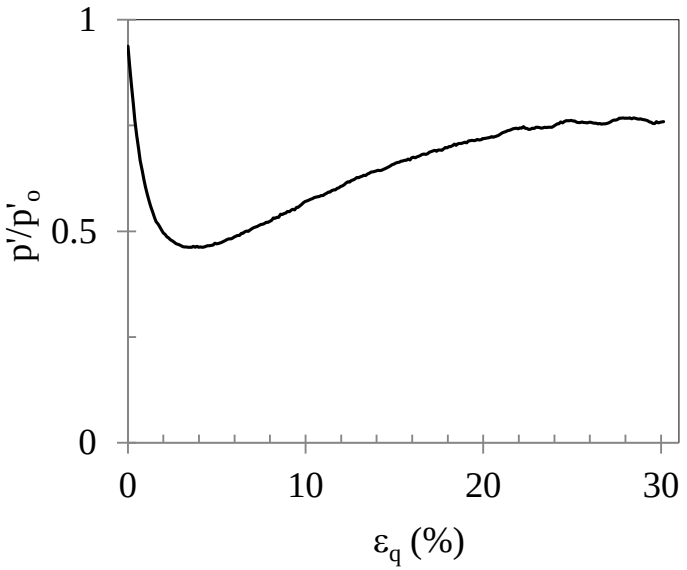
1
0.5
0
p'/p'o
0
10
20
30
εq (%)

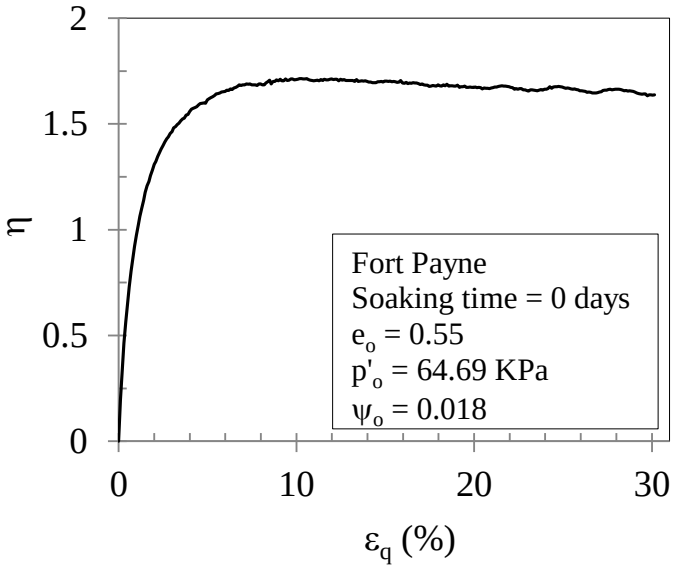
2
1.5
1
0.5
0
η
0
10
20
30
εq (%)
Fort Payne
Soaking time = 0 days
eo = 0.55
p'o = 64.69 KPa
ψo = 0.018

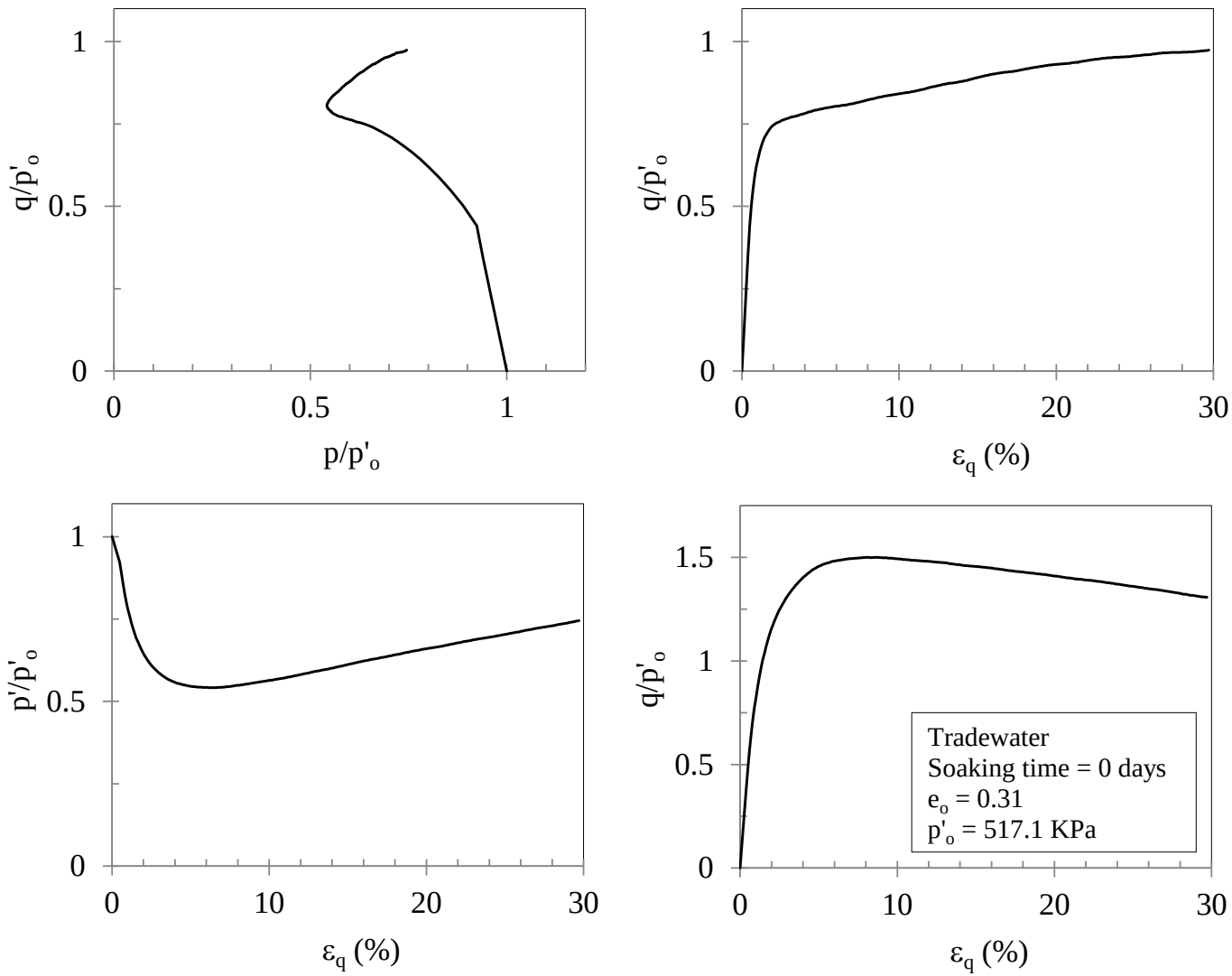
q/p'o
p/p'o
εq (%)
p'/p'o
Tradewater
Soaking time = 0 days
eo = 0.31
p'o = 517.1 KPa

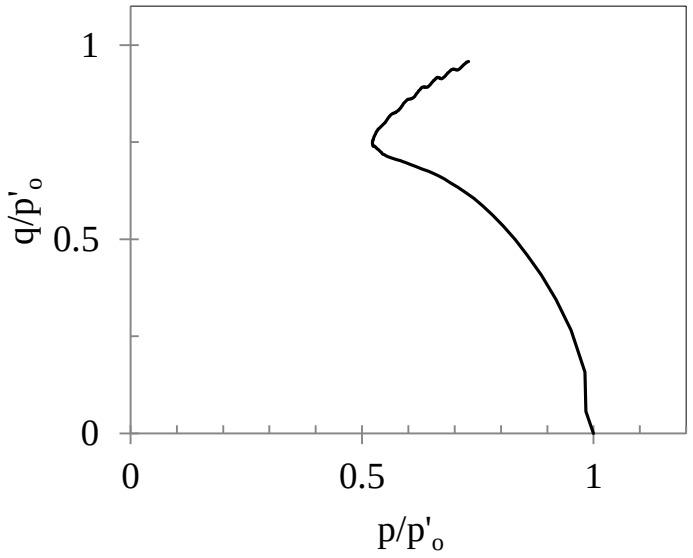
1
0.5
0
q/p'o
0
0.5
1
p/p'o

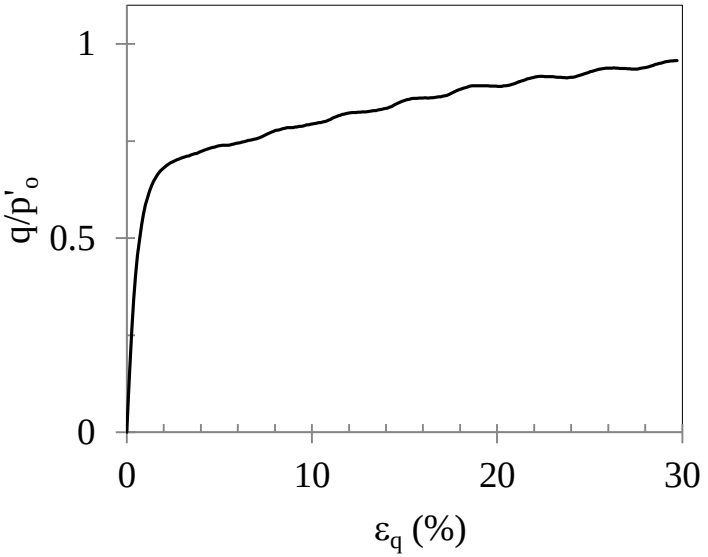
1
0.5
0
q/p'o
0
10
20
30
εq (%)

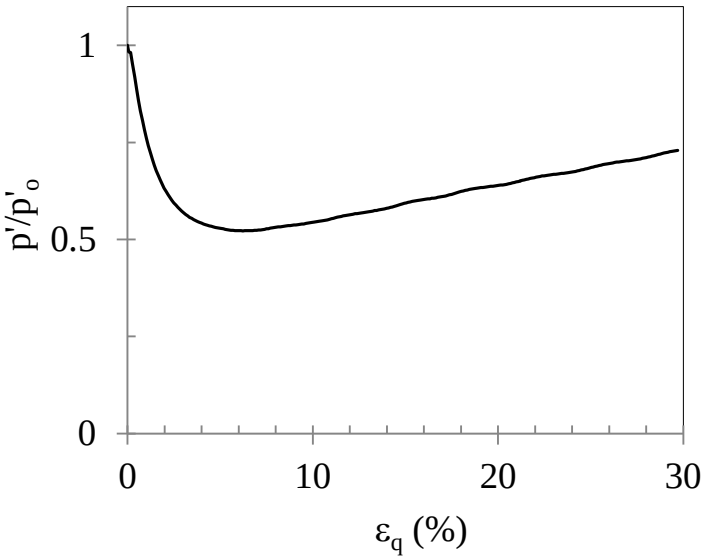
1
0.5
0
p'/p'o
0
10
20
30
εq (%)

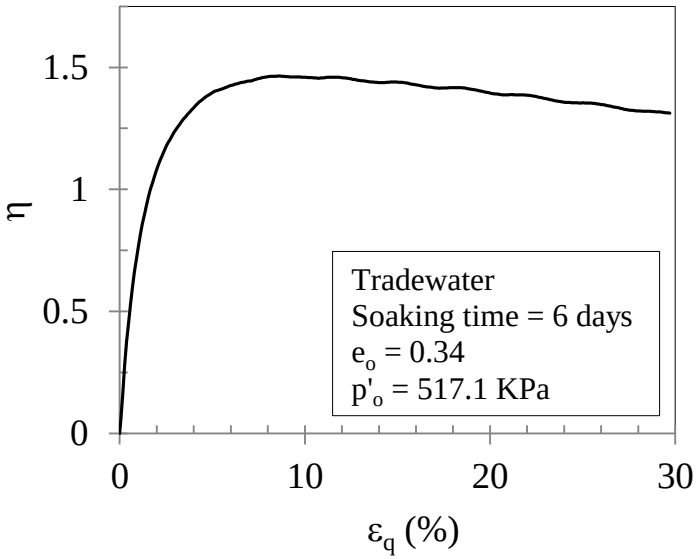
1.5
1
0.5
0
η
0
10
20
30
εq (%)
Tradewater
Soaking time = 6 days
eo = 0.34
p'o = 517.1 KPa

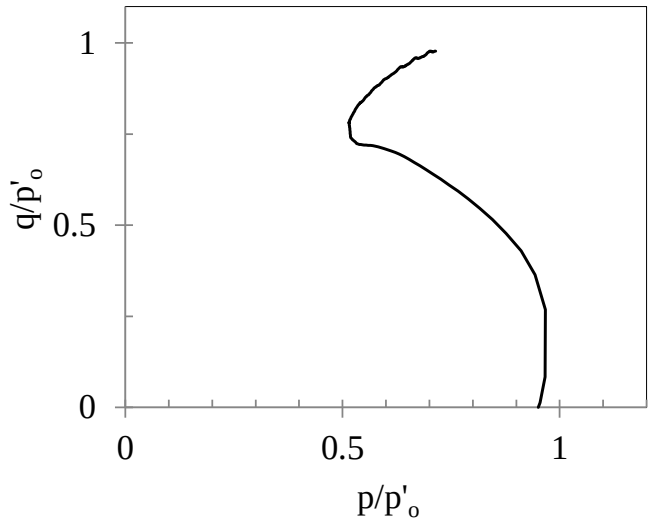
1
0.5
0
0
0.5
1
q/p'o
p/p'o

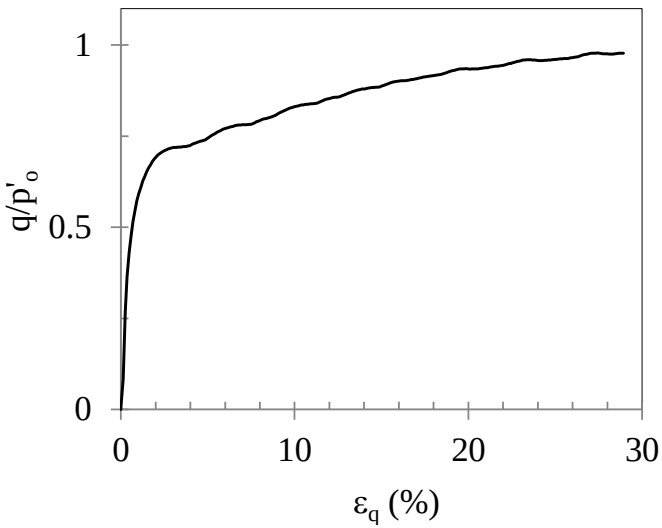
1
0.5
0
0
10
20
30
q/p'o
εq (%)

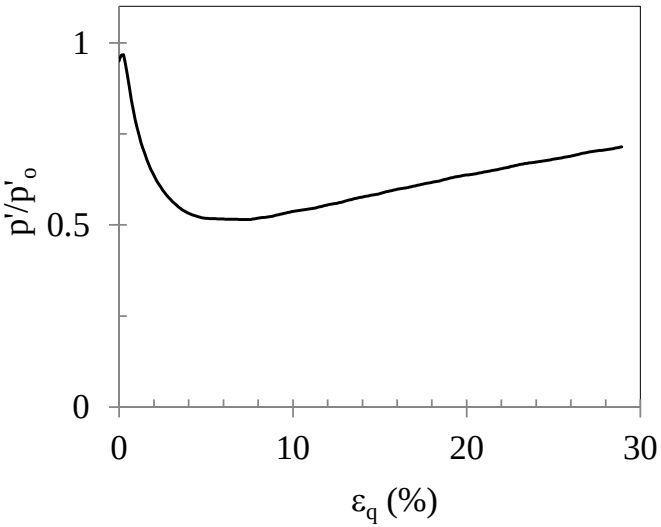
1
0.5
0
0
10
20
30
p'/p'o
εq (%)

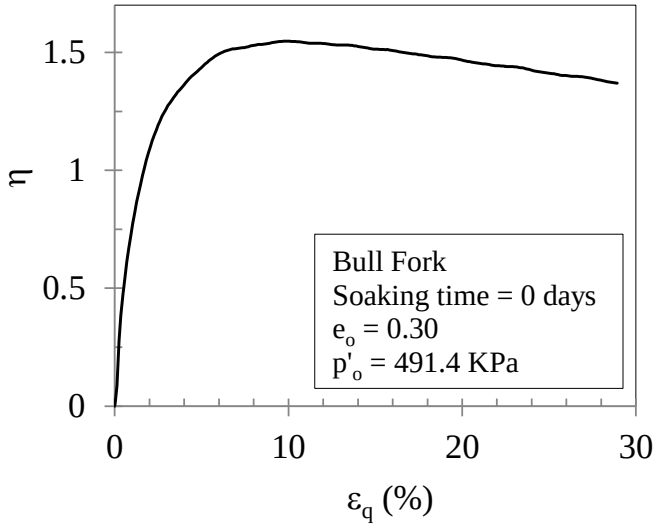
1.5
1
0.5
0
0
10
20
30
η
εq (%)
Bull Fork
Soaking time = 0 days
eo = 0.30
p'o = 491.4 KPa

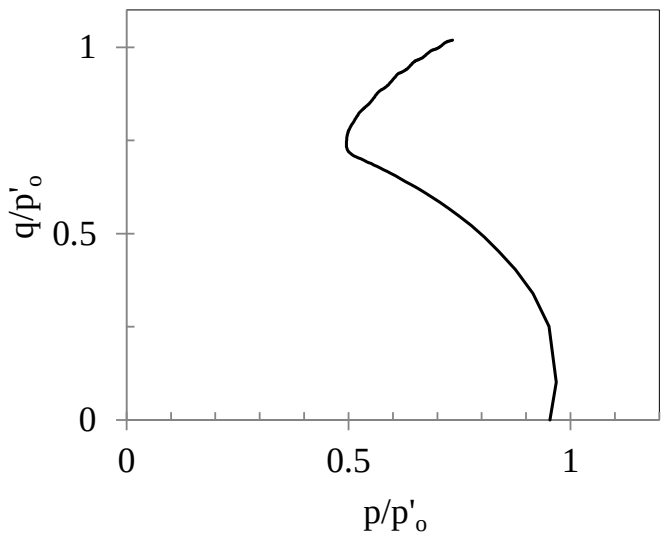
1
0.5
0
q/p'o
0
0.5
1
p/p'o

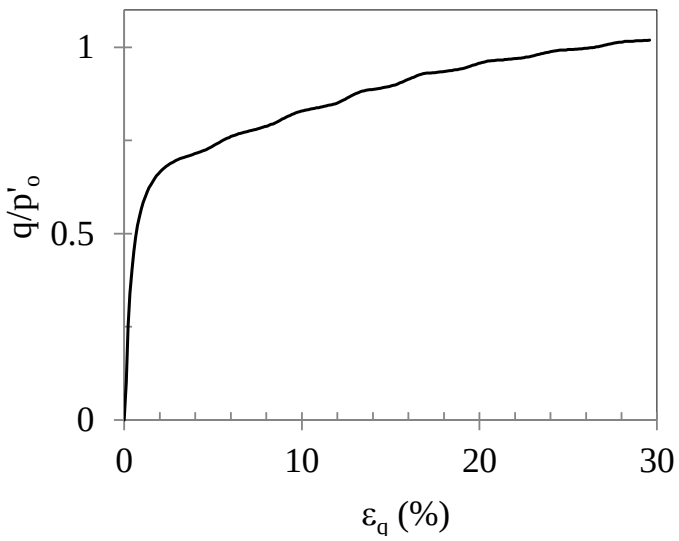
1
0.5
0
q/p'o
0
10
20
30
εq (%)

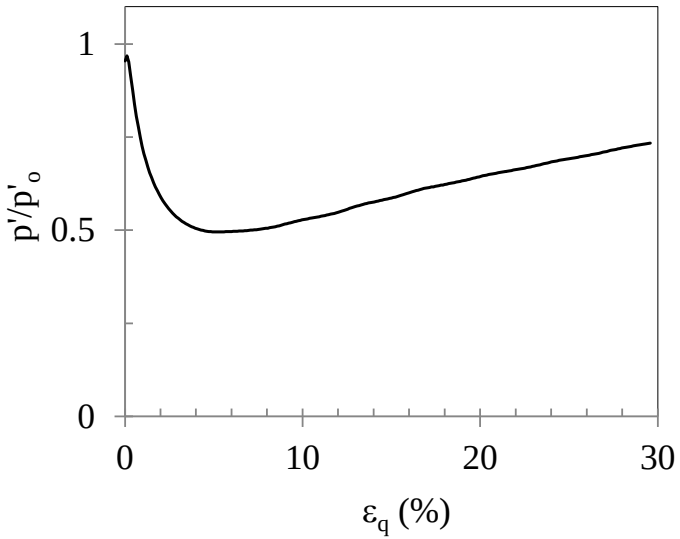
1
0.5
0
p'/p'o
0
10
20
30
εq (%)

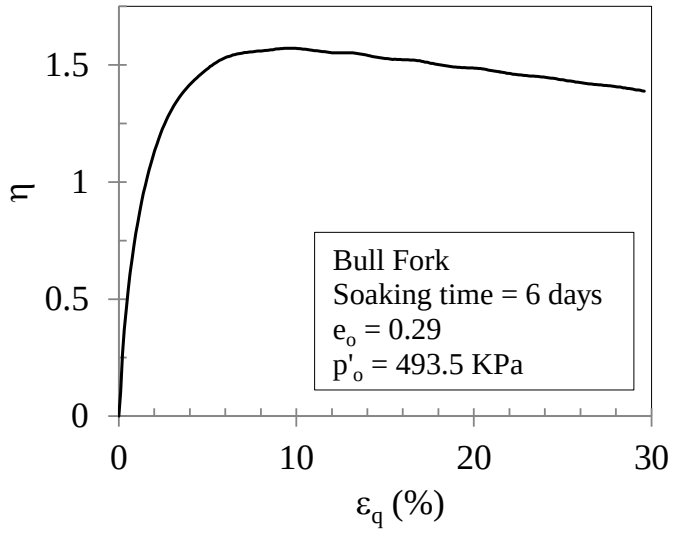
1.5
1
0.5
0
η
0
10
20
30
εq (%)
Bull Fork
Soaking time = 6 days
eo = 0.29
p'o = 493.5 KPa

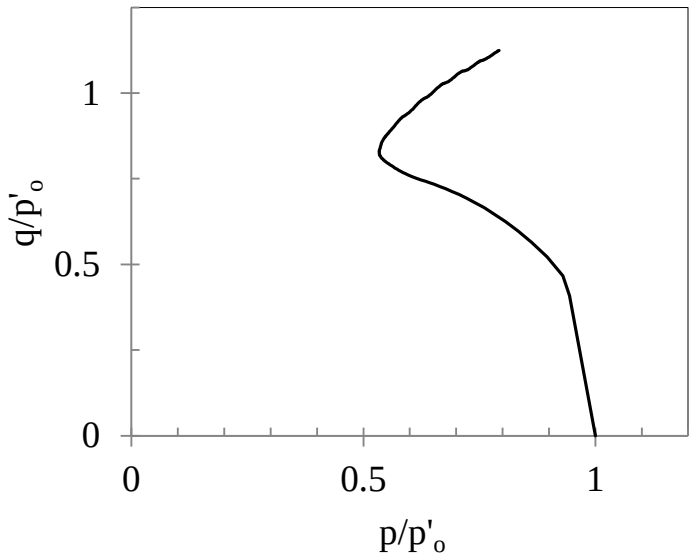
q/p'o
p/p'o
0
0.5
1

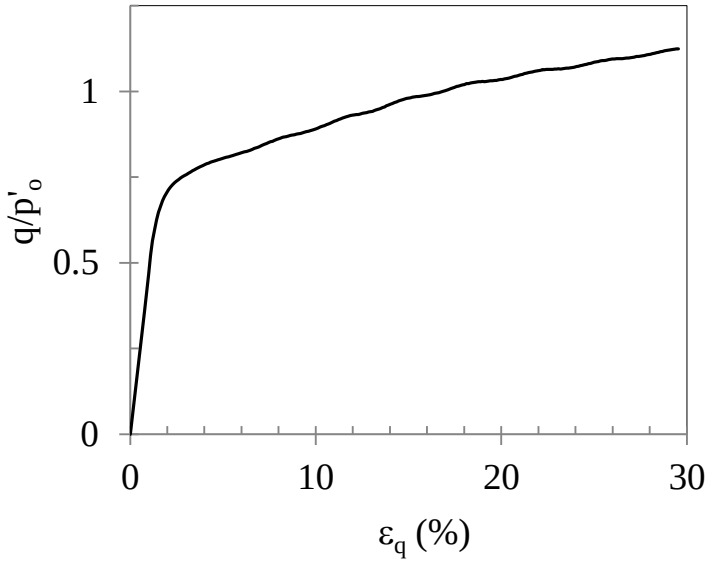
q/p'o
εq (%)
0
10
20
30
0.5
1

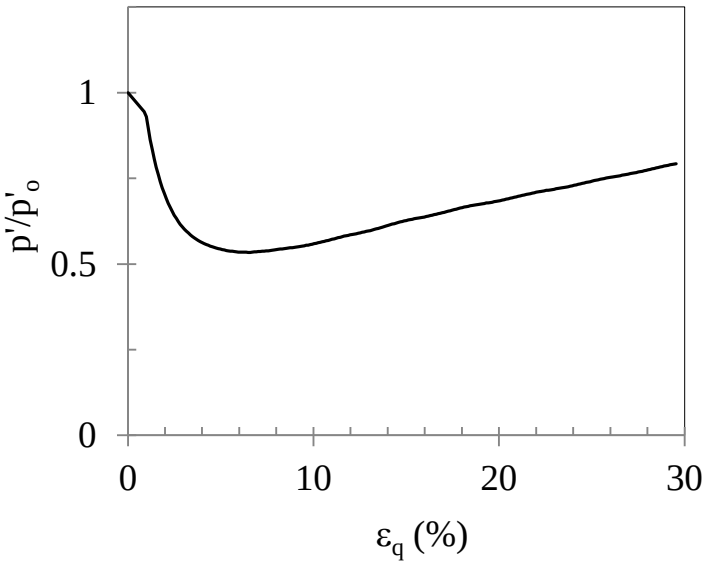
p'/p'o
εq (%)
0
10
20
30
0.5
1

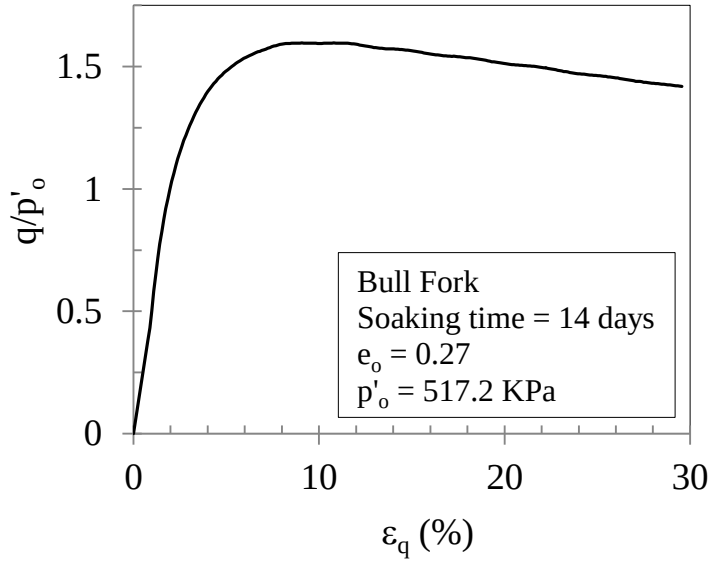
q/p'o
εq (%)
Bull Fork
Soaking time = 14 days
eo = 0.27
p'o = 517.2 KPa
0
10
20
30
0.5
1
1.5

APPENDIX J

STRESS - DILATANCY PATH

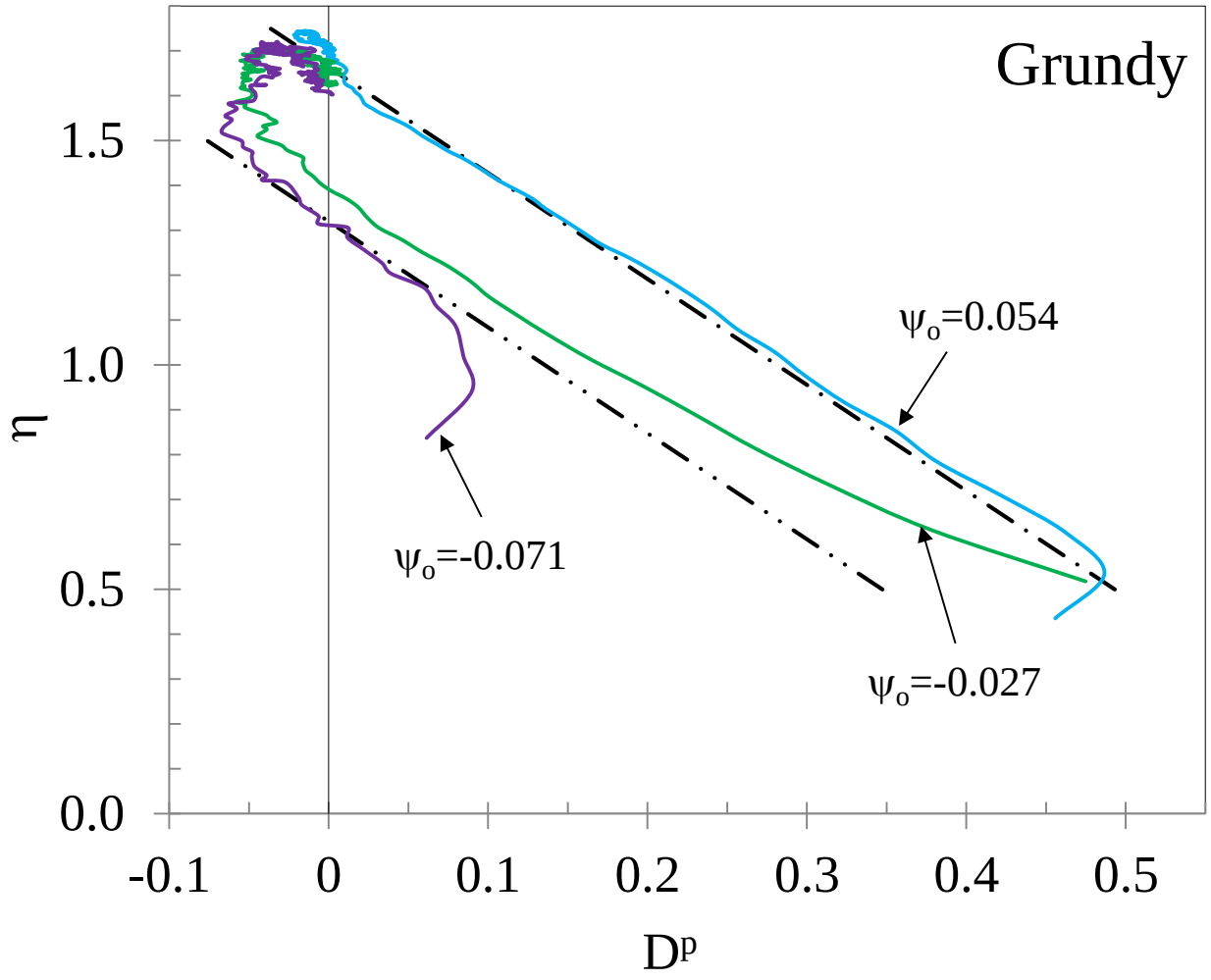
Grundy
1.5
1.0
0.5
0.0
η
-0.1
0
0.1
0.2
0.3
0.4
0.5
Dp
ψo=0.054
ψo=-0.071
ψo=-0.027

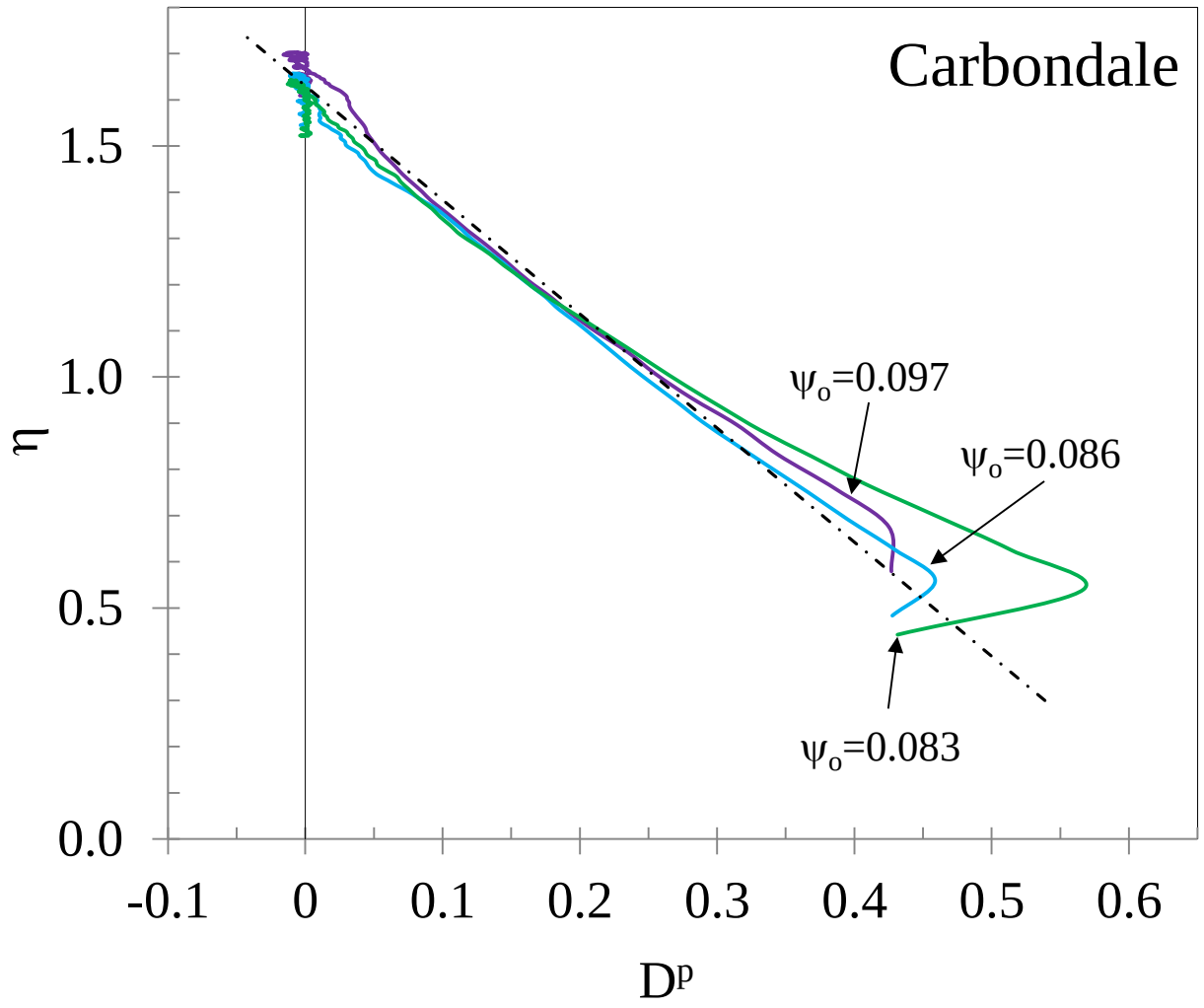
Carbondale
1.5
1.0
0.5
0.0
η
-0.1
0
0.1
0.2
0.3
0.4
0.5
0.6
Dp
ψo=0.097
ψo=0.086
ψo=0.083

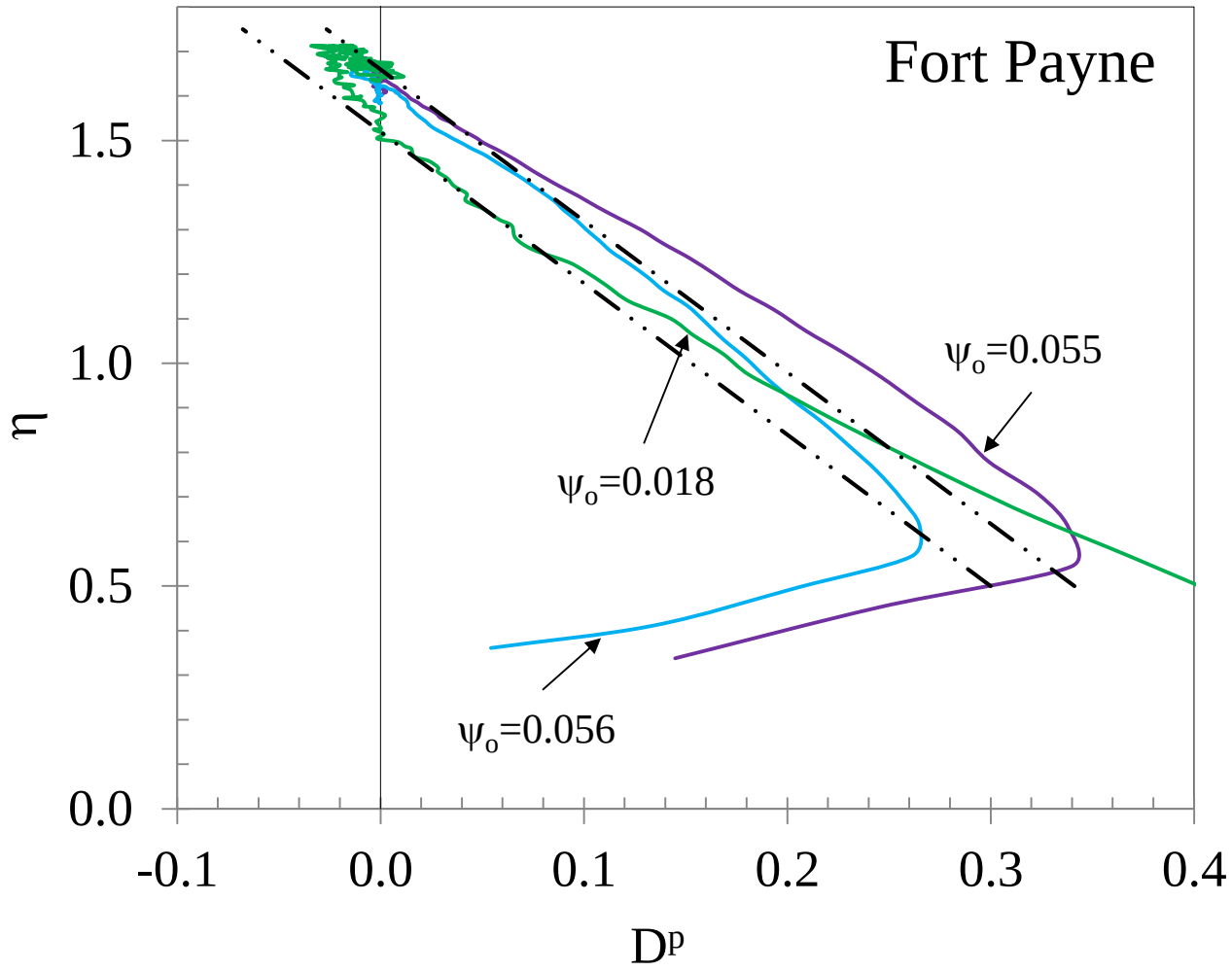
Fort Payne
1.5
1.0
0.5
0.0
η
-0.1
0.0
0.1
0.2
0.3
0.4
Dp
ψo=0.055
ψo=0.018
ψo=0.056

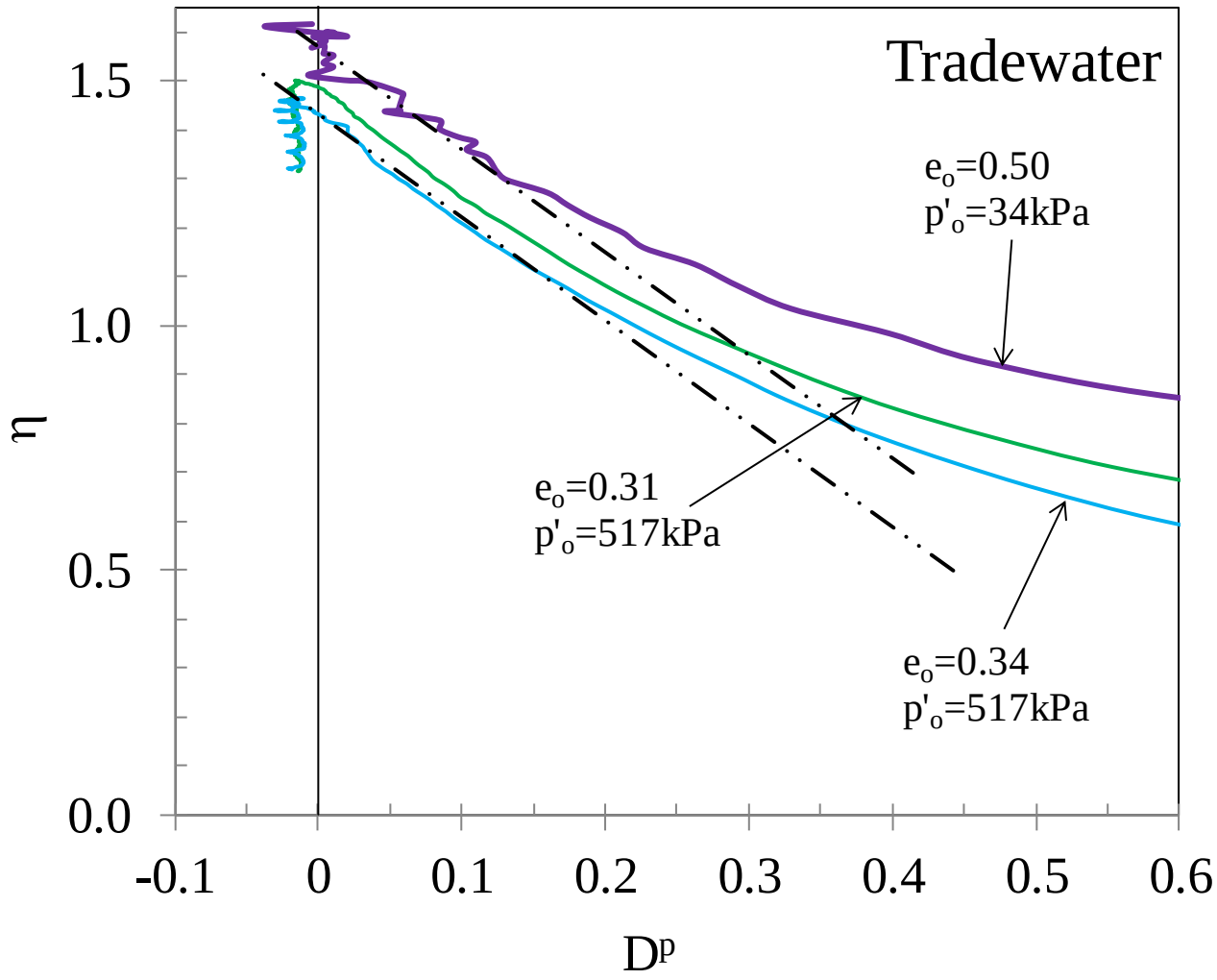
Tradewater
e_o=0.50
p'$_o$=34kPa
e_o=0.31
p'$_o$=517kPa
e_o=0.34
p'$_o$=517kPa
η
D^p
1.5
1.0
0.5
0.0
-0.1
0
0.1
0.2
0.3
0.4
0.5
0.6

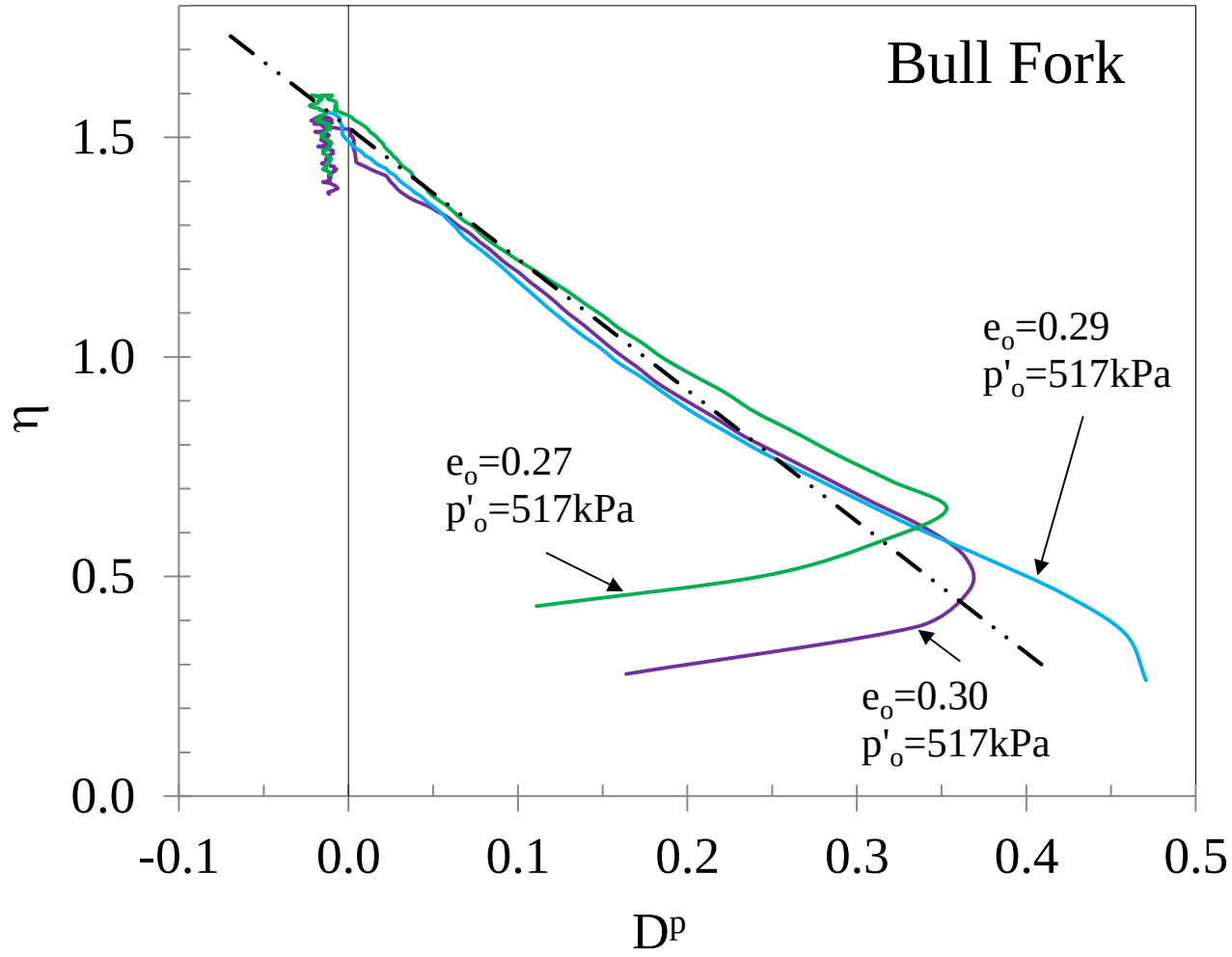
Bull Fork
1.5
1.0
0.5
0.0
η
-0.1
0.0
0.1
0.2
0.3
0.4
0.5
Dp
eo=0.29
p'o=517kPa
eo=0.27
p'o=517kPa
eo=0.30
p'o=517kPa

APPENDIX K

CODE

J1. CAMCLAY CODE

```
Sub OriginalCamClay()
' This code is a modification of the code by Shuttle http://www.itasca-udm.com.
' Undrained triaxial compression version
'Geometry
    pc = po / Exp(1)
    e_lamda = eo + lamda * Log(po)
    e_kapa = eo + kapa * Log(po)
    gama = eo + (lamda - kapa) * Log(pc) + kapa * Log(po)
'Elastic constants
    Kmax = ((1 + eo) / kapa) * po
    Gmax = (3 * (1 - 2 * nu) / (2 * (1 + nu))) * Kmax
'Critical state
    pcs = Exp((gama - eo) / lamda)
'Initial values
    eq = 0
    eqe = 0
    eqp = 0
    ep = 0
    epe = 0
    epp = 0
    p = po
    q = 0
    eta = q / p
    ph = po
    ph_star = po
'Start the loop
    eqmax = 0.3
    step = 5000
    Deqp = eqmax / step
```

```
For j = 1 To step
   dilatancy = Mc - eta
   Depp = dilatancy * Deqp
   Dp = -Depp * ((1 + eo) / kapa) * p
   pold = p
   p = p + Dp
   'Hardening rule. Wood: hardening relationship p 116
   ph = ph + (Depp * ph * (1 + eo) / (lamda - kapa))
   'New yield surface
   eta = Mc * Log(ph / p)
   qold = q
   q = eta * p
   Dq = q - qold
   'Pore pressure
   Du = po + q / 3 - p
   'Elastic behavior
   K = ((1 + eo) / kapa) * p
   G = (3 * (1 - 2 * nu) / (2 * (1 + nu))) * K
   'Strains
   Deqe = Dq / (3 * G)
   Depe = -Depp
   Deq = Deqp + Deqe
   Dep = Depp + Depp
   eqe = eqe + Deqe
   epe = epe + Depe
   eqp = eqp + Deqp
   epp = epp + Depp
   eq = eqe + eqp
   ep = epe + epp
   Next j
End
End Sub
```

J2. MODIFIED CAMCLAY CODE

```
Sub ModifiedCamClay()
' This code is a modification of the code by Shuttle http://www.itasca-udm.com.
' Undrained triaxial compression version
'Geometry
    pc = po / 2
    e_lamda = eo + lamda * Log(po)
    e_kapa = eo + kapa * Log(po)
    gama = eo + (lamda - kapa) * Log(pc) + kapa * Log(po)
'Elastic constants
    Kmax = ((1 + eo) / kapa) * po
    Gmax = (3 * (1 - 2 * nu) / (2 * (1 + nu))) * Kmax
'Critical state
    pcs = Exp((gama - eo) / lamda)
'Initial values
    eq = 0
    eqe = 0
    eqp = 0
    ep = 0
    epe = 0
    epp = 0
    p = po
    q = 0
    eta = q / p
    ph = po
    ph_star = po
'Start the loop
    eqmax = 0.3
    step = 5000
    Deqp = eqmax / step
```

```
For j = 1 To step
   'This if is only for ModifiedCamClay because dilatancy is 0/0 when eta=0
   If eta = 0 Then
      dilatancy = Mc
   Else
      dilatancy = (Mc ^ 2 - eta ^ 2) / (2 * eta)
   End If
   Depp = dilatancy * Deqp
   Dp = -Depp * ((1 + eo) / kapa) * p
   p = p + Dp
   'Hardening rule. Wood: hardening relationship p 116
   ph = ph + (Depp * ph * (1 + eo) / (lamda - kapa))
   'New yield surface: Modified Cam Clay
   eta = Mc * ((ph / p) - 1) ^ 0.5
   qold = q
   q = eta * p
   Dq = q - qold
   'Pore pressure
   Du = po + q / 3 - p
   'Elastic behavior
   K = ((1 + eo) / kapa) * p
   G = (3 * (1 - 2 * nu) / (2 * (1 + nu))) * K
   'Strains
   Deqe = Dq / (3 * G)
   Depe = -Depp
   Deq = Deqp + Deqe
   Dep = Depp + Depp
   eqe = eqe + Deqe
   epe = epe + Depe
   eqp = eqp + Deqp
   epp = epp + Depp
   eq = eqe + eqp
   ep = epe + epp
```

```
    Next j
End
End Sub
```

J3. NORSAND CODE

```
Sub NorSand()
' This code is a modification of the code by Shuttle http://www.itasca-udm.com.
' Undrained triaxial compression version
'Geometry
    'Current ncl and url line
    e_lamda = eo + lamda * Log(po)
    e_kapa = eo + kapa * Log(po)
'Elastic constants
    Kmax = ((1 + eo) / kapa) * po
    Gmax = (3 * (1 - 2 * nu) / (2 * (1 + nu))) * Kmax
    Ir = Gmax / po
    Ik = Kmax / po
'Critical state and State parameter
    ec = gama - lamdaNS * Log(po)
    psio = eo - ec
    pc = Exp((gama - eo) / lamdaNS)
'Initial values
    eq = 0
    eqe = 0
    eqp = 0
    ep = 0
    epe = 0
    epp = 0
    p = po
    q = 0
    eta = q / p
    psi = psio
    G = Gmax
'Imagine condition
    pi_p = Exp((eta / Mtc) - 1)
    p_i = pi_p * po
    psi_i = psio + lamdaNS * Log(pi_p)
    Mi = Mtc - N * chi * Abs(psi_i)
'Start the loop
    eqmax = 0.35
    step = 5000
    Deqp = eqmax / step
For j = 1 To step
        'Flow Rule
        Mi = Mtc - N * chi * Abs(psi_i)
        dilatancy = Mi - eta
        Depp = dilatancy * Deqp
        Dp = -Depp * Ik * p                    'Dp = -Depp * ((1 + eo) / kapa) * p
        p = p + Dp
```

```
        'Get current dilation limit
        psi_i = psi + lamdaNS * Log(pi_p)
        Dmin = chi * psi_i
        pi_p_max = Exp(-Dmin / Mi)
        'Hardening/Softening rule
        Dpi_pi = H * ((1 / pi_p) ^ 2) * (pi_p_max - pi_p) * Deqp
        pi_p = pi_p * (1 + Dpi_pi)    'pi_p = pi_p * (1 + Dpi_pi - (Dp / p))
        p_i = pi_p * p
        'New yield surface
        qold = q
        eta = Mi * (1 + Log(pi_p))
        q = eta * p
        Dq = q - qold
        'Void ratio and state parameter
        ec = gama - lamdaNS * Log(p)
        psi = eo - ec
        'Pore pressure
        Du = po + q / 3 - p
        'Strains
        Deqe = Dq / (3 * G)
        Depe = -Depp
        Deq = Deqp + Deqe
        Dep = Depp + Depp
        eqe = eqe + Deqe
        epe = epe + Depe
        eqp = eqp + Deqp
        epp = epp + Depp
        eq = eqe + eqp
        ep = epe + epp
        'Elastic behavior
        K = ((1 + eo) / kapa) * p
        G = (3 * (1 - 2 * nu) / (2 * (1 + nu))) * K
        Ir = G / p
        Ik = K / p
    Next j
End
End Sub
```

J4. ICGG CODE

```
Sub ICGG()
' This code is a modification of the code by Shuttle http://www.itasca-udm.com.
' Undrained triaxial compression version
'Geometry
   'Current ncl and url line
   e_lamda = eo + lamda * Log(po)
   e_kapa = eo + kapa * Log(po)
'Elastic constants
   Kmax = ((1 + eo) / kapa) * po
   Gmax = (3 * (1 - 2 * nu) / (2 * (1 + nu))) * Kmax
   Ir = Gmax / po
   Ik = Kmax / po
'Critical state and State parameter
   ec = gama - lamdaNS * Log(po)
   psio = eo - ec
   pc = Exp((gama - eo) / lamdaNS)
'Initial values
   eq = 0
   eqe = 0
   eqp = 0
   ep = 0
   epe = 0
   epp = 0
   p = po
   q = 0
   eta = q / p
   psi = psio
   G = Gmax
'Imagine condition
   pi_p = ((1 / mu) - (((1 - mu) / mu) * eta / Mtc)) ^ (-mu / (1 - mu))
   p_i = pi_p * po
   psi_i = psio + lamdaNS * Log(pi_p)
   Mi = Mtc
'Start the loop
   eqmax = 0.35
   step = 5000
   Deqp = eqmax / step
For j = 1 To step
      'Flow Rule
      dilatancy = (Mi - eta) / mu
      Depp = dilatancy * Deqp
      Dp = -Depp * Ik * p          'Dp = -Depp * ((1 + eo) / kapa) * p
      p = p + Dp
```

```
        'Get current dilation limit
        psi_i = psi + lamdaNS * Log(pi_p)
        Dmin = chi * psi_i
        pi_p_max = ((1 / mu) - (((1 - mu) / mu) * ((Mtc - (1 - N) * Dmin) / Mi))) ^ (-mu / (1
- mu))
        'Hardening/Softening rule
        Dpi_pi = H * ((1 / pi_p) ^ 2) * (pi_p_max - pi_p) * Deqp
            pi_p = pi_p * (1 + Dpi_pi)
            p_i = pi_p * p
        'Dpi = Dpi_pi * p_i
        'p_i = p_i + Dpi
        'pi_p = p_i / p
        'New yield surface
        qold = q
        eta = (Mi / (1 - mu)) * (1 - mu * (1 / pi_p) ^ ((1 - mu) / mu))
        q = eta * p
        Dq = q - qold
        'Void ratio and state parameter
        ec = gama - lamdaNS * Log(p)
        psi = eo - ec
        'Stress ratio at image condition
        Mi = Mtc - (mu - (1 - N)) * chi * Abs(psi_i)
        'Pore pressure
        Du = po + q / 3 - p
        'Strains
        Deqe = Dq / (3 * G)
        Depe = -Depp
        Deq = Deqp + Deqe
        Dep = Depp + Depp
        eqe = eqe + Deqe
        epe = epe + Depe
        eqp = eqp + Deqp
        epp = epp + Depp
        eq = eqe + eqp
        ep = epe + epp
        'Elastic behavior
        K = ((1 + eo) / kapa) * p
        G = (3 * (1 - 2 * nu) / (2 * (1 + nu))) * K
        Ir = G / p
        Ik = K / p
    Next j
End

End Sub
```

REFERENCES

Abeyesekera, R. A., Lovell, C. A., and Wood, L. E. (1979). "Strength Testing of Compacted Shale." *Geotechnical Testing Journal*, 2(1), 11 - 19.

Bishop, C.S., Armour, D. W., and Hopkins, T. C. (1986). "Design of highway embankments on unstable natural slopes" *Final Report, UKTRP-86-22*, University of Kentucky Transportation Research Program, Lexington, Kentucky.

Aziz, M., Towhata, I., Yamada, S., Qureshi, M. U., and Kawano, K. (2010). "Water-induced granular decomposition and its effects on geotechnical properties of crushed soft rocks." *Natural Hazards and Earth System Science*, 10(6), 1229-1238.

Baldi, G., and Nova, R. (1984). "Membrane penetration effects in triaxial testing." *Journal of Geotechnical engineering*, 110(3), 403-420.

Bjolykke, K. (1998). "Clay mineral diagenesis in sedimentary basins-a key to the prediction of rock properties. Examples from the North Sea Basin." *Clay minerals*, *33*(1), 15-34.

Boggs, S. (2009). *Petrology of sedimentary rocks.* 2nd Ed., Cambridge University Press. Cambridge.

Bolton, M. D. (1986). "The strength and dilatancy of sands." *Geotechnique*, 36(1), 65-78.

Bryson, L. S., Gomez-Gutierrez, I. C., and Hopkins, T. C. (2012). "Development of a new durability index for compacted shale." *Engineering Geology*, 139, 66-75.

Budhu, M. (2008). *Soil mechanics and foundations*, 3rd Ed., John Wiley and Sons, New York.

Caswell, R. H., and Trak, B. (1985). "Some geotechnical characteristics of fragmented Queenston Shale." *Canadian geotechnical journal*, 22(3), 403-408.

Essington, M. E. (2003*). Soil and water chemistry: An integrative approach*, . CRC press.

Chilingarian, G. V., and Yen, T. F. (Eds.). (2011). *Oil shale.* Elsevier, New York.

Collins, I. F., (2005). "The concept of stored plastic work or frozen elastic energy in soil

mechanics." *Geotechnique*, 55(5), 373-382.

Franklin, J. A., and Chandra, R. (1972, May). "The slake-durability test." *International Journal of Rock Mechanics and Mining Sciences and Geomechanics Abstracts*, 9(3), 325-328.

Hale, B. C., Lovell, C. W., and Wood, L. E. (1981). "Development of a laboratory compaction-degradation test for shales." *Transportation Research Record* 790, Transportation Research Board, Washington, D.C.

Hopkins, T. C. (1988). "Shear strength of compacted shales." *Final Report UKTRP-88-1*, University of Kentucky Transportation Research Program, Lexington, Kentucky.

Hopkins, T. C. (2007). "Compaction of Mixtures of Hard Rocks and Soft Shales and Non-durable Shales Using Impact Compactors." *Final Report KTC-07-18/SPR 339-07-1F*, University of Kentucky Transportation Research Program, Lexington, Kentucky.

Hopkins T. C. and Beckham T. L (1998). "Embankment construction using shale." *Final Report KTC-98-2*, University of Kentucky Transportation Research Program, Lexington, Kentucky.

Jackson, M. L. (1969). *Soil Chemical Analysis-Advanced Course. Soil Chemical Analysis-Advanced Course*, 2nd Ed. U. of Wisconsin Press, Madison.

Jefferies, M. G. (1993). "Nor-Sand: a simple critical state model for sand." *Geotechnique*, 43(1), 91-103.

Jefferies, M.G. (1997). "Plastic work and isotropic softening in unloading." *Geotechnique*, 47(5), 1037-1042.

Jefferies, M., and Been, K. (2004). *Soil liquefaction: a critical state approach.* Taylor and Francis, London and New York.

Jefferies, M., and Been, K. (2000). "Implications for critical state theory from isotropic compression of sand." *Geotechnique*, 50(4),419-429.

Kalinski, M. E., Karem, W. A., and Little, L. M. (2010). "Estimating hydrocompression potential of mine spoils from a site in eastern Kentucky using dry unit weight and

moisture content." *International Journal of Mining, Reclamation and Environment,* 24(4), 350-362.

Karathanasis, A. D. (2008). *Thermal analysis of soil minerals. Methods of Soil Analysis Part 5—Mineralogical Methods*. Soil Science Society of America.

Karathanasis, A. D., and Hajek, B. F. (1982). "Revised methods for rapid quantitative determination of minerals in soil clays." *Soil Science Society of America Journal*, 46(2), 419-425.

Kunze, G. W., and Dixon, J. B. (1986). *Pretreatment for mineralogical analysis. Methods of Soil Analysis: Part 1—Physical and Mineralogical Methods,* 2nd Ed., Agronomy Society of America and Soil Science of America, Madison, Wis.

Lade, P. V., and Hernandez, S. B. (1977). "Membrane penetration effects in undrained tests." *Journal of the Geotechnical Engineering Division,* 103(2), 109-125.

Lagaly, G., Ogawa, M., Dérkány, I. E., Bergaya, F., Theng, B. K. G., and Lagaly, G. (2006). *Handbook of clay science.* Vol. 1, Elsevier Ltd., The Netherlands.

Lawton, E. C., Fragaszy, R. J., and Hetherington, M. D. (1992). "Review of wetting-induced collapse in compacted soil." *Journal of geotechnical engineering*, 118(9), 1376-1394.

Li, X. S. (1997). "Modeling of dilative shear failure." *Journal of geotechnical and geoenvironmental engineering*, 123(7), 609-616.

Li, X. S., Dafalias, Y. F., and Wang, Z. L. (1999). "State-dependant dilatancy in critical-state constitutive modelling of sand." *Canadian Geotechnical Journal*, 36(4), 599-611.

Li, X. S., and Dafalias, Y. F. (2000). "Dilatancy for cohesionless soils." *Geotechnique,* 50(4), 449-460.

Lim, Y. Y., and Miller, G. A. (2004). "Wetting-induced compression of compacted Oklahoma soils." *Journal of geotechnical and geoenvironmental engineering,* 130(10), 1014-1023.

Lindgreen, H., Drits, V. A., Sakharov, B. A., Jakobsen, H. J., Salyn, A. L., Dainyak, L.

G., and Krøyer, H. (2002). "The structure and diagenetic transformation of illite-smectite and chlorite-smectite from North Sea Cretaceous-Tertiary chalk." *Clay Minerals*, 37(3), 429-450.

Liu, M. D., and Carter, J. P. (2002). "A structured Cam Clay model." *Canadian Geotechnical Journal*, 39(6), 1313-1332.

Manasseh, J., and Olufemi, A. I. (2008). "Effect of lime on some geotechnical properties of Igumale shale." *Electronic Journal of Geotechnical Engineering*, 13(A), 1-12.

Liang, Y., and Lovell, C. W. (1983). "Strength of field compacted clays." *Canadian Geotechnical Journal*, 20(1), 36-46.

Machan, G., Szymoniak, T., and Siel, B. (1989). "Evaluation of shale embankment construction criteria." *Final Report OR83-02*, Oregon Department of Transportation., Salem, Oregon.

McDowell, R. (1986). "The Geology of Kentucky – a text to accompany the Geologic Map of Kentucky." <http://pubs.usgs.gov/prof/p1151h/contents.html> (2013).

Murray, H. H. (2006). *Applied Clay Mineralogy: Occurrences, Processing and Applications of Kaolins, Bentonites, Palygorskitesepiolite, and Common Clays*. 1st Ed., Elsevier, New York.

Mitchell, J., and Soga, K. (2006). *Fundamentals of Soil Behavior*. 3rd Ed., John Wiley and Sons, New Jersey.

Nahazanan, H., Clarke, S., Asadi, A., Md Yusoff, Z., and Huat, B. K. (2013). "Effect of Inundation on Shear Strength Characteristics of Mudstone Backfill." *Engineering Geology*, 158(1), 48-56.

Nichols, G. (2009). *Sedimentology and stratigraphy*. 2nd Ed., Wiley-Blackwell, Malden, Ma.

Noble, D. F. (1977). "Accelerated weathering of tough shales" *Final Report*, No. VHTRC-78-R20, Virginia Highway and Transportation Research Council, Charlottesville, VA.

Nova, R. (1982). *A constitutive model for soil under monotonic and cyclic loading. Soil*

mechanics-transient and cyclic loads. (eds G. N. Pande and O. C. Zienkiewicz). Chichester: Wiley, pp. 343–373.

Nova, R., and Wood, D. M. (1979). "A constitutive model for sand in triaxial compression." *International Journal for Numerical and Analytical Methods in Geomechanics*, 3(3), 255-278.

Oakland, M. W., and Lovell, C. W. (1985). "Building embankments with shale." *26th Symposium of Rock Mechanics*, Rapid City, S.D., 305-312.

Pye, K., and Miller, J. A. (1990). "Chemical and biochemical weathering of pyritic mudrocks in a shale embankment." *Quarterly Journal of Engineering Geology and Hydrogeology*, 23(4), 365-382.

Reeves, G. M., Sims, I., and Cripps, J. C. (2006). *Clay materials used in construction*. Geological Society of London.

Roscoe, K. H., and Burland, J. B. (1968). "On the generalized stress-strain behaviour of wet clay." *Engineering Plasticity*, Cambridge University Press, Cambridge, England, 365-609.

Roscoe, K. H., Schofield, A., and Thurairajah, A. (1963). "Yielding of clays in states wetter than critical." *Geotechnique*, 13(3), 211-240.

Shamburger, J. H., Patrick, D. M., and Lutton, R. J. (1975). "Design and construction of compacted shale embankments, Volume 2, Survey of problem areas and current practices." *Final Report, No. FHWA-RD-75-61*, United States Department of Transportation.

Schofield, A. N., and Wroth, P. (1968). *Critical state soil mechanics*. McGraw-Hill, New York.

Sposito, G. (1989). *The chemistry of soils.* Oxford University Press, New York.

Shuttle, D., and Jefferies, M. (2010). "Norsand: description, calibration, validation and applications." <http://itasca-udm.de/media/download/norsandm/NorSand_M.pdf> (2010).

Strohm, W. E. (1980). "Design and construction of shale embankments: summary." *Final*

Report, No FHWA-TS-80-219, United States Department of Transportation.

Surendra, M. (1980). "Additives to control slaking in compacted shales." Doctoral dissertation, Purdue University, Lafayette, Indiana.

Tucholke, B. E., Sibuet, J. C., Klaus, A., et al. (2004). "Drilling the Newfoundland Half of the Newfoundland–Iberia." *Proceedings of the Ocean Drilling Program, Initial Reports Volume 210, Prepared by the, ocean drilling program*, Texas AandM university.

Wallace, A., and Terry, R. E. (Eds.). (1998). *Handbook of soil conditioners: substances that enhance the physical properties of soil.* Marcel Dekker, New York.

Walther, J. V. (2009). *Essentials of geochemistry.* Jones and Bartlett, Sudbury, Massachusetts.

Wolf, J. A. (2008). "A plasticity model to predict the effects of confinement on concrete." Doctoral dissertation, California Institute of Technology, Pasadena, California.

Wood, D. M. (1991). *Soil behaviour and critical state soil mechanics.* Cambridge university press, New York.

Wu, T. H., Randolph, B. W., and Huang, C. S. (1993). "Stability of shale embankments." *Journal of geotechnical engineering*, 119(1), 127-146.

Yoshida, N., and Hosokawa, K. (2004). "Compression and shear behavior of mudstone aggregates." *Journal of geotechnical and geoenvironmental engineering*, 130(5), 519-525.

Yu, H. S. (2006). *Plasticity and geotechnics.* Springer, New York.

VITA

EDUCATION

UNIVERSITY OF KENTUCKY, Lexington, Kentucky

Fall 2013

Ph.D. in Civil Engineering

Dissertation: Development of a constitutive model of compacted shales and determination of the effect of weathering on its parameters

UNIVERSIDAD NACIONAL DE COLOMBIA, Bogotá D.C., Colombia

December 2001

M.Sc. Geotechnical Engineering, Civil Engineer Department

Meritorious Thesis: Expansion of cavities in materials with non-linear shear strength envelope

UNIVERSIDAD DE CALDAS, Manizales, Colombia

June 1995

B.Sc. Geologist, School of Geology

WORK EXPERIENCE

UNIVERSITY OF KENTUCKY, Lexington, Kentucky

2008 – 2013

Teaching Assistant CE 471G Soil Mechanics, CE579 Geotechnical Engineering

Research Assistant performing advanced soil mechanics tests.

ROCAS Y MINERALES S.A.S. (Rocks and Minerals Inc.), Bogotá D.C., Colombia

Geotechnical/Geological Engineer

2001/2002-2003/2004-2008

Analysis of slope stability and hazard assessment in open pit mines. Instrumentation for blast mitigation, monitoring and control in open pit mines. Geological modeling of coal, limestone, and sand deposits using Geocom-Surpac and Carlson SurvCADD. Taught training for Geocom-Surpac.

GEOINGENIERIA S.A. Bogotá D.C., Colombia
July - August 2002
Geologist
Photogeological interpretation to identify landslides in Cordillera Oriental, Casanare, Colombia.

UNIVERSIDAD NACIONAL DE COLOMBIA, Bogotá D.C., Colombia
Instructor Workshop I - laboratory of Civil Engineering
January 2001-May 2001

INGEOMINAS, Manizales and Bogotá D.C., Colombia
1990 – 1997
Geologist (Institute of Geology and Mining of Colombia)
Study of volcanic and tectonic earthquakes.

PROFESSIONAL ORGANIZATIONS
American Society of Civil Engineers
Society for Mining, Metallurgy & Exploration

HONOR AND AWARDS
UNIVERSITY OF KENTUCKY
Lyman T. Johnson Academic Year Fellowship
2009 – 2012
UNIVERSIDAD NACIONAL DE COLOMBIA
First class with distinction
1999 - 2000

PUBLICATIONS
Bryson, L.S., Gomez-Gutierrez, I.C., Hopkins T.C. (2012). "Development of a new durability index for compacted shale" *Engineering Geology*, Vol. 139-140, 66-75.

Gomez-Gutierrez, I.C., Bryson, L.S., and Hopkins T.C. “Correlations between Geotechnical Properties and the Swell Behavior of Compacted Shales”. GeoFrontiers 2011, Dallas, Texas, 13-16 March 2011.

Bryson, L.S., Gomez-Gutierrez, I.C., and Hopkins T.C. “Correlations between Durability and Geotechnical Properties of Compacted Shales”, GeoFrontiers 2011, Dallas, Texas, 13-16 March 2011.

Gómez-Gutierrez, I.C., Silva-Castro, J.J. and Hernández-Rodriguez, F. “Cálculo de probabilidad de falla para taludes mineros y su aplicación en un talud de las minas de agregados del Tunjuelo en Bogotá D.C.” (Probability of mine slope failure), Congreso Colombiano de Geotecnia, Cartagena de Indias, Colombia, Octubre 2006.

Gómez-Gutierrez, I.C. and Hernández-Rodriguez, F. “Expansión de cavidades con envolventes curvas de resistencia” (Expansion of cavities in materials with non-linear shear strength envelope), Congreso Colombiano de Geotecnia, Medellín, Colombia, Noviembre 2002.

Gómez-Gutierrez, I.C. and Hernández-Rodriguez, F. “Expansión de cavidades cilíndricas en un continuo elástico plástico perfecto” (Expansion of cavities in a elastic-perfectly plastic continuum), VI Congreso Colombiano de Elementos Finitos y Modelamiento Numérico, Bogotá, Colombia, Mayo de 2002.